The High Energy Telescope on Solar Orbiter
-
Development and Validation of the Onboard Data Processing

Dissertation
zur Erlangung des Doktorgrades
der Mathematisch-Naturwissenschaftlichen Fakultät
der Christian-Albrechts-Universität zu Kiel
vorgelegt von

Robert Elftmann

Kiel, Mai 2020

Erster Gutachter:	Prof. Dr. R.F. Wimmer-Schweingruber
Zweiter Gutachter:	Prof. Dr. H. Kersten
Tag der mündlichen Prüfung:	21.07.20
Zum Druck genehmigt:	21.07.20

Zusammenfassung

Die Raumsonde Solar Orbiter der Europäischen Raumfahrtorganisation ESA wurde erfolgreich am 10.02.2020 von Cape Canaveral in den USA gestartet. Im Laufe der sieben jährigen nominellen Missionsphase wird sie sich bis auf eine Distanz von 0.27 astronomischen Einheiten an die Sonne annähern um diese zu studieren. Solar Orbiter wird dazu beitragen offene wissenschaftliche Fragen zu den Vorgängen auf und innerhalb der Sonne zu beantworten. Dazu ist die Raumsonde mit einer Anzahl an wissenschaftlichen Messinstrumenten ausgestattet, die sich aus Fernerkundungs- sowie In-situ-Instrumenten zusammensetzt. Eines dieser Messinstrumente ist der Energetic-Particle-Detector (EPD), der aus vier separaten Teleskopen besteht: dem Suprathermal Electron and Proton - Teleskop (STEP), dem Electron and Proton Telescope (EPT), dem Suprathermal Ion Spectrograph (SIS) und dem High Energy Telescope (HET). HET misst Elektronen mit Energien zwischen 0.45 bis 18 MeV, Protonen mit Energien zwischen 7 bis 105 MeV und Schwerionen im Energiebereich von 7 bis zu mehreren hundert MeV/nuc. Dabei können die individuellen Teilchen- und Ionenspezies identifiziert werden und sogar eine Trennung der Heliumisotope ^{3}He und ^{4}He bis zu einem Verhältnis von 1% ist möglich. Damit ist HET in der Lage die energieabhängige Teilchenkomposition von solaren energiereichen Teilchenereignissen in den angegebenen Energiebereichen zu messen und einen Einblick in deren Beschleunigungs- und Propagationsprozesse zu liefern.
Diese Arbeit beschäftigt sich mit der Entwicklung der onboard Datenverarbeitung des HET, welche die wissenschaftlichen Daten definiert, die zur Charakterisierung der gemessenen Teilchenumgebung zur Verfügung stehen.
Als Teil der im Rahmen dieser Arbeit durchgeführten Vorstudien wird der Einfluss der Instrumententemperatur auf die Messung von Schwerionen in Bezug auf den von HET verwendeten Szintillationskristall untersucht. Dabei wird gezeigt, dass die Nichtlinearität in der Lichtausbeute, genannt Ionisationsquenching, welche durch hohe Ionisationsdichten bei der Detektion von Schwerionen auftreten, im Falle des untersuchten Szintillationskristalls temperaturunabhängig ist. Die Ergebnisse dieser Studie wurden in der Zeitschrift “Nuclear Instruments and Methods in Physics Research Section B: Beam Interactions with Materials and Atoms”, Volume 451 (2019), veröffentlicht. Basierend auf den Ergebnissen können für die Entwicklung der onboard Datenverarbeitung bestehende Modelle zur Vorhersage

des Ionisationsquenchings genutzt werden.
Aufgrund der Telemetrielimitierung für die Instrumente auf Solar Orbiter ist es notwendig, dass gemessene Daten bereits vor der Übermittlung kategorisiert und ausgewertet werden. Die als Teil dieser Arbeit entwickelte onboard Datenverarbeitung wird nachvollziehbar und detailliert beschrieben. Die im Rahmen dieser Arbeit erstellten Simulationen, welche die Wechselwirkung von geladenen energiereichen Teilchen mit HET beschreiben und für die Entwicklung der onboard Datenverarbeitung notwendig sind, werden ebenso präsentiert und dokumentiert. Die damit entwickelte onboard Datenverarbeitung analysiert detektierte Teilchen und ordnet sie entsprechend ihrer Energie und Teilchenspezies in vordefinierte Histogramme ein. Basierend auf diesen Histogrammen werden Datenprodukte definiert, die Ausschnitte der Histogramme in vordefinierten Kadenzen zur Verfügung stellen. Um aus diesen Ausschnitten Rückschlüsse auf die Teilchenumgebung zu ziehen, werden Umrechnungsfaktoren im Rahmen dieser Arbeit berechnet und zur Verfügung gestellt.
Mittels der entwickelten Datenprodukte und deren Umrechnungsfaktoren werden die Möglichkeiten des HET für die Messung von solaren energiereichen Teilchenereignissen basierend auf Simulation mit zu erwartenden spektralen Eigenschaften und Kompositionen sowie Messungen von Instrumenten früherer Missionen aufgezeigt.
Für eine Validierung der onboard Datenverarbeitung sowie der definierten Datenprodukte werden Messungen an einem Schwerionenbeschleuniger sowie die ersten Daten der Mission genutzt. Basierend auf den ersten Daten, gemessen in einer realen isotropen Teilchenumgebung, lässt sich feststellen, dass HET die erwarteten Daten liefert und in großen Teilen wie vorhergesehen funktioniert. Erste Optimierungen der HET Datenverarbeitung, um diese an die reale Teilchenumgebung anzupassen, wurden ebenfalls im Rahmen dieser Arbeit entwickelt und bereits auf dem Instrument installiert.
Neben den primär wissenschaftlichen Ergebnissen, wie z.B. der Temperaturunabhängigkeit vom Ionisationsquenching, stellt diese Arbeit mit den präsentierten Informationen eine vollständige Dokumentation des HET dar, die es Wissenschaftlern in Zukunft ermöglichen wird, die Messdaten des HET nachzuvollziehen, korrekt zu interpretieren und nötigenfalls Anpassungen an der onboard Datenverarbeitung vorzunehmen.

Abstract

The Solar Orbiter spacecraft of the European Space Agency ESA was successfully launched on the 10th of February 2020 from Cape Canaveral, USA. During the seven-year nominal mission phase, it will travel as close as 0.27 astronomical units to the Sun to study it from up-close. Solar Orbiter will help to address open scientific questions concerning the physical processes on the surface and within the Sun. For this purpose, the spacecraft is equipped with several scientific instruments, divided into remote sensing and in-situ instrumentation. One of these instruments is the Energetic-Particle-Detector (EPD), consisting of four individual telescopes: the Suprathermal Electron and Proton - telescope (STEP), the Electron and Proton Telescope (EPT), the Suprathermal Ion Spectrograph (SIS), and the High Energy Telescope (HET). HET measures electrons with energies between 0.45 up to 18 MeV, protons with energies between 7 to 105 MeV and heavy ions in the range of 7 to several hundred MeV/nuc. It also identifies individual particle and ion species and achieves a separation for ^{3}He and ^{4}He isotopes of up to a 1% ratio. With that, HET measures the energy-dependent particle composition of solar energetic particle events in the given energy ranges and provides insight into their acceleration and propagation processes.
In this work, the onboard data processing of HET is developed. It defines the available scientific data for the characterization of the measured particle environment.
As part of the pre-development studies, the influence of the instrument's temperature on the measurement of heavy ions with HET's scintillation crystal is investigated. The analysis has shown, that the non-linearity in light output, called ionization quenching, is independent of temperature in case of the scintillation material used in HET. Ionization quenching originates from high ionization densities in the scintillation material when detecting heavy ions. The results are published in form of a peer-reviewed paper in "Nuclear Instruments and Methods in Physics Research Section B: Beam Interactions with Materials and Atoms", Volume 451 (2019). Based on these results, existing ionization quenching prediction models can be used for the development of the onboard data processing.
Due to the limited available telemetry bandwidth of Solar Orbiter, it is necessary to categorize and evaluate measured data prior to transmission to Earth. Since this is a sophisticated compression process, a detailed description of the onboard

data processing, developed in the scope of this thesis, is provided. The performed simulations, describing the interaction of energetic charged particles with HET, which are essential for the development of HET's onboard data processing are presented in detail. Based on the simulation data, the onboard data processing of HET is developed. The resulting procedures analyze measured particles and assign them to pre-defined histograms based on the particle's energy and species. Based on these histograms, data products are defined, which provide selected parts of these histograms in pre-defined cadences. The necessary conversion factors for inferring the measured particle environment based on the defined data products are calculated and provided as part of this thesis.
According to the developed data products and their calculated conversion factors, the capabilities of HET for the detection of solar energetic particle events are investigated and presented using simulations of the expected spectral properties and particle compositions, as well as using measurements of instruments of previous missions.
The onboard data processing of HET and the defined data products are validated, based on experiments at a heavy ion acceleration facility and the first mission data. From the first data measured by HET during the mission in a real isotropic particle environment, it can be concluded, that HET delivers the expected data and performs as expected in most aspects. Based on this data, optimizations of the onboard data processing are developed in the scope of this thesis and are installed on the HET instrument.
In addition to the primary scientific results, e.g. the temperature independence of ionization quenching, this work provides a complete documentation of HET, containing essential information for scientists to understand and correctly interpret the data measured by HET and to develop further optimizations of the onboard data processing if necessary .

Contents

Acronyms

AU	Astronomical Unit
BGO	$Bi_4Ge_3O_{12}$
CME	Coronal Mass Ejection
DP	Data Product
DPI	Data Product Item
EPD	Energetic Particle Detector
FM	Flight Model
GCR	Galactic Cosmic Ray
GEANT	GEometry And Tracking
HIMAC	Heavy Ion Medical Accelerator in Chiba
HET	High Energy Telescope
ICU	Instrument Control Unit
MIP	Minimal Ionizing Particle
PE	Polyethylene
PFM	Proto Flight Model
SEP	Solar Energetic Particle
SSD	Solid State Detector

1. Introduction

ESA's Solar Orbiter mission, launched in February 2020, aims to study the Sun from up-close using a combination of remote-sensing and in-situ instrumentation. As part of the in-situ instrumentation, the High Energy Telescope (HET) measures high-energy particles, namely electrons, protons and heavy ions up to iron, emitted from the Sun. For ions, HET covers an energy range from 7 MeV/nuc up to over 100 MeV/nuc. The measurement of high-energy particles with HET will support Solar Orbiter's scientific goals, especially the investigation of the acceleration mechanisms of Solar Energetic Particles (SEPs). In order to detect these high-energy particles, the instrument uses several solid state detectors as well as a high density scintillation crystal, Bi_4 Ge_3 O_{12} (BGO). Due to strict telemetry bandwidth restrictions of Solar Orbiter, onboard data processing and the pre-selection of scientifically useful data is necessary. This thesis covers the development and testing of the onboard data processing of HET. This thesis aims to provide a full and detailed documentation of HET and its onboard data processing, so that the measured data can be correctly interpreted and the full capabilities of the instrument can be used by current and future scientists also in several years of time.
The first part of the thesis gives an introduction into the Solar Orbiter mission itself and the necessary theoretical background for the detectors and the physical phenomena that shall be studied with HET. Furthermore, the HET instrument itself is introduced and its design explained.
In the subsequent part of the thesis, the simulation toolkit, used for the design of the onboard data processing of HET is introduced along with a model to predict a non-linearity in light output of the $Bi_4Ge_3O_{12}$ (BGO) scintillation detector. The non-linearity is known as ionization quenching and needs to be taken into account for the detection of heavy charged particles with scintillation detectors. Furthermore, the obtained results of a test campaign, performed in the scope of this work, for the investigation of the temperature dependence of ionization quenching for BGO is presented. This campaign, as part of the pre-development activities performed for the development of the onboard data processing, is necessary due to the operational temperature range of HET, between -30 to +20 °C, expected during the Solar Orbiter mission.
A complete description of the development of the onboard data processing of

HET based on simulation and experimental data is given as one of the main aspects of this thesis.
Subsequently, the developed onboard data processing and the used models are validated using experimental data from a heavy ion accelerator facility.
Another main aspect of this thesis is the calculation of the response factors of the supplied scientific data products of HET which are used to determine the in-situ particle flux. The instrument only detects a statistical sample of the in-situ particle distributions which makes a calculation of the conversion factors necessary.
The thesis closes with a presentation of the capabilities of the HET instrument and the presentation of first data obtained after the first months after launch.

2. The Solar Orbiter mission

The Solar Orbiter mission was selected by the European Space Agency (ESA) as the first medium (M1) class mission for the Cosmic Vision program 2015-2025 (Southwood, 2005; ESA, 2011). For the Cosmic Vision program a scientific concept was selected covering four different fields of space exploration (Southwood, 2005):

1. What are the conditions for planet formation and the emergence of life?
2. How does the solar system work?
3. What are the fundamental physical laws of the universe?
4. How did the universe originate and what is it made of?

Already in 1998 during the "Crossroads for European Solar and Heliospheric Physics"- meeting, the heliospheric community recommended a Solar Orbiter mission to answer key scientific questions of the solar system and the Sun itself (Marsch et al., 1998). With the selection of this mission for the Cosmic Vision program, the long history of Sun observations by previous missions like Helios, Ulysses, SOHO and STEREO will be continued and will provide further insight into the understanding of heliophysics. In this chapter, the Solar Orbiter mission will be introduced in detail, the key scientific objectives of the mission will be discussed and by this, their importance for the scientific community will be pointed out.

2.1 Mission Orbit

The orbit of Solar Orbiter combines key characteristics of several previous missions and is thus unique. Though the orbit had to be adjusted several times due to re-scheduling of the launch date, the main orbit characteristics remained the same:

- Close-up measurements and observations of the Sun
- High latitude observations of the Sun's polar regions

- Highly elliptical orbit

The current operational orbit for the performed February 2020 launch has a planned aphelion of 1.2 Astronomical Unit (AU) and a 0.28 AU perihelion. This orbit is shown in fig. 2.1. The orbit will be reached within two years after launch by using gravity assist maneuvers at Earth and Venus. During the perihelion phases Solar Orbiter will almost co-rotate with the Sun. During these phases processes on the Sun's surface can be monitored for an extended period of time by the remote-sensing instrumentation. The remote-sensing instrumentation measures electromagnetic radiation in different wavelengths. Starting at radio waves over optical light up to γ-radiation, for example particle acceleration sites can be identified or certain plasma parameters of the solar corona can be remotely measured. The particles ejected at the acceleration sites can be measured by the in-situ instruments once they reach the spacecraft. By combining the remote sensing and in-situ measurements links between particle characteristics and the acceleration processes can be investigated. To perform the planned high-latitude observations of the Suns polar regions, additional gravity assist maneuvers at Venus will be used to increase the orbital inclination to the ecliptic plane up to 24° at the end of the nominal mission phase. This mission phase is planned to end seven years after launch. During the extended mission phase the inclination is further increased to 33° (ESA, 2020a; Walsh and De Groof, 2020).
In 2018 Parker Solar Probe (PSP) was launched to the Sun. This mission features a comparable orbit to that of Solar Orbiter and is supposed to perform measurements even closer to the Sun with a distance of only 0.044 AU. The aphelion of the mission is 0.73 AU (Guo et al., 2014). Due to the comparable orbit and the overlapping operation times of both missions, multi-point observations close to the Sun can be performed with the two spacecraft, which is a unique and unprecedented opportunity for the scientific community. Thus, Parker Solar Probe will provide valuable input to the scientific goals of Solar Orbiter, which are discussed hereafter.

2.2 Scientific goals

The Solar Orbiter mission outline has foreseen to provide insight to the second scientific question of the Cosmic Vision program for 2015-2025 by answering the central question of heliospheric physics: How does the Sun create and control the heliosphere?
In order to answer this fundamental question, the scientific goals are broken down into four distinct fields of research that are to be covered (ESA, 2011):

i) How and where do the solar wind plasma and magnetic field originate in the corona?

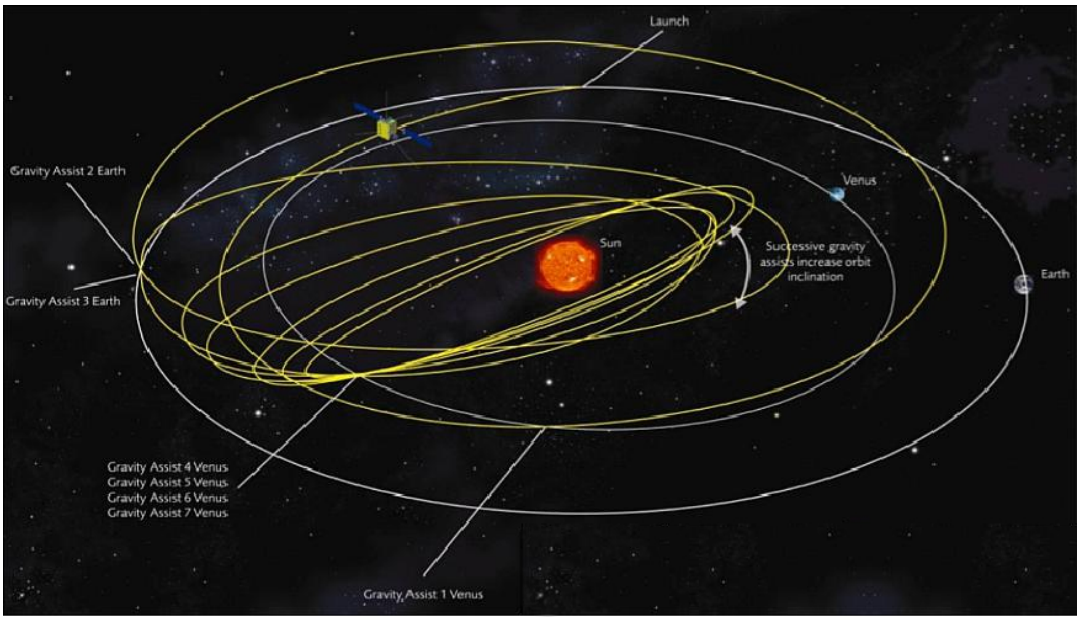

Figure 2.1: The orbit of Solar Orbiter for the February 2020 launch. After ESA (2020b).

ii) How do solar transients drive heliospheric variability?

iii) How do solar eruptions produce energetic particle radiation that fills the heliosphere?

iv) How does the solar dynamo work and drive connections between the Sun and the heliosphere?

These key questions can be translated to tasks of the Solar Orbiter mission, which are to identify the origin and mechanisms of the solar wind, the heliospheric and the solar magnetic field as well as to investigate the acceleration processes and mechanisms that create Solar Energetic Particles (SEPs) and transient interplanetary disturbances. By fulfilling these tasks, Solar Orbiter will contribute significantly to the understanding of modern heliophysics. By breaking down the scientific questions of the Solar Orbiter mission, specific requirements on the scientific payload and the mission design itself can be created. For each of the questions the connection to the current scientific status and an explanation will be given by looking into each of the specific questions and how Solar Orbiter will be able to address them.

i) How and where do the solar wind plasma and magnetic field originate in the corona?

The Sun fills our heliosphere with a supersonic plasma wind, which affects planetary atmospheres and influences Earth's magnetosphere. This ejected plasma wind, known as solar wind, can be classified into two populations, the slow solar wind with speeds between 300 - 400 km/s and the fast solar wind with speeds around 700 km/s. From the Ulysses mission it is known, that during solar minimum the slow solar wind can be measured in the equatorial regions of the Sun, while the fast solar wind originates from coronal holes at higher latitudes closer to the poles. This is shown in fig. 2.2, where measurement data of three Ulysses orbits (McComas et al., 2008) are displayed. While the fast solar wind is rather steady in speed and composition, the slow solar wind is highly variable in the charge states of the ions, its composition and speed. In Ulysses second orbit during solar maximum the origin of both solar wind types is no longer as distinct as in solar minimum and a mixture of the two streams at all latitudes is observed, as shown in fig. 2.2 (b). The terms solar minimum and solar maximum refer to the activity of the Sun during its 11 year cycle. After the 11 year cycle, the magnetic polarity of the Sun is reversed, so that a complete cycle takes 22 years. Indicators of solar activity are for example, the number and size of sunspots as well as the number of solar flares and coronal protuberances. Fig. 2.2 (c) shows the similar conditions as in (a), but after the Sun's magnetic field pole reversal. Until this date, it is unclear how the solar coronal plasma is generated and how it is released from the coronal magnetic field. The source of the magnetic field which is carried by the solar wind is also under debate. While most of the Sun's magnetic field is closed in the lower corona and the chromosphere, a part of the magnetic field reaches farther out and is dragged into the heliosphere by the solar wind. The investigation of the solar magnetic field is difficult, as the configuration of these open field lines, which are dragged out by the solar wind, is depending on the magnetic configuration in the lower layers of the Sun. The magnetic configuration in the lower layers is highly variable due to magnetic reconnection and the movement of the magnetic field line foot points on the photosphere. Thus the generation of the open field lines and their distribution on the solar surface can not be sufficiently explained. (Verscharen et al., 2019; McComas et al., 2008; ESA, 2011).

Solar Orbiter will address this question by using its combined in-situ and remote sensing capabilities. With these, the in-situ measured plasma properties can be correlated with the observed solar structures, especially during the near-corotating orbit phases, and thus the origin of the plasma can be determined (ESA, 2011; Marsch et al., 2002; Carr et al., 2006).

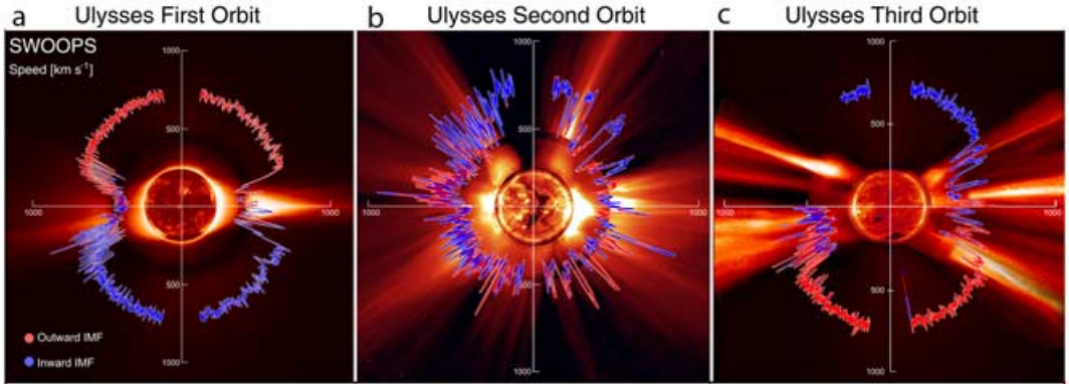

Figure 2.2: The data of the first and the third Ulysses orbit was measured during Solar Minimum. During the second orbit, the Sun was in solar maximum. Shown for all three cases is the solar wind speed depending on the solar latitude with color coded magnetic field polarity (McComas et al., 2008).

ii) How do solar transients drive heliospheric variability?
Beside the steady outflow of the solar wind, additional solar transient phenomena are frequently observed. These include flares, SEPs, eruptive prominences, shock waves and coronal mass ejections (CMEs). The latter are the largest transient phenomena. During a Coronal Mass Ejection (CME) large magnetic structures of masses up to 10^{14} kg and velocities up to 3500 km/s can be ejected from the Sun (Webb and Howard, 2012). The acceleration mechanisms of the phenomena is also unclear, though it is essential for the prediction of 'space weather'. The term space weather refers to the influence of the Sun to Earth environment like the magnetosphere, ionosphere and thermosphere that might affect human life or health and also Earth orbiting satellites (Schwenn, 2006). These transient phenomena have a significant impact on the Earth's upper atmosphere and even deform Earths magnetic field. The CMEs can create shock waves in the corona and heliosphere that accelerates coronal particles to very high energies. Though a basic understanding of CME creation could be achieved with previous missions, it is yet unclear why no prominence plasma can be found in CMEs at 1 AU, when the prominence eruption is the main release candidate. However, Gloeckler et al. (1999) reports CME encountered by the ACE spacecraft on 2-3 of May 1998 which was associated with a prominence eruption. This CME shows a unusual composition, which is suspected to originate from cooler prominence plasma.
Furthermore current theoretical models predict that the magnetic field inside the CME is resembled by a twisted magnetic flux rope while at 1 AU often a more complex magnetic field structure is observed.
Solar Orbiter will measure these transient phenomena close to the Sun and additionally provide remote sensing data of the magnetic configuration on the Sun. With this data, important steps for the understanding of the creation and propagation of these phenomena on the Sun can be made, by improving the current

MHD models. The advantage of Solar Orbiters close approach is that transport effects have altered the initial structures and plasma distributions to a much smaller degree compared to measurements at 1 AU and thus provide necessary information to identify the acceleration and release mechanisms of these phenomena. Additionally, Solar Orbiter will be able to monitor the source regions of these transients with an unprecedented resolution in remote sensing instruments both in and out of the ecliptic plane. Thus pre-eruption signatures can be studied and provide input to improve our theoretical understanding (Webb and Howard, 2012; ESA, 2011).

iii) How do solar eruptions produce energetic particle radiation that fills the heliosphere?

Particles from the Sun, that are accelerated to very high energies, e.g. during solar flares or at shocks formed by CMEs, are known as Solar Energetic Particles (SEPs). The acceleration mechanisms of these particles are not fully understood, although two main candidate concepts exist. The first is the acceleration at shock fronts. In this scenario particles are scattered back and forth into a moving or turbulent magnetic field. Each time the particle is reflected into a shock front it gains a small amount of energy. As this is a stochastic process, the acceleration mechanism is known as stochastic or Fermi acceleration. This acceleration mechanism is mostly found when a CME or Corotating Interaction Region (CIR) drives a shock front. In this shock front particles are continually accelerated as the CME moves through the heliosphere. However, the influence of the seed population and the shock geometry are not well understood (Desai et al., 2006; Mewaldt, 2006; ESA, 2011). Another possible acceleration mechanism is magnetic reconnection. With this mechanism, particles can be directly accelerated to high energies by strong electric fields. This happens when large magnetic loop structures reconnect or are rearranged at the Sun (Aschwanden, 2006). Most of the accelerated particles are trapped in their magnetic loops, producing X- and γ- rays as they travel inside the loop. The radiation can be detected and is used to probe the local plasma parameters, e.g. the plasma density, and to identify the acceleration site (ESA, 2011). Particles which are accelerated on open magnetic field lines can escape into the heliosphere. These escaping particles can be highly enriched in certain ion species, for example ^{3}He, where enrichment factors between 10^3 to 10^4 are observed compared to the coronal plasma (ESA, 2011; Drake et al., 2009). When these ejected particles are detected at 1 AU, characteristic signatures of the acceleration and injection processes are superimposed by transport effects. Therefore an identification of the dominant processes is no longer possible.

With Solar Orbiter it will be possible to answer these questions, as the acceleration signatures of the individual processes will still be distinguishable and in a almost pristine state. With the combination of remote sensing instrumentation, probing the photon spectrum of the acceleration site and in-situ instrumentation,

measuring the accelerated particles, Solar Orbiter is well equipped to disentangle signatures of the particle transport and particle acceleration processes.

iv) How does the solar dynamo work and drive connections between the Sun and the heliosphere?
The magnetic field of the Sun dominates the heliosphere. It is believed to be generated by a dynamo that shows an 11-year activity cycle that does not only influence the magnetic field but all solar phenomena. During this cycle the magnetic field performs a pole reversal. The current models that are used to predict the Sun's global behavior are not reliable in their predictions. The magnetic flux that is transported by meridional circulation and near-surface flows from decaying active regions to the poles are not well mapped and understood (Dikpati and Gilman, 2008). Thus, the solar dynamo models lack constraints especially for the high latitudes where the turnover from poleward flow to subduction is taking place (Dikpati and Charbonneau, 2002). These regions can not be characterized in detail from the ecliptic plane.
With Solar Orbiter it will be possible to measure the near-surface flows, the meridional flow and the differential rotation at different latitudes (ESA, 2011). During its mission, Solar Orbiter will leave its orbit in the ecliptic and reach heliographic latitudes of up to 33°. With these measurements Solar Orbiter will provide the necessary constraints for the solar dynamo models and therefore will help to improve our understanding of the processes in and on the Sun.

2.3 Instrument Payload

To achieve the scientific objectives of the Solar Orbiter mission, the scientific payload was selected according to the needs of the heliospheric community (ESA, 2011). Here a brief overview of the payload is given along with a short description of each instrument. In table 2.1 the scientific payload is given, divided into remote-sensing and in-situ instrumentation.
The Extreme Ultraviolet Imager (EUI) is composed of two high-resolution telescopes to provide high-resolution images of structures from the chromosphere to the corona in the Extreme Ultraviolet (EUV) regime. Furthermore EUI is equipped with an imager to provide EUV images of the whole Sun. These will be used to provide the context for other imagers such as METIS and SPICE (Rochus et al., 2020).
The Multi Element Telescope for Imaging and Spectroscopy (METIS) coronograph will image the solar corona simultaneously in visible and UV-light between 1.7 and 9 solar radii, showing the dynamics of the solar corona with high temporal and spatial resolution. Using the images created by METIS, the link between the solar atmosphere and the inner heliosphere can be provided (Antonucci et al., 2019).

SPICE is an EUV imaging spectrograph with high spatial, spectral and temporal resolution. It will provide composition information as well as temperature, density and flow of the plasmas in the solar atmosphere. These can be used to investigate the outflow and ejection processes which link the solar surface and corona to the heliosphere (SPICE Consortium, 2019).
The Polarimetric and Helioseismics Imager (PHI) is a wavelength tunable polarization sensitive imager, which will provide maps of the magnetic vector and the line-of-sight velocity of the plasma in the solar photosphere (Solanki et al., 2019).
The Solar Orbiter Heliospheric Imager (SoloHI) will image the flow and transient disturbances in the solar wind over a wide field of view. This is achieved by detecting the visible light of the Sun which is scattered by solar wind electrons. With this information, for example the origin and evolution of the solar wind can be investigated (Howard et al., 2019).
The Spectrometer/Telescope for Imaging X-rays (STIX) will provide information on the timing, location, intensity and spectra of the accelerated electrons and high temperature thermal plasmas by providing image spectroscopy of solar thermal and non-thermal X-ray emission (Krucker et al., 2020).
RPW is a combination of in-situ and remote sensing instrumentation. It measures magnetic and electric fields at high cadences and will furthermore be able to measure electromagnetic and electrostatic waves in the solar wind in-situ (Maksimovic et al., 2020).
The Solar Wind Plasma Analyser (SWA) will perform in-situ measurements to determine the density, velocity and temperature of solar wind electrons and will also provide ion composition measurements of the solar wind (ESA, 2011).
These measurements will supplemented by the Energetic Particle Detector (EPD), which extends the energy range for electrons and different ion species to higher energies. The EPD suite is capable of measuring suprathermal up to high-energy particles of SEP events and determine their composition and energy spectra of different charged particle and ion species (Rodriguez-Pacheco et al., 2019).
The Magnetometer (MAG) will provide high precision in-situ measurements of the heliospheric magnetic field. (Carr et al., 2006). In order to determine the link between the in-situ oberservations with the remote-sensing observations, the magnetic connection the spacecraft and the observed remote location on the Sun needs to be kown. By using numerical models, remote measurements by PHI and the in-situ measurements of the solar magnetic field by MAG and RPW, this link is provided.

Remote-sensing instrumentation
EUI: Extreme Ultraviolet Imager
METIS: Choronograph
SPICE: Spectral Imaging of the Coronal Environment
PHI: Polarimetric and Helioseismic Imager
SoloHI: Heliospheric Imager
STIX: X-ray Spectrometer/Telescope
In-Situ instrumentation
EPD: Energetic Particle Detector
MAG: Magnetometer
RPW: Radio and Plasma Waves
SWA: Solar Wind Plasma Analyser

Table 2.1: Scientific payload of the Solar Orbiter mission (ESA, 2011).

3. Particle matter interactions and particle detectors

In chapter 2 the scientific aims of the Solar Orbiter missions are described and a brief description of the contribution of each instrument is given. This work covers different aspects of the HET as part of the EPD suite. HET is designed to determine the in-situ particle flux of high-energy charge particles in the MeV energy range. In order to understand the instrument and its concept, the interaction of these highly energetic charged particles with matter will be explained. In addition, the particle detector types, which are used in HET are introduced and the particle detection mechanism of these detectors is explained.

3.1 Charged particle matter interactions

The most important interaction process for energetic charged particles with matter are inelastic collisions with the electrons of the traversed material. In this inelastic collision energy is transferred from the charged energetic particle to the hull electrons of the traversed materials, by which the electrons can be excited to higher energy levels or the atoms of the traversed material can be ionized. Thus, the total energy loss of an energetic charged particle when passing through matter is determined by each of these short interactions. Based on this inelastic collision model and by applying quantum-mechanical and relativistic corrections to it, the Bethe-Bloch-equation, given in eq. 3.1, with $\beta \doteq v/c$, was developed (Bloch, 1933; Lindhard and Sörensen, 1996):

$$-\frac{dE}{dx} = \frac{4\pi n z^2}{m_e v^2}\left(\frac{e^2}{4\pi\epsilon_0}\right)^2\left[\ln\left(\frac{2m_e v^2}{I\cdot(1-\beta^2)}\right)-\beta^2\right] \tag{3.1}$$

$$n = \frac{N_A Z_T \rho_T}{A_T \cdot u} \tag{3.2}$$

With this formula, the mean energy loss per path length, -dE/dx, of a particle with a given velocity v and charge z in a given material with the density ρ_T, an atomic mass number $\mathrm{A_T}$, an atomic charge number $\mathrm{Z_T}$ and the materials mean ionization potential I can be calculated. Figure 3.1 shows the energy loss

for 3 MeV Protons and 3 MeV/nuc He ions in silicon. With decreasing particle velocity, the energy loss per path length -dE/dx increases up to a maximum. This maximum is called the Bragg-peak. On the left-hand side of the Bragg-peak the energy loss increases roughly as 1/E, on the right hand side, the energy loss per path length quickly falls to 0 and the particle has deposited all its remaining energy. The drop-off in energy loss per path length after the Bragg-peak originates from charge-pickup at low energies. With decreasing speed, the interaction time of each coulomb interaction increases, and thus the energy loss of a single interaction increases (Knoll, 2010).
The energy loss of a charged particle in a solid state detector is subject to statistical fluctuations, due to the statistical nature of energy loss by ionization. The energy deposition of a charged particle in a material is the sum of a number of single interactions with the hull electrons as described in previously. Thus the central limit theorem can be applied to the process and the energy loss distribution can be approximated by a Gaussian distribution. This is the case, under the assumption that the typical energy loss in a single interaction is small compared to the total energy loss of the particle. Such a distribution is shown in fig. 3.2 (a), using a GEometry And Tracking (GEANT)4 simulation of a 70 MeV proton beam measured by a 6 mm silicon Solid State Detector (SSD). GEANT4 is introduced in detail in chapter 5, as the figures shall be merely used for illustration here. When the assumption that the typical energy loss is small compared to the total energy loss is no longer valid, the central limit theorem can no longer be applied. In this case, a Landau-like distribution is observed, which is the case for thin detectors (Landau, 1965). "Thin" is related to the particle range, which mainly depends on the particle type and its energy (Meroli et al., 2011). This distribution is illustrated in fig. 3.2 (b) using a GEANT4 simulation of a 70 MeV proton beam measured by a 300 µm detector. In this case the energy deposition distribution is asymmetric with a tail towards higher energies. This tail originates from the small number of collisions, where each individual collision has the probability to transfer a comparatively large amount of energy due to the creation of δ-electrons. An analytic approximation of the Landau distribution, which is commonly used, was developed by Moyal (1955). The Moyal distribution is given in eq. 3.3 (Moyal, 1955):

$$f(x,\sigma) = \frac{1}{\sqrt{2\pi}} \exp\left[-\frac{1}{2}\left(\frac{x-x_0}{\sigma} + \exp\left(-\frac{x-x_0}{\sigma}\right)\right)\right] \tag{3.3}$$

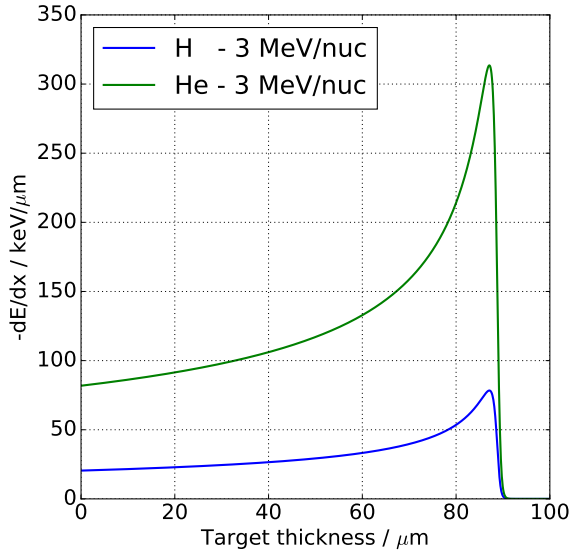

Figure 3.1: Using eq. 3.1 the energy loss per path length can be calculated. Here it is shown for fully charged H and He ions with an energy of 3 MeV/nuc.

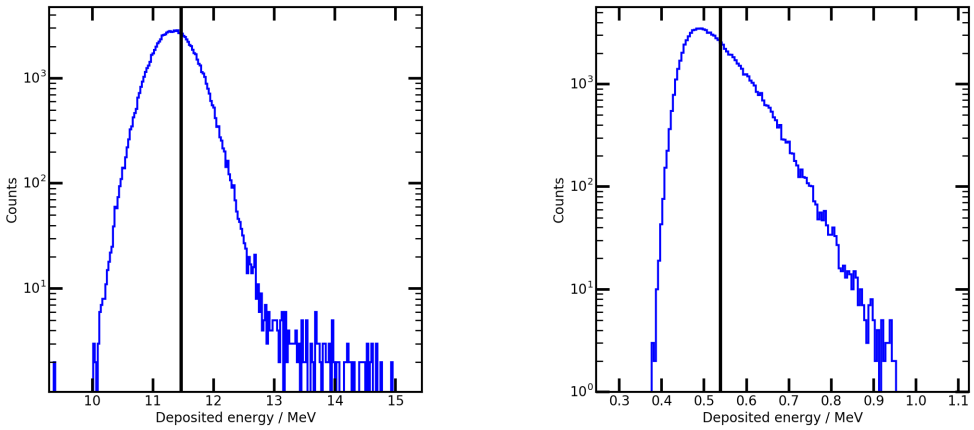

(a) A 6 mm thick silicon SSD shows a Gaussian energy deposition distribution for the protons.

(b) A 300 µm thick silicon SSD shows a Landau energy deposition distribution for the protons.

Figure 3.2: Simulation of a 70 MeV proton beam measured by silicon SSDs of two different thicknesses. The mean energy loss given by the Bethe-Bloch-equation is shown for reference by the black lines.

3.2 Secondary particle production

When a charged particle travels through a material, it interacts with the orbital electrons of the traversed materials atoms, as described in sec. 3.1. In case the orbital electrons gain sufficient energy to be removed from the host atom, it can travel a short distance within the absorber medium. However, if these electrons are generated near the surface of a material, the electrons may escape and can be measured as so called secondary or delta electrons. The amount of generated delta electrons depends on the primary particles charge, so that heavier ions produce more secondary particles compared to lighter ions (Saro et al., 1996).
While delta electrons are mostly produced by the interaction of the primary particle with the orbital electrons by coulomb interactions, another type of secondary particles can be produced by hard collisions. During these hard collisions, the primary energetic particle interacts with the nucleus of a target atom. During this interaction, usually the primary energetic heavy ion fragments into lighter ions (Zeitlin and La Tessa, 2016). These ion fragments inherit a significant amount of the primary particles energy, so that they continue to travel through the target and thus the fragments can be detected as energetic ions.

3.3 Particle detectors

In order to explain how HET can contribute to the scientific objectives of the Solar Orbiter mission, the detector types used in the HET instrument, semiconductor detectors and scintillators, will be introduced. While semiconductor detectors are often used when high-energy resolution is required, scintillators are used for the detection of highly energetic particles and γ-rays because of their high density and high atomic number. The resulting high stopping power of scintillators results in a high energy loss per particle path length for highly energetic charged particles. The difference in energy resolution in both detector types results from the energy that is required to produce one information carrier. For semiconductor materials, the amount of energy to produce one electron-hole pair is in the order of few eV while for scintillation detectors more than 100 eV are required to produce one photon (Kumar et al., 2018; van Eijk, 1997). Thus energy measurements with scintillators are more affected by statistical fluctuations that limit their energy resolution.

3.3.1 Semiconductor detectors

Semiconductor detectors are widely used for the detection of energetic particles, as they offer many desirable features for this purpose like fast timing characteristics, a compact size and very high energy resolution. However, they are prone to radiation damage which increases their leakage current (Lindström, 2003).

	Silicon	Germanium
Atomic number	14	32
Density (g/cm^3)	2.33	5.32
Intrinsic carrier density (cm^{-3})	1.5 x 10^{10}	2.4 x 10^{13}
Energy per electron-hole pair at 77 K (eV)	3.72	2.96

Table 3.1: Properties of silicon and germanium from Knoll (2010). Both materials are commonly used for semiconductor detectors.

Semiconductor materials convert the deposited energy of an incident energetic particle into electron-hole pairs. The number of generated electron-hole-pairs is proportional to the energy deposition of the incident particle. The two mainly used semiconductor materials are silicon and germanium, where silicon is mainly used in the charged particle spectroscopy and germanium for γ-ray detection, as the high atomic number of germanium enhances the cross section for photon detection. The most important properties of these two materials are listed in table 3.1. The minimum energy to produce one electron-hole pair in a semiconductor material is determined by the band-gap between the valence- and conduction band. In order to detect radiation using semiconductor materials a charge-carrier free depletion region has to be created. Commonly this is achieved by combing a negative (n-type) and a positive (p-type) doped material. The free charge-carriers of both sides recombine so that a region empty of free charge carriers is created. This region can be expanded by applying a reverse voltage to the electrodes of the semiconductor material. With the applied reverse current, the electron-hole pairs, generated for example by incident energetic particles, are measured as a current pulse from which the energy of the incident particle can be determined. In the non-depleted regions near the electrodes, the detection of energy deposition is not possible. The generated charge carriers are not collected, since no electric field is present in this area.
In HET Passivated Implanted Planar Silicon (PIPS) detectors are used. These detectors are created from high purity silicon wafers which are mildly n-type due to donor impurities. The surface of the wafer is passivated by oxidation at elevated temperatures to suppress surface leakage currents. At the designated entrance window locations, the oxide layer is removed using photolithography and a thin p-type layers is created via boron ion implantation. The rear surface is converted into n^+-material by arsenic ion implantation and forms a blocking electrical contact. The electrical contacts are created by aluminum evaporation and patterning through photolithography (Knoll, 2010; Kemmer, 1984).

3.3.2 Scintillation detectors

Scintillators are materials, which emit visible light after energy has been deposited in the material e.g. by an energetic charged particle. The light creation process in scintillators is known as luminescence, in which hull electrons of the scintillation materials are excited to higher energy levels and emit visible light upon relaxation. The energy to create one photon in most scintillation materials is in the order of several hundred electron volts. Thus, scintillators are mainly used for the detection of energetic particles or photons that deposit large amounts of energy. The development of new luminescent materials is still ongoing (van Eijk, 1997; Van Eijk, 2001). There are two basic types of scintillators, organic and inorganic. The scintillation mechanism in organic scintillators is based on molecules. Therefore these offer the ability to be dissolved in liquids, gases or even plastics and thus can be manufactured in any desired shape. The scintillation mechanism in inorganic scintillators is based on their crystal structure and thus, these have to be grown. Inorganic scintillators offer a higher stopping power compared to organic scintillation materials and are thus often used for the detection of highly energetic charged particles, for example in HET. Inorganic scintillators are divided into intrinsic and doped scintillators. While in doped scintillators, impurities are added to achieve luminescence, in intrinsic scintillators the luminescence is an inherent material feature. The most important scintillator properties for the detection of charged energetic particles are density, effective atomic number, the emission spectrum and the decay time. The effective atomic number is the averaged atomic number of a compound material and the decay time is defined as the time the intensity of a light pulse takes to reduce to 1/e. The density and effective atomic number define the stopping power of the material as well as the cross section for different particle species. The emission spectrum is important to match the scintillator to the light detection device, commonly a photodiode or a photomultiplier tube. The scintillation mechanism will be explained according to fig. 3.3 with the band-gap model (Pedrini, 2005) for inorganic scintillation materials. The relaxation of the electronic excitations is divided into 4 phases of which each differs in its timescale. After electronic excitations, e.g. absorption of a high-energy photon, an electron (e) is raised from the core band to high energy states of the conduction band. During the first relaxation phase the dominating processes are inelastic $e - e$ scattering for the electrons in the conduction band $e \rightarrow e + e + h$ and Auger-processes for the holes (h) $h \rightarrow e + h + h$. Both processes lead to a multiplication of electron hole pairs. While the electrons relax to lower energies in the conduction band, the holes relax towards higher energy states. The timescale of this phase is $\approx 10^{-16}$ to 10^{-14} s and ends when the thresholds for both processes are undershot. The threshold for the $e - e$ scattering is $\approx$ 2-3 E_g. The timescale of the second phase is between $\approx 10^{-14}$ to 10^{-12} s and is dominated by thermalization processes of the electrons $e \rightarrow e + ph$ and holes $h \rightarrow h + ph$. At the end of the phase all holes are located

at the top of the valence band and the electrons are located at the bottom of the conduction band. During the third phase localizations of electrons and holes may take place in timescales of $\approx 10^{-12}$ to 10^{-10} s. A possible localization process is the capture of electrons or holes by traps $e + c^+ \rightarrow c^0 + ph$, $h + c^- \rightarrow c^0 + ph$ (Pedrini, 2005). In this case the de-excitation is non-radiative. In intrinsic (non-doped) scintillators, for example $Bi_4Ge_3O_{12}$ (BGO), the scintillation mechanism is attributed to another localization process. For these materials the scintillation process is based on the formation of self-trapped excitons (STE) (MORI et al., 2002). STE's are formed by self-trapping of holes and the formation of vacancy centers (V_k), $h \rightarrow V_k + ph$ and subsequent recombinations of electrons with these vacancy centers $V_k + e \rightarrow exc$. The electron-hole pair is locally bound and trapped in its own lattice distortion field (Williams and Song, 1990). Due to the exciton formation the energy level is located between the conduction and valence band. This is important to avoid self-absorption of the emitted photons. The final stage of the relaxation process, in which the luminescence photons are emitted, takes place on timescales between $\approx 10^{-10}$ and 10^{-8} s. The emitted photons can be measured using a light detection device like a photomultiplier tube or a photodiode. Since for most cases the scintillation light output is proportional to the energy of the incident particle, its energy can be measured.

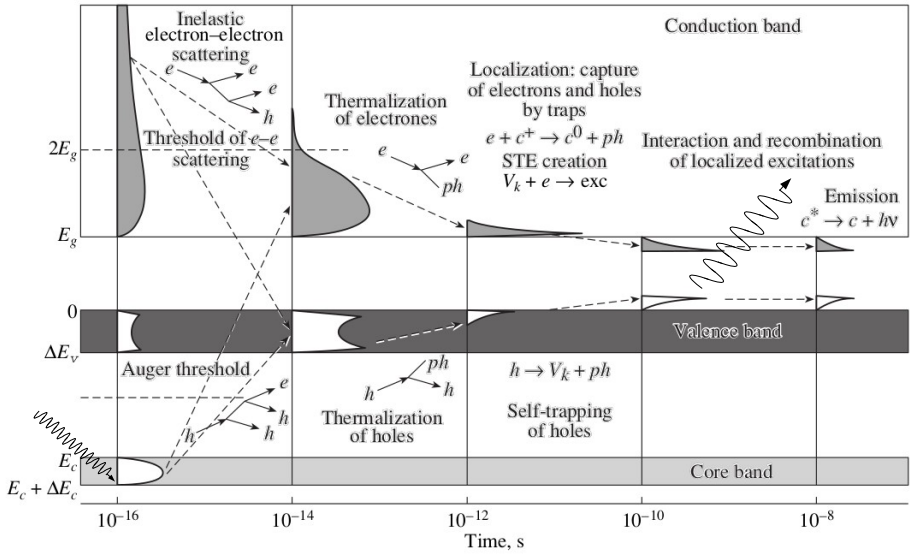

Figure 3.3: Illustration of the relaxation processes in a scintillation material after an electronic excitation by a γ-ray. After Pedrini (2005).

Scintillator non-linearities

For the ideal scintillation detector the light output is unaffected by external influences and is always proportional to the energy deposition of a particle. In

reality, scintillation detectors may suffer from different effects that introduce non-linearities to the light output. During the manufacturing of a scintillation material, there are two effects that may reduce the light output. These effects are impurity- and concentration quenching and originate from the presence of impurities or too high dopant concentration in the crystal (Pidol et al., 2004). As these effects need to be considered prior to the production of a scintillation material, they are inherent scintillator characteristics and can not be corrected after production. Non-linearities in the light output can be also observed due to external causes. The most important aspects for space applications that create these non-linearities are:

- Temperature
- Ionization density in the material

The light output of many scintillation detectors is temperature dependent. This dependency is found for organic as well as inorganic scintillators and is still investigated (Peralta, 2018; Weber et al., 2003; Buranurak et al., 2013). This effect leads to an invalidation of the calibration in temperature unstable environments and thus to incorrect energy measurements. For most scintillation materials, the light output decreases with increasing temperatures (Weber et al., 2003; Melcher and Schweitzer, 1985). This behavior is attributed to thermal excitations of electrons which then perform radiationless transitions. This process competes with the radiative transition and its probability increases with temperature (Melcher and Schweitzer, 1985).
The amount of scintillation light created in a scintillation detector also depends on the local ionization density in the material. High ionization densities lead to a significant reduction of scintillation light. This effect is known as ionization quenching and was first investigated by Birks (1951). For low ionization densities the light output per path length dL/dx in a scintillation material is proportional to the energy deposition per path length dE/dx, of an energetic charged particles, multiplied with the scintillation efficiency S as given in eq. 3.4:

$$\frac{\mathrm{d}L}{\mathrm{d}x} = S\frac{\mathrm{d}E}{\mathrm{d}x} \tag{3.4}$$

For high ionization densities eq. 3.4 transforms into eq. 3.5, with the material specific Birks quenching factor k_B (Birks, 1951):

$$\frac{\mathrm{d}L}{\mathrm{d}x} = S\frac{\frac{\mathrm{d}E}{\mathrm{d}x}}{1 + k_\mathrm{B}\frac{\mathrm{d}E}{\mathrm{d}x}} \tag{3.5}$$

The local ionization density inside the scintillation material is dependent on the particle species (A,Z) and also the particles energy according to the Bethe-Bloch-equation (Lindhard and Sörensen, 1996). Pedrini (2005); Belsky et al. (1996);

Pedrini et al. (1994) suspect, that closed spaced electronic excitations may lead to interactions of correlated e-h pairs (excitons) with other uncorrelated low energy electrons or holes. The closed spaced electronic excitations result from the difference of mobility of the fast electrons and the slow holes. The interaction of correlated and uncorrelated charge carriers prevents the creation of new excitations and thus reduces the total amount of produced scintillation light. The probability of this interaction is highly dependent on the ionization density. The effect of ionization quenching is investigated for many scintillation materials. Models to predict the quenching are constantly developed and improved (Horn et al., 1992; Tammen et al., 2015). A continuous development is necessary, as the quenching prediction models are empiric and are often limited to a specific experimental application, like a specific ion species, a limited energy range or a specific scintillation material.

Bismuth Germanium Oxide (BGO)

The High Energy Telescope (HET) uses as scintillator in order to stop high energetic heavy particles. A complete introduction to the HET instrument and its detectors is given in sec. 4.3. For HET, $Bi_4Ge_3O_{12}$ (BGO) was selected as a scintillation material. BGO combines high density with a high mean atomic number which results in a high overall stopping power for charged particles. Because of this, BGO has become a widely used scintillation material for many different applications like medical screening (Positron Emission Tomography), γ-ray spectroscopy or in high energy physics experiments (Melcher and Schweitzer, 1985; Avdeichikov and Bergholt, 1994; Weber et al., 2003). The most important characteristics of BGO are given in table 3.2 along with the values for thallium doped caesium iodide (CsI(Tl)) for comparison. Thallium doped caesium iodide is also a commonly used scintillator for example in the Radiation Assessment Detector of the Mars Science Laboratory (Hassler et al., 2012).
The light output of BGO is dependent on temperature. As described in sec. 3.3.2 this effect needs to be corrected in temperature unstable environments. Figure 3.4 shows the scintillation efficiency of BGO as a function of temperature. With increasing temperature, the scintillation efficiency is drastically reduced. This is attributed to thermal excitations of electrons which lead to radiationless transitions that compete with the luminescent transitions. Due to these radiationless transitions not only the light output but also the decay time is reduced with increased temperature (Melcher and Schweitzer, 1985).

	$Bi_4Ge_3O_{12}$	CsI(Tl)
Density / g/cm^3	7.13	4.51
Peak emission / nm	480	560
Index of refraction	2.15	1.80
Effective atomic number	74	54
Material hardness / Mho	5	2
Decay constant	300	700 (fast), 7000 (slow)

Table 3.2: Most important properties of BGO and CsI(Tl). Extracted from Avdeichikov and Bergholt (1994); Chaiphaksa et al. (2018); Saint-Gobain Crystals (2017).

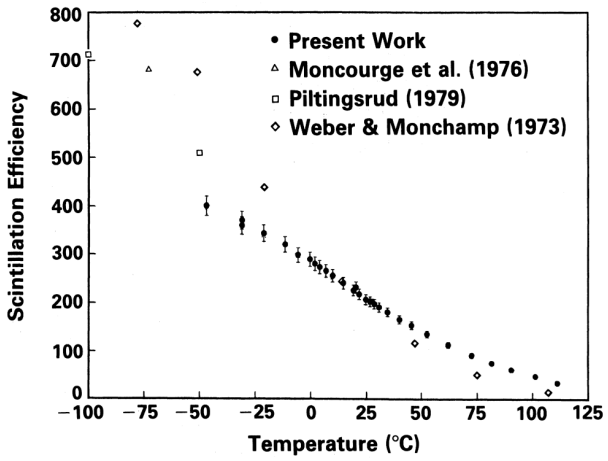

Figure 3.4: Temperature dependant light output of BGO, excited by 662 keV gamma rays (Melcher and Schweitzer, 1985).

4. The High Energy Telescope

In the previous chapters, the background for the Solar Orbiter mission as well as the most important theoretical aspects related to HET are introduced. In this chapter HET as part of the EPD suite is introduced along with the other instruments of the suite. Following this introduction, the scientific contribution of HET to the objectives of Solar Orbiter is given in detail in sec. 4.2. The design of the HET instrument itself is presented afterwards in sec. 4.3.

4.1 The Energetic Particle Detector

In sec. 2.3 the Energetic Particle Detector (EPD) suite is introduced as part of the in-situ instrument payload of Solar Orbiter. EPD's task is to measure the characteristics of SEPs in a wide energy range. The energy ranges of the individual instruments of the EPD detector suite are displayed in fig. 4.1. The SupraThermal Electron Proton (STEP) sensor and the Electron Proton Telescope (EPT) are designed to measure low energy electrons, protons and helium, from ≈2 keV to ≈6.4 MeV for particles that can be stopped in the sensor head of the instruments (Rodriguez-Pacheco et al., 2019). The Suprathermal Ion Spectograph (SIS) is designed to measure heavy ions in a low- to medium energy range, from ≈ 10 keV/nuc to ≈ 20 MeV/nuc (Rodriguez-Pacheco et al., 2019). All of the instruments of the EPD suite are controlled by a common Instrument Control Unit (ICU). The ICU is the connection between the Solar Orbiter spacecraft and the indidivual EPD instruments. The ICU provides power to the instruments, via a Low Voltage Power Supply (LVPS) and handles all communication between the spacecraft and the instruments via a Central Data Processing Unit (CDPU) (Rodriguez-Pacheco et al., 2019).

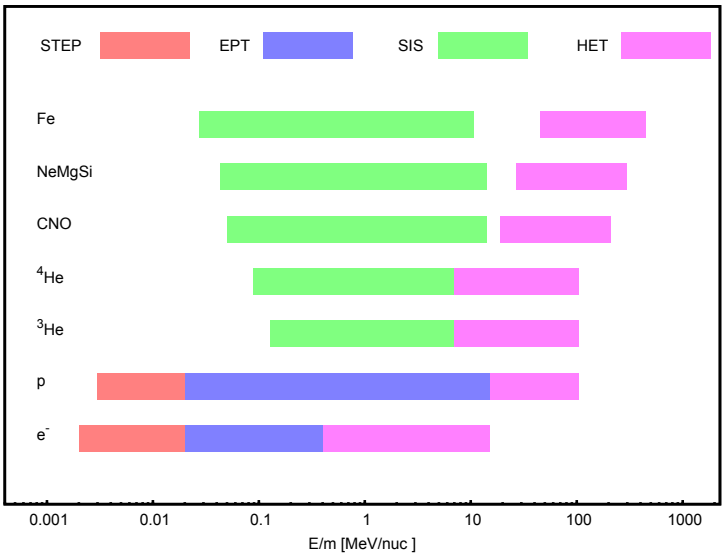

Figure 4.1: Energy ranges of all 4 instruments of the EPD suite (Rodriguez-Pacheco et al., 2019).

HET was designed to cover the high energy range for electrons, protons and also for several heavy ion species from ≈7 MeV/nuc to ≈500 MeV/nuc for ions that stop in the sensor head (Rodriguez-Pacheco et al., 2019). Two EPT-HET units, Flight Model (FM)1 and FM2, are mounted on the Solar Orbiter spacecraft. The location of these units is illustrated in fig. 4.2. One unit, FM1, will be located on the -Y panel of the spacecraft and will measure particles in the ecliptic plane with two viewing directions: sun and anti-sun. The SEPs do not stream directly from the Sun towards the spacecraft, but follow the heliospheric magnetic field. This magnetic field is resembled by an Archimedean spiral, known as the Parker spiral (Parker, 1958). The Parker spiral is named after E. Parker and originates from the rotation of the Sun. As the Sun's magnetic field is carried into interplanetary space, the Sun itself and thus the footpoints of the magnetic field lines rotate. The inclination of the spiral varies with distance to the Sun. However, as the instruments have a fixed pointing angle on the spacecraft an optimal pointing angle needs to be determined. In order to calculate this angle for the sun and anti-sun unit, 1 hour average magnetic field data measured by the Helios-1 spacecraft was used, as illustrated in fig. 4.3 (Rodriguez-Pacheco et al., 2019). The Helios mission had an orbit, which is comparable to that of the Solar Orbiter mission going as close to the Sun as 0.29 AU. For the EPT-HET sun and anti-sun unit an optimal angle of 35° in the ecliptic plane was calculated (Rodriguez-Pacheco et al., 2019).

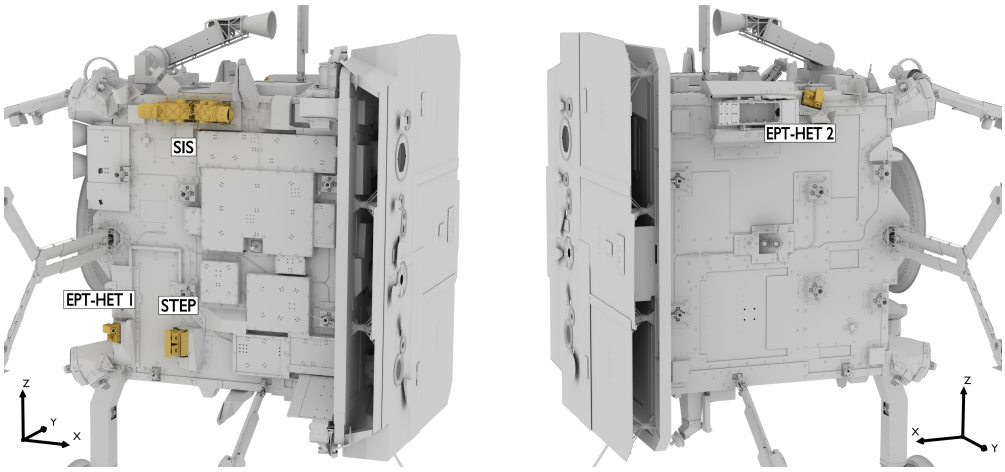

Figure 4.2: Location of the EPD instrument on the Solar Orbiter spacecraft. The X-axis of the coordinate system points towards the Sun. On the left hand side the -Y panel of the spacecraft is shown with the SIS, STEP and EPT-HET FM1 units. On the +Y side only the EPT-HET FM2 is located.

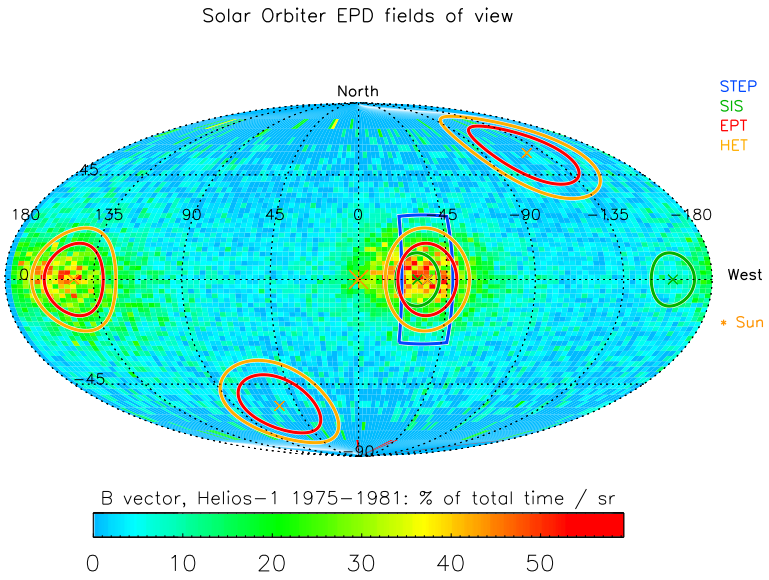

Figure 4.3: Shown is the field of view of all EPD sensors in the spacecraft frame. The field of view of the two HET units is shown in orange. The background plot is created using 1 hour average magnetic field distribution observed by the HELIOS-1 spacecraft Rodriguez-Pacheco et al. (2019).

The other EPT-HET unit, FM2, is located on the +Y panel of the spacecraft and will measure particles perpendicular to the ecliptic plane in north and south direction. With these four viewing directions, measurements of the anisotropy of SEP fluxes can provide an insight into the transport effects that affected the

particles on their way to the observer. The investigation of transport effects and anisotropy studies with HET are discussed in more detail in sec. 4.2.3.

4.2 Scientific contribution of HET

In sec. 2.2 the scientific goals of the Solar Orbiter mission are presented. As part of the EPD instrument suite, HET was designed to support the scientific goal #3: "How do solar eruptions produce energetic particle radiation that fills the heliosphere?". To illustrate how HET will support this scientific goal, different solar phenomena related to this scientific goal will be introduced and HETs contribution to their understanding will be pointed out.

4.2.1 Solar Energetic Particle events

SEP events are often divided into impulsive and gradual events (Reames, 2013). They do not only differ in their duration and the wavelengths of electromagnetic emission at the source, but also in their in-situ particle composition and fluences, so that it can be concluded that both types can be associated with different acceleration and injection processes. In Table 4.1, several features of impulsive and gradual SEP events are compared to illustrate the differences between the two event classes. With the remote sensing instrumentation of Solar Orbiter, the electromagnetic emission at the source can be detected and using the in-situ instrumentation, the particle composition and fluences can be measured.
Gradual events are named after the gradual increase and longer duration in the in-situ measured particle fluences, compared to impulsive events, where a sharp increase over a few hours in the in-situ measured particle fluences is observed (Desai and Giacalone, 2016). Furthermore, gradual and impulsive SEP events can be distinguished based on the electromagnetic emissions at their source regions, called radio bursts. While impulsive events are always accompanied by type III radio bursts, this is not the case for gradual events. These are accompanied by type II and IV bursts (Desai and Giacalone, 2016; Cane et al., 1986). In fig. 4.4 the electromagnetic emission during an SEP event is shown with the different radio burst classifications. The classification is performed based on the observed drift in frequency. The electromagnetic emission of the radio bursts is created due to Langmuir oscillations by fast electrons streaming through the coronal plasma. The frequency of these oscillations depends on the local plasma density. In case of the type III bursts, where a fast drift towards lower frequencies is observed, the electrons generating the electromagnetic emission are accelerated on open field lines (Reid and Ratcliffe, 2014; Buttighoffer, 1998).

	impulsive	gradual
Particles	electron-rich	proton-rich
$^3He/^4He$	highly enhanced	no enhancement
Fe/O	highly enhanced	no enhancement
Duration	hours	days
Metric radio bursts	III, V	II,III, IV
Coronograph observation	-	CME
Event rate/year	$\approx$ 1000	$\approx$ 10

Table 4.1: Properties of impulsive and gradual SEP events based on Reames (2013); Cane and Reames (1990); Desai and Giacalone (2016).

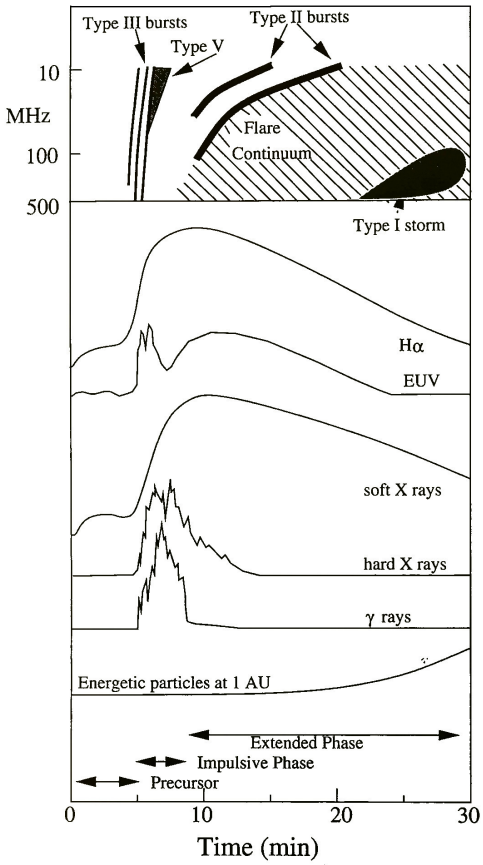

Figure 4.4: Solar electromagnetic radiation during different phases of an SEP event Kallenrode (2004).

Impulsive SEP event studies

The origin of impulsive SEP events is still under debate. For many of these impulsive SEP events the acceleration mechanism can be identified. For example, impulsive solar flares are observed as a possible particle acceleration source. In these cases, where flares or microflares are observed, they are accompanied by narrow CMEs or EUV jets. However, in some cases, no flare can be observed (Bučík et al., 2018; Nitta et al., 2006).
One possible acceleration candidate is magnetic reconnection in the lower corona. The magnetic configuration for this process is illustrated in fig. 4.5. The looped magnetic field lines intercept in the lower corona and reconnect with field lines of opposite polarity. The sudden release of magnetic energy leads to an acceleration of particles by electromagnetic fields, resonant wave-particle interactions and subsequent stochastic acceleration, but no flare can be observed (Rodriguez-Pacheco et al., 2019). If the particles are accelerated on open field lines, they can escape into interplanetary space. This can be seen in the impulsive SEP event characteristic type III bursts, which are attributed to electrons propagating along the open field lines (Buttighoffer, 1998). Due to the resonant wave-particle interactions, enrichments in certain ion species are observed, for example, the ^{3}He to ^{4}He ratio can be enhanced by a factor of $\approx 10^3$ and the Fe to O ratio by a factor of 10 compared to solar coronal values (Nitta et al., 2006). Due to the enhancement of ^{3}He, impulsive SEP events, are also known as ^{3}He-rich events. To find candidate periods for impulsive SEP events, the Fe/O ratio is often used. This ratio shows a bimodal distribution with two peaks and is better suited compared to the ^{3}He and ^{4}He ratio, which shows more variation (Reames, 2017). HET is able to measure several different ion species and determine the elemental abundances in SEP events. Therefore it will be possible to determine the Fe/O ratio with HET, to identify possible periods of impulsive events close to their source. Dalla et al. (2017) report, that the Fe/O ratio in SEP events can be further used as a tracer for transport effects. In their study, they find that the Fe/O ratio decays over time at 1 AU and it is claimed, that this can be attributed to gradient and curvature drifts, which effect the two ion species differently. These effects could be further investigated using the heavy ion measurements of HET in combination with measurements at 1 AU. The additional measurements close to the Sun, where the populations are almost undisturbed by transport effects may provide further insights into the different gradient and curvature drift processes. In general, the abundances of certain elements and isotopes is a useful indicator of the origin, acceleration mechanism and transport processes of SEPs. Thus the candidate concept of magnetic reconnection as the energy release process could be validated by particle abundance measurements in combination with the remote sensing instrumentation of Solar Orbiter. HET will contribute to that by measuring element abundances of electrons and several ion species up to Ni ions and is additionally able to distinguish between the two He iosotopes ^{3}He and ^{4}He

in an energy range between ≈7 to 41 MeV/nuc. Tammen (2016b) shows that the ^{3}He to ^{4}He can be measured down to a ratio of 1% with HET. The measurement of the ^{3}He to ^{4}He ratio over a wide energy range by HET will support the study of impulsive SEP events to identify acceleration and injection processes that lead to the significant enhancements in ^{3}He in those events.

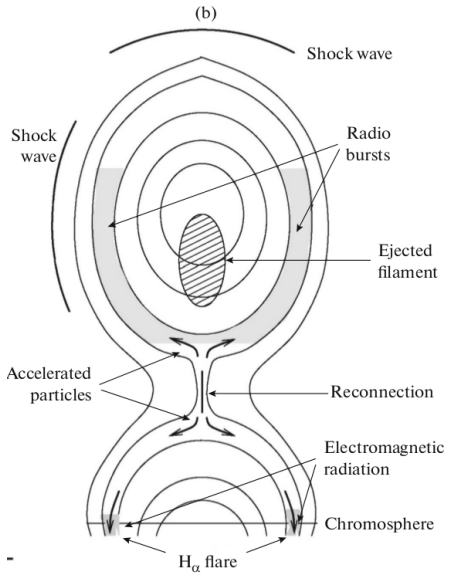

Figure 4.5: Illustration of the magnetic configuration for magnetic reconnection Minasyants et al. (2016).

Gradual SEP event studies

Gradual SEP events are almost always accompanied by CMEs. Thus, the origin of highly energetic particles has been linked to diffusive shock acceleration processes (see sec. 2.2) at the shock fronts of these CMEs (Nitta et al., 2006; Kahler, 2001). During CMEs, large quantities of coronal plasma and its accompanying magnetic field are released from the Sun (Reames, 2017). For these gradual events, the charge state of the measured ions is consistent with the plasma temperature of the ambient coronal plasma, in contrast to impulsive SEP events, where higher ion charge states are measured (Nitta et al., 2006). Furthermore, the ion abundances found in most gradual SEP events match the solar wind abundances, thus for most SEP events a possible seed population can be identified. However, for some gradual events enhancements in certain ion species are found, compared to the solar wind (Mason et al., 1999). The enhancement of ^{3}He is mostly attributed to impulsive events, so that the source of this enhancement is still investigated, as a clear separation between gradual and impulsive is not possible for these events. The origin of this enhancement is yet unclear, but it might be possible that these

particles are remnants of previous impulsive SEP events (Mason et al., 1999). Fisk and Gloeckler (2008) find an enrichment of Fe and ^{3}He in the suprathermal tails of the solar wind compared to normal solar abundances. These particles may also play a role as a seed population for the observed enhancement of specific ion species in gradual SEP events. Finally, the seed population, which leads to the enhancement is not identified. A determination of the pristine SEP composition at different energies provides valuable information on the injection processes and the seed population of these events. With HET measurements close to the Sun, this pristine SEP composition can be sampled for many heavy ion species in a wide energy range. Close to the Sun, the SEP composition and energy distributions are less affected by shocks or other transport and acceleration processes. Furthermore, multi-spacecraft measurements close to the Sun can reveal the origins of wide-spread events observed at 1 AU. At this distance the distinction between a broad particle injection source or a broadening due to transport effects is difficult to perform (Dresing et al., 2014). Together with the high-energy particle instruments, HET and LET of EPI-HI, onboard of Parker Solar Probe (Guo et al., 2014), the necessary multi-point observations can be provided. Using the He isotope separation capabilities of HET, the source of the ^{3}He enrichment in the ^{3}He enriched gradual SEP events can be investigated.
Reviewing the properties of the impulsive and gradual SEP events given in table 4.1, HET will be able measure the ^{3}He to ^{4}He ratio, the Fe to O ratio and also the H to He ratio. With the measurement of these ratios, impulsive and gradual SEP events can be identified and characteristics of these events can be assigned to the according class.
Kahler (2001) also investigated the influence of enhanced ambient SEP seed populations at the time of the CME by correlating 2 and 20 MeV proton peak intensities with the speed of CMEs. They conclude, that the peak intensities of SEP events at 1 AU are depending on the CME speed and can be influenced by the energy spectrum of the event. However, the large variations in peak flux intensities at a certain CME speed can not be fully attributed to the influence of the energy spectrum. An influence of an enhanced ambient SEP population could not be concluded in the investigation. With HET the proton intensities at several different energies can be measured and thus a proton energy spectrum in the high energy range of SEPs can be obtained. These measurements may provide a clearer picture of the influence of ambient SEP seed populations and to the peak fluxes of SEP events. Due to the unique orbit of Solar Orbiter, the studies can be performed in the inner heliosphere where the SEP event characteristics are less altered and the overall SEP event structure is less broadened by transport effects.

4.2.2 High-energy electron detection

Highly energetic electrons can be found in impulsive SEP events, as shown in table 4.1. However, the shocks found in gradual SEP events can also accelerate electrons to relativistic energies (Reames, 2017). Using electron measurements of HET, the release time of the particles from the acceleration site can be determined. As illustrated in fig. 4.4, impulsive SEP events are accompanied by strong electromagnetic radiation in different wavelengths. Combining the HET data with X-ray and EUV-observations by the remote sensing instruments on Solar Orbiter, the reconnection site can be identified and information on the phenomena on the solar corona can be gained. In detail, the STIX instrument will provide measurements of the X-rays produced by the energetic electrons at the acceleration site, that are detected by HET once they are released and reach the spacecraft (Reames, 2017; Rodriguez-Pacheco et al., 2019).

4.2.3 Transport effects and particle flux anisotropies

The energetic charged particles released from the Sun are affected by several transport effects. Scattering for example leads to an isotropization of the particle flux, so that a particle event may be measured from all direction at the observers location. Particles measured from the rear direction of the observer are an indicator for the processes and conditions along the magnetic field line behind the observer. With the HET measurements close to the Sun, the transport processes themselves can be investigated. While at 1 AU the SEP distributions are altered due to scattering, focusing or perpendicular diffusion, the distributions are more pristine close to the Sun. Thus, Solar Orbiter will help to understand these transport effects by providing additional inputs close to the injection sites. With this information, transport models can be tested and improved. As described in sec. 4.2.2 for the high-energy electron detection, HET will provide particle compositions and energy distributions for SEPs. While this is routinely done by many spacecraft at 1 AU, HET will provide these measurements close to the Sun. At these distances, the particles are less affected by the different transport effects, so that the change in the measured distributions close to the Sun, compared to 1 AU and beyond, can be used to investigate the particle transport effects. The study of transport effects is further supported by the four viewing directions of HET, which allows to study the anisotropy of energetic particles at different energies. Anisotropy studies provide information on the particle distribution in space at the location of observation. For example, it can be identified, whether a beamed or isotropic particle distribution is present. Thus information on the transport processes, like scattering and diffusion, and their influence on particle propagation, e.g. change in the mean free path of a particle, can be gained. Without this kind of information it is difficult to distinguish between an event, where the

particles are released gradually at the Sun and are detected rather undisturbed by the observer or an event where the injection is impulsive but the distribution is broadened due to scattering (Dresing et al., 2014; Gómez-Herrero et al., 2015).

4.2.4 Measurement of anomalous cosmic rays

An additional scientific objective which can be addressed by HET on Solar Orbiter is the study of the so called Anomalous Cosmics Rays (ACR). Though this is not one of the primary scientific objectives of Solar Orbiter, due to the special orbit of the spacecraft a study of the radial dependence in the C/O ratio of the Anomalous Cosmic Rays (ACR) is possible. Already in 1974 and 1975 anomalous features in the low energy Galactic Cosmic Ray (GCR) spectra have been reported (Klecker et al., 1975; Webber et al., 1975; von Rosenvinge and McDonald, 1975; Mewaldt et al., 1975). Klecker et al. (1977) reports anomalous features in the energy spectra for heavy ions ($Z \geq 2$) in the cosmic rays during solar quiet times measured during the IMP-8 mission and presents a summary of the so far observed anomalous features:

- The abundance ratios of C/O are drastically different from solar and galactic cosmic ray composition
- N and Ne are enhanced at low and high energies (Klecker et al., 1975; Webber et al., 1975; von Rosenvinge and McDonald, 1975), while Li, Be and B are not (Mewaldt et al., 1975).
- Anomalous O, N and He components are correlated with high-energy cosmic ray flux measured by neutron monitors
- Pioneer-10 and -11 measurements reveal a anomalous flux increase with radial distance up to at least 5 AU.

In fig. 4.6 quiet time spectra (the spectrum in absence of SEPs) for the solar minimum period from 1974 to 1978 are given for several ion species. While H shows the expected $I(E) \propto E^1$ dependence for GCR the other ion species show an upturn in the spectrum. The energy dependence of the particle flux results from the adiabatic energy loss of the expanding plasma. The upturn in the spectrum is caused by the ACR component (Moraal, 1993; Christian, 1987).

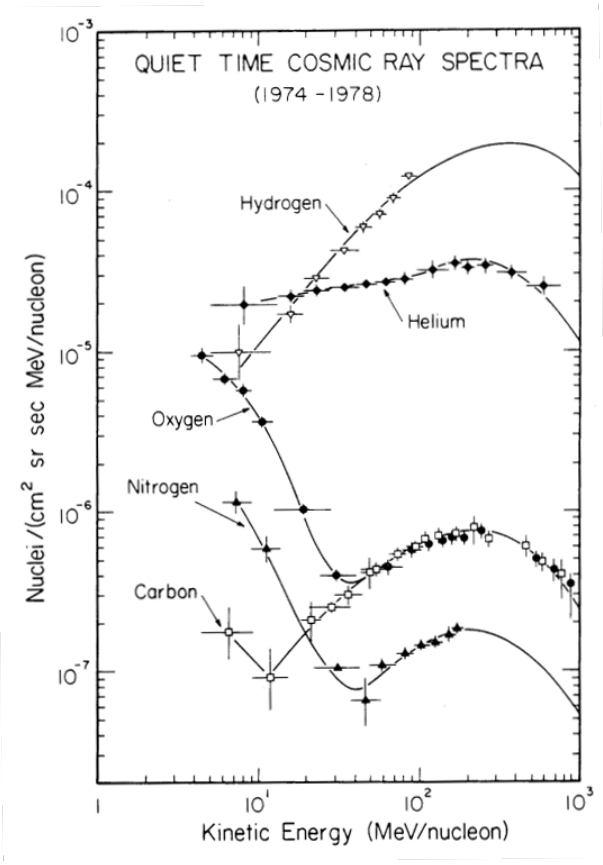

Figure 4.6: H, He, C, N, O quiet time energy spectra measured at 1AU over the period from 1974 to 1978. In the low energy regime anomalous enhancements are observed (Christian, 1987).

Today the ACR component is believed to originate from interstellar neutral particles which enter the heliosphere and then become ionized as pick-up ions due to charge exchange with solar wind ions or UV radiation (Fisk et al., 1974). Ion species with a high first ionization potentials like He, N, O and Ne are able to reach within distances of a few AU to the Sun, prior to ionization. Subsequent to the ionization, the particles are affected by the Lorentz force and follow the outward bound solar wind. Since the 70s it was considered that these particles are accelerated at the heliospheric termination shock, a boundary inside our heliosphere where the solar wind is decelerated to subsonic velocities, and then diffuse into the heliosphere (Fisk et al., 1974). However, the acceleration of the ACR at the termination shock could not be supported by the measurements of the Voyager spacecraft. Both spacecraft crossed the termination shock but did not observe the expected peak in ACR fluxes at the termination shock but rather a maximum roughly 1 AU downstream (Cummings et al., 2008). Hence, in the recent years, new acceleration processes and descriptions which are in agreement to the measurements obtained by Voyager have been formulated (e.g. Zhao et al.,

2019). During the inward motion of the accelerated ACR particles the ACR are affected by transport effects similar to the GCR and their intensities are reduced with decreasing distance to the Sun Moraal (1993). Thus, studying the radial and latitudinal distribution of ACRs in the heliosphere and determining their energy spectra, can provide insight into the transport effects in the heliosphere. Marquardt et al. (2018) derived quiet time energy spectra for the time period between 1975 - 1977 of C and O in the energy range of 9 to 80 MeV/nuc for distances between 0.3 and 1 AU to the Sun. For the investigation, the E-6 instrument onboard Helios-1 and Helios-2 was used. With HET on Solar Orbiter the Helios study of the ACR can be repeated. The quiet-time measurements performed with the Helios spacecraft at distances between 0.3 and 1 AU can be studied 40 years later with HET to investigate for example the solar cycle dependence of these ACR energy spectra. The smaller geometrical factor of HET (see chapter 9) to the E-6 is partially compensated by the use of two EPT-HET units. The advantage of HET is that it features state of the art detectors and read-out electronics that are fully configurable during the mission. If necessary, the onboard data processing of HET can be updated to feature dedicated data products adjusted to the study of the anomalous cosmic rays.

4.2.5 Summary of the scientific contribution of HET

The unique orbit of Solar Orbiter combined with the remote-sensing and in-situ instrumentation will provide important contributions to the understanding of our Sun. HET will support this by measuring the composition and energy spectra of highly energetic charged particles over a wide energy range. These measurements may help to identify the injection processes and the seed population of gradual SEP events.
Furthermore, HET will provide the ^{3}He to ^{4}He ratio and also the Fe to O ratio, which both can be used to identify time periods with impulsive SEP events. The measurement of the ion species abundances close to the Sun may provide insight into the acceleration and injection processes of these events before their signatures are altered by transport effects.
In combination with the elliptical orbit of Solar Orbiter and the four viewing directions of HET, transport effects in the heliosphere can be investigated by determining the energy and particle distributions at different latitudes and different distances to the Sun.
By combining the high-energy electron measurements of HET with the remote sensing capabilities of Solar Orbiter, the acceleration site of these particles can be identified and the remote-sensing signatures can be mapped to the in-situ measured characteristics of the particles.
With HET it will also be possible to measure the anomalous cosmic ray energy spectra 40 years after they have been measured during the Helios mission. With a comparison of the measurement data, the solar cycle dependence of these par-

Mass / g	1491
Power / W	5.2 W
Dimensions (X,Y,Z) / mm	146 x 166.7 x 157

Table 4.2: Properties of the EPT-HET FM units (Martin, 2016).

ticles can be investigated.
It can be summarized, that HET will help to identify the injection, acceleration and transport processes of highly energetic charged particles emitted from the Sun.

4.3 Design of the HET instrument

Figure 4.7 shows the EPT-HET Proto Flight Model (PFM) on an aluminum carrier plate. EPT and HET share a common electronic box in which the signal processing electronics and the power supply of both units is located. The HET sensor head is the left one of the two sensor heads. EPT-HET is a rather compact and low-weight instrument and to give a better impression of the unit, the key properties for one EPT-HET unit are given in table 4.2.

In fig. 4.8 a schematic of the HET sensor head is shown. It consists of 4 PIPS Solid State Detectors (SSDs) (see sec. 3.3.1) which are symmetrically arranged around a scintillation detector. With its double-ended sensor head HET is capable of detecting particles from two directions. The SSDs are manufactured by Canberra with a nominal thickness of 300 µm. The entrance SSDs, named HET-A, feature 2 segments, while the two inner SSDs, named HET-B, feature three segments. The segmentation enables an adjustment of the geometric factors as well as a trajectory analysis of detected particles. The outermost segment of the HET-B detectors is used as a guard ring. Particles passing through this segment did not enter the instrument through the entrance window or were scattered inside the telescope head and thus are neglected. The diameters of the individual detector segments of the silicon detectors are also given in fig. 4.8. In order to stop highly energetic heavy particles and thus achieve the required energy range, BGO (see sec. 3.3.2), was chosen as a scintillation material. The scintillation crystal is hexagonal with a thickness of 2 cm. The edges of each face are also 2 cm long. The scintillation light is detected by two Hamamatsu S3590-19 PIN photodiodes (Hamamatsu Photonics, 2012). The photodiodes are glued on two opposing surfaces of the crystal using Dow Corning 93-500 Space Grade Encapsulant (Dow Corning, 2013), a transparent rubber-like glue (Kulkarni, 2014b). The crystal, including the two photodiodes, is wrapped in two layers Millipore cellulose filtration paper (140 µm thickness each with 0.45 µm pore size) and

several layers of PTFE tape avoid the loss of scintillation light (Kulkarni, 2014a; Tonetto et al., 1999). The telescope aperture is closed with a thin foil to limit the flux of low energetic particles on the HET-A detectors. Electrons with an energy below ≈150 keV and Protons with an energy below ≈2.5 MeV will be stopped in the foil. Each telescope aperture foil consists of 25.4 µm aluminum and 50.8 µm Kapton, with the aluminum side facing towards the outward direction. Furthermore the foil protects the detectors from solar illumination, which could cause degradation due to thermal stress.

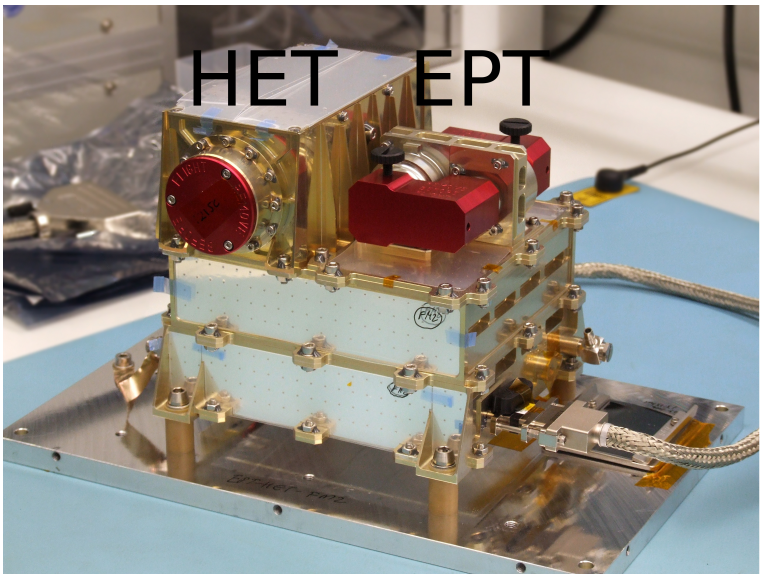

Figure 4.7: EPT-HET PFM on an aluminum carrier plate. The visible reflective surfaces are equipped with second surface mirrors to reflect possible stray light. During flight, the units are also covered with a Multi-Layer-Insulator (MLI) to reduce the heating due to solar illumination. The red items protect the telescope entries during storage and are removed before flight.

4.4 HET electronics and signal processing

For a better understanding of HETs capabilities, the electronics and the signal processing chain shall be briefly discussed. The signal processing chain is sketched in fig. 4.9 and each step of the signal processing shall be explained by reference to the corresponding step in that figure.

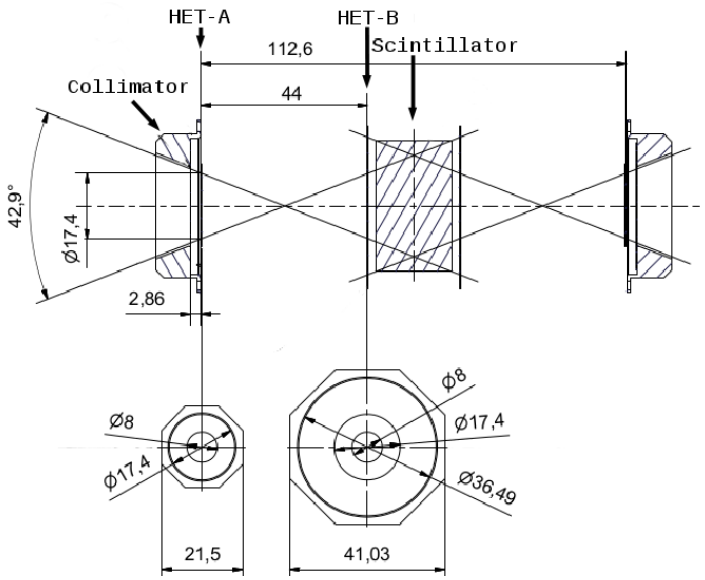

Figure 4.8: Schematic of the HET sensor head including the silicon detector dimensions. The dimensions are given in mm.

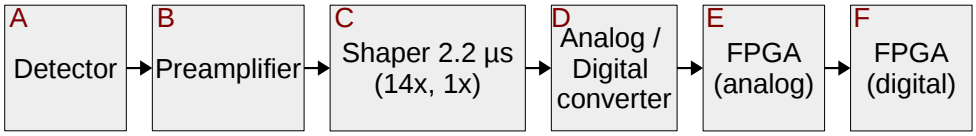

Figure 4.9: Signal processing chain of the HET detectors.

All HET detectors are connected to charge sensitive preamplifiers (B). These charge sensitive preamplifiers convert the measured charge pulse of a detector into a voltage pulse which is proportional to the measured charge pulse.
The preamplifiers are followed by shapers (C) with a shaping time of 2.2 µs and two different gains, 14x and 1x. With the dual gain read-out a higher energy range can be covered. The only detectors, which do not feature the dual-gain read-out are the HET-B guard segments, which only feature single gain read-out.
An Analog to Digital Converter (ADC), (D) in fig. 4.9, converts the analog voltage signal from the shapers to an digital signal. At high ADC values (above ADC values of ≈40000), a non-linear behavior of the ADC is observed. To avoid using data affected by this non-linearity, the low gain channels are used once the signal in the high gain channels exceeds an ADC value of 35000.
All ADCs are read out in parallel by an Field Programmable Gate Array (FPGA) at 1 MHz (E). This FPGA performs a pulse shape analysis of the signal. To distinguish the two FPGAs, this FPGA was named “analog”, as it is part of the

analog processing chain. The sampling procedure for the pulse shape analysis is performed for all detectors in parallel. The analysis yields three values for each channel: Pulse height (A-value), pulse age (B-Value) and the phase. The pulse height is proportional to the energy of the particle. To each pulse height, a pulse age is assigned. The pulse age can be used to identify if the maximum of the signal is determined. In case the current analyzed pulse-height of the signal has a higher amplitude than the previous, it is assigned a pulse age of one. But in case the current analyzed pulse-height of the signal has a lower amplitude than the previous one, the maximum of the signal is found and the pulse age is increased consecutively for each next sample of the signal by 1. This means, that a valid detection of the maximum pulse-height has at least a pulse age value of 2. The phase value is related to the discretization by the ADC clock and thus gives the phase of a discretized value in respect to the ADC clock. A more complete description is given in Böttcher (2011).
After pulse shape analysis performed by the "analog" FPGA, the event is further processed by the "digital" FPGA (F). The peak values obtained from the pulse shape analysis are checked against the Level 1 trigger where thresholds for each channel are defined. A trigger on the HET unit is a short program, that analyses a particle event upon detection. While the Level 1 trigger performs a threshold comparison for each channel, the level 2 trigger checks the different channels for coincidence / anti-coincidence and thus categorizes the event. The level 1 and level 2 trigger are explained in more detail in sec. 7.2. If pre-defined coincidence conditions for certain detectors are met, the event is scientifically analyzed by the Level 3 trigger. This trigger performs a scientific evaluation, a particle classification and stores the event into pre-defined histograms according to the particle species. The HET Level 3 triggers are described in detail in sec. 7.3. Additionally, a more complete introduction into the different HET triggers is given in the beginning of chapter 7.
Before the full descriptions of the different trigger levels and especially the development of the HET level 3 trigger is presented in chapter 7, it is necessary to provide more information on the tools that are to used for the development. Since it is not possible, to fully characterize an instrument for highly energetic particle detection by experiments, it is necessary to use simulation tools which are able to predict the interaction of these highly energetic particles with the instrument. Thus, in the next chapter 5, the simulation toolkit, which is used for the design of the onboard data processing of HET, is introduced and the details for the implementation of HET in this toolkit are given.

5. HET GEANT4 simulation

Not all operational cases of a spaceborne particle detection instrument can be tested with particle experiments prior to the launch of the mission. Therefore simulation toolkits need to be used which are capable of substituting the experiments. These simulation toolkits need to be able to use a detailed geometrical model of the instrument as an input and simulate physical interactions of particles with the instrument. The output of the toolkit should be the response of the detectors of the instrument to the incident particle radiation. The following chapter will explain the simulation setup used for all HET simulations covered in this thesis, if not specified otherwise. The data of these simulations will be used to design and test the onboard data processing for HET, described in chapter 7, and also to calculate the geometrical response factors of the instrument, described in chapter 9. The latter will be used to calculate the actual particle flux in space from the measured count rates of the instrument. As these simulations are crucial for the operation and usage of the instrument, a detailed description of the simulation setup is given.

5.1 GEANT4

For the HET simulations the GEometry And Tracking (GEANT)4 toolkit version 10.1 patch 2 is used (Agostinelli et al., 2003). The GEANT4 toolkit is developed at CERN for the simulation of particle interactions with matter. It is well established and widely used by a large number of projects and experiments and in many different fields (Allison and Amako, 2006). The toolkit provides libraries for physical interaction processes like hardronic, electromagnetic or even optical interactions over a large energy range and is able to track individual particles and their secondary particles in a user-defined geometry. Each particle is separately tracked and each track is divided into several steps. During each of these steps interactions are selected for the particle with Monte-Carlo methods based on defined physical processes (Allison and Amako, 2006). That means that for each step a process is selected from a list of possible processes depending on their probability (cross sections). Due to the stochastic selection of processes it is necessary to simulate a large number of particles. The interactions that

the particles may undergo in the GEANT4 simulation are defined in so called "physics lists". There are pre-defined physics lists available but it is also possible to tailor user-defined physics lists for specific tasks. For this work, a pre-defined physics list "QGSP_BERT", for high energy physics was selected. This physics list is recommended by D. Wright (2013) and covers standard electromagnetic processes to simulate interaction processes of highly energetic charged particles with matter and is such well suited for the simulations of HET. The process of ionization quenching, described in sec. 3.3.2 is not taken into account in the simulation directly. The necessary prediction for the ionization quenching for the data obtained from the simulation is addressed in sec. 5.4.

5.2 Modeling of the instrument

To reproduce the simulation results used in this thesis a detailed description of material implementation and the instrument modeling is given. All distances and dimensions for the instrument are taken from the CAD data, which was used for the manufacturing of the individual parts of the instrument. Figure 5.1 shows a side-view of the GEANT4 implementation of the HET unit that shall be used for illustration. The simulation includes the electronic box of the EPT-HET unit and a fully equipped sensor head. The main importance for the HET simulation, is the correct implementation of the sensor head components including the distances and dimensions of the collimator and the detectors. The dimensions of the silicon detectors are given in the sensor head drawing in fig. 4.8 presented in sec. 4.3. Housing, collimator and detector carrier dimensions are directly obtained from the CAD files and are not given here, as these parts are complex and the dimensions need to be obtained from several drawings. In table 5.1 all used materials for the individual components are given. The geometry of each part is converted into either simple geometric forms or for complex geometries the part is divided into polygons or several sub-parts. The HET sensor head housing is simplified, to reduce the simulation time. Thus, non-important details of the sensor head housing are neglected, so that it is resembled by a rectangular box with a wall thickness of 1 mm. These simplifications include the screws and screw-slots and also the triangular stiffening structures outside of the sensor head. They are considered non-important for the design of the onboard data processing as they are not located in the nominal particle acceptance path of HET. The triangular stiffening structures are visible in the photograph of the EPT-HET unit displayed in sec 4.3, fig. 4.7. The implementation of the stiffening structures and screws are planned for future simulations to create a more accurate model. However, a significant change in simulation results is not expected. All other details of the sensor head are implemented as close to reality as possible.

Part	Material	Implemented as	Density g/c^3	Reference
Housing	Aluminum	Al	2.70	-
BGO cage	Aluminum	Al	2.70	-
HET entrance cone	Aluminum	Al	2.70	-
Entrance foil	Kapton Aluminum	C_{22} H_{10} N_2 O_5 Al	1.43 2.70	(Shah et al., 2003)
Silicon detectors	Silicon	Si	2.33	-
Silicon detector carriers	Kapton	C_{22} H_{10} N_2 O_5	1.42	(Shah et al., 2003)
Photodiode (Si)	Silicon	Si	2.33	-
Photodiode (Ceramic)	White ceramic	Al_2O_3	3.90	(MakeItFrom.com, 2019a)
BGO	BGO	Bi_4 G_3 O_{12}	7.13	(Avdeichikov and Bergholt, 1994)
PTFE scintillator wrapping	Polytetrafluoroethylene	C_2F_4	2.16	(MakeItFrom.com, 2019b)

Table 5.1: Materials of the parts used in the simulation and their implementation.

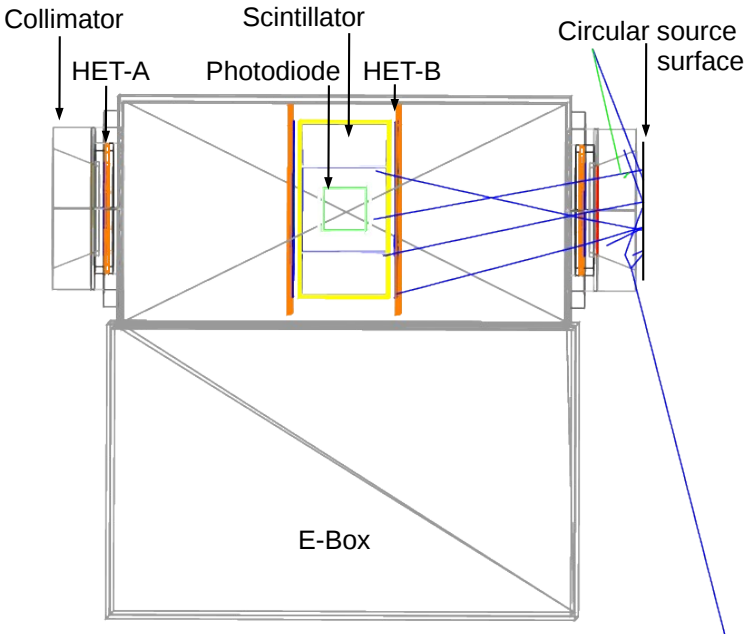

Figure 5.1: Side view of the GEANT4 simulation setup of HET. Only the contour lines of the parts are shown. On top of the electronic box (E-Box) the sensor head is located. All important components of the sensor head are included in the simulation. The blue lines are protons emitted from the source surface, which is illustrated by the black line in front of the collimator. The detector carriers of the SSDs are displayed in orange and the crystal cage in yellow.

5.3 Particle source definition

The particle source is an important part of the simulation setup. In GEANT4, the particle source can either be a single point, a surface or even a volume. For particle instruments in space, an isotropic flux needs to be simulated. For HET

the simulation of an isotropic flux is necessary e.g. for the design of the onboard data processing logic and also for the subsequent calculation of the geometrical factors. An isotropic flux can be achieved by either creating a spherical source surface around the instrument and injecting particles from all sides or to use a planar source surface with a cosine-law angular distribution (Santin, Giovanni (ESA / ESTEC and RheaTech Ltd, 2008). In the latter case, the geometry of the source needs to be selected such that the particles coming from the source cover at least the instruments field of view. In case of HET, the quantity of ion species that needs to be simulated and the high energy range of HET require run-time optimization of the simulation. Therefore, the approach of using a source surface that is placed directly in front of the collimator of the instrument with a distance of 13.85 mm in front of the HET-A solid state silicon detector was selected. The source is therefore directly located in front of the entrance collimator of the HET detector head as illustrated in fig. 5.1. The use of a spherical source around the HET instrument has the drawback that most of the injected and tracked particles will not create a valid event in the HET detection logic. For selected simulation setups, this spherical source surface could provide additional information for rare cases, where a particle is not coming from the nominal view cone of an instrument but is scattered into the view cone e.g. by a collimator. In case of HET, where for all triggers at least a coincidence detection in two separate detectors is necessary, this is considered a rare case. The particle fluxes for SEP events at high particle energies which are able to penetrate the HET housing are reduced compared to lower energies Reames (2017). In combination with the coincidence logic it can be considered that only a diminishing fraction of these rare particles will not be discarded by the data processing logic of HET. Still, for future simulations a spherical source can be used to study the effect of these cases in detail.
For the current HET simulations a circular planar source is used. The minimal radius of the circular source surface can be easily calculated from geometrical considerations taking into account the distances and sizes of the HET detectors. The minimal radius of the source surface and the actual used one for the ABnC, ABC and penetratring trigger is given in table 5.2. For the GCR trigger, with an increased field of view, the same information is given in table 5.3. As described in sec. 4.3 the full opening angle of the instrument is given as $\phi_{ent} \approx 43°$ for the ABnC, ABC and penetrating trigger. With a source diameter of 33 mm the margin for the half- angle is 7.82°, so that particles can still be scattered from the collimator into the detectors and the nominal entrance angle is well covered. The particles are generated randomly on the defined source surface with an initial azimuthal angle ϕ and polar angle θ. These angles are not restricted in the simulations, so that θ ranges from 0 to $\frac{\pi}{2}$ and ϕ from 0 and 2π. Still, the angular distribution follows the cosine-law, as pre-defined for the particle source. The primary energy E of each particle is sampled from a chosen statistical distribution. For all HET simulations a power law with an index of -1 is chosen, so that the

intensity I is given by eq. 5.1.

$$I(E) \sim E^{-1} \tag{5.1}$$

The HET data processing logic and the subsequent histograms are all logarithmically binned. By using a power law spectrum with an index of -1, each logarithmic primary energy bin of the simulation contains the same amount of particles.
The simulated energy ranges for the different trigger classes are given in table 5.4. Since each trigger is sensitive to a defined energy range, only this energy range with an additional margin is simulated, in order to achieve high statistics for particles within the sensitive energy range. In each case, the upper energy range is selected with a significant margin, as higher energetic particles can lead to contaminations at lower energies.

ABnC & ABC & Pen.	Minimal	Used
Diameter / mm	28.35	33
Half- angle	21.58°	29.4°

Table 5.2: Size of the source surface in front of the HET-A detector of the GEANT4 simulation for the three main HET trigger classes: ABnC, ABC and penetrating.

GCR	Minimal	Used
Diameter / mm	100.2	118
Half- angle	35.6	41

Table 5.3: Size of the source surface in front of the HET-A detector of the GEANT4 simulation for the GCR trigger.

Particle species	ABnC & ABC	Pen. and GCR
Electrons	0.1 - 100 MeV	15 - 500 MeV
Protons	5 - 200 MeV	80 - 2 GeV
Helium	20 - 800 MeV	80 - 2 GeV/nuc
Heavy ions	5 - 200·Z · $\sqrt{(A)}$ MeV	80 - 2 GeV/nuc

Table 5.4: Energy limits for the different particle species for the different HET level 3 trigger classes. For the heavy ions, the atomic charge number Z and mass number M of the particle are used to calculate the maximum energy limit for the ABnC and the ABC case.

5.4 Ionization quenching prediction for the BGO scintillator

In sec. 3.3.2 the effect of ionization quenching is explained. For particles, which produce low ionization densities in a scintillator, the relation between energy deposition and scintillation light production is linear. For particles that produce high ionization densities the relation is no longer linear as the light output is quenched. The effect of ionization quenching is qualitatively illustrated using fig. 5.2. The figure shows experimental data (black), measured with the EPT-HET engineering model in July 2016 at the Heavy Ion Medical Accelerator in Chiba (HIMAC), Japan. The HIMAC facility provides highly energetic heavy ion particle beams for different ion species. The experimental data is compared to GEANT4 simulation data (red), which resembles the experimental setup. A detailed explanation of the calibration process, including a temperature correction, and the HIMAC specific simulation setup is given in chapter 8 as this section shall focus on the introduction of the ionization quenching correction, using the data merely as an illustration. For these simulations, a directional particle beam is used, as in the experiment. As explained in chapter 5, the GEANT4 simulation calculates the energy deposition of a particle in a defined material. The process of scintillation light production and therefore the effect of ionization quenching is not covered in the simulation. The y-axis of fig. 5.2 shows the energy deposition in the inner segment of the HET-B detector. Comparing the simulation (red) and experimental (black) data of the HET-B detector, a good agreement is found for all ion species in both panels. For the SSDs, no energy dependent non-linearities are expected and the agreement proves, that the performed simulation is able to reproduce the experiment. The x-axis of fig. 5.2 shows the deposited and thus expected measured energy for the simulation (red) and the measured energy in the experiment (black) of the BGO scintillator. The H and He ions show a good agreement, as these light particles create only low ionization densities in the scintillator and thus, the amount of lost light due to ionization quenching is very low. In the left hand panel of fig. 5.2, the heavier particles (C, O and Ar) show a mismatch between experiment and simulation that increases with ion mass. The mismatch is attributed to the effect of ionization quenching.
In Tammen et al. (2015) a generalized quenching prediction model for BGO is developed. The model can predict the scintillation light loss in BGO due to ionization quenching for several ion species. Therefore the data processing of HET can be performed with simulation data to which this quenching prediction model is applied. The necessity of using simulation data for the data processing development is already discussed at the beginning of chapter 5. Without a quenching prediction model, a correct onboard data processing can not be designed.
Tammen et al. (2015) used eq. 5.2, which is the integral of the Birks equation (eq. 3.5 sec. 3.3.2) with the approximation for the energy loss per path length

dE/dx in eq. 5.3 to perform a fit to the light yields of different ion species measured at HIMAC.

$$L(E, A, Z) = \int dL = \int_0^{x_{max}} S \frac{\frac{\mathrm{d}E}{\mathrm{d}x}}{1 + k_\mathrm{B} \frac{\mathrm{d}E}{\mathrm{d}x}} dx \tag{5.2}$$

$$\frac{dE}{dx} = \frac{CAZ^2}{E^{0.7}} \tag{5.3}$$

An example of the fit result for carbon ions is shown in fig. 5.3. Carbon ion measurements at different energies and the corresponding simulation data is shown. The y-axis shows the energy measured by the BGO scintillator during the experiment. The measured energy is determined from the scintillators light yield. On the x-axis, the energy deposition in the BGO scintillator as obtained from GEANT4 simulations for the corresponding experimental setup is given. Particles that do not induce ionization quenching are expected on the diagonal line. The solid red line represents a numerical solution of eq. 5.2. With this, the light yield for carbon measurements at other energies can be predicted.
Two parameters, $f_1 = S$ and $f_2 = C \cdot k_\mathrm{B}$ were determined for each of the available ion species (He, C, O, Si, Ne, Fe). Tammen et al. (2015) derived a functional dependency of these two parameters depending on the ion species charge number Z, as given in eq. 5.5 and 5.6 for BGO.

$$dL(E, A, Z) = \int_{E_0}^{E_{max}} f_1(Z) \frac{1}{1 + f_2(Z) A Z^2 E^{-0.7}} dE \tag{5.4}$$

$$f_1(Z) = \min(1.043, 1.109 \cdot \exp(-0.089 \cdot Z) + 0.344) \tag{5.5}$$

$$f_2(Z) = 0.851 \exp(-0.272 \cdot Z) \tag{5.6}$$

With this charge number dependency, the model is generalized for more ion species. A complete description of the model development with more detailed derivation of the equations is given in Tammen et al. (2015); Tammen (2016b). To calculate the predicted measured energy from the GEANT4 simulation output, the path length integral given in eq. 5.2 is transformed to an energy dependent integral using eq. 5.3. This transformation results in the integral given in eq. 5.4 which can be solved numerically for each simulated ion. Applying the quenching prediction model to the data shown in the left hand panel of fig. 5.2, the mismatch for the heavy ion species between simulation and experiment is corrected, as shown in the right hand panel of fig. 5.2. A detailed quantitative verification of the quenching prediction model is given in chapter 8.
The quenching prediction model does not take the temperature of the scintillator into account. In case of Solar Orbiter, where variable temperatures for the instruments are expected during the mission, a possible temperature dependence of the effect of ionization quenching needs to be investigated. This investigation is described in the next chapter 6.

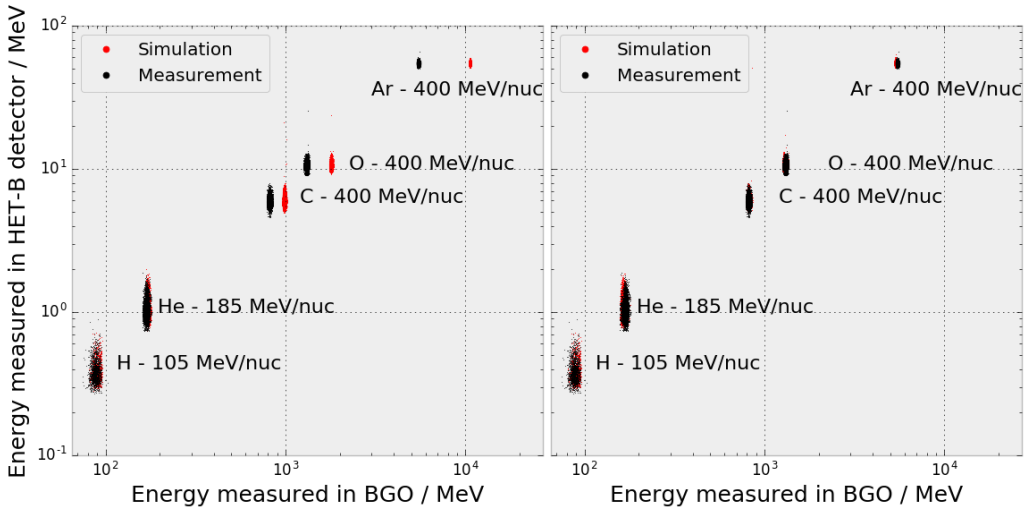

Figure 5.2: Illustration of the effect of ionization quenching in BGO using data from HIMAC 2016. The displayed data has not been used for instrument calibration. Left hand side: Comparing the "measured" energy of the GEANT4 simulation with that of the experiment, a mismatch for the heavy ions (C, O and Ar) is observed. Right hand side: Using the quenching prediction model by Tammen et al. (2015), the measured energy deposition in the experiment can be reproduced with the simulation data.

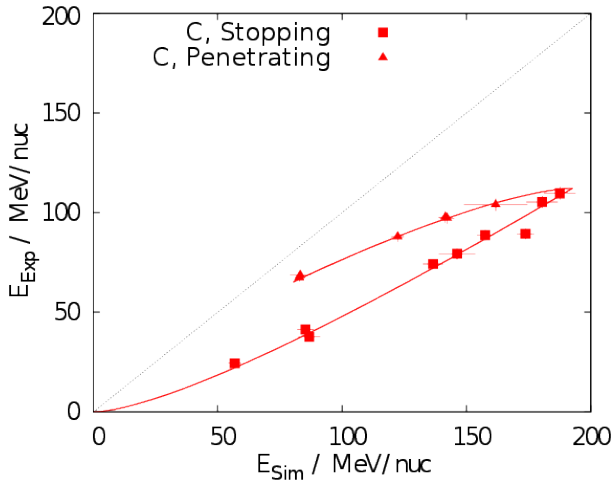

Figure 5.3: The y-axis shows the energy measured by the BGO scintillator during the experiment. On the x-axis, the energy deposition in the BGO scintillator as obtained from GEANT4 simulations for the corresponding experimental setup is given. Particles that do not induce ionization quenching are expected to be located on the diagonal line. The solid red line represents a numerical solution of eq. 5.2. Figure from Tammen (2016a).

6. HET temperature dependence

In sec. 3.3.2 the strong temperature dependence of the BGO scintillation light output is illustrated. However, not only the BGO crystal itself shows a temperature dependence, but also many of the electronic components that are part of the signal processing chain like capacitors and resistors. These components were selected for their temperature stability but due to the operational temperature range of the EPT-HET units from -30 °C to +17 °C (according to thermal models by Gomez (2017)) a change of the characteristic values of the electronic components is to be expected. For this reason a temperature calibration for all detectors of both EPT-HET FM units was performed. The calibration is described in detail by Böttcher (2018).
However, with the temperature calibration of HET it could not be clarified if the process of ionization quenching itself is temperature dependent. As described in sec. 3.3.2 the mechanisms behind the effect of ionization quenching are not fully understood and are merely described by empirical formulas (Birks, 1951). However, as the effect is related to electron excitations and subsequent non-radiative de-excitations, ionization quenching itself could be affected by temperature. Previous studies investigating the temperature dependent light output of BGO used γ rays as these are easily available from radioactive sources (Melcher and Schweitzer, 1985; Weber et al., 2003; Tsuchida et al., 1997). For the temperature calibration of the HET FM units, cosmic muons were used. Both particle species, the γ rays and cosmic muons, do not induce ionization quenching. Thus, in order to investigate the temperature dependence of ionization quenching, heavy ion measurements at an ion accelerator facility are necessary. These heavy ion species produce high ionization densities in the scintillation material and therefore induce ionization quenching. If a temperature dependence of ionization quenching is found, the model, proposed for the prediction of ionization quenching for HET by Tammen et al. (2015) would need to be improved in order to take the BGO crystals temperature into account.
As part of this work, several studies performed at Heavy Ion Medical Accelerator in Chiba (HIMAC), Japan, lead to the conclusion that the effect of ionization quenching in BGO is independent of temperature. In the following, the methods and results leading to this conclusion are discussed.

6.1 BGO-Thermal experiment

In a first approach to investigate a possible temperature dependence of ionization quenching, the EPT-HET Engineering Model (EM) 2 was modified with a cooling system. However, as the results from this approach were inconclusive a complete new instrument was constructed to conduct the experiments necessary for the investigations. The main drawbacks of the modified HET EM2 is the large amount of power necessary to cool the whole instrument, the indirect measurement of the crystal temperature at the BGO cage and bad temperature coupling of the BGO crystal due to the reflective wrapping between the crystal and its holder. The new instrument, simply named BGO-Thermal instrument, is designed such, that these drawbacks are circumvented. Figure 6.1 shows a cut through the BGO-Thermal instrument. The temperature of the BGO crystal is directly controlled by a single Peltier element on which the crystal is glued. Furthermore the temperature of the BGO crystal is directly monitored on its surface by a G15K4D489-NTC (TE-Connectivity, 2014). The electronic box (ii), which contains the readout electronics and the power supplies is fixed on top of an aluminum box which serves as the sensor head (i). The sensor head contains a hexagonal BGO scintillation crystal in flight quality with two Hamamatsu S-3590-08 photodiodes for the light detection. A photodiode of the same type is used as a tracking detector to restrict the instruments aperture. A complete description of the instrument itself including all used parts is given in Elftmann et al. (2019). The paper, as part of this thesis, is given in the appendices sec. A.2.

Temperature dependence of ionization quenching in BGO

The BGO-Thermal instrument was taken to the Heavy Ion Medical Accelerator in Chiba (HIMAC) to investigate the temperature dependence of ionization quenching by measuring four different ion species at different energies. As the energy deposition per path length, dE/dx of all four ion species is different, these are well suited to investigate the effect. This is the case since the energy deposition per path length is the main parameter for ionization quenching, as explained in sec. 3.3.2. The setup at HIMAC is shown in fig. 6.1. A thin plastic scintillator (b) is located directly behind the beam exit (a). This scintillator is part of the HIMAC setup and measures the ion flux. The beam diameter is adjusted to $\approx$1 cm for each ion species. The ion beam at HIMAC is mono-energetic. In order to alter the ion energy, PE blocks (c) of different thicknesses are used as absorbers. For each ion species two energies were selected to obtain additional data points for the investigation. For each energy, data was taken at different temperature steps. In fig. 6.2 these data points at different temperatures are shown for two carbon measurements with two different absorber thicknesses, which result in two different energies of the carbon ions. With increasing temperature, the amount

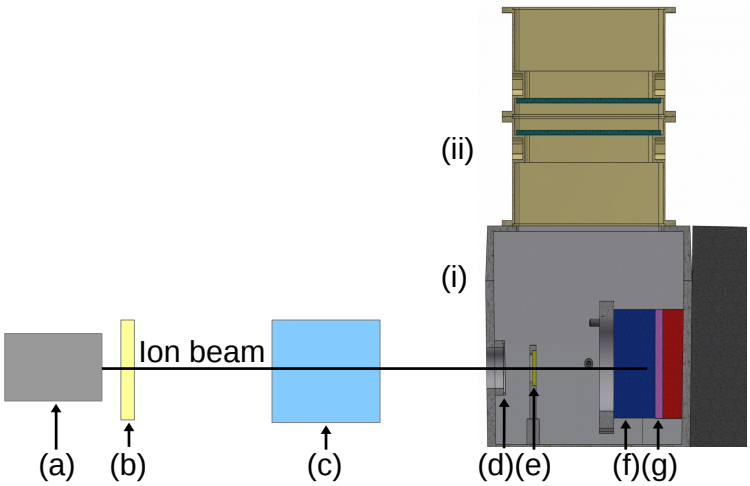

Figure 6.1: The ions exit the accelerator line through the beam extruder (a) and the ion flux is measured by a thin plastic scintillator (b). The optional PE absorber (c) can be used to alter the energy of the ions, since the accelerator provides only a mono energetic particle beam. Ions enter the instrument through a thin aluminum entrance window (d) and pass through a tracking photodiode (e). The temperature of the BGO crystal (f) is regulated by the Peltier device (g). Elftmann et al. (2019)

of measured light decreases for both measurements. The aim was to investigate, if the relative decrease with temperature is identical for all ion species and energies. Thus, for all measured ion species at the different energies, each light output curve is normalized to 20 °C for comparison. A more complete description of the data processing and temperature normalization is given in Elftmann et al. (2019). With the data collected by the instrument two main results were obtained. The first result was, that the temperature dependence of all ion species and all energies is almost identical as shown in fig. 6.3. No trend regarding ion species or ion energy could be found. The deviation of the encircled data points can be explained by a hysteresis effect, as they have been measured from cold to hot temperatures instead of hot to cold as the others. The hystersis effect is connected to the glue-detachment covered in sec. 6.2. It can be concluded, that the effect of ionization quenching itself is independent of the scintillation materials temperature. This result implies that the quenching prediction model by Tammen et al. (2015) used for HET is valid at all temperatures. The analysis of the data as well as a detailed discussion of the results is given in Elftmann et al. (2019). The second main result was that the two photodiodes showed a different behavior regarding the temperature dependent light output of the scintillation crystal that are discussed in the next section, sec. 6.2.

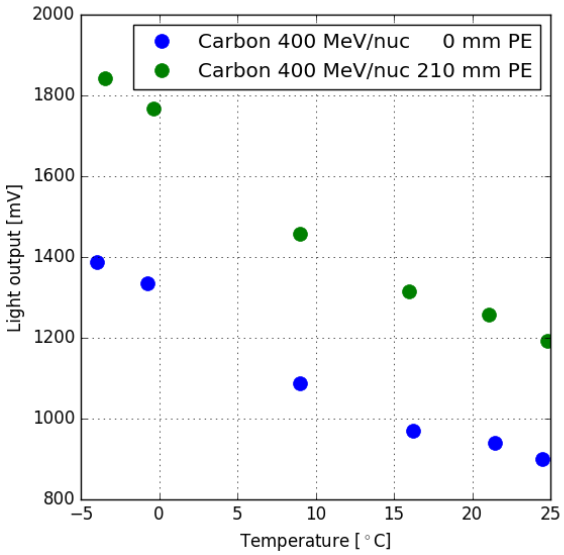

Figure 6.2: Example of the light output curves of two carbon measurements. Each data point resembles a measurement at a certain temperature. Elftmann et al. (2019)

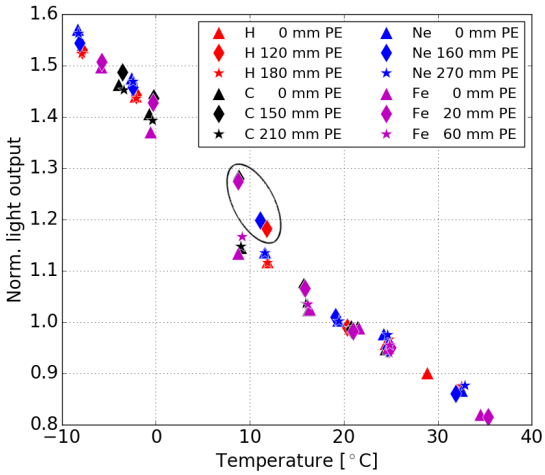

Figure 6.3: Comparison of the normalized light output curves (individually normalized to 25 °C) for different ion species at different energies. The encircled data points have been measured from cold to hot temperatures instead of hot to cold as the others. This hysteresis effect is discussed in detail in Elftmann et al. (2019).

6.2 Photodiode to scintillator coupling in HET

The studies performed with the BGO-Thermal instrument revealed a different behavior with temperature regarding the light detection efficiency of the two scintillator readout photodiodes. In fig. 6.4 one of the light output curves for Ne ions is shown for illustration for both photodiodes. Generally the slopes of the two photodiodes are identical but between 10 and 20 °C the light detection efficiency of photodiode #2 drops compared to photodiode #1. From the results of Melcher and Schweitzer (1985) displayed in sec. 3.3.2 such a drop in the temperature dependent light output curve of the BGO crystal is not expected. To investigate the origin, several experiments have been performed. It could be concluded that the photodiodes themselves were working correctly but the most probable point of failure was the gluing technique. As described in sec. 4.3, Hamamatsu S3590-19 PIN photodiodes, (Hamamatsu Photonics, 2012) are glued with Dow Corning 93-500 Space Grade Encapsulant (Dow Corning, 2013) to the crystal surface to detect the scintillation light. The gluing technique was qualified by testing for partial or complete glue detachment by thermal cycling of the scintillation detector package (Kulkarni, 2014b). Figure 6.5 shows a sketch of the photodiode mounting on the crystal. The shaded area represents the glue which fills the ceramics housing. The ceramics casing of the photodiode is in direct contact with the crystal surface.

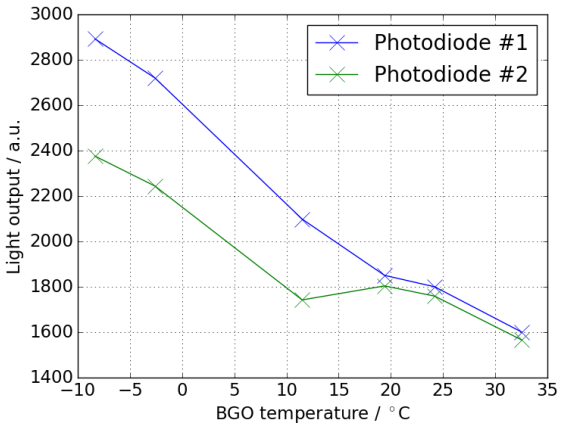

Figure 6.4: Illustration of the different light detection efficiencies of the two readout photodiodes with Ne ions measured at HIMAC. Between 10 and 20 °C the light detection efficiency of photodiode #2 drops so that it detects significantly less light at lower temperatures compared to photodiode #1.

While cooling, the glue starts to contract due to thermal stress. With a study using cosmic muons it was found that at ≈ 18 °C photodiode #2 starts to behave differently regarding the light detection efficiency compared to photodiode #1. The contraction of the glue at this temperature is 6 µm, according to eq. 6.1 tak-

ing into account the temperature of ≈ 23 °C during the gluing of the photodiode:

$$\Delta d = \alpha_l \cdot \Delta T \cdot d \tag{6.1}$$

Equation 6.1 is the standard equation for calculating linear thermal expansion. The coefficient of linear expansion α is taken from Dow Corning (2013) and the thickness of the glue d from Hamamatsu Photonics (2012). The calculated contraction is sufficient so that the glue partly detaches from the silicon surface and an optical barrier is created. This reduces the light collection efficiency of the photodiode. The detachment area seems to be related with the individual gluing process as all tested photodiodes are affected by a different degree. This effect was found to be fully reversible so that it could not be detected after the thermal cycles which are part of the BGO crystal gluing qualification.

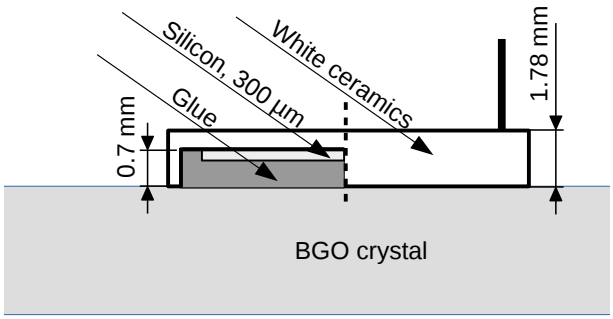

Figure 6.5: Illustration of photodiode mounting on the crystal surface after Hamamatsu Photonics (2012). The grayish area is filled with glue. The contact surface between photodiode and crystal is treated with a primer.

The major implication for HET of this finding is, that a cross calibration of the instruments is not possible. This is an essential information for the future operation of the two HET units onboard Solar Orbiter in case an in-flight calibration needs to be performed. All tested light-readout photodiodes showed a different temperature behavior so that a temperature calibration of one unit may not be used on an other. As described in sec. 4.3 the energy deposition in the BGO crystal is calculated from the mean signal of both photodiodes. Based on the data presented in fig. 6.4, a worst case uncertainty estimation of a cross calibration of $\approx 17\%$ is obtained. This is the case if both photodiodes of one unit show a temperature dependent behavior like photodiode #1 shown in fig. 6.4 and the photodiodes of the second HET unit show a temperature dependent behavior like photodiode #2. Though the exact value is not representative, the order of magnitude of this uncertainty is large for a calibration. Therefore all units need to be calibrated separately in case of an in-flight temperature calibration of the HET instrument needs to be performed.

The implication for future projects in temperature unstable environments where scintillators are used, is that a different gluing technique needs to be used. For example, if the height of the ceramics housing of the photodiodes could be reduced the detachment of the glue might be circumvented as the complete photodiode could react to contraction of the glue.
To summarizes the findings of this chapter, it can be concluded that with the results presented in sec. 6.1 no temperature dependence for the effect of ionization quenching in BGO is present. Thus, the ionization quenching prediction model for the BGO scintillator, introduced in sec. 5.4, does not need to be modified to be temperature dependent and can be used for the design of the onboard data processing of HET as is. The following chapter 7, gives a description on how the onboard data processing of HET is developed using simulation data obtained with the simulation setup given in chapter 5 and the quenching prediction model by Tammen et al. (2015). The implications of the last part of this chapter, given in sec. 6.2, do not affect the development of the onboard data processing of HET. The effect of the glue-detachment of the photodiodes and the resulting loss of scintillation light observed below 20 °C is covered by the temperature dependent calibration performed by Böttcher (2018). However, in case an in-flight calibration is performed, it is important to perform these separately for each HET unit.

7. HET data processing

One of the major difficulties of spacecraft send into the inner heliosphere is the limited telemetry to transfer measured data to Earth. Ideally, the data of a scientific instrument for particle detection, like HET, would be available in the best time and energy resolution the instrument can provide. A data format that is capable to fulfill these demands in case of HET, is the Pulse-Height-Analysis (PHA) data. This data format is capable of providing the response of every single detector for a single particle detection. However, this data format is highly telemetry intensive and in case of Solar Orbiter, the available telemetry budget is strictly limited due to the orbit (see sec. 2.1). Thus, it is necessary to pre-select and compress most of the available scientific data.
In order to provide data for the investigation of the scientific objectives which are supported by HET (see sec. 4.2), an on-board selection and compression of the data is performed. This is a challenging task, as the pre-selection and compression of the data should not impact the scientific capabilities of the instrument.
HET is capable of performing an on-board analysis of the data based on pre-defined programs, so called triggers. The triggers are divided into certain levels, one, two and three, based on their complexity. With these triggers, the data is categorized, evaluated and finally added to pre-defined histograms. Sending the complete histograms would still be too telemetry intensive, so that a further data selection and compression is necessary. During the selection, the counts in several bins of a histogram may be summarized to one number, so called Data Product Items (DPIs). The DPIs are part of so called data products (DPs). For most cases, the Data Products (DPs) are defined for a specific ion species, e.g. carbon, with a fixed cadence and this DP features several DPIs to provide an energy resolution. The telemetry can be further reduced by applying a compression scheme to the number of counts in each DPI. The data products and according data product items are further introduced and illustrated in the individual HET level 3 trigger sections 7.3.1, 7.3.5 and 7.3.6, respectively.
As explained, HET features three different trigger levels to categorize and evaluate a detected particle. The level 1 and 2 triggers are only used to select the appropriate level 3 trigger for a detected particle by requiring certain coincidence conditions of the HET detectors. The level 1 and 2 triggers are described in sec. 7.1 and sec. 7.2, respectively. In the different level 3 triggers the actual anal-

ysis of a detected particle is performed. There are a total of 4 different level 3 triggers in order to provide the best possible scientific data for different science aspects:

1. The AB not C (ABnC) trigger, designed for particles that stop in one of the HET-B detectors.

2. The ABC trigger, designed for particles that stop in the thick scintillation crystal (C).

3. The penetrating trigger, designed for particles that penetrate all four silicon solid state detectors and the scintillation crystal.

4. The GCR trigger, which has a similar design as the penetrating trigger, but is reduced in complexity and is designed for particles which pass through both HET-B detectors and through the scintillation crystal. Therefore a higher field of view compared to the HET penetrating trigger is achieved.

The two stopping triggers, ABnC and ABC provide the best energy resolution of all four triggers and are capable resolving the two He isotopes, ^{3}He and ^{4}He, which is important for the identification of SEP acceleration mechanisms as described in sec. 4.2. Particles with higher energies, which even penetrate the scintillation crystal, are evaluated by the penetrating trigger. This trigger extends the energy range of HET, but a clear ion species separation for heavy ions is not possible. Additionally to the three level 3 triggers for SEPs, a trigger designed for the detection of Galactic Cosmic Ray (GCR) is available. The maximum fluxes of SEPs are significantly higher compared to the flux of the GCRs (Wiedenbeck, 2013). Therefore the GCR trigger features a significantly higher field of view. This enables the study of short term phenomena in the GCR particle flux, e.g. Forbush-decreases (Lockwood, 1971). The data evaluation and the available histograms of each level 3 trigger are described in the sections 7.3.1, 7.3.5 and 7.3.6, respectively.
In this chapter, the full onboard data processing chain is introduced. It is necessary, that the full detail of the development of the onboard data processing is given, as no other documentation exists. Scientists working with data measured by HET need to be able to understand the data selection and processing by HET in order to correctly interpret the measured data. Furthermore, this information is necessary for the optimization or adaptation of the onboard data processing of HET if necessary.
Starting with the descriptions of the level 1 trigger in sec. 7.1 and subsequently the level 2 trigger, in sec. 7.2, the general particle categorization into the different level 3 trigger classes is explained. After this, in sec. 7.3, a complete description of the development of the HET level 3 triggers is given in sec. 7.3. The development of these triggers to process the measured data onboard of HET is mainly

performed using the simulation data obtained from the GEANT4 simulations, as presented in chapter 5, which is post-processed by the quenching prediction model, described in sec. 5.4. Section 7.3 starts with a description of the two HET level 3 stopping triggers, given in sec. 7.3.1, including the particle species specific histograms, in which an particle is stored once its species is identified and it is evaluated by the level 3 stopping trigger. Before the same is done for the penetrating and GCR level 3 triggers in sec. 7.3.5 and sec. 7.3.6, a short explanation of the relative threshold value selection is given as additional information for the level 3 triggers in sec. 7.3.4. In sec. 7.3.7 the high-flux mode of HET is introduced that affects all HET level 3 triggers. In this mode, the field of view of HET can be reduced to avoid a saturation of the data processing electronics during times of high particles flux. This section is followed by sec. 7.4 which gives an introduction into the path length correction that is applied to the energy deposition in the SSDs based on the track of an incident particle. The chapter ends with delivering information on the data product categories in sec. 7.5, the data production definitions for the Nominal_stable data products for HET level 3 triggers in sec. 7.5.1 and information on PHA data in sec. 7.5.2.

7.1 HET level 1 trigger

In combination with the HET level 2 triggers, the HET level 1 triggers are used for the selection of the appropriate level 3 trigger for a detected particle. The HET level 1 triggers represent a simple comparison of the energy deposition of the measured energies to pre-defined thresholds for all HET detectors. This comparison is routinely performed after the detector signal analysis. In table 7.1 the thresholds for the level 1 triggers are given. The threshold is always set for all segments of a detector and both directions, if not specified otherwise. During periods of high particle flux, the instrument can be set to a high flux mode. In this mode the field of view for electrons and protons, the most abundant SEPs, is reduced by using only the inner HET-A segments for the detection of these particles. The high flux mode is addressed separately in sec. 7.3.7. During nominal operation, all SSD segment thresholds are set to 50 keV for the high-gain. This threshold was selected to ensure that the energy range of the level 3 triggers are not affected and that the detectors are not triggered by electronic noise. If the measured energy in one of the detectors reaches the defined threshold, the corresponding level 1 trigger bit is set for the appropriate channel. Additionally, a counter register which is available for each detector, is increased each time the detector exceeds the threshold. The counters are available for instrument diagnostics. In order to further characterize the detected particle and to select the correct level 3 trigger for it, the level 2 triggers are used, which are described in sec. 7.2.

Detector	Description	Threshold	Mode
HET-Ao	HET-A outer segments	6.2 MeV	High flux
HET-A	HET-A	50 keV	Nominal
HET-B	HET-B	50 keV	Nominal
HET-BG	HET-B guard segments	50 keV	Nominal
HET-C1	Scintillator	4 MeV	Nominal
HET-C2	Scintillator channel 1	4 MeV	Nominal

Table 7.1: Level 1 trigger thresholds for the HET high gain channels. While in high flux mode, the threshold the outer segments of both HET-A detectors is increased as described in detail in sec. 7.3.7.

7.2 HET level 2 trigger

The level 2 trigger continuously analyzes the level 1 trigger bits for pre-defined coincidences of certain detectors. Based on the detector coincidences for the measured particle, the appropriate level 3 trigger is selected. The conditions for the different coincidence cases are given in table 7.2. In case of the ABnC and ABC level 3 trigger, the two entrance detectors need to be above the trigger threshold, while the opposing detectors need to be below the trigger threshold. The event is classified with the level 3 trigger class 1 or 2, depending on which HET-A and HET-B detectors have been triggered. In the current implementation, the HET level 2 forward and backward penetrating trigger are assigned to a single HET level 3 penetrating trigger. The directional identification of an incoming particle is performed in the level 3 code and is not based on the level 2 coincidence condition.The HET level 3 penetrating trigger and the GCR trigger share the same level 3 trigger class. The two cases are discriminated at the start of the penetrating trigger which is the entry point for events which are assigned with a level 3 trigger class of 3. If one of the pre-defined coincidence conditions is met, the event is further processed by the appropriate level 3 trigger and a level 2 counter register is increased. If no condition is met, the event is discarded. The different trigger conditions are sketched in fig. 7.1 to give a graphical illustration of the different trigger cases.

Coincidence condition	Level 3 trigger class	Description
$A1 \wedge\ B1 \wedge\ \overline{A2 \vee\ B2}$	1	HET forward stopping in B1 or C
$A2 \wedge\ B2 \wedge\ \overline{A1 \vee\ B1}$	2	HET backward stopping in B2 or C
$A1 \wedge\ B1 \wedge\ B2$	3	HET forward penetrating
$A2 \wedge\ B2 \wedge\ B1$	3	HET backward penetrating
$B1 \wedge\ B2 \wedge\ (\overline{A1 \vee\ A2})$	3	HET galactic cosmic rays trigger

Table 7.2: Level 2 trigger definitions for HET. Each detected particle is classified into one of the three different HET trigger classes. The HET level 3 penetrating trigger and the HET galactic cosmic rays (GCR) trigger share the same trigger class (3) and are executed consecutively.

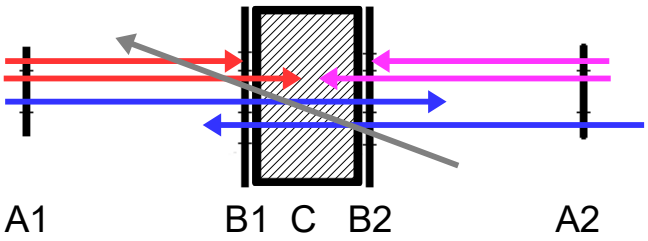

Figure 7.1: This sketch illustrates the different level 2 trigger or coincidence conditions given in table 7.2. The arrows represent valid example particle trajectories. Red for class 1, magenta for class 2, blue for class 3 penetrating and gray for class 3 GCR.

7.3 HET level 3 triggers

After a particle event is classified by the level 2 trigger into one of the three level 3 trigger classes (1, 2 or 3), it is sent to the appropriate level 3 trigger. The assignment of the level 3 trigger classes to the different level 3 triggers is shown in table 7.2. HET features four different level 3 triggers, the ABnC and the ABC level 3 triggers for stopping particles, and the penetrating and GCR level 3 triggers for particles which do not stop in the sensor head. In general, the HET level 3 triggers perform an advanced evaluation of a particle event and if this meets the pre-defined requirements, the event is added to a histogram. In case the requirements are not met, the event is discarded. Example requirements are the energy deposition in different detectors, which are compared to pre-defined thresholds or

Explanation	New naming scheme
max(HET-Ai,HET-Ao)	A
max(HET-Bi,HET-Bo)	B
Scintillation Crystal	C
A+B	AB
A+B+C	ABC

Table 7.3: For the description of the level 3 trigger histograms and the level 3 trigger logic, a new nomenclature for the energy deposition in the respective detectors is introduced, in order to improve the readability of the given explanations.

a comparison of the energy deposition in individual SSD segments. After the successful evaluation of an event, the particle is added to a histogram. These steps reduce the required telemetry as only events that are expected to be scientifically important are processed and are available for further evaluation. The usage of pre-defined histograms instead of transmitting each event that meets the predefined requirements, a further reduction in telemetry is achieved. However, due to the telemetry limitation, it is not possible to transmit complete histograms. Thus, the counts of several bins of a histogram can be combined to so called Data Products (DPs). HET features more than 100 DPs for the different level 3 trigger classes and the individual particle and ion species. Each DP is subdivided into several Data Product Items (DPIs), each resembling a different energy range of a DP. The data products are assigned to a category that defines their temporal availability for the data evaluation as explained in sec. 7.5. The layout and selection of these data products is also performed as part of this thesis.
In the following sections, the different level 3 triggers of HET are illustrated and the onboard data evaluation processes is described. Furthermore the different histograms which are generated by the level 3 triggers are shown for illustration along with the nominal data products of each histogram. In table 7.3 a new nomenclature for the detector names is introduced in order to improve the readability of the HET level 3 trigger logic descriptions.

7.3.1 HET stopping trigger

When an event is classified as class 1 or 2 by the level 2 trigger it is sent to the level 3 stopping trigger. After a general evaluation of the event, it is either classified as stopping in B or as stopping in C. The classification is based on the energy deposition measured in C. The first case is named AB not C (ABnC)-trigger, and the latter case ABC-trigger. Depending on this classification, the event is evaluated differently and stored in one of the pre-defined histograms.

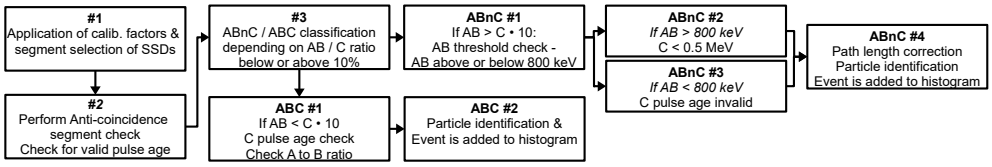

Figure 7.2: Illustration of the HET level 3 stopping trigger using a flow chart representation. Each step is described in detail in the text. Steps #1 - #3 are the general part of the HET level 3 stopping trigger. After these steps, events are categorized to either stop in the B detector or the C detector.

The design of the trigger is explained using the flowchart presented in fig. 7.2 by reference to each # in the flow chart. In the first step (#1 in fig. 7.2), the energy deposition in each SSD segment is calculated by applying calibration factors to the measured ADC values. Additionally, the segment with the highest energy deposition of each detector is identified (e.g. A = max(Ai,Ao)) in order to determine the segment which the particle has traversed. This is only done for the SSDs on the entrance side of the particle. Due to the design of the HET level 2 trigger, the incoming direction of the particle is known from the level 2 trigger class.
In the second step (#2 in fig. 7.2), a pulse age and threshold comparison for the anti-coincidence segments is performed. As explained in sec. 4.4, the pulse age of a valid trigger signal is at least 2. For the anti-coincidence check, the energy deposition in the B13G segment needs to be below 40 keV or below 10% of the energy deposition in B. Most relative thresholds in HET are set to 10% due to ion fragmentation and delta electron production of heavier ion species, as discussed in sec. 7.3.4. The production of delta electrons is described in sec. 3.2.
In last step (#3 in fig. 7.2) of the general part of the HET level 3 stopping trigger, it is tested whether the particle stopped in the B detector and is thus classified as ABnC or if it stopped in C, and is thus classified as ABC. The classification is performed by comparing the summarized energy deposition in both SSDs (AB=A+B) with the energy deposition in C. If more than 10% of the total energy of an event is deposited in C, the event is considered to be stopping in C. Otherwise the event is further processed as an ABnC event. The 10% relative threshold represents an acceptable energy uncertainty for the total energy if the particle stops in B. This uncertainty is taken into account for the calculation of the responses of the affected DPs in sec. 9.2.

Level 3 ABnC trigger

In fig. 7.3 an example particle detection with the ABnC trigger is given for illustration and a better understanding of the following ABnC trigger explanation. In this example, the particle enters the telescope through the nominal field of view, penetrates the inner segment of the A1 detector and stops in the inner segment of the B detector.
When a detected particle is classified as ABnC in step #3 in fig. 7.2, the first step, ABnC#1 in fig. 7.2, of the ABnC level 3 trigger is executed. In this step it is checked, whether the summed energy deposition in both SSDs, AB, is above or below 800 keV. In case the energy deposition in AB exceeds 800 keV, step ABnC#2 in fig. 7.2 is executed. In this case, the energy deposition in C is checked to be below 500 keV. If more energy is deposited in the scintillation detector, the particle is considered to penetrate the B detector and thus is discarded. The use of an absolute threshold (500 keV) instead of a relative threshold e.g. 10% C to AB ratio, is necessary in this step. Particles which penetrate the B detector produce a particle population, which may contaminate lighter ions. This population can be referred to as a "tail" towards lower y-axis values. Thus an absolute threshold in C is introduced to limit the length of this tail. Though the scintillator threshold of 0.5 MeV seems to be low, even for the heaviest ion species almost all particles which are to be detected with the ABnC trigger are correctly processed in this step. As an example, 95% of the "nominal" Fe ions are correctly processed. Falsely discarded particles are taken into account in the calculation of the response factors, described in sec. 9.2. For illustration, the length-limited tail is visible fig. 7.8 at high AB/A values. The figure itself is explained as part of the particle separation technique in sec. 7.3.2.
In case the summed up energy deposition in both SSDs is less than 800 keV the event may be still valid and step ABnC#3 in fig. 7.2 is executed. But a correct determination of the energy deposition in the scintillator may not be possible due to the signal to noise ratio in this energy regime. Thus an invalid pulse age for the scintillator is demanded to further process the event. An invalid pulse age is given, when no clear peak in the preamplifier signal could be found (see sec.4.4).
In the last step of the ABnC trigger, ABnC#4 in fig. 7.2, a path length correction for the A detector is performed. Due to its complexity, the path length correction is explained separately in sec. 7.4. After the path length correction is applied, the particle species identification is performed and the event is added to the species specific ABnC histogram. The particle identification method for the ABnC level 3 trigger as well as the histogram selection is explained separately in the following sec. 7.3.2.

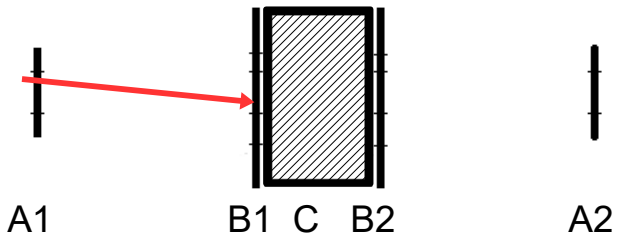

Figure 7.3: Example illustration of a valid ABnC particle detection. The detection would also be valid for the A2 and B2 detectors (other direction) or the outer segments of the A and B detectors.

Level 3 ABC trigger

In case the C to AB ratio is more than 10% in step #3 in fig. 7.2, the particle is stopping in the scintillator and is processed by the ABC trigger. In fig. 7.4 an example particle detection with the ABC trigger is given for illustration. In this example, the particle enters the telescope through the nominal field of view, penetrates the inner segments of the A1 and B1 detectors and stops in C. In step ABC#1 in fig. 7.2 a pulse age check for the scintillator is performed to validate the correct detection of the particle. For the particle identification, the minimum energy deposition of both SSDs is used, min(A,B). Due to the high energy of the particle, it is considered to be approximately the same in both detectors in most cases. By using the minimum energy deposition value from both detectors, statistical fluctuations in the energy deposition of the particles in one of the detectors can be neglected. These fluctuations can lead to the formation of a so called Landau-tail in the energy deposition distribution of these particles. The origin of the Landau-tail is described in detail in sec. 3.1. In seldom cases the energy deposition in the two individual SSDs differs by a factor of up to 10000 for heavy ions. Thus a minimum A to B ratio of 0.1 is introduced. This is shown for Fe ions processed by the HET level 3 stopping trigger with a simulated primary energy between 5 to 695 MeV/nuc in fig. 7.5, with ABC as the sum of the energy deposition in both SSDs and the scintillator. The black line illustrates the minimum ratio for A to B of 0.1. With the used simulation setup, the ratio of particles above this A to B ratio to the amount of particles below this ratio is ≈2.5. However, this number is expected to be highly depending on the source geometry. The particle above the black line in fig. 7.5 are the main ion population which is to be detected. The origin of particles below the black line was investigated for some particles species using the GEANT4 simulations. It was found that the origin of these signals are particles which do not enter the instrument through the nominal field of view but penetrate the B detector and stop in C. Prior to

this, the particles create secondary particles (e.g. delta electrons) while interacting with the housing or detector carriers. These secondary particles deposit energy in the A detector segments and exceed the defined threshold of 50 keV. The creation of the secondary particles is explained in sec. 3.2. These events are considered valid by the ABC level 3 trigger if the A/B ratio is not taken into account. These particles would not contribute to the main ion population due to their significantly different energy deposition in the individual detectors. Still, these particles can contaminate lighter particle species.
In the last step of the ABC trigger, ABC#2 in fig. 7.2, particles of the main ion population are added to an ion species specific histogram. The particle identification method for the ABC level 3 trigger as well as the histogram selection is explained separately in sec. 7.3.2.

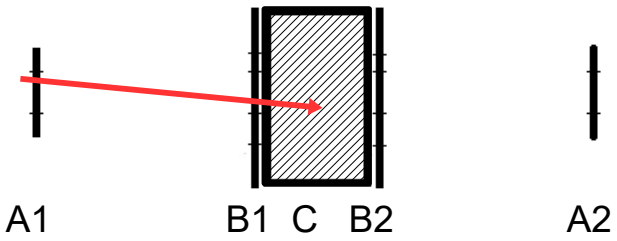

Figure 7.4: Example illustration of a valid ABC particle detection. The detection would also be valid for the A2 and B2 detectors (other direction) or the outer segments of the A and B detectors.

7.3.2 Particle separation technique for level 3 stopping triggers

The particle separation and identification method for both HET stopping triggers uses a version of the E_{tot} vs. dE/dx-method. With this method, electrons and different ion species can be identified. The method uses the total energy deposition E_{tot} and the energy deposition in a thin detector dE/dx to identify the particle species. From the Bethe-Bloch equation, see eq. 3.1 in sec. 3.1, the energy loss, dE, per path length, dx, of a particle can be approximated by eq. 7.1:

$$\frac{dE}{dx} \propto -\frac{Z^2 m}{E_{tot}} \tag{7.1}$$

With the additional information of a particles total energy E_{tot}, a term can be derived that is only dependent on the particles mass m and charge Z as given in

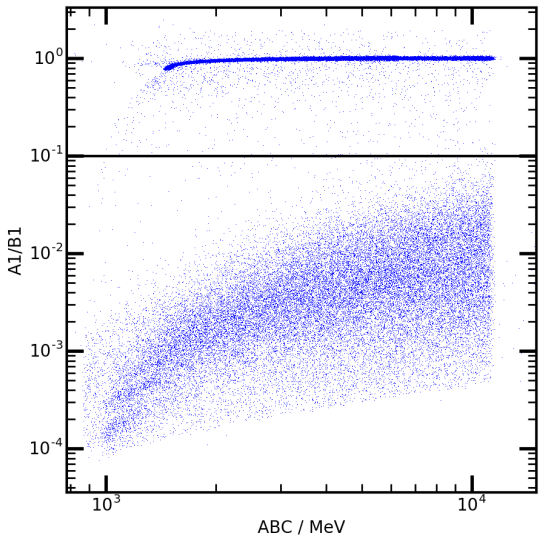

Figure 7.5: Illustration of A to B ratio cut for the ABC trigger using a GEANT4 simulation of Fe ions with an energy range between 5 to 695 MeV/nuc. The black line illustrates the A to B ratio threshold of 0.1.

eq. 7.2:

$$E_{tot} \cdot \frac{dE}{dx} \propto -Z^2 m \tag{7.2}$$

Thus, the particle species can be derived with the information of the total energy of a particle E_{tot} and the energy loss in a thin detector, dE/dx.
For the HET stopping level 3 triggers a modified version of this technique, E_{tot} / dE/dx vs. E_{tot} · dE/dx is used for particle identification. This method to evaluate the data is beneficial for particle species selection via defined thresholds and also for the data product definitions. For a better understanding how the particle separation is achieved using this technique, different steps are shown in fig. 7.6 with electrons, protons and helium ions for particles which stop in the scintillator. Starting with a simple E_{tot} vs. dE/dx-plot (a), the individual particle species can already be distinguished as predicted in eq. 7.2. By using E_{tot} · dE/dx on the y-axis (b), the alignment of the particle species is adjusted. The individual ion species can now be identified with using y-axis values (e.g. a value of 10^8 keV^2 separates protons from helium ions in fig. 7.6 (b)). With this method, the individual ion species can be selected by a minimum and maximum y-axis value for each ion species. The extent of the histogram can be reduced by using E_{tot} / dE/dx on the x-axis (c). The individual ion species are vertically aligned and thus the necessary amount of histogram bins, which translate into memory on the HET unit, is reduced. Data products for each ion species can be defined using a minimum and maximum y-axis value and dividing the x-axis

range into several bins for energy resolution. With a final modification shown in fig. 7.6 (d), the ion species can be horizontally aligned. This is achieved by using $E \cdot (dE/dx)^{1.5}$ on the y-axis. A horizontal alignment is favorable for the automated generation of the data products on the unit, due to restrictions of the FPGA memory addressing. The fact that the ion species in the histogram are not aligned horizontally without this additional rotation factor, is because the relation given in eq. 7.1, which is used to plot the data, neglects the correction terms of the Bethe-Bloch-equation (eq. 3.1 in sec. 3.1).

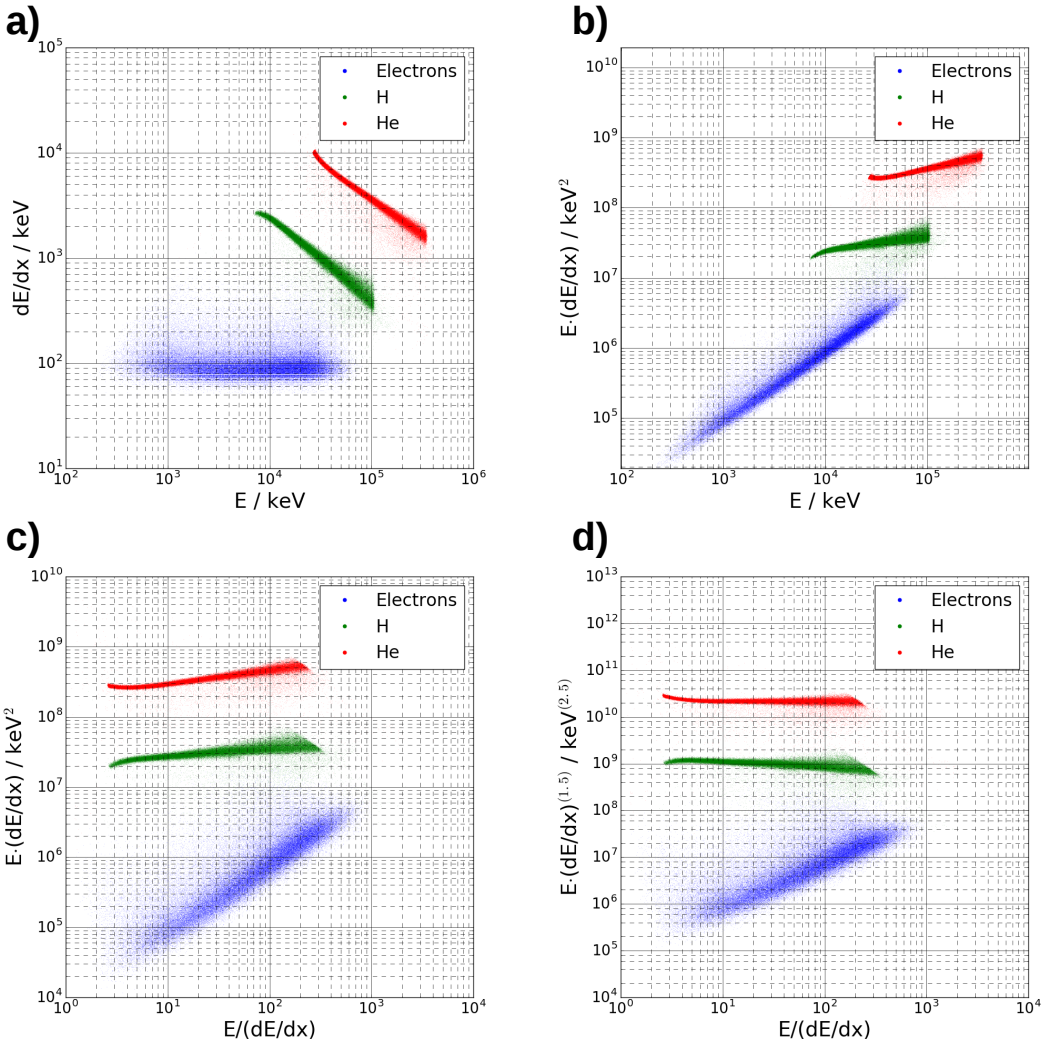

Figure 7.6: Illustration of the particle separation technique, which is used for both HET level 3 stopping triggers. For this illustration, data evaluated by the level 3 ABC trigger for stopping particles is used.

After an event is processed by the ABnC or ABC stopping level 3 trigger, the event is evaluated using the E / dE/dx vs. $E \cdot (dE/dx)^{1+\gamma}$ -technique to determine the particle species. The rotation factors γ are -0.25 for the ABnC and 0.5 for the ABC level 3 stopping triggers and are determined for an optimal horizontal alignment of He ions. Although the difference between the two rotation factors is not intuitive, the difference can be seen in fig. 7.7 for a simulation using He ions with an energy range of 5 to 200 MeV/nuc. The total energy ABC is calculated by A+B+C, for the dE/dx value the energy deposition in the A detector is used. The upper part, above the black line, are particles stopping in B. In this part of the curve, a negative slope towards lower y-axis values is observed. When the particles start penetrating the B detector, below the black line, the penetrating tail towards lower y-axis values is observed. The particles in this penetrating tail mostly stop in the scintillator's Millipore and PTFE wrapping (see sec. 4.3). Particles on the right side of the green line in fig. 7.7 penetrate the wrapping and deposit energy in C. Thus the y-axis values increase and a positive slope towards higher ABC·A -values is observed. Because of the two different slopes for particles stopping in B and particles stopping in C, two different rotation factors are necessary.

By using the introduced particle identification scheme, all species that shall be stored together in one histogram are selected using a minimum and maximum AB·A or ABC·min(A,B) value. The thresholds for the histogram selection are given in table 7.4 and are illustrated in fig. 7.8 for the ABnC and in fig. 7.9 for the ABC level 3 stopping trigger. The introduction of thresholds to select different ion species that are to be stored or combined in a histogram is necessary, since there are different requirements for the individual ion species. For example, He ions are stored in a 2D histogram with the maximum possible resolution to separate the two He isotopes ^{3}He and ^{4}He. However, this resolution is not needed for the ions heavier than He. Using the same resolution for the heavy ions as for He would exceed the available histogram memory of the HET unit. For both figures, fig. 7.8 and fig 7.9, simulation data of electrons and ion species up to Ni is used. The displayed ion species are not scaled for abundances, to achieve a good illustration, even of the rare ion species. The "uncut data" in both figures is not stored in any histogram and thus discarded. For the ABnC and ABC trigger, ion species heavier than helium are combined to a heavy ion histogram. Detailed information on the individual histograms that are created by HET unit are given in the following sec. 7.3.3.

7.3.3 Histogram definitions for level 3 stopping triggers

After the evaluation of the particle species using the threshold given in table 7.4 the particles is added to a species specific histogram. All available histograms of the ABnC and ABC level 3 trigger are displayed and discussed in detail. Fur-

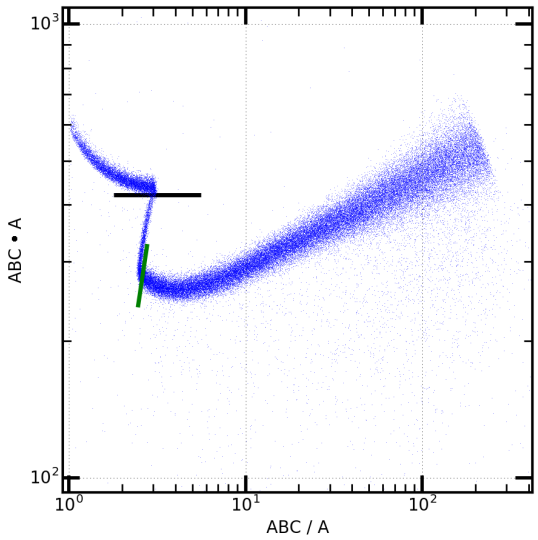

Figure 7.7: Visualization for the origin of the different rotation factors used for the ABnC and the ABC HET level 3 trigger cases using a GEANT4 simulation of He ions with an energy range between 5 to 200 MeV/nuc. While particles stopping in B show a negative slope, particles stopping in C show a positive slope. Particles above the black line stop in B, below the black line and left of the green line penetrate B without depositing any or significant energy in C. Particles on the right side of the green line stop in C.

thermore the nominal data product items are shown for each histogram. For some histograms, specific evaluation steps are introduced and are described. All histograms are shown in their actual resolution, as they are available on the HET units. The data product items as well as the histograms are designed for the most abundant SEP ion species according to Reames (2017) (electrons, H, ^{3}He, ^{4}He, C, N, O, Ne, Mg, Si, S, Ar, Ca, Fe, Ni) and are not scaled for abundance to allow a good visibility of even the very rare ion species.

Electron histograms

As discussed in sec. 4.2, measurements of highly energetic electrons with HET can be used for different scientific applications. Among the introduced applications are for example release time studies from the acceleration site (Rodriguez-Pacheco et al., 2019; Agueda et al., 2014), forecast for the arrival time of the SEPs event ions (Malandraki et al., 2015) or the use of the electron data for the investigation of anisotropy events (Dresing et al., 2014). Here, the design of the HET level 3 electron histograms are explained.

Species	ABnC / $MeV^{1.75}$ min	ABnC / $MeV^{1.75}$ max	ABC / $MeV^{2.5}$ min	ABC / $MeV^{2.5}$ max
electron	1e-3	1	0.002	2
Proton	12	30	12	50
^{3}He, ^{4}He	30	420	50	1200
Heavy ions	420	-	1200	-

Table 7.4: Thresholds for the ABnC and ABC level 3 stopping trigger particle discrimination.

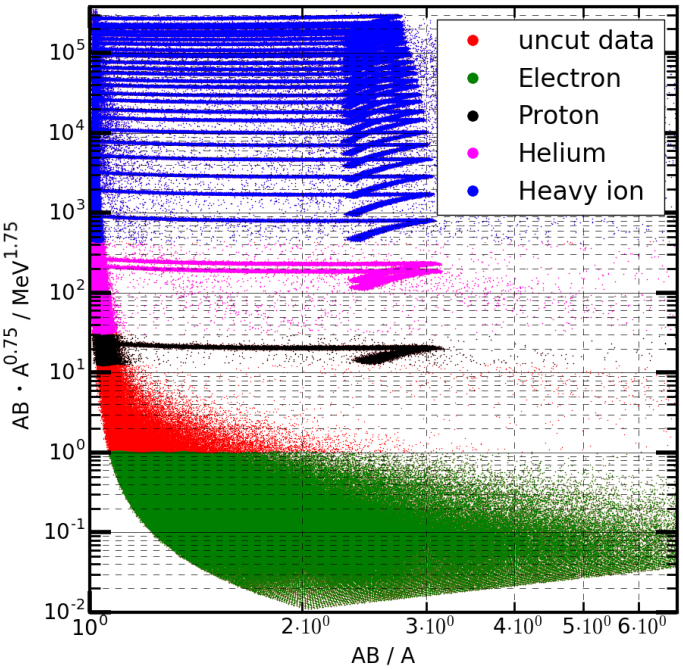

Figure 7.8: Visualization of the particle separation threshold values given in table 7.4 for the ABnC trigger. The displayed simulation data shows electrons and all ion species up to Ni, processed by the ABnC level 3 trigger logic. The uncut data, shown in red, is discarded. The tails visible for each ion species at high AB/A values originate from particles penetrating the B detector without depositing sufficient energy in C to be considered as stopping in C. The individual ion species are not scaled for SEP abundances to improve the visibility of the rare ion species.

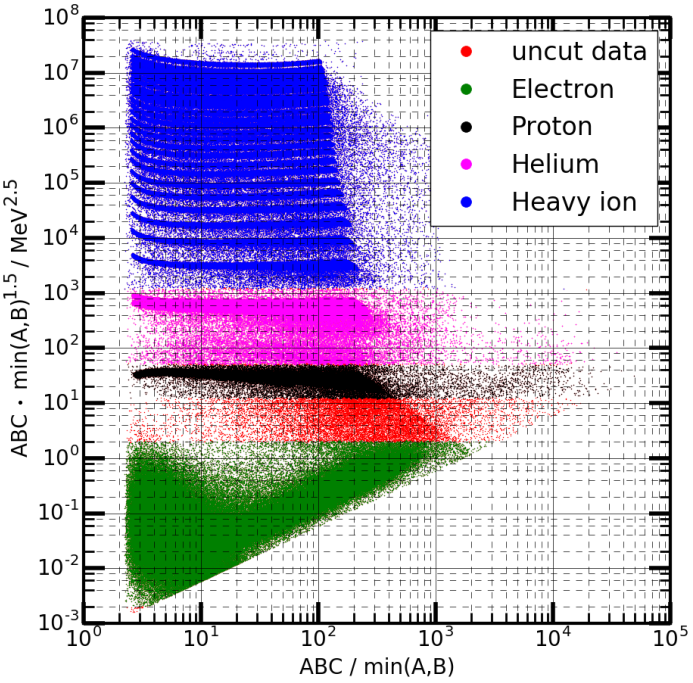

Figure 7.9: Visualization of the particle separation threshold values given in table 7.4 for the ABC trigger. The displayed data is composed of simulation data for electrons and all ion species up to Ni, processed by the ABC level 3 trigger logic. The uncut data, shown in red, is discarded. The individual ion species are not scaled for SEP abundances to improve the visibility of the rare ion species.

ABnC electron histogram

Electrons identified by the ABnC level 3 trigger are stored in a 1D histogram of AB (A+B). The histogram features 160 logarithmic bins, ranging from 0.150 to 150 MeV with 16 bins per octave, which is the maximum possible resolution of the HET unit. The ABnC electron histogram is shown in fig. 7.10. Electrons are more likely to be scattered from surfaces and are also more likely to straggle while traversing a material compared to ions. This is related to the fact, that charged particles interact with the electrons of a material. As both interacting particles have the same mass, the incident electrons are more likely to be scattered from their initial direction. Due to this high probability for straggling and scattering of the incident electrons, the primary energy distribution of the displayed energy deposition histogram in fig. 7.10 is smeared out. This means, that there is no significant difference in the primary energy distribution of electrons near the left edge of the gray box to electrons near the right edge of the black box displayed in fig. 7.10. For these reasons only one nominal ABnC data product for electrons is available, as shown in fig. 7.10 with a primary energy range 450 to 900 keV.

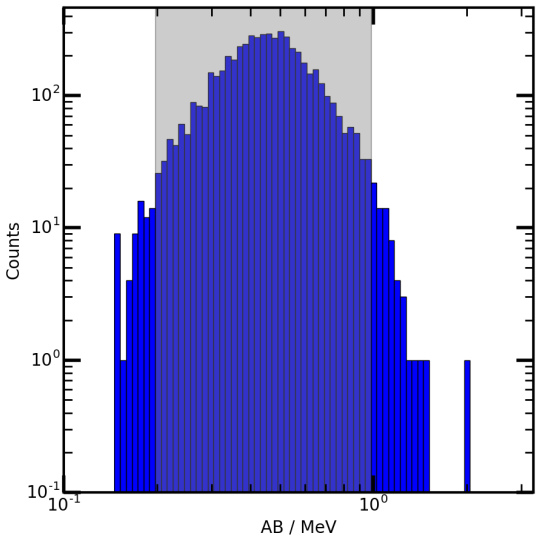

Figure 7.10: ABnC electron histogram including the nominal data product illustrated by the gray box. The definition of the data product is given in sec. 7.5.1.

ABC electron histogram

Electrons identified by the ABC level 3 trigger are stored in a 1D histogram of ABC (A+B+C). The histogram features 128 logarithmic bins, ranging from 0.25 to 38 MeV with 16 bins per octave, which is the maximum possible resolution. The ABC electron histogram is shown in fig. 7.11. Similar to the lower energy electrons covered by the ABnC trigger, the higher energy electrons covered by the ABC trigger also show high straggling and scattering. For this reason only three data product items, resembled by the gray boxes in fig. 7.11 are used. The primary energy distributions of the electrons in these three data product items smeared out and thus highly overlaps. The primary energy range covered by the three data nominal electron data products is 1 to 18 MeV.

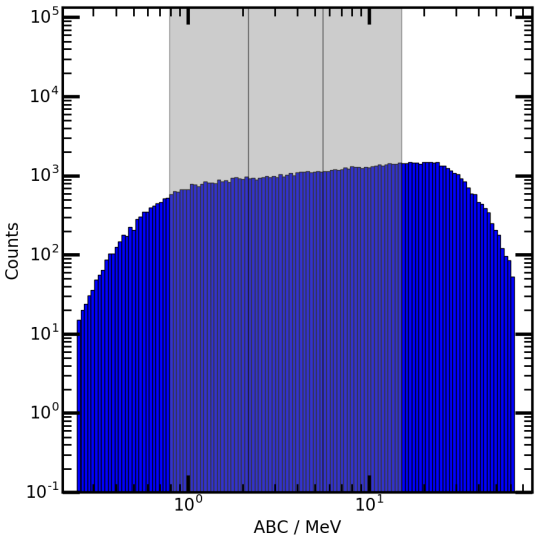

Figure 7.11: ABC electron histogram including the nominal data products as gray boxes. The definition of the data products is given in sec. 7.5.1.

Proton histograms

In sec. 4.2 examples for the scientific applications of high-energy protons measurements, which can be supported by HET, are given. For example, Kahler (2001) correlate 2 and 20 MeV proton peak intensities with the speeds of CMEs, to investigate the influence on SEP peak intensities by the SEP event spectra and the influence of enhanced ambient SEP seed populations at the time of the CME. With HET, this correlation can be further studied at different distances to the Sun over a wide energy range. Furthermore, together with electrons, protons are the most abundant SEPs. Due to their high abundance in SEP events and their higher linear energy transfer compared to electrons, protons pose a high radiation risk for manned space missions and even electronic components of satellites (Desai and Giacalone, 2016). SEP prediction and propagation models are used to reduce the risks due to highly energetic protons (Malandraki et al., 2015). Measurements of highly energetic protons by HET can be used to test and improve SEP prediction and propagation models. Here, the design of the HET level 3 proton histograms are explained.

ABnC proton histogram

The binning of the 1D ABnC proton histogram is identical to that of the 1D ABnC electron histogram. Particles that are identified as protons by using the threshold defined in table 7.4 are stored in this 1D histogram over the energy deposition in AB. As described in sec. 7.3.1, for the ion species, a penetrating tail is observed, originating from particles which penetrate the B detector. The particles do not

deposit sufficient energy in C to be considered as ABC. In a 2D histogram, these particles can be identified as the penetrating tail. For the 1D histogram, these particles would contaminate the stopping particle distribution as they can not be identified. Thus a simple threshold check in A is performed, that is only applied for ABnC protons. In this case, a threshold value of 3.1 MeV in A is identified to be efficient to distinguish between protons stopping in B and protons penetrating B. If the energy deposition is below this value, the proton penetrates the B detector. In fig. 7.12 the effect of this threshold value is illustrated. The population shown in blue is the nominal ABnC population which stops in B. The red and the green populations are protons which penetrate B but do not trigger the scintillation detector. The length of the tail is influenced by the exact thickness of the scintillators reflective wrapping. As this is not known, the tail is divided into two parts as illustrated in fig. 7.12 by using a y-axis $(E \cdot (dE/dx)^{0.75})$ threshold value of 16 $MeV^{1.75}$. The first tail population (red) are not affected by the scintillator wrapping thickness while the second tail population (green) is affected. Each tail population is summed up in a counter which is available as a data product. Only the protons that are identified to stop in B (shown in blue in fig. 7.12) are stored in the 1D proton histogram, shown in fig. 7.13 with the nominal data products. The primary energy range of the nominal proton ABnC data products ranges from 6.9 to 9.6 MeV.

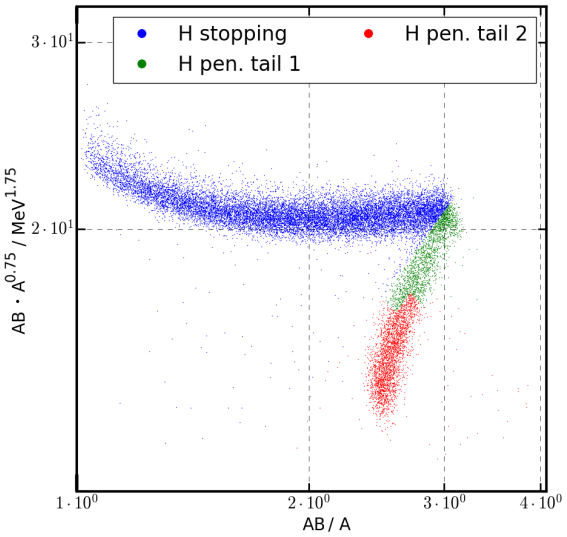

Figure 7.12: For the ABnC level 3 trigger, the proton penetrating tail is excluded from the 1D histogram by a 3.1 MeV threshold check in A. The tail is divided into two regimes using a y-axis threshold value of 16 $MeV^{1.75}$.

After the analysis of the first data obtained within the first month after launch, presented in chapter 11, the ABnC trigger was updated. It was found, that the proton 1D histogram is dominated at low deposited energies by particles with a low AB/A ratio. As discussed in sec. 11.1.1, these particles are no protons but heavier ions. Thus, only particles with an AB/A ratio $\geq$1.2 are added to the proton 1D histogram after configuration version 8 of HET, installed on 12.05.20 in both HET FMs.

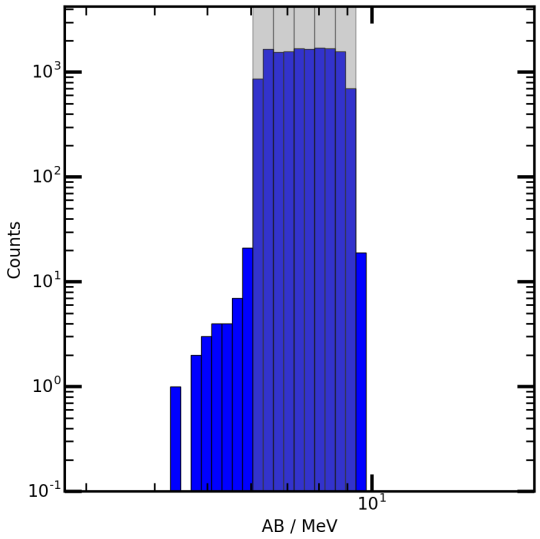

Figure 7.13: The ABnC proton 1D histogram with the nominal data product items shown as gray boxes. The histogram does not contain protons penetrating B. The definition of the data products is given in sec. 7.5.1.

ABC proton histogram

The ABC proton 1D histogram features 128 logarithmic bins of ABC. The bins range from 6 MeV up to 1480 MeV with 16 bins per octave. For particles stopping in the scintillator, no penetrating tail is visible, because the energy deposition in the crystal is large compared to energy deposition in the wrapping and the threshold of the second B detector. The energy lost in the scintillator wrapping is taken into account when calculating the responses of the individual ABC DPIs as described in sec. 9.2 using the GEANT4 simulation. Particles which are identified as protons stopping in the scintillator are directly added to the histogram. The histogram is shown in fig. 7.14 with the nominal data product. This data product contains 31 data product items (gray boxes). The primary energy range of the nominal proton ABC data products ranges from 10.6 - 105 MeV.

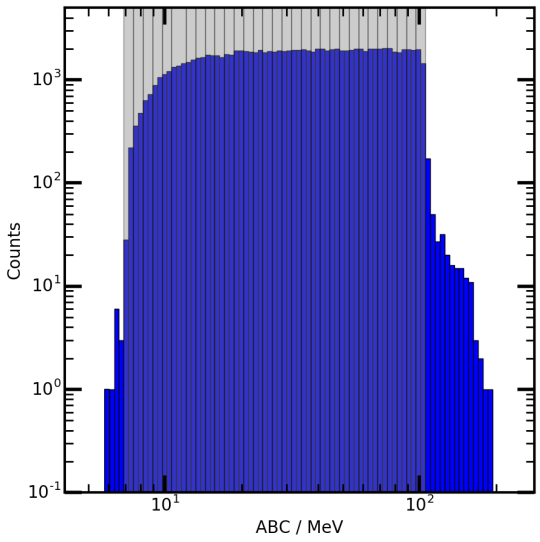

Figure 7.14: The ABC proton 1D histogram with the nominal data product items shown as gray boxes. The definition of the data products is given in sec. 7.5.1.

Helium histograms

In sec. 4.2 it is pointed out, that the isotope ratio of ^{3}He and ^{4}He may give insight into the injection processes and the seed population for SEP events. Enrichments in ^{3}He are routinely found in impulsive SEP events but can also be found in some gradual SEP events (Nitta et al., 2006; Mason et al., 1999). Thus the HET He histograms are designed to offer the maximum energy resolution HET can provide to distinguish between the two He isotopes to determine the ^{3}He enrichment over a wide energy range. The ^{3}He and ^{4}He isotope separation capabilities of HET are studied in detail in Tammen (2016b)

ABnC helium histogram

In order to separate both He isotopes in the ABnC helium histogram, it is beneficial to categorize particles identified as He by the ABnC level 3 trigger regarding their trajectory inside the sensor head. Particles detected by both outer segments of the A and B detectors show a broader energy deposition distribution compared to inner-outer or inner-inner coincidences. This topic is further discussed for the determination of a path length correction in sec. 7.4. For the isotopic separation of He, only non outer-outer coincidences are used. The separation is performed in the 2D histogram shown in fig. 7.15. The histogram features 16 logarithmic bins of AB/A in x-direction, ranging from 1 to 4 with 8 bins per octave. In y-direction the histogram features and 32 logarithmic bins of AB·A$^{0.75}$ in y-direction from 110 to 430 MeV$^{1.75}$ with 16 bins per octave. Thus, in y-direction the maximum

possible resolution is used to ensure the isotopic separation capability. The upper population in fig. 7.15 is ^{4}He and the lower is ^{3}He. At higher AB/A values, the penetrating tail of ^{4}He contaminates ^{3}He. The ^{3}He contamination by the ^{4}He ions can be corrected for, with information from the other, non-contaminated, bins. Under certain assumptions, the spectral shape and the ^{4}He to ^{3}He ratio can be calculated from the others bins and the expected contamination of ^{3}He can be derived.

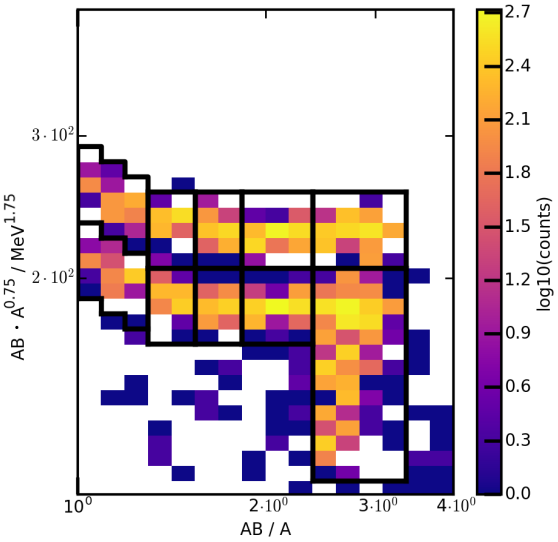

Figure 7.15: Helium ions detected by the ABnC trigger are divided into two trajectory cases. The inner-outer and inner-inner segment trajectory events are stored in this 2D histogram. Outer-outer trajectory cases are stored in the 1D histogram shown in fig. 7.16. The He nominal ABnC data product items for both isotopes are illustrated with black boxes. The upper displayed population is ^{4}He and the lower one ^{3}He. The definition of the data products is given in sec. 7.5.1.

Since only inner-inner and inner-outer segment trajectories are stored in the 2D histogram, an additional 1D histogram is used to store the outer-outer segment trajectories. The binning of this 1D histogram is identical to these of the electron and proton ABnC 1D histograms. The 1D He histogram is shown in fig. 7.16. Analog to the proton ABnC 1D histogram, the He ions which would be located in the penetrating tail (penetrating B, and not triggering C) are removed from the 1D histogram data using a 12.3 MeV threshold check in A. The removed ions are not stored separately as their flux can be estimated from the 2D histogram data products. After the analysis of the first data obtained within the first month after launch, presented in chapter 11, the ABnC trigger was updated. It was found, that the He 1D histogram is dominated at low deposited energies by particles

with a low AB/A ratio. As discussed in sec. 11.1.1, these particles are no He ions but heavier ions. Thus, only particles with an AB/A ratio ≥1.2 are added to the He 1D histogram after configuration version 8 of HET. The 2D He ABnC histogram is not affected by this change.

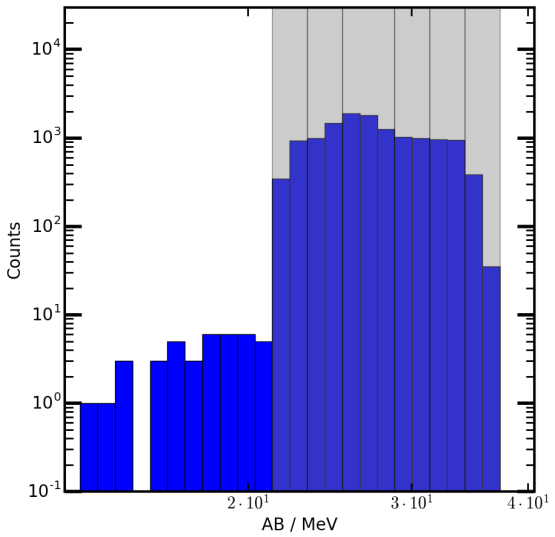

Figure 7.16: Outer-outer segment trajectories events of He ions are stored in a 1D histogram. Similar to the ABnC proton evaluation, the penetrating tail of the He ions is removed using a threshold value of 12.3 MeV in the A detector. The nominal He ABC data product items are illustrated with gray boxes. The definition of the data products is given in sec. 7.5.1.

ABC helium histogram

Particles identified as He by the level 3 ABC trigger are stored in a 2D histogram with 32 logarithmic bins of ABC/min(A,B) in x-direction from 2 to 512 with 4 bins per octave. In y-direction the histogram has 32 logarithmic bins of ABC·min(A,B)$^{1.5}$ from 300 to 1200 MeV$^{2.5}$ with 16 bins per octave. The histogram including the data products for ^{4}He and ^{3}He is shown in fig. 7.17. The histogram is rotated in the internal HET memory to enable an efficient placement of the data products, as the definition of the data product items has limitations. At higher ABC/min(A,B) values, the ^{4}He distribution broadens in y-direction, so that the low abundant ^{3}He is contaminated. This is related to an observed broadening of the energy deposition distribution in C at higher primary energies (higher ABC/min(A,B) values). In the overlapping region, no data product items for ^{3}He are placed.

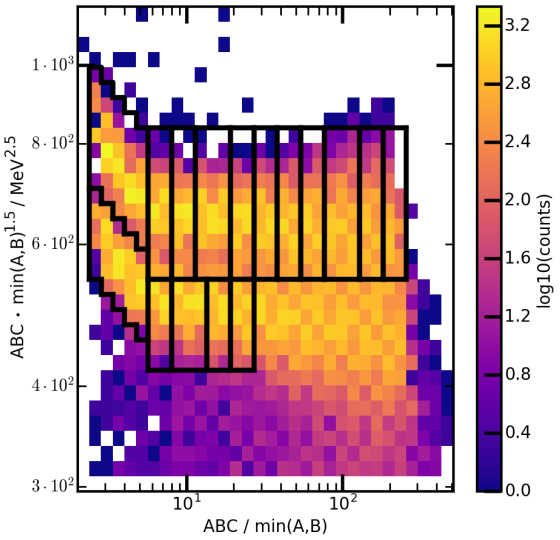

Figure 7.17: Helium ions identified by the ABC level 3 trigger are stored in a 2D histogram. The nominal data product items for both He isotopes are illustrated with the black boxes. The upper displayed population is ^{4}He and the lower one ^{3}He. At high energies the ^{3}He population is highly contaminated by the ^{4}He population, therefore no additional data product items in this energy range for ^{3}He are defined. The definition of the data products is given in sec. 7.5.1.

Heavy ion species histograms

In sec. 4.2, scientific applications for heavy ion (ions heavier than He) measurements are given. To give one example, the Fe/O ratio was used by Dalla et al. (2017), who found a time dependence in this ratio for different observer locations. The higher drift of Fe ions compared to the O ions was attributed to the higher charge-to-mass ratio of Fe compared to O ions. These heavy ion studies can be supported by HET, even at close distances from the Sun. Here, the HET level 3 heavy ion histograms are explained.

ABnC heavy ions species histogram

All ions heavier than He are added in one 2D histogram by the ABnC trigger logic. The histogram is shown in fig. 7.18. It features 32 logarithmic bins of AB/A in x-direction from 1 to 4 with 16 bins per octave. In y-direction the histogram has 128 logarithmic bins of AB·$A^{0.75}$ from to 410 to $2 \cdot 10^7$ $MeV^{1.75}$ with 8 bins per octave. The histogram features 5 data product items for each of the main abundant ions (C, N, O, Ne, Mg , Si, S, Ar, Ca, Fe, Ni) (Reames, 2017) and additionally one data product item per ion group for the penetrating tails, i.e. the particles penetrating the B detector without triggering C, is defined.

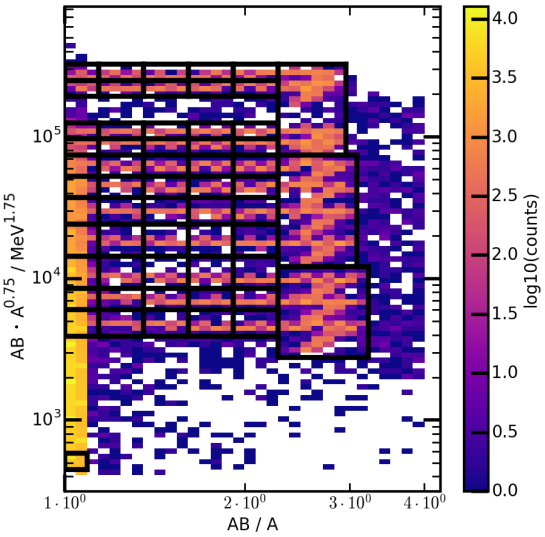

Figure 7.18: All ions heavier than He are stored in one 2D histogram by the ABnC level 3 trigger. At high AB/A values data product items are defined to measure the penetrating tails for different ion groups. In the lower left corner of the histogram an additional data product is defined to estimate the background population at low AB/A values. For each of the main abundant SEP ions (Reames, 2017) several data product items are defined. Starting from the bottom, these ion species are: C, N, O, Ne, Mg , Si, S, Ar, Ca, Fe, Ni. The definition of the data products is given in sec. 7.5.1.

Because these tails extend over several ion species, a separation of the individual ion species is not possible and the tails are summed up for each group. The energy range covered by the ABnC nominal data products is 14.5 to 18.4 MeV/nuc for O ions, which are given here as an example. The responses and energy ranges of all ion species for all triggers are supplied as response matrices, as discussed in sec. 9.2. At low x-axis values, a particle population along the y-axis is observed. This population originates from highly energetic ions with an energy range above that of the ABnC trigger. These highly energetic ions are able to penetrate the HET collimator and thus do not enter the sensor head through the nominal field of view. The ions pass through the A detector and the B detector is triggered by secondary particles. An explanation for the generation of secondary particles is given in sec. 3.2. The energy deposition in B is therefore orders of magnitude lower compared to A. The delta electrons detected by the B detector are emitted either from a collision with the sensor head housing or are emitted from the A detector when the ion passes through it. These particles only contaminate the lowest primary energy bins for the ions. To quantify the contamination of the low energy data product items, a single data product is defined, as shown in the lower left corner in fig. 7.18. Using this background data product and the information obtained from the other data product items of the ions, the contamination of the low energy data product items can be investigated.

ABC heavy ions species histogram

The ions heavier than He are stored in one 2D histogram by the ABC trigger logic. The histogram has 32 logarithmic bins of ABC/min(A,B) in x-direction ranging from 2 to 512 with 4 bins per octave. In y-direction the histogram has 128 logarithmic bins of ABC·min(A,B)$^{1.5}$, ranging from to 2000 to $1.3 \cdot 10^8$ MeV$^{2.5}$ with 8 bins per octave. The ABC heavy ion species histogram is shown in fig. 7.19 with the nominal data product items, which are defined for the most abundant SEP species (C, N, O, Ne, Mg , Si, S, Ar, Ca, Fe, Ni) (Reames, 2017). The energy range covered by the ABC nominal data products is 25.5 to 235 MeV/nuc for O ions, which are given here as an example. The response of all ion species for all triggers are supplied as response matrices, as discussed in sec. 9.2.

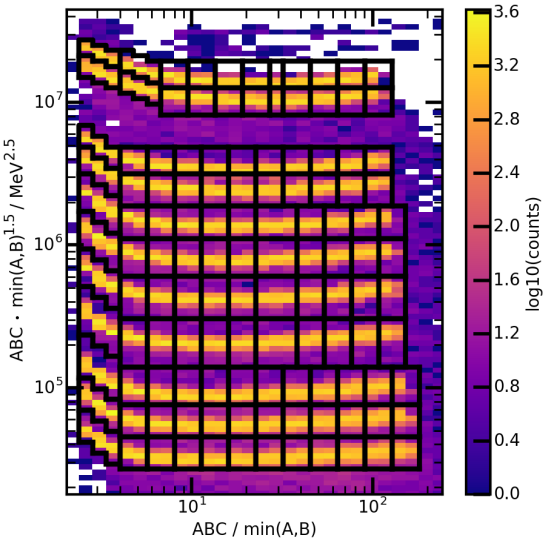

Figure 7.19: Heavy ions identified by the ABC level 3 trigger are stored together in a 2D histogram. For each of the main abundant SEP ions (Reames, 2017) several data product items are defined. Listed from histogram bottom to top the ion species are: C, N, O, Ne, Mg , Si, S, Ar, Ca, Fe, Ni. The definition of the data products is given in sec. 7.5.1.

7.3.4 Crosstalk and relative detector thresholds

For the HET level 3 triggers, a 10% relative threshold between two detectors or segments is used in most cases. The necessity of a relative threshold, instead of the requirement to have only energy deposition in one segment, originates from crosstalk and from secondary particle production. Crosstalk is an unwanted electronic effect, where one signal line affects the signal in another signal line. In

the case of HET, there are three different possible origins for the crosstalk effects. These are:

- Inter-segment crosstalk (Crosstalk between two neighboring detector segments)
- Crosstalk by pins (Crosstalk between neighboring signal lines)
- Crosstalk by preamps (Crosstalk between neighboring preamplifiers)

For all three listed cases, the crosstalk was identified to be less than 1% using several ion species from the HIMAC 2016 heavy ion measurement campaign. These results suggest to use a 1% threshold between two neighboring segments. However, for heavy ions an additional effect has to be taken into account, which is affected by this threshold definition. Heavy ions are able to produce secondary particles when interacting with matter, e.g. when passing through a detector. These secondary particles are able to deposit significant energy in a neighboring detector segment. For example, if a heavy ion penetrates both inner segments of the SSDs on one side, it can generate a number of delta electrons while passing through the A detector. If these delta electrons deposit more than 1% of the energy in any other segment of B, which is deposited by the ion in the inner segment of B, then the event would be discarded. Using a measurement with Fe ions from the HIMAC 2016 measurement campaign, the effect of the relative threshold value for heavy ions was investigated. Fe ions are optimally suited for this investigation as the number of secondary electrons is depending on the charge of the primary particle, as discussed in sec. 3.2. In case of this Fe measurement, a 10% threshold leads to an increase of 6% of statistics in the main ion population compared to a 1% relative threshold in case of the ABC trigger. The term main ion population refers to the bins in the histograms (ABnC,ABC) where the data products for the respective ion species are defined and which are of scientific interest. Of course, the 10% threshold introduces a 10% uncertainty in the dE/dx value (min(A,B)) for the ABC level 3 trigger, as an event is still valid if less than 10% of a particles energy are deposited in a neighboring SSD segment. However, in the present logarithmic binning this 10% uncertainty is translated to a maximum shift of 1 histogram bin. This maximum shift of 1 histogram bin is considered acceptable taking into account the 6% increase in statistics of the main ion population for the investigated measurement.

7.3.5 HET penetrating trigger

In fig. 7.20 a sample trajectory for the HET level 3 penetrating trigger is given. The particle penetrates all inner segments of the SSDs and thus also penetrates the scintillation detector.
Before the actual design of the HET penetrating level 3 trigger is explained, the general concept of penetrating particle measurements with HET is discussed. The penetrating particle trigger extends the measurement range of HET into the GeV-range with reduced energy resolution. Since the total energy of a particle is not known for penetrating particles, a different technique for particle and incoming direction identification is used. The BGO scintillator, which is located between the four SSDs acts as a thick energy absorber for the particles. Thus the particles will loose a significant amount of energy when passing through the scintillator. This can be used for the determination of the particles incoming direction, as the energy deposition per path length increases with decreasing energy (see eq. 3.1 in sec. 3.1). Thus, in HET a particle will deposit less energy in the SSDs on the entrance side, than on the exit side of the telescope as long as it losses sufficient energy in the scintillation detector. Using the ratio of the energy deposition from the two sides, the incoming direction of a particle can be determined. However, for Minimal Ionizing Particles (MIPs), i.e. particles with relativistic energies, the identification of incoming direction is no longer possible, as the energy loss in the scintillator and the SSDs is low compared to the particles total energy. For the lighter ion species, an ion species separation using the HET penetrating trigger is still possible, even for the MIPs. With higher masses a species identification is no longer possible and only groups of ions, e.g. C, N and O, can be identified. Minimal ionizing electrons can not be distinguished from the minimal ionizing protons. In this case, a correction using the spectral information obtained from other data product items is necessary. The energy range of the protons for the penetrating trigger, which is given here as an example, is 105 MeV up to relativistic energies (MIPs).

Design of the HET penetrating level 3 trigger

When an event is classified as class 3 by the level 2 trigger, (ABB or BB coincidence) the event is passed to the level 3 penetrating trigger. The level 3 penetrating trigger evaluates a particle event regarding its energy deposition in individual detectors and, if all pre-defined conditions are met by the event, it is added to the penetrating trigger histogram. Unlike the ABnC and ABC trigger, all ion species are added to the same histogram regardless of their direction or particle species. The design of the trigger is explained using the flowchart presented in fig. 7.21 by reference to each # in the flow chart.

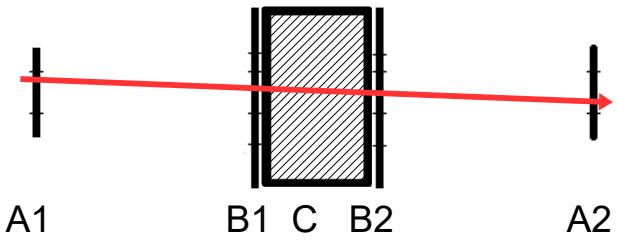

Figure 7.20: Example illustration of a valid HET level 3 penetrating particle detection. The detection would also be valid for the outer segments of the A and B detectors.

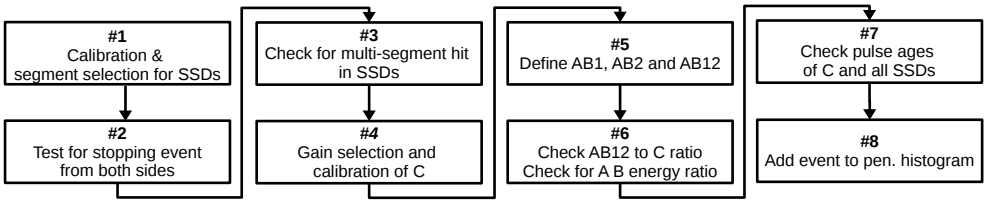

Figure 7.21: HET level 3 penetrating trigger illustration using a flow chart. Each step is described in detail in the text.

The event classification as class 3 by the level 2 trigger suggests either an ABB- or a BB-coincidence as given in table 7.2. Thus in the HET level 3 penetrating trigger a check is performed, which detector coincidences were detected. If only the BB-coincidence is detected, the event is directly evaluated by the HET level 3 GCR trigger. In case of a ABB coincidence, the event is evaluated by the HET penetrating level 3 trigger and is also processed by the GCR trigger afterwards.
The first step of the penetrating trigger, #1 in fig. 7.21, is to apply calibration factors to each SSD and to identify the segments of the SSDs with the highest energy deposition.
In the next step, #2 in fig. 7.21, the particle event checked whether it is stopping in C and or fully penetrating. By design, only 3 of the 4 SSDs are checked for coincidence by the penetrating level 2 trigger, as given in table 7.2. However, the B detector on the opposing side, could be triggered due to different reasons, e.g. by a particle that actually stopped in the BGO crystal and delta electrons triggered the B detector. Thus, an additional check is performed prior to the analysis of the penetrating level 3 trigger logic. The most probable reasons for an energy deposition above 50 keV in the B detector behind the BGO crystal could be ion fragmentation or delta electron production. Furthermore it could

be possible, that the ion itself barely reaches the B detector and deposits just more than 50 keV. Therefore the energy deposition in B on the entrance side is compared to the energy deposition in all segments of the B, including guard segment, and A detector on the exit side. If all detector segments on the exit side are below 10% of the energy deposition of the main segment of B on the entrance side, the event is re-classified as stopping and sent to the level 3 stopping trigger. If this is not the case, the next step of the penetrating trigger, #3 in fig. 7.21, is executed. A check for a multi-segment hit is performed for each SSD. A multi-segment hit can be created e.g. by ion fragmentation or production of delta electrons. Ion fragmentation in the thick scintillation crystal may cause a incorrect directional identification. The residuals of the main particle can deposit less energy in the SSDs on the exit side compared to the initial ions energy deposition in the SSDs on the entrance side. The lower threshold for the multi-segment hit is 30 keV. If a particle deposits more than 30 keV in the auxiliary segment of a detector, it is checked, if this energy deposition is more than 10% of the energy deposition in the main segment. If this is the case, the event is discarded. Using experimental data from the January 2017 HIMAC run, it was found that a 1% threshold suppresses events which are attributed to the wrong direction by ≈80%. However, a 1% segment threshold is not necessary for the energy resolution, as described in sec. 7.3.4 for heavy ion measurements, and reduces the statistics of correctly allocated events by ≈60% for the used experimental data set. Thus a 10% threshold is used, which limits the energy difference between the energy deposition in the main and the auxiliary SSD segments to 10%. With this, a suppression of events allocated to the wrong direction by ≈50% is achieved. The reduction of events on the correct side is ≈20% due to the 10% energy resolution restriction. The reduction in correctly allocated events is taken into account for the calculation of the data product responses, described in sec. 9.2. Additional evaluation steps are used in the next steps of the penetrating trigger to further identify and reject ion fragmentation events. A simple summation of SSD segments for all SSDs can not be performed due to code length limitations.
The concept of the further evaluation is explained using fig. 7.22 for illustration. For a better discriminability of the individual ion species a scatterplot is used, showing only the most common SEP ion species (H, He, C, N, O) (Reames, 2017) up to oxygen, which enter the telescope from one side, the A1 side. The ions species are not scaled for abundance to achieve a better individual visibility. The shown scatterplot was the baseline for the HET penetrating trigger histogram. For the x-axis, the energy deposition in the BGO scintillator, C, is used, instead of using the combined energy deposition in the SSDs, as it offers a better separation of the ion species, despite the effect of ionization quenching.
Thus, in step #4 in fig. 7.21, calibration factors are applied to the measured energy deposition in C.
In fig. 7.22 the four different panels share the same x-axis, but use different concepts for the y-axis to illustrate the data processing steps. In general, the energy

ratio between two SSDs on opposing sides of the telescope are used to identify the particles direction. In the uppermost panel of fig. 7.22, only the ratio between the two B detectors is used for the y-axis. However, this has two major disadvantages. The first is an overlap of the MIPs, for example of He, with the tails of lighter ions, is this case protons. Secondly, without checking the energy deposition in the A detectors, particles that fragment in the BGO crystal can not be identified in some cases. Thus the incoming direction of the particle could falsely identified, since instead of depositing more energy in the SSD segment behind C, the ion fragment deposits less energy compared to what the complete ion would deposit. Therefore the ratio between the SSDs on the two sides of C is reversed to what would be expected. This effect is more pronounced for heavier ions, as these create more fragments in C. Both effects, the overlap of the MIPs and the incorrect directional estimation, can be reduced using the approach shown in the second and third panel of fig. 7.22. In the second and third panel, both SSDs of each side are used instead of only the B detectors. By using the minimal deposited energy of the two detectors of one side, the MIP distributions are more compact. Thus, in step #5 in fig. 7.21, AB = min(A,B) is defined in the trigger. As described in sec. 3.1, the energy deposition in a detector may show a so called Landau-tail. Though the energy deposition in both SSDs on one side of the BGO scintillator is almost identical, using the minimum of A and B on one side, particles in the Landau-tail of the distribution are discarded (see sec. 3.1). However, using AB=min(A,B) introduces a more severe directional-misidentification due to fragmentation, visible in the second panel of fig. 7.22 for C, N and O. In order to for correct this, in step #6 in fig. 7.21, a maximum energy deposition ratio between the A and B detector of one side is derived. According to fig. 7.23, $B/A < 6$ should be used to exclude fragmentation events, as illustrated with oxygen ions in fig. 7.23. For Fe ions the optimal B/A ratio is even higher, but a further increase, would lead to more accepted fragmentation events for the less heavy ions. The improvement due to the B/A ratio visible when comparing the second with the third panel of fig. 7.22.

Though the events which show signatures of fragmentation are already significantly reduced, a further reduction can be achieved by introducing a comparison of the energy deposition in the SSDs and the scintillator C. The optimal ratio for comparison is found by using the definition of AB12 = min(AB1,AB2). The determined ratio range is between a factor of 10 and 500 as illustrated by the lines in fig. 7.24. This is checked in step #6 in fig. 7.21 and all particles events that do not comply to these ratios are discarded, due to signatures of fragmentation. The effect of this check is shown in the lowest panel of fig. 7.22.

In the next step, #7 in fig. 7.21, a pulse age check is performed for all used detector segments and for both channels of the scintillator.

All these prior steps define the main event evaluation of the HET penetrating level 3 trigger that is applied to each individual event. In the very last step, #8 in fig. 7.21, the particle event is stored in the HET level 3 histogram if all

the previous steps evaluated positive. The HET level 3 penetrating histogram is shown in fig. 7.25 in its final configuration with the correct binning and data product items. The histogram has 48 logarithmic bins on the x-axis (energy deposition in C), starting at 4 MeV, with 4 bins per octave and 32 logarithmic bins of min(A1,B1)/min(A2,B2) also with 4 bins per octave in the y-axis ranging from 1/16 to 16. The histogram is designed such, that all ion species up to Fe can be accommodated. For non-minimal ionizing particles, the incoming direction of the particle can be determined using the AB1/AB2 ratio. In case a particle is minimally ionizing, the energy deposition in the SSDs on both sides is almost identical and a AB1/AB2 ratio of ≈ 1 is achieved. Figure 7.25 also shows the nominal data products for the penetrating trigger. The definitions for Nominal_stable data products are given in table 7.8.

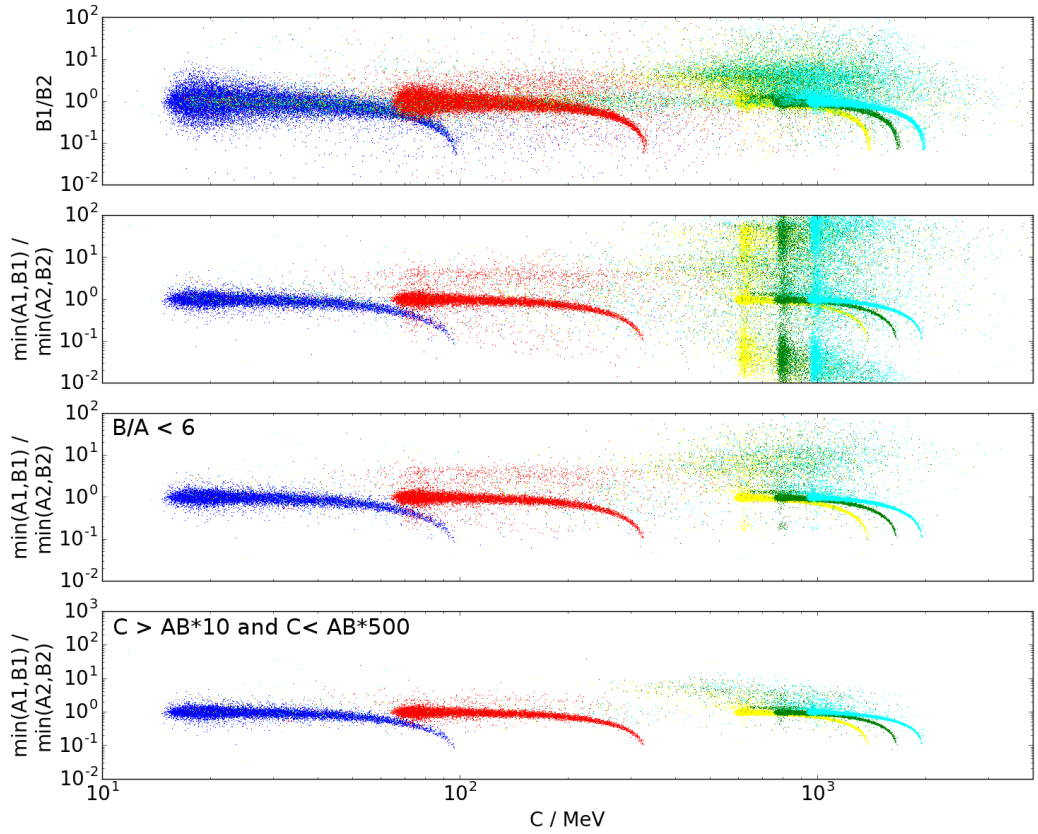

Figure 7.22: Selection of the different options to determine the incoming direction from the energy deposition in the SSDs. H is shown in blue, He in red, C in yellow, N in green and O in cyan. Each panel shows different approaches or improvements for the penetrating level 3 trigger that are described in the text.

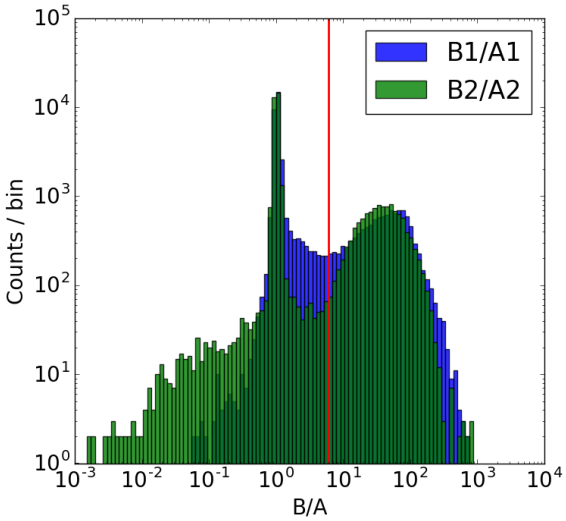

Figure 7.23: Selection of the optimal AB ratio to suppress fragmentation events using a simulation of oxygen ions. This is the case when one of the SSDs measures a significantly lower amount of energy compared to the other SSD on the same side due to fragmentation.

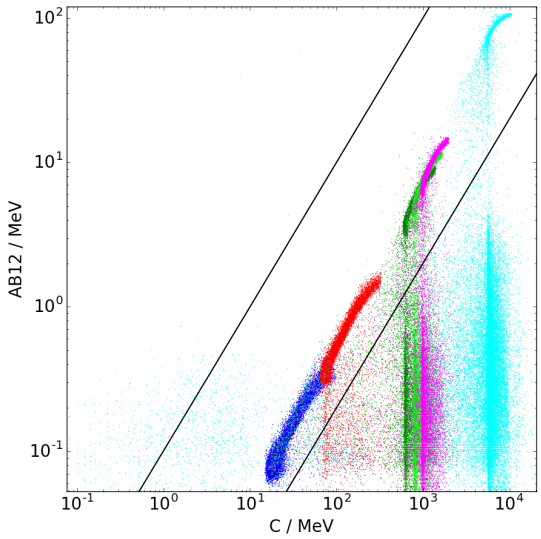

Figure 7.24: Selection of the AB12 to C ratio. AB12 multiplied by 10 needs to be smaller than the energy deposition in C, and AB12 multiplied by 500 needs to be higher than the energy deposition in C. Otherwise the event is discarded. These ratios are illustrated by the two black lines. The ions species used for illustration are H (blue), He (red) , C (green), N (light green), O (magenta) and Fe (light blue) ions with an energies of 100 to 3000 MeV/nuc.

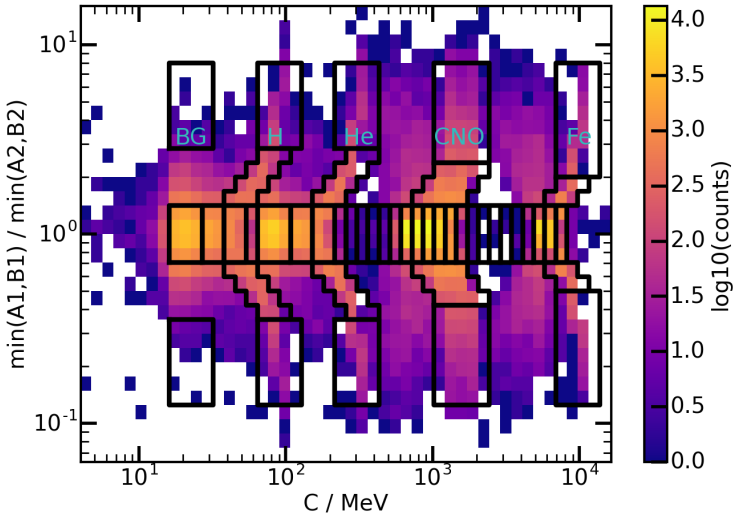

Figure 7.25: HET level 3 penetrating histogram with the correct binning and visualized data product items as black boxes. The Nominal_stable data products are given in table 7.8 in sec. 7.5.1. The BG-boxes are used to estimate the background. C, N and O share data product items, as they can not be resolved with the used histogram resolution.

7.3.6 HET GCR trigger

In fig. 7.26 a sample trajectory for the GCR trigger is given. In this example the particle penetrates the outer segments of the B detectors and thus also penetrates the scintillation detector. The energy deposition in the scintillator is then added to a histogram.

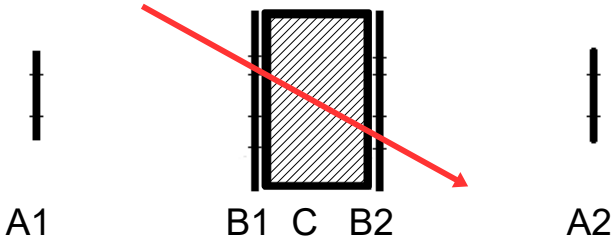

Figure 7.26: Example illustration of a valid GCR particle detection. The detection would also be valid for the inner segments of the B detectors.

The HET level 3 GCR trigger is an addition to the HET level 3 penetrating trigger which is described in sec. 7.3.5. The aim of the GCR trigger is to measure the rare GCR protons with the highest achievable field of view that HET can provide. The increase in the field of view is achieved by using only the two B detectors and the C detector. With this setting, not only particles entering the sensor head through the telescope opening are accepted, but also particles entering through the thin aluminum housing of the sensor head, so that the increase in field of view is on the cost of energy resolution. There are three entry points points to the HET level 3 GCR trigger. All particles, that are assigned trigger class 3 (see table 7.2) are tested at the beginning of the penetrating level 3 trigger regarding their coincidence conditions. If only a BB-coincidence is detected, the particle is directly sent to the GCR trigger. In case that an ABB-coincidence is detected, the particle is first evaluated by the penetrating trigger and afterwards sent to the GCR trigger, regardless of successful or unsuccessful evaluation by the penetrating level 3 trigger. The GCR trigger design is very similar to that of the HET penetrating trigger but highly reduced in complexity and thus reduced in code length and evaluation time.
The GCR trigger is explained using the flowchart in fig. 7.27. The first step, #1 in fig. 7.27, is that calibration factors are applied to the SSDs and the segment with the maximum energy deposition of each SSD is determined.
The next step, #2 in fig. 7.27, does the same for the scintillator C.
In the next step, #3 in fig. 7.27, B_{min} = min(B1,B2) is calculated for the further evaluation. Additionally, the highest measured signal in the anti-coincidence segments of the B detectors is defined as B3max = max(B1G,B2G).

Subsequently in the next step, #4 in fig. 7.27, the two values are compared. The maximum energy deposition in the anti-coincidence segments, B3max, is checked to be below 10% of B_{min}.

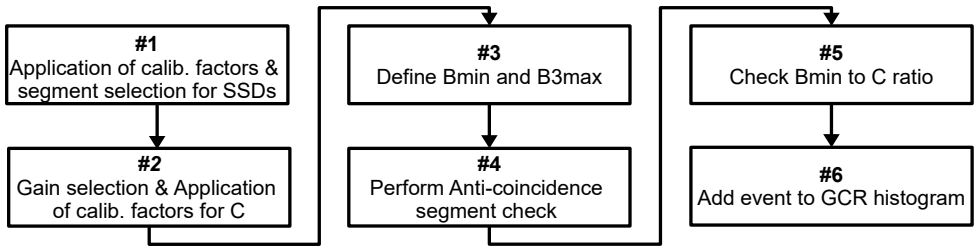

Figure 7.27: HET level 3 GCR trigger illustration using a flow chart. Each step is described in detail in the text.

Finally, the last evaluation step, #5 in fig. 7.27 is a comparison between Bmin and C, identical to the check performed in the penetrating trigger in #6 of fig. 7.21, to detect ion fragmentation.
If these evaluation steps are successful, as per step #6 in fig. 7.27, the particle is added to a 1D histogram of the energy deposition in C. The histogram is binned in 256 logarithmic bins with 16 bins per octave starting at 4 MeV up to 257 GeV. In fig. 7.28 the 1D GCR histogram for a proton simulation with a power law energy spectrum with an index of -1 ranging from 80 MeV to 2 GeV is given for illustration. The nominal data products cover an energy range for protons from 157 MeV up to relativistic energies (minimum ionizing particles).

7.3.7 High flux / nominal mode

Similar to the Electron Proton and Helium Instrument (EPHIN) on the SOlar Heliospheric Observatory (SOHO), HET features a special configuration for periods with high particle fluxes (Müller-Mellin et al., 1995). High particle fluxes may occur close to the Sun during intensive SEP events. During time periods with high particle fluxes, the HET data processing electronics may be saturated for the particle processing. This saturation may lead to dead time effects, so that not all events can be evaluated and even the chance of multi-coincidence detection of particles may occur. The latter case refers to the possibility, that two incoming primary particles can be detected as one single particle. To assure a full functionality of the instrument during these periods, the geometrical factor of HET can be reduced by a factor of ≈4.6. The reduction in geometrical factor is achieved, by increasing the level 1 threshold of the A outer segments. The geometrical factors for all trigger level 3 classes are calculated and given

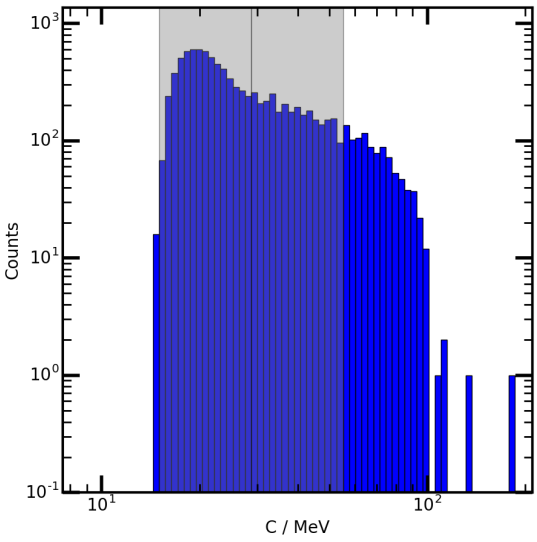

Figure 7.28: The 1D GCR histogram for a simulation of 80 MeV to 2 GeV protons. The visible peak in the histogram results from the relativistic proton which are MIPs. At higher deposited energies, where no data product items (black boxes) are placed, the proton population is contaminated by relativistic He ions, which are not shown here.

in sec. 9.2. The threshold is selected to suppress the particle species with the highest expected fluxes. These particles are electrons and protons in the ABnC energy range, as SEP event fluxes are reduced towards higher energies as shown in Mewaldt et al. (2005) for several ion species and electrons in different SEP events. An increase of the level 1 threshold of the A outer segments influences the ABC and penetrating level 3 trigger as well. The energy deposition of particles in the ABC and penetrating energy ranges in A is lower compared to particles in the ABnC level 3 trigger energy range. The effect of the increased threshold for all affected triggers is illustrated in fig. 7.29. The GCR trigger is unaffected by this threshold increase. The left panel (a) in fig. 7.29 shows the energy deposition in A plotted versus the summed up energy deposition in the A and B detectors (ABnC trigger). The black line illustrates the selected threshold of 6.2 MeV for the outer A detector segment in order to suppress the protons and electrons. Since higher energetic particles deposit less energy in the A detector according to the Bethe-Bloch equation (see eq. 3.1 in sec. 3.1), even heavier ion species than electrons and protons are suppressed in the ABC stopping and the penetrating trigger. This is illustrated by the black line in panels (b) and (c) in fig. 7.29. In case of the ABC stopping trigger, most of the ^{3}He and ^{4}He ion population is suppressed due to the threshold. In case of the penetrating trigger, ion species up to the CNO group are suppressed. For the affected ion species, the suppres-

sion only concerns the outer A detector segment. The inner A detector segment still detects these particles nominally, so that the high flux mode is just a reduction in geometrical factor for the affected particles and they are not completely suppressed.

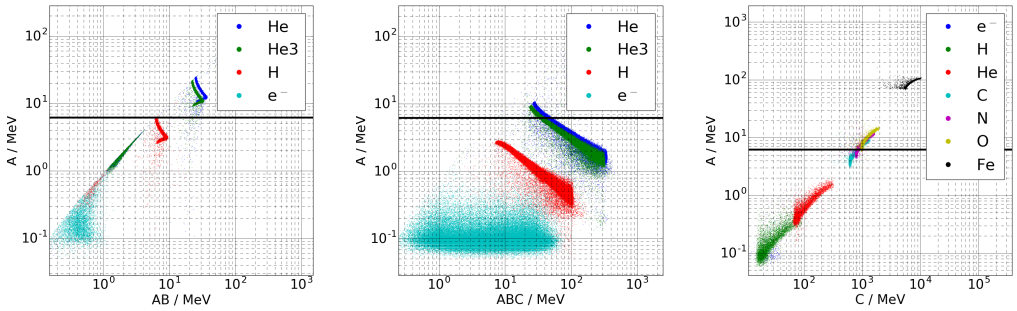

(a) Illustration of the A detector outer threshold increase for the ABnC trigger.

(b) Illustration of the A detector outer threshold increase for the ABC trigger.

(c) Illustration of the A detector outer threshold increase for the penetrating trigger.

Figure 7.29: Illustration of the effects using the high flux mode of HET. The threshold of the outer A detector segment is increased to 6.2 MeV, illustrated by the black line in the plots. This threshold has different effects on the three different level 3 triggers.

7.4 Path length correction

The trajectory of a particle in a multi-detector telescope influences its energy deposition in the individual detectors. However, due to the segmentation of the A and B detectors, the trajectory of an energetic particle can be partially reconstructed in HET. Three different trajectory cases can distinguished as illustrated in fig. 7.30:

1. Inner-Inner (blue)
2. Inner-Outer / Outer - Inner (green)
3. Outer-Outer (red)

The nominal detector thickness of each silicon detector in HET is 300 μm. However, when the particles trajectory is inclined, the particles path length in the detector material is increased as can be seen in fig. 7.30. This leads to an increase in energy deposition in the detector, depending on the particles trajectory. The HET species separation and the 2D histograms rely on the E dE/dx vs. E / dE/dx

technique, where dE/dx is the deposited energy in one of the A or B detectors. Thus the exact location of an event in a histogram would be influenced by the particles trajectory. For this reason the dE/dx value needs to be corrected with a path length correction. To determine the correction parameters for the different cases, protons covering the energy range of the ABnC and ABC trigger are used for the evaluation. Protons are the most common SEP particles and the coarse energy resolution of the penetrating trigger does not require this correction. The evaluation is performed with a GEANT4 simulation. The setup is described in chapter 5. GEANT4 provides the entry and exit position of a particle that passes through a detector. With these positions the path length can be calculated given by the length of the resulting 3D vector. In fig. 7.31 the path length distributions for the three trajectory cases are given. For case 2, both distributions are given to illustrate that these are identical within the statistical fluctuations. Each distribution shows the path length within the corresponding A segment and the mean value that is used for the correction. The particle trajectory a real particle can not be with HET. Therefore the approach of using a general correction factor from a path length distribution is used. In table 7.5 the path length correction values for each trajectory case is given. Using the inner-inner trajectory case as the nominal one, the correction factors for the other cases, inner-outer or outer-outer, are calculated based on this value. In the level 3 trigger of HET these three cases are distinguished and tested for. For particles stopping in the B detector (ABnC trigger), the dE/dx value, which in this case is the energy deposition in the A detector is corrected using the appropriate path length correction factor. For particles stopping in the BGO crystal (ABC trigger), either the A or the B detector is used for the dE/dx value, depending which detected less energy. This approach is described in the level 3 trigger development section 7.3. After either the A or B detector is selected, the path length correction is applied.
The approach of using a linear correction is not optimal, as the energy deposition according to the Bethe-Bloch-equation (Lindhard and Sörensen, 1996) is not linear. This is especially true for lower energetic particles. However, due to the very limited computing power and the limitation of mathematical operators (addition, subtraction, multiplication, division) of the FPGA it is not possible to perform a more precise correction onboard the spacecraft for the science data. For the PHA data the correction can be performed on ground and therefore a better correction can be applied. To illustrate the effectiveness of the onboard approach, in fig 7.32 the energy deposition for He ions at different energies for the three trajectories is given. The energy deposition of the ions is calculated using the Bethe-Bloch-equation and then the relative deviation to the mean path length for the inner-inner trajectory is calculated. As expected, at low energies a high deviation of up to $\approx 2.8\%$ is observed and though the correction reduces the mismatch, it can not be reduced to $\leq 1.1\%$ for the outer-outer trajectory case for the low energy detection threshold of 6.8 MeV/nuc. At high energies the path length correction can reduce the mismatch to $\leq 0.1\%$.

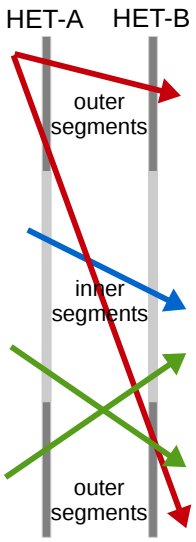

Figure 7.30: Illustration of the three trajectory cases. The path length in the detector material increases depending on the particles trajectory.

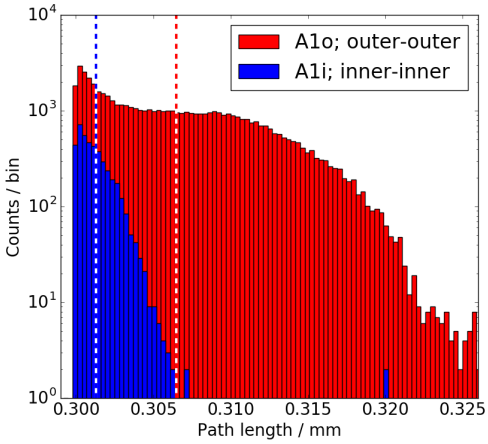

(a) Path length distributions for inner-inner and outer-outer coincidences.

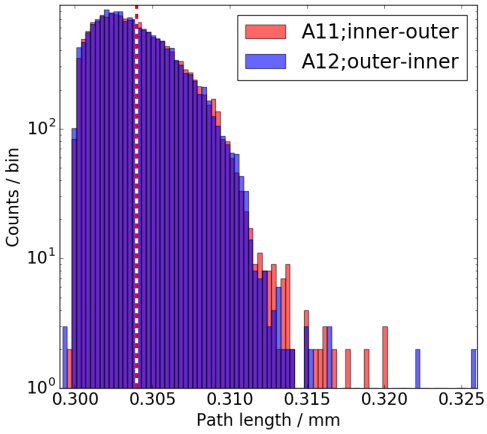

(b) Path length distributions for inner-outer and outer-inner coincidences.

Figure 7.31: Path lengths for the three trajectory cases. The dashed lines show the mean of each distribution. For the study protons, which are the highest abundant ion species in SEP events have been used in an energy range from 5 to 200 MeV covering both stopping level three triggers sufficiently.

Trajectory	Trajectory case	Mean path length / mm	PLC
inner-inner	1	0.301	1
inner-outer outer-inner	2	0.304	0.991
outer-outer	3	0.306	0.983

Table 7.5: Mean path length value given for each trajectory case and the according calculated Path Length Correction (PLC) factor.

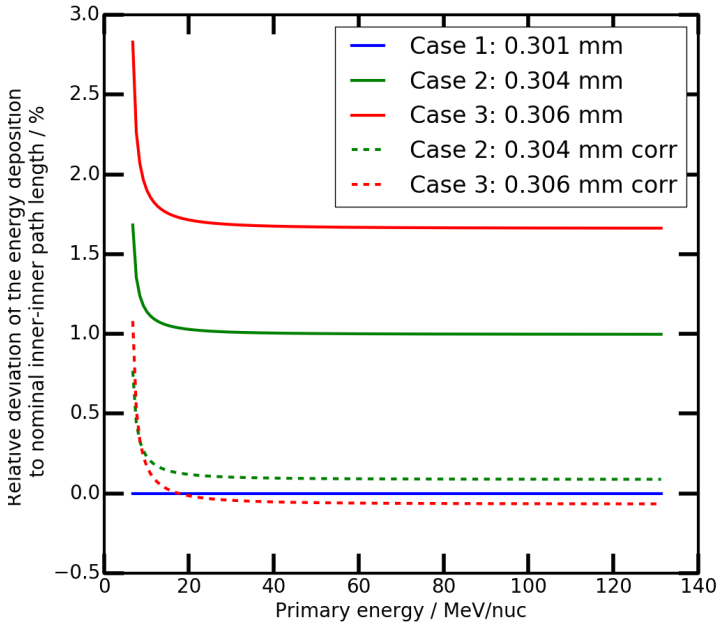

Figure 7.32: To illustrate the effectiveness of the path length correction for other ion species, the deviation in the energy deposition for the mean path lengths of the three trajectory cases for He ions in the ABnC to ABC energy range are given. As pointed out in sec. 4.2 the precise measurement of He ions is of high importance for the scientific objective. Hence, these are used for illustration. The energy deposition is calculated using the Bethe-Bloch-Formula. The different colors represent the different trajectory cases as shown in fig. 7.30.

7.5 Data products

In sec. 7.3.1, sec. 7.3.5 and sec. 7.3.6 the level 3 histograms for the stopping triggers, the penetrating trigger and the GCR trigger are shown, respectively. Based on these histograms, the data products and their data product items are defined, which summarize several histogram bins to a single number in order to reduce the required telemetry of the HET instrument. All of the level 3 histograms, displayed in sec. 7.3.1, sec. 7.3.5 and sec. 7.3.6 show the nominal data product items. Each data product is defined with a fixed cadence, which defines the temporal resolution. A data product may contain several data product items, which then define the energy resolution. Data products are assigned to categories, which are defined for the Solar Orbiter mission. Each category has its own purpose and a telemetry budget. These categories and their purpose shall be introduced in this section.
All instruments of EPD, including HET, provide data products divided into three different categories, as defined in the EPD telecommand / telemetry interface control document (Duatis, 2015), each category with a fixed telemetry budget:

1. Low Latency
2. Nominal
3. Burst (selective downlink)
4. Service 20 (S20)

The complete list of all data products and their data product items defined during this work is given in the appendices sec. A.1 for all data product categories.
Low Latency data
The purpose of the low latency data products is to identify scientifically interesting time periods and to check the instrument's health status. From all categories, the low latency data is earliest available but is highly limited in telemetry compared to the nominal and burst data. Therefore the low latency data products are reduced in cadence and energy resolution compared to the other categories. The low latency data is always generated by HET and is available for all time periods, except when the unit is switched off during orbital maneuvers.
Nominal data
Like the low latency data, the nominal data products are always generated by the unit and are available for all time periods. However, the nominal data products are significantly delayed compared to the low latency data products. During periods when Solar Orbiter is behind the Sun, as seen from Earth, the delay may be as high as 180 days. The nominal data products contain the scientifically most important data products with a good energy and time resolution and represent the standard data HET will provide for scientific purposes. For EPT-HET,

the nominal data is divided into Nominal_stable and Nominal_unstable. The Nominal_unstable data products are used for less important ion species and also contain data products for instrument diagnostics. As the name indicates, these products may change during the course of the mission. The Nominal_stable data products will stay unchanged during the course of the mission and contain the scientifically most important data products. The Nominal_stable data product definitions of HET are given in sec. 7.5.1 with the necessary information on how they are defined in each of the corresponding level 3 histograms. The nominal data products can be generated in two modes, "far" and "close", depending on the location of the spacecraft. The modes refer to the distance of the spacecraft to the Sun, so that in "close" mode, the data products are sent at higher cadences compared to the "far" mode. At closer distances to the Sun, the particle fluxes are significantly higher, so that a statistically significant sample of the particle can be detected in short accumulations times (Ruzmaikin et al., 2005). There is no change in the amount or definition of the nominal data products when changing the modes, only the cadences are adjusted. The mode switch is performed manually via telecommand. In the appendices sec. A.1, the energy ranges, cadences and responses of all HET DPs is given in "far" mode. The cadence conversion from "far" to "close" mode is also given.

Burst data

During special time slots and on demand, burst data generated from HET can be provided. Although burst data products are routinely generated by HET, they are only stored for a certain time on the spacecraft. If not requested, the data is deleted. The burst data offers an even better energy and time resolution for certain data products. The "far" and "close" mode change of HET affects also the burst mode. The cadences are identical in both modes but in "far" mode, two additional data products for electrons are generated at a high cadence, which are otherwise routinely generated in "close" mode as a nominal data product. Thus, in "close" mode, these two data products are disabled in burst mode.

Service20 data

The service20 products are used to trigger other instruments on the spacecraft during SEP events to go into a burst mode. HET does not provide this kind of data products.

PHA data

Additionally to the data products, Pulse-Height-Analysis (PHA) data is supplied by each unit. This data is used for in-depth diagnostics of the instrument health and calibration status, since delivers the raw pulse-height data for all detectors for selected events. Since this format is very telemetry intensive, only a small sample of events can be delivered. A full description of the PHA data supplied by HET is given in sec. 7.5.2.

7.5.1 Nominal_stable data product tables

In sec. 7.5 the different data product categories, which are generated by HET are explained. Among the given three categories, Low-Latency, Nominal and Burst, the data products of the Nominal mode are the default data products used for science. Thus these are displayed in the histograms given in sec. 7.3.3 for ABnC and ABC, sec. 7.3.5 for the penetrating trigger and in sec. 7.3.6 for the GCR trigger. In the following, the definitions of the Nominal_stable data products for all four trigger classes are given. By this definitions, the data products, as defined based on the level 3 histograms can be reconstructed. The definitions are given in table 7.6 for the ABnC, in table 7.7 for the ABC and in table 7.8 for the penetrating and GCR trigger, respectively. The last column gives the number of the contained data product items, that are defined within the data product. The given values for x and y are the ones used to define the boxes and bins for the data products based on the level 3 histograms. In this section, the Nominal_stable data products shall be given as an example for the nominal data product definitions. However, in the histograms the Nominal_stable as well as the Nominal_unstable data products are displayed.
Table 7.6 contains the Nominal_stable data products for the ABnC trigger. Using this table, the data products for the most important particle species can be reconstructed. In table 7.7 the Nominal_stable data products for the ABC trigger are given. For the two stopping triggers, x-values are either given in MeV or in E_{tot} to dE/dx ratio, depending in the histogram type. The histogram type, 1 or 2D, can be identified by the presence of a y-value in the according row. Table 7.8 contains the Nominal_stable data product of the penetrating trigger. The y-values for the boxes enabling a directional identification are given for the sunward / north (particles coming from A1B1) direction. The values for the other direction is the inverse of the given y-values.
Each of the defined data product items has a defined response to different particle species in a given energy interval. In order to calculate the particle flux from the summarized histogram counts, supplied by a data product item, the response of the data product item needs to be known. The calculation of these responses is presented in in sec. 9.2 and a full list off all calculated response factors and energy ranges of all individual data product items is given in the appendices sec. A.1.

DP name	x-value start	x-value end	y-value start /MeV$^{1.75}$	y-value end /MeV$^{1.75}$	#
NO_HETB_p	6.05 MeV	9.33 MeV	-	-	5
NO_HETB_tail_high_p	1.00	2.00	-	-	1
NO_HETB_H_p	6.05 MeV	9.33 MeV	-	-	1
NO_HETB_e	0.20 MeV	0.98 MeV	-	-	1
NO_HETB_he3_tail1	1.00	1.30	189	234	1
NO_HETB_he3	1.30	2.38	166	206	4
NO_HETB_he4_tail1	1.00	1.30	234	291	1
NO_HETB_he4	1.30	2.38	206	256	4
NO_HETB_he	21.25 MeV	37.32 MeV	-	-	6
NO_HETB_c	1.00	2.28	3915	6038	5
NO_HETB_n	1.00	2.28	6038	8539	5
NO_HETB_o	1.00	2.28	8539	14361	5
NO_HETB_fe	1.00	2.28	193219	250574	5

Table 7.6: In this table, the definitions of Nominal_stable data product items for the ABnC trigger are given. The used DP nomenclature is "NO" for Nominal_stable, "HETB" for particles stopping in B (ABnC trigger) and an identifier for the ion species e.g. "p" for protons.

DP name	x-value start	x-value end	y-value start /MeV$^{2.5}$	y-value end /MeV$^{2.5}$	#
NO_HETC_p	6.89 MeV	105.5 MeV	-	-	31
NO_HETC_H_p	6.89 MeV	105.5 MeV	-	-	3
NO_HETC_e	0.79 MeV	15.0 MeV	-	-	3
NO_HETC_H_e	30.0 MeV	50.0 MeV	-	-	1
NO_HETC_he3_tail1	2.38	5.66	543	704	1
NO_HETC_he3	5.66	26.91	418	543	5
NO_HETC_he4_tail1	2.38	5.66	704	996	1
NO_HETC_he4	5.66	256.00	543	837	11
NO_HETC_c_tail1	2.38	4.00	41348	69539	1
NO_HETC_c	4.00	181.02	26811	45090	12
NO_HETC_n_tail1	2.38	4.00	69539	116950	1
NO_HETC_n	4.00	181.02	45090	75833	12
NO_HETC_o_tail1	2.38	4.00	116950	233901	1
NO_HETC_o	4.00	181.02	75833	139078	12
NO_HETC_fe_tail1	2.38	4.00	14969672	21170313	1
NO_HETC_fe_tail2	4.00	6.73	11543195	16324543	1
NO_HETC_fe	6.73	128.00	8162271	12587943	11

Table 7.7: In this table, the definitions of the Nominal_stable data product items for the ABC trigger are given. The x-values for the 2D histograms are given in total energy deposition in A+B+C divided by min(A,B) and thus are unitless. The y-axis values are the product of A+B+C times min(A,B)$^{1.5}$ and thus given in units of MeV$^{2.5}$. The used DP nomenclature is "NO" for Nominal_stable, "HETC" for particles stopping in C (ABC trigger) and an identifier for the ion species e.g. "p" for protons.

DP name	x-value start /MeV	x-value end /MeV	y-value start	y-value end	#
NO_HETP_p	62.76	125.51	0.12	0.35	1
NO_HETP_p	37.32	62.76	0.35	0.71	1
NO_HETP_p	15.69	52.77	0.71	1.41	3
NO_HETP_he	211.09	422.18	0.12	0.35	1
NO_HETP_he	149.26	251.03	0.35	0.71	1
NO_HETP_he	52.77	211.09	0.71	1.41	4
NO_HETP_cno	1004.12	2388.21	0.12	0.42	1
NO_HETP_cno	710.02	1688.72	0.42	0.71	1
NO_HETP_cno	502.06	1420.04	0.71	1.41	6
NO_HETP_fe	6754.89	13509.77	0.12	0.50	1
NO_HETP_fe	5680.16	9552.85	0.50	0.71	1
NO_HETP_fe	4776.43	8032.96	0.71	1.41	3
NU_HETG_p	15.02	55.11	0.00	0.00	2

Table 7.8: In this table, the definitions of the Nominal_stable data product items for the penetrating trigger and the Nominal_unstable data product for the GCR trigger is given. The x-axis values are the energy deposition in C, given in MeV. The y-axis values are the ratios of min(A1,B1)/min(A2,B2) and thus unitless. The used DP nomenclature is "NO" for Nominal_stable, "HETP" for penetrating particles (penetrating trigger) and an identifier for the ion species e.g. "p" for protons.

7.5.2 PHA data

In sec. 7.5 a short introduction to the PHA data is already given. Here, a full introduction to the PHA data supplied by HET shall be given.
The different HET level 3 triggers fully process an event and, if evaluated successfully, the event is added to a histogram. The data product items provide the amount of counts from selected bins of these histograms. Thus, all additional information of the particle detection event, like the energy deposition in the individual detectors, is lost. HET features Pulse-Height-Analysis (PHA) data to offer a flexible analysis of data and evaluate the performance of the instrument based on a detailed event analysis. The PHA format stores pulse height, pulse age and phase values among other information for all detector channels of a single event. Since this data format is telemetry intensive, only a few events can be send. In total one EPT-HET unit offers 16 1 kB PHA buffers, which are sent once an hour. For HET 13 of the 16 available buffers are used and the invalid buffer is shared by 3 triggers (penetrating, ABnC and ABC stopping and GCR). The other 3 buffers are used by EPT. To ensure a diversity of PHA events, regarding ion species and trigger type, different PHA classes are defined and a sample of each is transmitted. The different PHA classes are given in table 7.9. Not only valid level 3 trigger events are stored in the PHA buffers, but also a selection of invalid events is stored. The total number of PHA buffers is limited, so that all invalid events and the GCR trigger have to share one PHA buffer. To increase the statistics of the rare heavy ion events, for the ABnC, the ABC and the penetrating level 3 trigger heavy ions have their own PHA buffer. For the ABnC and ABC trigger, the heavy ions are additionally divided into two groups using an additional threshold for both stopping triggers, which is also given in table 7.9.

Buffer name	Buffer description for level 3 trigger event
het_pha_pen_invalid	Penetrating invalid event
het_pha_pen_gcr	GCR level event, same buffer as het_pha_pen_invalid
het_pha_pen	Penetrating event
het_pha_pen_highZ	Penetrating event with C > 600 MeV
het_pha_highZ_ABC	Heavy ion species (S to Fe) stopping in C, threshold $> 1.2 \cdot 10^6$ MeV$^{2.5}$
het_pha_ion_ABC	Heavy ion species (Li to Si) stopping in C, threshold $\leq 1.2 \cdot 10^6$ MeV$^{2.5}$
het_pha_a_ABC	He stopping in C
het_pha_p_ABC	H stopping in C
het_pha_e_ABC	e^- stopping in C
het_pha_highZ_AB	Heavy ion species (S to Fe) stopping in B, threshold $> 55 \cdot 10^3$ MeV$^{1.75}$
het_pha_ion_AB	Heavy ion species (Li to Si) stopping in B, threshold $\leq 55 \cdot 10^3$ MeV$^{1.75}$
het_pha_a_AB	He stopping in B
het_pha_p_AB	H stopping in B
het_pha_e_AB	e^- stopping in B
het_pha_stop_invalid	stopping trigger invalid event, same buffer as het_pha_pen_invalid

Table 7.9: Available PHA buffers for HET. The naming is identical to the naming scheme in the HET configuration. The threshold for the stopping heavy ion species are located between Si and S ion species in the respective 2D histograms at the approximate location of P. The thresholds for the selection of e, H and He for the stopping PHA buffers are the same as given in table 7.4.

In the HET configuration version 0008, a modification affecting some of the ABnC PHA buffers is introduced. The configuration update was uploaded to the FM units on 12.05.2020. An event is only added to the H, He and heavy ion PHA buffers if the AB/A ratio is above 1.2, to suppress contamination of lighter ion species by heavier ion species. Details are given in chapter 11, where the first in-flight PHA data is analyzed.

8. HET data product validation

In sec. 7.3 the onboard data processing development of HET is described. For this development, mainly simulation data, obtained with the simulation setup presented in chapter 5 in combination with the quenching prediction model, presented in sec. 5.4 is used. This is necessary as not all aspects of the instrument can be evaluated using experimental data as described in chapter 5. As described in sec. 5.4 the quenching prediction model is used to include the effect of ionization quenching in the simulation data. This effect reduces the produced scintillation light in the BGO scintillator, based on the energy deposition per path length of a given charged particle. Since this quenching prediction model is essential for the design of the HET onboard data processing and the subsequent definitions of the data product items, the model itself needs to be validated. However, more importantly, not only the quenching prediction model, but also the onboard data processing by the different level 3 triggers needs to be validated using experimental data. Thus, in the first part, sec. 8.1, of this chapter, the preparation of the experimental data for a comparison with the simulation is given. In the second part, sec. 8.2, the validation of the quenching prediction model, by comparison to experimental data is given. Finally, in sec. 8.3 the output of the penetrating level 3 trigger and the ABC level 3 trigger is compared for simulation and experimental data.

8.1 Preparation of experimental data

The dataset that is used for the validation of the quenching prediction model was measured at Heavy Ion Medical Accelerator in Chiba (HIMAC) in July 2016 with the EPT-HET EM2 model. The hardware design of the EM2 model is identical to that of the EPT-HET flight models. The only difference is the quality of the electronic components, that are commercial standard in the EM2 model and space qualified in the flight models. The most important fact for the validation of the quenching prediction model is that the HIMAC July 2016 data has not been used for the design of the quenching prediction model itself. Hence it can be considered as valid test sample for the validation of the quenching prediction model. For the creation of the model data from previous HIMAC runs was used

with additional ion species at different energies (Tammen et al., 2015).
Figure 8.1 (a) shows a photograph of the experimental setup at HIMAC, while (b) shows the schematic of the setup for better understanding. The setup is identical to the setup at HIMAC used for the BGO-Thermal studies described in sec. 6.1. Directly behind the beam extruder a thin plastic scintillator is located, which is used to monitor the ion flux. To alter the energy of the ions, Polyethylene (PE) absorbers blocks are placed between the instrument and the plastic scintillator. This is necessary since HIMAC provides only a mono-energetic ion beam.
An overview of the ion species of this measurement campaign and their primary energies are given in table 8.1.

Ion	Primary energy / MeV/nuc
H	160
He	230
C	400
N	400
O	400
Ar	400

Table 8.1: Ion species measured during the July 2016 HIMAC campaign.

Simulation setup:
To validate the quenching prediction model, a detailed simulation model, which includes all necessary components of the HIMAC setup needs to be created. The EPT-HET EM2 model is modeled as described in sec. 5.2, as it is mostly identical to the FM in terms of the hardware. For the simulation of the HIMAC experiments all important features of the setup have been taken into account and shall be briefly introduced. The details of the implementation for HIMAC-specific parts are given in table 8.2. The distance between the beam extruder and the instrument, 70 - 80 cm, is adjusted for each simulation run according to the appropriate experimental setup. Another addition to the simulation setup presented in sec. 5.2 is an additional plastic scintillator in the beam line. To measure the particle flux of the ion beam, an EJ-212 plastic scintillator, wrapped in 10 µm mylar and an outer layer polyvinyl chloride with a thickness of 0.1 mm, is used. The thickness of the plastic scintillator, ranging from 0.2 mm to 3 mm, is adjusted based on the ion species. The PE absorber blocks which are used to adjust the energy of the ions are implemented as a single block, instead of several individual blocks. However, for the ion energy the total absorber thickness is the relevant value. Unlike the simulations for the design of the onboard data processing, the complete simulation volume is filled with air at ambient pressure, since this was also the case at HIMAC.

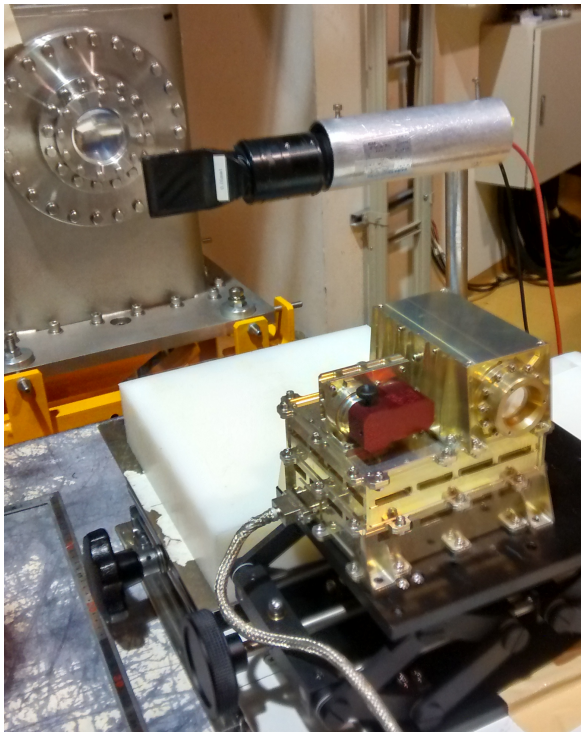

(a) Image of the setup during the July 2016 measurement run. In this case no absorber is used.

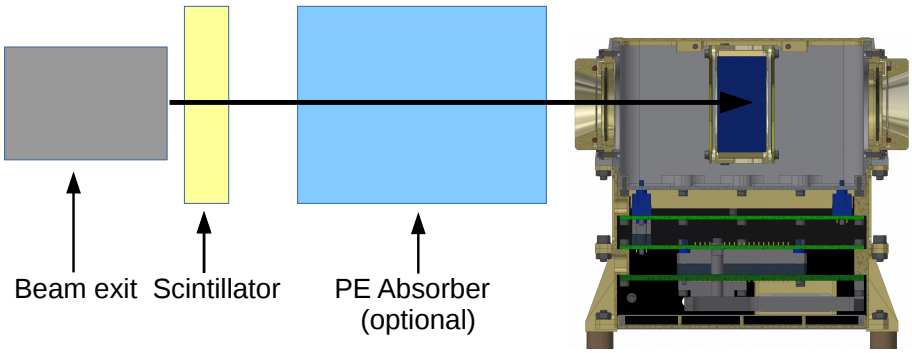

(b) Schematic of the HIMAC setup with the CAD model of HET.

Figure 8.1: Experimental setup at the HIMAC accelerator facility.

Part	Implemented as	Density / g/cm^3	Reference
Air	78% N, 21% O, 1% Ar	$1.184 \cdot 10^{-3}$	Standard Ambient Temperature and Pressure
EJ-212 scintillator	52% H, 48% C	1.023	Eljen-Technology (2016)
Polyethylene Absorber	C_2H_4	0.96	Measured

Table 8.2: Geant4 implementation of specific parts of the experimental setup at HIMAC. This table is an addition to table 5.1 in sec. 5.2 where the GEANT4 implementation of HET and the used materials is given.

8.1.1 Calibration

In sections 3.3.2 and in chapter 6 it is described that the light output of BGO is temperature dependent. This effect needs to be taken into account for experimental data in order to create a correct calibration and compare experimental data to simulation data. However, for the EM2 model there is no data available to create this model specific temperature correction. To create at least a qualitative temperature correction model for the HET EM2 unit, data of the BGO-Thermal instrument, as presented in fig. 6.3 of chapter 6 is used. During the HIMAC experiments in July 2016, the temperature of the BGO crystal varied between ≈25 °C at the start of the experiment to ≈29 °C after reaching equilibrium temperature. To create a model in the specific temperature range, all ion species measured with the BGO-Thermal instrument for which data points in this temperature region are available, are used. These are displayed in fig. 8.2. In this temperature range the temperature dependency of the light output can be considered linear. The temperature dependent light output curves of the selected ion species are normalized to 25 °C. By fitting a linear function to the data points of the temperature dependent normalized light output curves, as shown in fig. 8.2, the temperature dependence, $c(T) = -0.013 \cdot T + 1.332$ of the BGO scintillator for the EM2 in the given temperature interval can be found. Using this, the according temperature correction function $f(T)$ can be calculated:

$$f(T) = 0.013 T/°C + 0.675 \tag{8.1}$$

The temperature correction function f(T) yields a temperature correction factor and is thus multiplied with the calibrated ADC value of the BGO detector. In chapter 6 it is pointed out that the temperature calibration for HET is unit specific. This is related to the glue detachment of the light detection photodiodes of the BGO scintillator. However, this detachment, which affects the light detection efficiency of the photodiodes significantly, is observed below ≈20 °C (see sec. 6.2).

The minimum temperature during the HIMAC experiments is ≈25 °C. Thus, the linear approximation of the BGO-Thermal data is considered as a valid temperature correction for the EM2 model during the HIMAC experiment. However, it is not possible to quantify the uncertainty because of the lack of temperature calibration data of the EM2 unit. The temperature dependence of the individual parts of the data processing chain and the SSDs is less then 0.1% over the HIMAC temperature range (Böttcher, 2018) and can therefore be neglected.

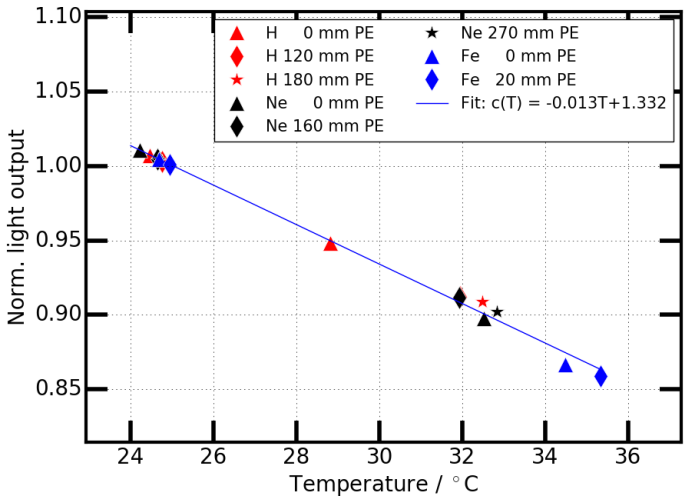

Figure 8.2: Normalized light output curves of the BGO-Thermal experiment. Data points are normalized to 25 °C. Further information on the data is presented in chapter 6.

With the thermal correction function and the results of the GEANT4 simulation, a calibration for the HET EM2 model can be created. For the calibration, the quenching prediction model is not applied to the simulation data. In table 8.3 the data that is used for the calibration with information of the absorber thickness and the unit orientation is presented. Only ion species and energies were selected which do not induce quenching or the quenching is considered to be neglectable based on previous studies (Tammen et al., 2015; Tammen, 2016b). Though He ions generally lead to ionization quenching in BGO, 230 MeV/nuc penetrating He ions are confirmed to not cause ionization quenching in the 2 cm thick crystal and can be used for calibration (Tammen et al., 2015). The HET EM2 unit delivers housekeeping data several times per minute. Part of the housekeeping data is the temperature of the BGO crystal cage, which is used for the temperature correction. The data, that is measured between two temperature values, is corrected using the mean of the two temperature values. The scintillation detector is calibrated as $E_{BGO}=(E_{pd1}+E_{pd2})/2$, where E_{pd1} and E_{pd2} is the measured energy in the respective photodiode. All solid state detector segments are calibrated as well using the data set presented in table 8.3 except for the guard segments of the B-detectors which are calibrated using only the data from table 8.3 with PE

absorbers, as measurements without absorbers lack the statistics for a calibration of these segments. For each measurement the position of the main ion peak is either determined with a Moyal- or a Gaussian function, depending on the peak shape (see sec. 3.1). By comparing the residuals of the fit for both functions, the optimal fit function for each peak is determined. To give an example of the fit to the data, the experimental data of the H ions with a primary energy of 160 MeV is used. In fig. 8.3, the measured energy in ADC values in the BGO is shown in blue and the fit of a Gaussian function to the data is shown in black. In fig. 8.4, the same is done for the HET-A1 inner segment. As the detector is thin compared to the range of the particle (see sec. 3.1), the energy deposition distribution can be approximated using a Moyal-function. Although, the fit and the data deviate towards higher energies, the peak position can be obtained using this method with sufficient accuracy. By performing the fitting procedure for

Ion	Absorber thickness / mm	Unit direction	mean temperature / °C
H	0	backward	25.0
H	20	backward	26.6
H	40	backward	27.4
H	50	forward	28.4
H	60	backward	27.8
He	0	backward	28.2
He	0	forward	28.3

Table 8.3: Measurements used for the calibration of the EM2. Mean temperatures are given for illustration.

all measurements listed in table 8.3, the position of the main ion peak, for the simulation in keV and for the experiment in ADC values, is determined. With this data, the calibration factors of the individual detectors and SSD segments, as listed in table 8.4 are obtained. Calibration factors are given for the high gain channels. The low- to high gain conversion is obtained by fitting a linear function to the low vs high gain data of a carbon measurement with a primary energy of 400 MeV/nuc. In figure 8.5 (a) the calibration curve for the BGO detector is shown. For the calibration the temperature correction function, given in eq. 8.1, is used. This results in a calibration, where all data points are well confined in the 95% confidence interval. The confidence interval is given by the red curves in fig. 8.5. Figure 8.5 (b) shows the calibration curve of the HET-A1 inner segment as an example for the calibration of the SSDs. For the SSDs, no temperature correction is necessary. All data points are well confined in the 95% confidence interval. With the temperature correction function for BGO, given in eq. 8.1 and the determined calibration factors, given in table 8.4, the validation of the quenching prediction model can be performed.

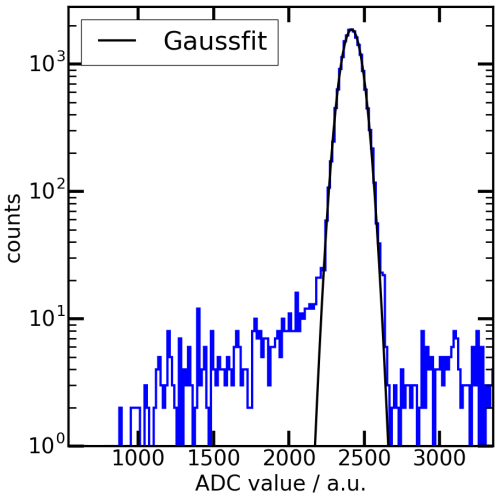

Figure 8.3: To determine the peak position of this proton measurement, a Gaussian function is fitted to the energy deposition (in ADC values) of the BGO scintillator.

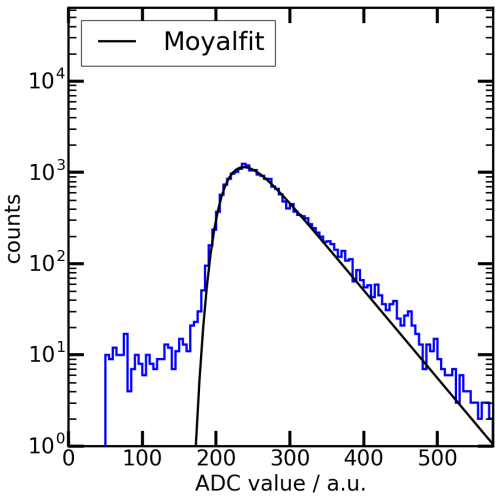

Figure 8.4: To determine the peak position of this proton measurement, a Moyal function is fitted to the energy deposition (in ADC values) of the inner segment of the HET-A1 detector.

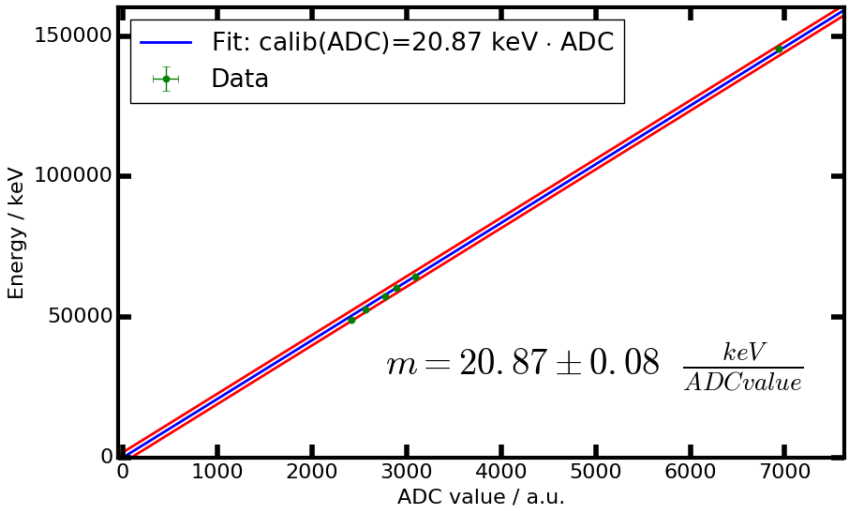

(a) Calibration curve of the BGO scintillation detector.

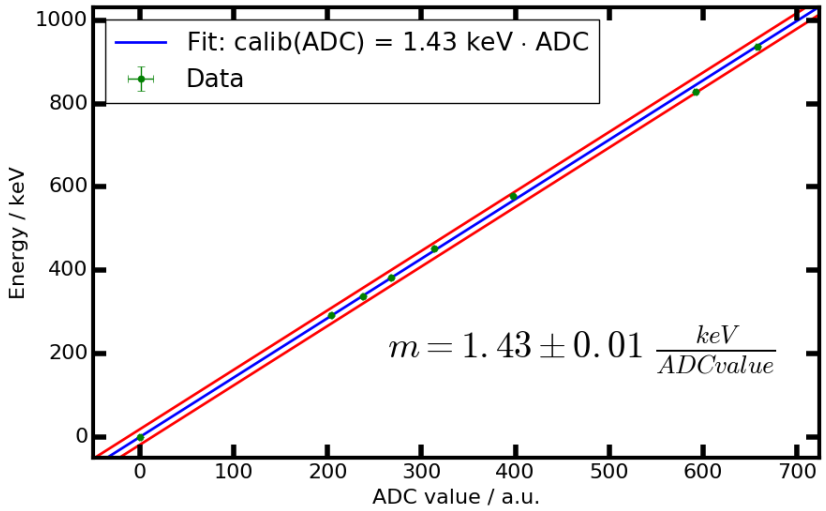

(b) Calibration curve of the inner segment of the HET-A1 detector.

Figure 8.5: Calibration curves examples of the EM2 model obtained from the HIMAC July 2016 campaign data given in table 8.3. All data points used for the calibration are well confined within the 95% confidence interval, given by the red curves, for all detector calibrations.

Segment / Detector	High gain calibration factor / keV/ADC-value	Low- to high gain conversion
HET-A1i	1.43 ± 0.01	13.12 ± 0.01
HET-A1o	1.38 ± 0.01	13.48 ± 0.01
HET-B1i	1.41 ± 0.01	13.30 ± 0.01
HETB1o	1.42 ± 0.01	13.16 ± 0.01
BGO	20.87 ± 0.08	13.30 ± 0.02
HET-B2i	1.43 ± 0.00	13.25 ± 0.01
HET-B2o	1.41 ± 0.00	13.27 ± 0.01
HET-A2i	1.40 ± 0.00	12.98 ± 0.01
HET-A2o	1.43 ± 0.00	13.35 ± 0.01
HET-B1G	0.98 ± 0.01	-
HET-B2G	0.97 ± 0.01	-

Table 8.4: Calibration factors for the EM2 unit for all detectors and detector segments as used for the HET level 3 trigger validation. In the third column, the low- to high gain conversion factors are given. The given uncertainties are obtained from the determination of the calibration factors, as shown in fig. 8.5.

8.2 Validation of the quenching prediction model

For the validation of the quenching prediction model for the BGO scintillator, the energy deposition measured during the experiment for a given ion species and absorber combination, is compared to the simulated energy deposition, to which the quenching prediction model is applied. In order to do this, the introduced calibration of the EM2 unit from the HIMAC July 2016 campaign, given in table 8.4 in combination with the temperature correction model, given in eq. 8.1, is used calibrate the experimental data. With this, the measured energy deposition during the experiment can be compared to the quenched and unquenched simulation data. The method to compare the calibrated experimental data and the quenched and unquenched simulation data is similar to the calibration of the EM2 unit. The energy deposition in a detector is determined using a fit of either a Moyal- or a Gaussian function, depending on the shape of the energy deposition distribution (see sec. 3.1). By determining the peak position of the energy deposition in a detector and comparing the results for the experiment and the quenched and unquenched simulation data, the accuracy of the quenching pre-

diction model can be evaluated. In table 8.5 two data points for ions penetrating the scintillation crystal and two data points for ions stopping in the scintillation crystal are exemplary given for each ion species measured during the HIMAC July 2016 campaign. Protons are not given, as protons only show low light losses due to ionization quenching and are thus not included in the quenching prediction model (Tammen et al., 2015).
Table 8.5 summarizes the results of the quenching prediction model verification. The first column gives the ion species, the second column the absorber thickness and the third column indicates whether the ions stop or penetrate the scintillation crystal. The fourth column gives the relative deviation between the energy deposition in the simulation and the experiment of the HET-A2 inner segment. Column number five and six give the relative deviation between the energy deposition in the experiment and the simulation (quenched column 5, unquenched column 6) of the BGO scintillator. In the following, the contents of table 8.5 are introduced and explained in more detail.
Since, SSDs are not affected by ionization quenching, they can be considered as a benchmark for the correctness of the simulation and its setup. For this reason in the third column of table 8.5, the relative deviation of the energy deposition in the HET-A2 inner segment which acted as the entrance detector during the measurements is provided. The main uncertainty of the simulation is the correct absorber thickness during the experiment. The total thickness of the absorber blocks is measured during the experiment. The absorber blocks are aligned optimally along the beam line, however a small tilt may lead to a significant increase in absorber thickness for the particles. The absorber thicknesses are given in the second column of table 8.5. For two given measurements two absorber thicknesses are given. In these cases, the absorber thickness was increased from the first measured value to the second corrected value. For these two cases, the deviation in the SSD energy deposition between simulation and experiment was found to be greater than 2% when directly using the thickness measured during the experiment. This deviation is an indicator for a tilt of the absorber, which leads to an increase of the absorber thickness for the energetic charged particle. Thus, for these two distinct measurements the absorber thickness has been iteratively increased to reduce the mismatch for the SSD to below 2%. The adjustment represents an inclination below $\approx 6°$. This small inclination is difficult to spot by eye during the experiment but can have a significant influence on the particle's energy for high absorber thicknesses.
In the fifth column of table 8.5 the relative deviation between the measured energy deposition, $E_{bgo,exp}$, and the simulated and quenched energy deposition, $E_{bgo,sim-q}$ in the BGO crystal is given. $E_{bgo,sim-d}$ is the energy deposition in the BGO scintillator, while $E_{bgo,sim-q}$ is the quenched energy deposition, which can be expected to be measured in the experiment. The sixth column gives the relative difference between the measured energy deposition $E_{bgo,exp}$ and the deposited energy $E_{bgo,sim-d}$ obtained from the simulation, to illustrate the difference with-

out the use of the quenching prediction model. The reduction of the mismatch between energy deposition and measured energy is significant, especially for the stopping particles, which have the highest energy deposition per path length. This unquenched energy deposition can not be used for the design of the level three triggers of HET nor to predict the location of the data product items in the histograms. By using the quenching prediction model for BGO the mismatch is highly reduced. For most data points the deviation for the quenched simulation data is below 5%. The highest deviation is observed for oxygen with 190.1 mm absorber thickness and the stopping argon ions. However these are still well within the given uncertainty ranges of the model (Tammen, 2016b) and the reason for the deviation can be explained. The highest uncertainty of the model is observed for particles barely entering the scintillation crystal, which is the case for the oxygen measurement with 190.1 mm absorber thickness. In case of Argon, the model uncertainties are slightly higher, as shown in table 8.5, since it has not been used for the development of the quenching prediction model. Therefore, the errors for this ion are expected to be larger and in the range of 20 to 5% for stopping and -10 to 10% for penetrating ions (Tammen, 2016b). However, the reduction of the mismatch by one order of magnitude using the quenching prediction model is still a significant improvement. From the outcome of this study it can be concluded that the output of the quenching prediction model by Tammen et al. (2015) is in good agreement with the measurement data. Therefore the simulation data in combination with the quenching prediction model is suitable to predict the ion species location in the level 3 histogram and correctly determine the primary energy of these particles for the data products.

8.3 Validation of HET Level 3 triggers

With the validation of the quenching prediction model, which demonstrates the good agreement between the energy deposition measured in the experiment and the calculated and quenched energy deposition in the simulation, it is clear that the simulation data is suitable to develop the HET level 3 trigger and determine the primary energy ranges for the data products. To further illustrate the comparability of the simulation and the experiment for the different trigger classes a selection of certain measurements from the HIMAC July 2016 measurement campaign are used. The energy range of HIMAC is too high to validate the ABnC level 3 trigger. Even with significant PE absorber blocks to reduce the energy of the particles, a meaningful statistic can not be achieved. However, the main concern for HET is the effect of ionization quenching which affects the BGO scintillation crystal.

Ion	Abs. thickness /mm	pen. or stop.	$\frac{E_{si,sim}-E_{si,exp}}{E_{si,sim}}$	$\frac{E_{bgo,sim-q}-E_{bgo,exp}}{E_{bgo,sim-q}}$	$\frac{E_{bgo,sim-d}-E_{bgo,exp}}{E_{bgo,sim-d}}$
He	100	pen.	- 0.3%	-2.5%	1.5%
He	150	pen.	-0.5%	-2.5%	2.6%
He	291.2	stop.	-1.4%	0.01%	23.9%
He	301.1 $\mapsto$ 302.9	stop.	-0.5%	-1.5%	26.0%
C	0	pen.	0.6%	-0.6%	17.1%
C	100.4	pen.	0.0%	0.8%	22.2%
C	210.8	stop.	- 0.7%	0.3%	42.7%
C	230.8	stop.	-1.4%	0.4%	46.1%
N	0	pen.	0.3%	-1.9%	22.1%
N	100	pen.	-0.1%	0.1%	29.0%
N	180.1	stop.	-0.1%	-2.5%	46.0%
N	200.1	stop.	-0.7%	-3.6%	50.1%
O	0	pen.	0.5%	-2.3%	26.7%
O	100	pen.	0.2%	-0.2%	36.0%
O	160.1	stop.	-0.2%	-3.2%	49.9%
O	190.1 $\mapsto$ 190.8	stop.	0.6%	-11.9%	58.2%
Ar	0	pen.	2%	-2.6%	48.6%
Ar	10	pen.	1.6%	-0.9%	50.6%
Ar	50.4	stop.	0.8%	4.0%	57.6%
Ar	65	stop.	0.4%	5%	59.4%

Table 8.5: Comparison of experimental and simulation data from the HIMAC July 2016 campaign. The third column gives the relative difference between simulation and the experiment in measured energy for the inner segment of the HET-A2 detector. The fourth column gives the relative difference between the simulation and the experiment in measured energy for the BGO when using the quenching prediction model for the simulation data by Tammen et al. (2015). The fifth column gives the relative difference between the simulation and the experiment in measured energy for the BGO without the quenching prediction.

Level 3 Penetrating trigger testing

To illustrate the validity of the quenching prediction model for the HET penetrating level 3 trigger, carbon ions are used. This ion species are significantly affected by ionization quenching as is shown in tab. 8.5. In fig. 8.6 (a), quenched simulation data is compared to combined measurement data (b) qualitatively. The measurement data is calibrated using the introduced calibration of the EM2 unit from the HIMAC July 2016 campaign, given in table 8.4 in combination with the temperature correction model, given in eq. 8.1. For the simulation, an energy spectrum from 100 MeV/nuc to 3 GeV/nuc is used, to cover the complete energy range of the HET penetrating trigger. The simulation is performed with the setup presented in sec. 5. In order to achieve an energy spectrum at the HIMAC accelerator facility, it is necessary to use a combination of wedge-shaped absorber blocks, since the ion beam itself is mono-energetic and offers a maximum energy of 400 MeV/nuc for the measured carbon ions. Thus, different measurements with wedge-shaped absorbers are combined to obtain a spectrum and determine the position of the carbon ions in the HET level 3 penetrating trigger histogram. By using absorbers, the experimental data shows a large amount of secondary particles, compared to the simulation. Due to the limitation of the maximum energy of the carbon ions during the experiment, the complete energy range of the HET level 3 penetrating trigger can not be covered. Thus the DPI, which shows the highest statistics in the simulation is not populated in the experiment. Still, the location of the main carbon ion population for most of the energy range of the penetrating level 3 trigger in the individual histogram bins still matches exactly for the simulation and the experiment. Though, this is expected from the results presented in tab. 8.5, a visualization as shown in fig. 8.6 provides a good impression of the results.

For a more detailed comparison of the simulation and measurement data, a measurement of carbon ions that have been measured without an absorber are used. For this measurement the primary energy of the particles is known from the accelerator settings. For measurements where an absorber has been used, the primary energy of the particle behind the absorber block can only be determined from the simulation. This would introduce a dependency on simulation data for the validation, which is not necessary for the penetrating trigger in the case of the chosen measurement. Figure 8.7 (a) displays the output of the HET penetrating level 3 trigger for the measured 400 MeV/nuc carbon ions. The majority of the counts are located in the "O8" box. Due to ion fragmentation in the scintillation crystal, a tail towards lower energy measured in C and lower min(A1,B1)/min(A2,B2) ratios is created i.e. secondary particles with lower A,Z than the primary particle are created and detected. Figure 8.7 (b) shows the counts in the data product boxes normalized to the total counts in the histogram. On the x-axis the primary energy range of each data product box is given as determined from the HET level 3 penetrating trigger design given in sec 7.3.5. The "O8" box (data product item)

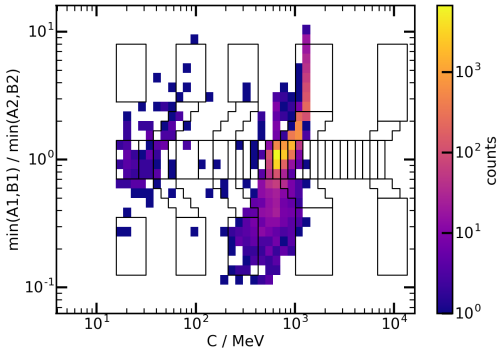

(a) Output of the HET penetrating level 3 trigger for carbon ions with energies from 100 MeV/nuc to 3 GeV/nuc.

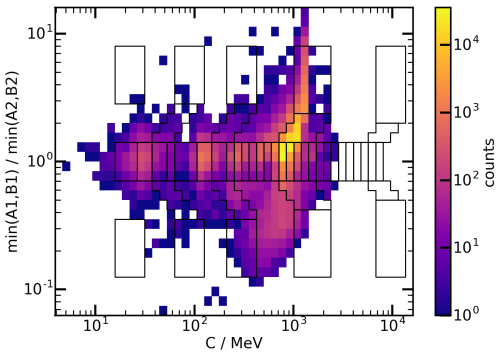

(b) Output of the HET penetrating level 3 trigger for a combination of different carbon ion measurements taken at HIMAC.

Figure 8.6: Comparison of simulated (a) and measured (b) carbon ions.

has a primary energy range of 360 to 610 MeV/nuc, so that the 400 MeV/nuc carbon ions should be contained in this box for the simulation as well as the experiment. In the experiment, 94% of the ions are contained in this data product item. In case of the simulation, 96% are contained in this data product item. Therefore it can be concluded that the majority of ions are correctly processed by the level 3 trigger and are allocated in the correct data product item for both, the simulation and the experiment. The "O9" box contains the ions from the high energy tail of the energy deposition distribution while "O7" contains fragmented particles that deposit less energy in the BGO crystal. Comparing fig. 8.7 (b) to fig. 8.8 (b) which shows the simulation of the HIMAC measurement, a mismatch for the counting statistics in the "O9" box and also for both flanks is observed. Comparing the energy deposition distribution of BGO for the carbon ions it was found that the distribution in the experiment is broader compared to the simulation. This leads to the relative increase in particles in the "O9" box. This and the relative increase in counts in the "O7" box in the experiment, result in the slightly lower amount of counts in the "O8" (94%) in the experiment to the 96% in the simulation. However, comparing these two numbers for the simulation and the experiment, it can be concluded that the simulation in combination with the quenching prediction model is able to reproduce or predict the reality and is thus well suited for the level 3 trigger design.
For illustration, in fig. 8.9 the simulation data without the post-processing by the quenching prediction model is shown. The energy deposition in C is shifted towards higher energies, so that 90% of the ions are located in the "O9" box. Thus an agreement between the experiment and simulation is not given, in case the quenching prediction model is not used. This underlines the necessity to use

the quenching prediction model for the post processing of the simulation data, as otherwise the location of the defined data product items would be incorrect for the measurement of real particles.
The observed broader energy distribution for the carbon ions in the experiment compared to the simulation was further investigated to understand its origin. An instrumental effect of broadening like electronic noise could be excluded due to the fact that the broadening is significantly higher than any expected electronic noise. In general, the electronic noise for the silicon detectors and for BGO is taken into in the simulation with 5 keV and 300 keV, respectively but can not reproduce the distributions found in the experiment. Further simulations with beam divergence or a misaligned instrument could also not reproduce this effect. The most probable source of this mismatch is that the scattering and secondary particle production in the simulation does not fully reproduce the reality. The broadening of the energy deposition distribution does not influence the level 3 trigger designs of HET itself. As described in sec. 7.3 the analysis of an event by the HET level 3 triggers mostly use relative, not absolute requirements / thresholds. This means, that there are no specific cut values specified in the HET level 3 trigger designs which were obtained with the simulation that are affected by the broader energy deposition distribution found in the experiment. The absolute requirements, for example on detector thresholds, were selected with a large margin so that the broadening of the energy deposition distribution in the observed order of 60% for BGO is well covered by the design.

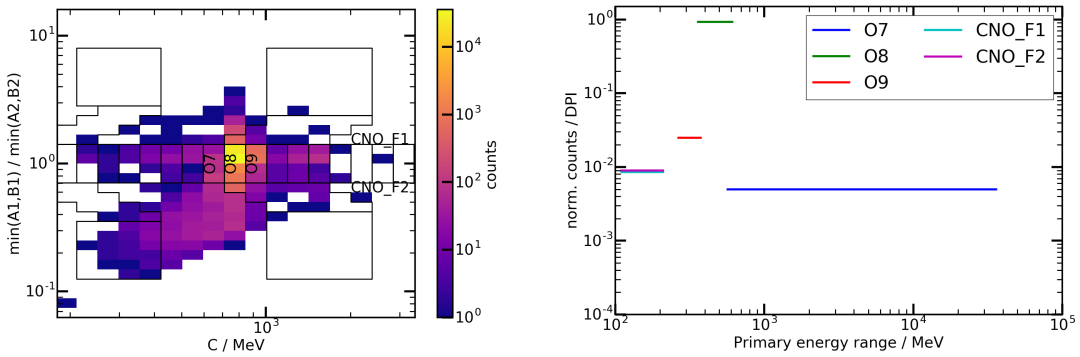

(a) Output of the HET penetrating level 3 trigger for 400 MeV/nuc carbon ions measured at HIMAC.

(b) The counts are normalized to the total measured counts in the level 3 penetrating histogram.

Figure 8.7: Measurement of 400 MeV/nuc carbon ions. For this measurement no absorber is present between the beam and the instrument.

The mismatch between the experimental and simulation data found for the "CNO_F1, CNO_F2" boxes is attributed to a secondary energy distribution in

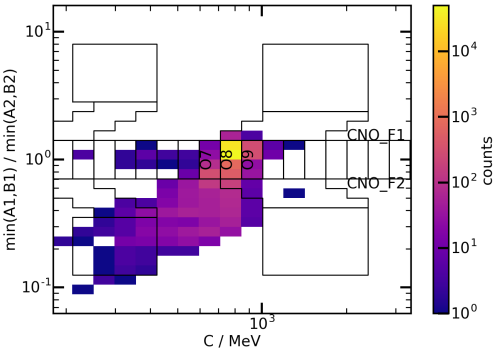

(a) Output of the HET penetrating level 3 trigger for simulated 400 MeV/nuc carbon ions.

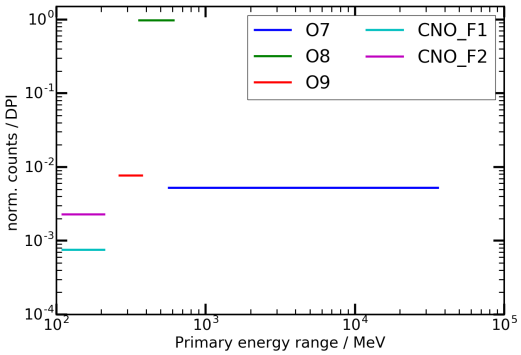

(b) The counts are normalized to the total measured counts in the level 3 penetrating histogram.

Figure 8.8: Simulation of 400 MeV/nuc carbon ions according to the setup at HIMAC used for the measurement shown in fig. 8.7.

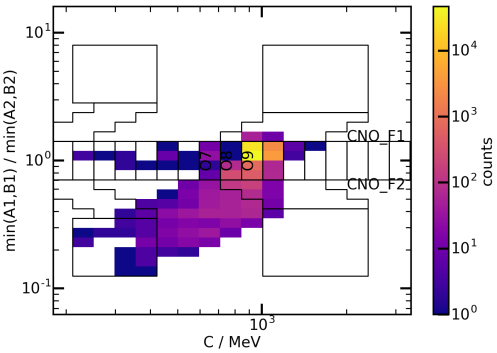

(a) Output of the HET penetrating level 3 trigger for simulated 400 MeV/nuc carbon ions.

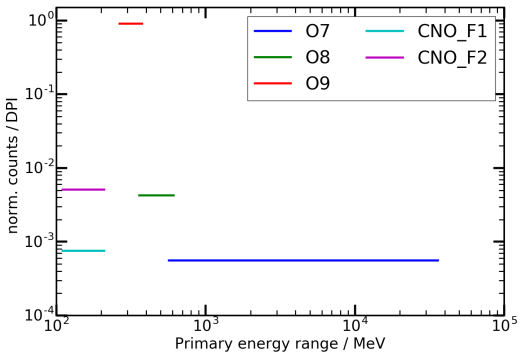

(b) The counts are normalized to the total measured counts in the level 3 penetrating histogram.

Figure 8.9: Simulation of 400 MeV/nuc carbon ions according to the setup at HIMAC used for the measurement shown in fig. 8.7. However, the quenching prediction model is not used in this case and a significant mismatch between the experimental data, shown in fig. 8.7, is observed.

the experimental data. This secondary distribution produces a tail towards lower energies as shown in fig. 8.10. Though this distribution is statistically not relevant, as it is in the order of 1% compared to the main ion peak, its origin is investigated. It was found that this effect is present in all silicon detectors. It is concluded that in rare cases one detector measures less energy compared to all other silicon detectors, regardless of its position in the telescope. For example, while the HET-A1, -B1 and -A2 detector measure an energy that is contained in the main energy distribution, the HET-B2 detector measures an energy from the secondary (lower) energy distribution. Therefore it is neither a beam effect nor a problem that effects only the entrance detectors. Several possible experimental effects could be excluded, like delta-electron production and ion fragmentation. If an ion fragments in the crystal, it deposits less energy in the SSDs behind the crystal. However, the energy deposition in the two SSDs would be comparable, unlike seen in the data. Crosstalk between segments could also be excluded by comparing energy deposition between segments and detectors. An incorrect pulse height due to the wrong pulse age of an event could also be excluded, as the pulse ages for the described inner segments case were all similar and within the expected range. Comparing the HIMAC 2016 July data of EPT-HET EM2 with the HIMAC 2017 July data of the flight model of the Lunar Neutron and Radiation Dose Detector (Wimmer-Schweingruber et al., 2020), this secondary energy distribution is also found in the silicon detector data of LND with the exactly same behavior. As LND uses the same read-out electronics as EPT-HET it can be concluded that this is an effect based either on the read-out electronics or other instrumental effects that could not be identified during this study.

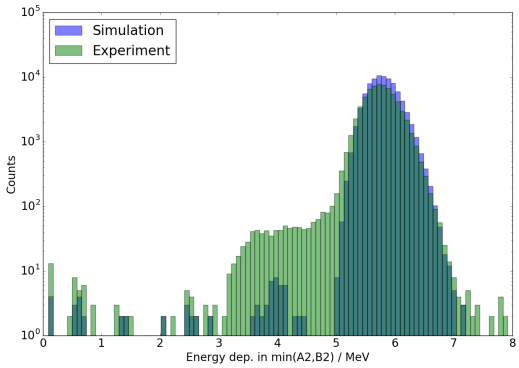

Figure 8.10: Energy deposition in the silicon detectors on the entrance side of the beam. The main ion distribution are in good agreement for the simulation and the experiment. However, the experimental data shows a second ion population with less energy deposition.

Level 3 ABC stopping trigger testing

Using the HIMAC July 2016 data, the ABC stopping trigger as presented in sec. 7.3 can be used to further validate the trigger design and the performed GEANT4 simulations with the quenching prediction model. The results of the quenching prediction model validation presented in sec. 8.2 show that a good agreement between simulation and experiment is found and thus the design of the ABC stopping trigger using quenched simulation data can be considered as valid for experimental data as well. In order to prove this, one measurement from the HIMAC July 2016 measurement campaign is selected for a more detailed analysis. For this, a measurement with oxygen ions with an initial energy of 400 MeV/nuc with an 160 mm PE absorber is used. A 160 mm PE absorber is used to reduce the primary ion energy, so that they stop in the scintillator and can be processed by the level 3 ABC trigger. The primary energy distribution behind the PE absorber can not be directly obtained from the experiment, so a GEANT4 simulation of the setup is used. The residual energy distribution after passing through the PE absorber is shown in fig. 8.11 for the oxygen ions. This residual energy distribution can be considered as the primary energy of the particles in the experiment when entering HET. The majority of the oxygen ions show a primary energy range of 152 - 158 MeV/nuc before entering the A2 detector. Additionally, the distribution shows a tail towards lower primary energies due straggling in the absorber. The amount of particles in this tail is in the range of 8%. Fig. 8.12 (a) shows the experimental data after it is processed by the ABC trigger. The black boxes in fig. 8.12 (a) display the defined nominal data product items for carbon (bottom row), nitrogen (middle row) and oxygen (top row). The use of an absorber block leads to the production of ion fragments with lower atomic mass and charge numbers. Another effect of the absorber is that the initially mono energetic ions show a broader primary energy distribution behind the absorber. Figure 8.12 (a) and fig. 8.13 (a), show the outcome of the ABC trigger for the experiment and the simulation, respectively. In both cases, the main ion peak is located in the nominal oxygen data product item # 10. From the outcome of the ABC level 3 trigger design presented in sec. 7.3.2, the energy range of this box is between 152 to 184 MeV/nuc. Thus, the oxygen ions are correctly allocated for the experiment and the simulation. As described for the penetrating trigger validation, the energy deposition in the experiment is broader, which can also be seen in the two histograms. However, looking at the (b) panels of fig. 8.12 and fig. 8.13 and comparing the normalized counts in the oxygen DPIs, a good agreement is found. The counts have been normalized using all counts in the ABC level 3 heavy ion histogram. The O 10 DPI contains 73% of the particles in the simulation while 70% are contained in that DPI in the experiment. In case of the O 9 DPI 10% are contained in the simulation and 7% in the experiment. The real data, measured during the experiments at HIMAC processed by the HET ABC level 3 trigger is in good agreement with the simulation data. Thus it can be concluded that the post-processed simulation

data is well suited to design the HET onboard data processing and also for the calculation of the responses of the instrument. This is important, as only with the simulation data, the response of each data product item to a given particle species can calculated. This is done in chapter 9, where the method to calculate the primary energy dependent response of the instrument to incident particles is explained.
For illustration, in fig. 8.14 the simulation data without the use of the quenching prediction model is shown. In this case, the ions are completely misaligned compared to the experimental data. The counts in the data product boxes, e.g. O 10, are not resulting from oxygen ions but rather from ion fragments. It is necessary to use the quenching prediction model as otherwise thresholds and data products would be incorrect for real particle measurements. However, it can be concluded that the processing of real experimental data by the ABC level 3 trigger is absolutely comparable to the processing of the simulation data to which the quenching prediction model has been applied. Thus in the next chapter, the post-processed simulation data can be used to calculate the instrument response to the different ion species and to calculate the primary energy ranges for each data product item, as given in chapter 9.

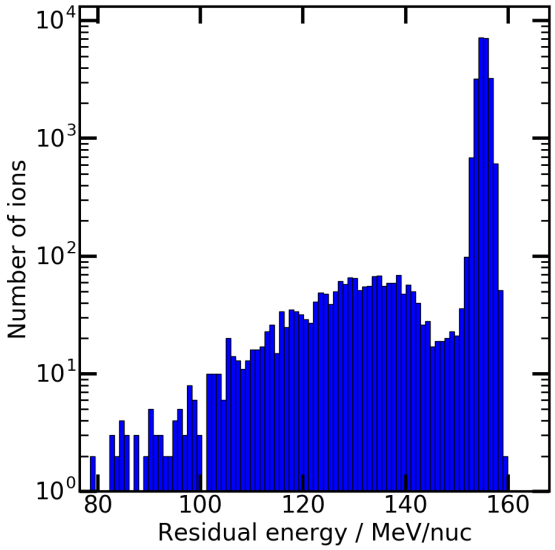

Figure 8.11: The residual energy distribution of oxygen ions after penetrating a 160 mm PE absorber obtained with a GEANT4 simulation.

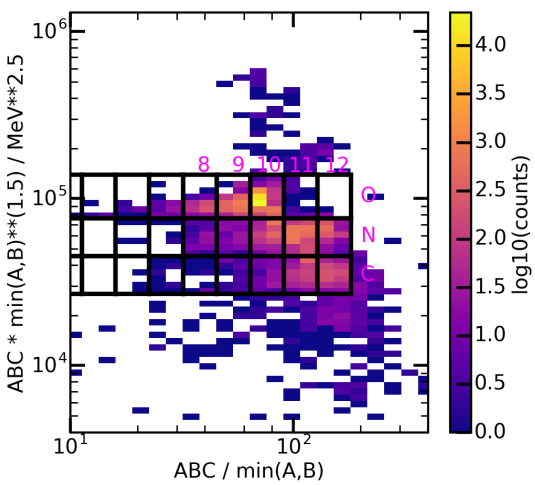

(a) Output of the HET ABC level 3 trigger for an oxygen ion measurement with an 160 mm PE absorber block.

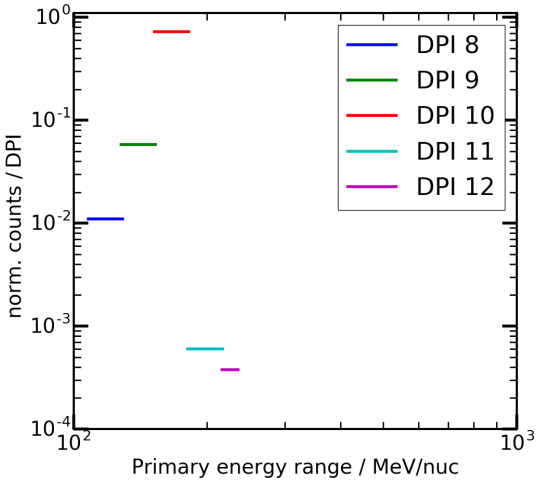

(b) Normalized counts of the individual oxygen data product items. The counts are normalized to the total measured counts in the histogram.

Figure 8.12: Measurement of 400 MeV/nuc oxygen ions with a 160 mm PE absorber from the HIMAC 2016 measurement campaign.

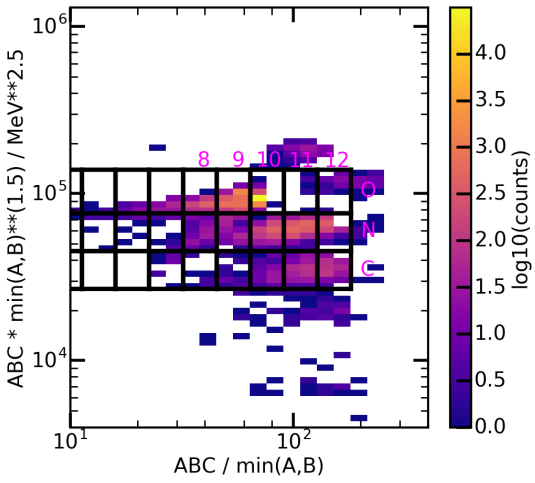

(a) Output of the HET ABC level 3 trigger using a GEANT4 simulation for oxygen ions with a primary energy of 400 MeV/nuc passing through a 160 mm PE absorber.

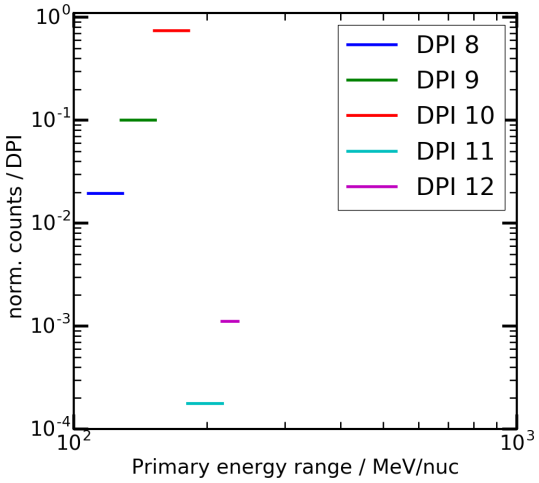

(b) Normalized counts of the individual oxygen data product items. The counts are normalized to the total measured counts in the level 3 ABC heavy ions histogram.

Figure 8.13: Simulation of 400 MeV/nuc oxygen ions according to the setup at HIMAC used for the measurement shown in fig 8.12.

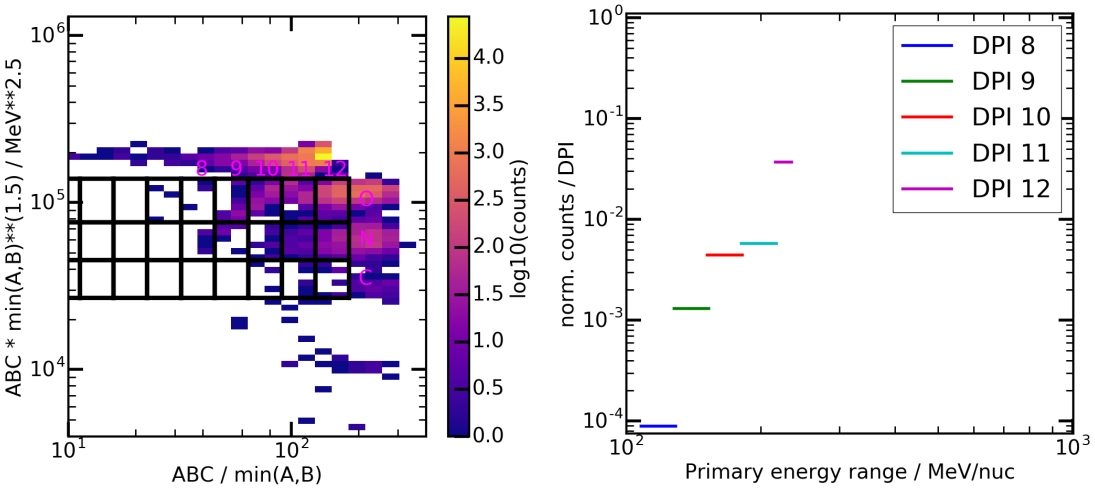

(a) Output of the HET ABC level 3 trigger using a GEANT4 simulation for oxygen ions with a primary energy of 400 MeV/nuc passing through a 160 mm PE absorber.

(b) Normalized counts of the individual oxygen data product items. The counts are normalized to the total measured counts in the level 3 ABC heavy ions histogram.

Figure 8.14: Simulation of 400 MeV/nuc oxygen ions according to the setup at HIMAC for the measurement shown in fig 8.12. However, in this case no quenching prediction model is used.

9. Calculation of geometrical- and response factors of HET

In sec. 7.3 the method for the particle identification and data processing of HET is explained. The information obtained from the instrument during its operation is a number of counts of the individual data product items in a given time interval. From this count rate, the in-situ particle flux, which is a physical property of the local environment, needs to be calculated. The conversion factor from a counting rate to a particle flux is known as the geometrical factor (Sullivan, 1971). In case the data processing of an instrument is taken into account for the conversion factor calculation, it is often referred to as a response factor. The geometrical factor is depending on the geometry and the sensitivity of the sensors. For an ideal detector with a perfect particle detection efficiency the relation between the observed counting rate, C, and the intensity of an isotropic particle flux, I, is given in eq. 9.1 with the geometrical factor, G. In the following, the geometrical factors of HET are calculated and presented in sec. 9.1. Subsequently, the calculation of the energy dependent response factors for the defined data product items is explained in sec. 9.1.

$$C = GI \tag{9.1}$$

9.1 Analytic calculation of the HET geometrical factors

For HET the geometrical factors can be analytically calculated under the assumptions that

- The particle trajectory is a straight line (no scattering in the detector)
- The particle type does not transform (no particle fragmentation)
- The detection efficiency is independent of the incoming particle angle (ideal telescope)

Under these assumptions Sullivan (1971) found a general equation, given in eq. 9.3, to calculate the geometric factor for two circular detectors with the radii

R_1 and R_2, separated by a distance l. S is the surface of the detector and Ω the domain of ω.

$$G = \int_\Omega \mathrm{d}\omega \int_S \mathrm{d}\sigma \cdot \hat{r} \tag{9.2}$$

$$= \frac{1}{2}\pi^2[R_1^2 + R_2^2 + l^2 - [(R_1^2 + R_2^2 + l^2)^2 - 4R_1^2R_2^2]^{1/2}] \tag{9.3}$$

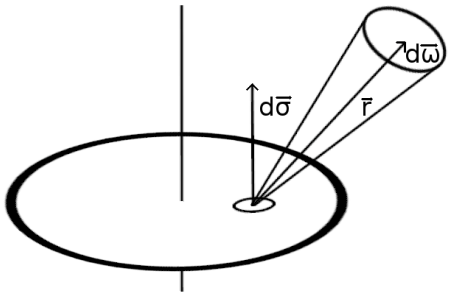

Figure 9.1: A single detector with a viewing direction in one hemisphere with a surface S. This figure helps to understand the assumptions leading to eq. 9.3. After Sullivan (1971).

For HET the geometrical factors can thus be easily calculated for the different level 3 trigger classes using the A and B detectors on one side for the ABnC and ABC coincidence and both A detectors for the penetrating coincidence. The detector distances and dimensions are given in sec. 4.3 in fig. 4.8. The collimator of the HET instrument does not obstruct the field of view defined by the detector distances and dimensions. Therefore the obtained geometrical factors are not influenced by the collimator. The results of the geometrical factor calculations are given in table 9.1. The very low geometric factors for the high flux mode do not impact all ion species of the different trigger classes. In the high-flux mode the threshold of the outer segment of the A detectors is increased from 50 keV to 6.2 MeV to suppress electrons and protons in the ABnC trigger as described in detail in sec. 7.3. The necessary assumptions for the analytical geometrical factor calculation do not reflect the reality. The calculated geometrical factors are not energy or particle species dependent and processes like particle fragmentation and scattering are neglected. Furthermore, the onboard data processing of the particle events by HET is not taken into account. To achieve more realistic and energy and particle type depending results, the computing power of modern PC's can be used to calculate response factors numerically. However, the obtained values from the analytic calculation are an indicator for the correctness of the response factors, which are derived in sec. 9.2.

Coincidence Condition	Trigger class	Geometric factor / cm^2 sr
A1 $\wedge$ B1	ABnC, ABC	0.271
A1 $\wedge$ B1 $\wedge$ C $\wedge$ B2 $\wedge$ B1	Penetrating	0.044
B1 $\wedge$ C $\wedge$ B2	GCR	0.770
A1i $\wedge$ B1	ABnC, ABC High flux	0.059
A1i $\wedge$ B1 $\wedge$ C $\wedge$ B2 $\wedge$ A2	Penetrating High flux	0.009

Table 9.1: Analytically calculated geometric factors for HET. For the ABnC and ABC triggers, only one side (A1,B1) is given. The values are identical for the A2,B2 side, as the distances and dimensions are identical.

9.2 Response factors of HET

The calculation of the energy and species dependent response factors for HET requires the use of simulations. The three assumptions, given in sec. 9.1, that were necessary for the analytic calculation of the geometrical factor are not needed when using a physical simulation. Since each particle is individually tracked in a simulation, the trajectory of the particle may change or it can undergo fragmentation. Furthermore the particle species and primary energy dependent response factors can be determined, as this information is known from the simulation. Additionally, the onboard data processing of the instrument is taken into account by post-processing the simulation data.
Equation 9.4 is used to calculate the response factor R for a specific data product item i and a given particle species x after Sullivan (1971). For the calculation the simulation with the source setup given in chapter 5 is used in which the particles are injected from a source surface with a source area A with a cosine law distribution in front of the collimator.

$$R(x,i,E) = A\frac{n_{det}(x,i,E)}{n_{sim}(x,E)}\int_0^{2\pi} d\phi \int_0^{\pi/2} \cos\theta \sin\theta d\theta = \pi A \frac{n_{det}(x,i,E)}{n_{sim}(x,E)} \quad (9.4)$$

The number of detected particles in a certain data product i is noted as n_{det} and the number of simulated particles for a given energy range from E_0 to E_{max} is noted as n_{sim}. As explained in chapter 5, in the used simulation setup, a source surface in combination with a cosine law angular distribution creates an isotropic flux on the detectors according to Santin, Giovanni (ESA / ESTEC and RheaTech Ltd (2008). The azimuth angle (ϕ) ranges from 0 to 2π and the polar angle (θ) from 0 to $\pi/2$ in the simulation.

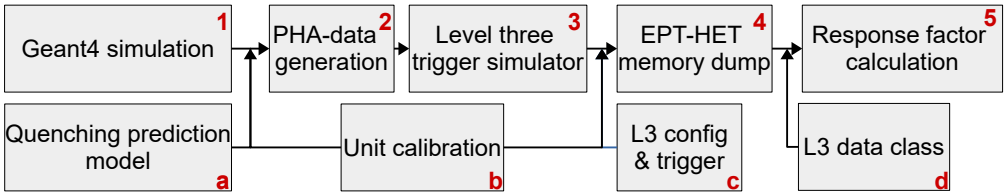

Figure 9.2: Flowchart for the calculation of the response factors. The main steps, 1 to 5 are given in the top row, while the bottom row, a to d, shows the necessary inputs by other modules.

In fig.9.2 the data processing for the calculation of the HET response factors is illustrated. The top row of the flowchart shows the main steps, while the bottom row shows inputs from other sources that are necessary for the main steps. The individual steps are referred to in the text by the given indices in fig.9.2.
The GEANT4 simulation data (1), obtained with the simulation setup given in chapter 5 is post-processed using the quenching prediction model (a) by Tammen et al. (2015), which is explained in sec. 5.4.
The post-processed simulation data is then converted into a PHA format (2) (see sec. 7.5.2 for details on the PHA format). In order to convert the energy values obtained from the simulation into the PHA-format, a HET unit calibration (b) is used. The calibration factors are applied reversely in this case, as they normally convert pulse-height values to energy. The exact calibration and its values are not important as long as the same calibration for the PHA-data generation (2) and the level 3 trigger simulator (3) is used.
In the next step, the obtained PHA-data (2) is run through a level 3 trigger simulator (3). This simulator performs an evaluation of the PHA data using the different level 3 triggers exactly as they are implemented on the HET units, based on the so called L3 configuration (c). Thus, every comparison or calculation is exactly performed as on a real HET instrument.
The output of the level 3 trigger simulator (3), when supplied with PHA-data (2), is a so called EPT-HET memory dump (4). This memory dump, contains all different level 3 trigger histograms, as introduced in sec. 7.3. The histograms are stored in such a way, that the counts in each histogram bin are stored in a unique memory address. Thus, by knowing the memory address range of a certain histogram, the histogram with the measured counts can be obtained.
With this memory dump (4), the counts in each level 3 histogram for a given PHA data set can be investigated. For example by using PHA-data containing protons with a certain primary energy range, the location (histogram bins) of these protons in the HET level 3 ABnC proton histogram can be determined.
Using the L3 data class (d), which contains the definitions of the data products and the according data product items, the counts in a given data product item can be obtained. In L3 data class, the memory addresses of a certain histogram,

which are to be summed up to create a specific data product item are given. With this information, the response factors (5) for a certain data product item can be calculated, according to eq. 9.4, since the number of detected particles in the data product item and the number of simulated particles is known.
In practice, a complete particle species data set, covering the energy range of a specific trigger, is divided into small logarithmically spaced primary energy ranges for the calculation of the response factors. Thus, for one particle species, multiple EPT-HET memory dumps are created. Each memory dump contains the histogram counts for a different primary energy range. For the primary energy binning, a total of 1720 logarithmic bins with 64 bins per octave is used, ranging from 1 keV to 122 GeV. With this information, the contribution to each histogram bin based on the primary energy of a particle species can be calculated. The L3 configuration, L3 data class and level three trigger simulator stored in the solo subversion directory: "asterix.ieap.uni-kiel.de/home/subversion/stephan" under "/solo/eda/python/solo/hetept". The simulation scripts, the quenching prediction model and scripts for the PHA file generation are stored in a git directory: "https://gitlab.physik.uni-kiel.de/solo/het-g4".
To illustrate the last part of the calculation (4-5), the HET Low Latency (LL) data product for protons stopping in AB is used. Since the LL data product of protons stopping in AB (level 3 ABnC trigger) features only two data product items, it is well suited for an illustration. In fig. 9.3 (a) the proton ABnC 1D histogram is shown using one specific of the 1720 EPT-HET memory dumps for protons. The shown memory dump contains protons with a primary energy between 8.65 and 8.74 MeV.

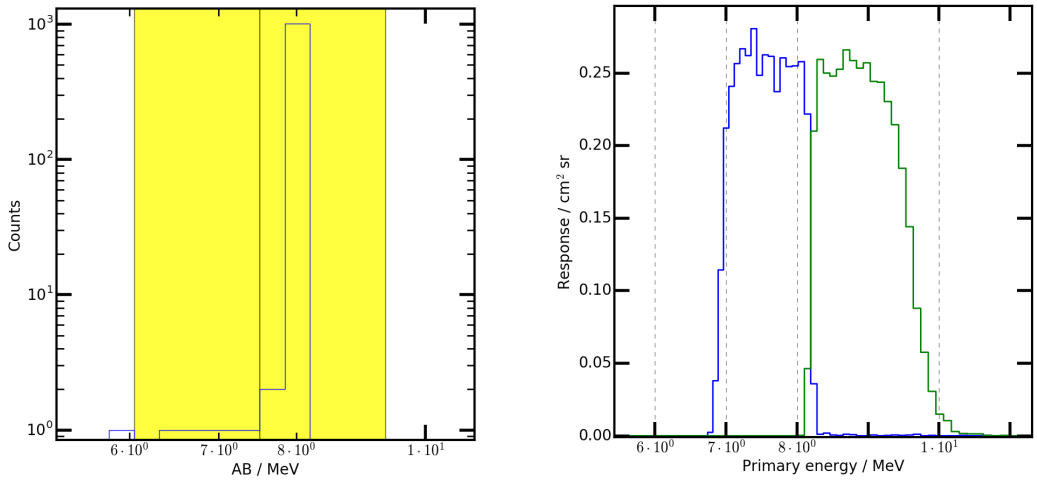

(a) Shown is the LL 1D ABnC proton histogram with the number of proton counts with a primary energy between 8.65 and 8.74 MeV of a GEANT4 simulation.

(b) By iteration over all primary energy ranges, using the different EPT-HET memory dumps, the response for the two DPIs depending on the primary energy is obtained.

Figure 9.3: Illustration for the calculation of the response factors using the LL ABnC data product for protons. The blue curve in panel (b) represents the left DPI and the green curve the right DPI shown in panel (a).

Therefore, the counts in each of the two LL data product items (LL_HETB_p_1/2) are resulting from protons in energy between 8.65 and 8.74 MeV. The two data product items are indicated by the two yellow boxes in fig. 9.3 (a). With the knowledge of the simulated number of protons in this energy range, the response is calculated according to eq. 9.4: From the simulation setup, the source area A is known. Furthermore the total amount of simulated protons n_{sim}(H,E) in the given energy range, 8.65 to 8.74 MeV, is known. From the histogram shown in fig. 9.3 (a) the number of counts n_{det}(H,LL_HETB_p_1/2,8.65-8.74 MeV) in the two respective DPIs is also known.
When this is iteratively done over the full primary energy range of interest, fig. 9.3 (b) is obtained. With the information of the response depending on the primary energy of the protons, the response of the two Data Product Items (DPIs) to protons is fully characterized and the primary energy range of the two data products for protons is known. Thus, the count rate measured by the provided by the data product items can be converted into the physically relevant particle flux. A comparison between the analytically calculated geometrical factors, as given in table 9.1, and the numerically calculated response factors, which take the onboard data processing and physical processes like scattering, ion fragmentation and secondary particle production into account is given at the end of sec. 9.2.1. When this is performed for all DPIs, the response depending on the primary en-

ergy for each DPI is obtained. However, in practice often a fixed energy range in combination with a fixed averaged response factor is used to calculate the particle flux from the counts of a DPI. Though with this method the particle flux measured by the instrument can be obtained, the method can be inaccurate, if the spectral shape of an observed SEP event is not taken into account in the method. In case the response curve is box-shaped, i.e. almost constant over the full primary energy range of a DPI, then an averaged response factor will be valid for almost all spectral indices of different SEP events. However, if the response curve shows a dependency on the primary energy, as shown for illustration in fig. 9.4, then the method to calculate the averaged response factor needs to take the spectral index into account. Fig. 9.4 shows the response curve of the second DPI of the NOM_HETP_p Data Product (DP) for a power law spectral shape with a spectral index of -1. The primary energy distribution of an SEP event is often power-law shaped and shows spectral indices between -1 to -3 (Kühl and Heber, 2019; Mewaldt et al., 2005). In case of HET two different approaches to calculate the flux from the measured counts in the individual data product items used, which are described in the next section. Both methods are able to take the spectral index into account.

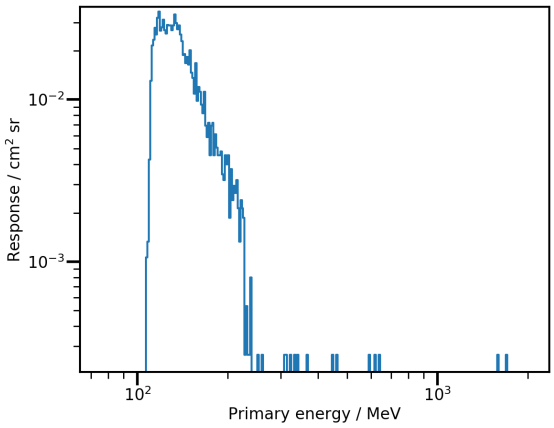

Figure 9.4: In this figure the response of the second bin of the NOM_HETP_P DP is shown. The response of the DPI decreases towards higher energies and thus an averaged geometrical factor is highly depending on the spectral index used to calculate the response spectrum.

9.2.1 Response factors for data products

For HET, two different approaches are provided to calculate particle flux based on the measured counts of a DPI. For a most accurate and flexible calculation of responses, a so called "response matrix" is supplied, containing the energy

dependent responses of a certain DPI for each of the 1720 logarithmic primary energy bins. In order to find the correct primary particle spectrum, the matrices can be weighed with different input spectra until the best matching spectrum is identified. However, based on the method, different averaged response factors and energy ranges of the individual DPIs will be derived. This can lead to complications when two HET spectra, derived with two different methods from the response matrices are compared. Thus, additionally to the response matrices, the energy ranges, averaged and averaged response factors for the HET DPIs are calculated and supplied using a unified method.

Response matrices

One example response matrix is given in fig. 9.5 for illustration. The low latency ABnC and ABC proton data products are used for illustration. Since the total number of the covered LL DPIs is only 12, it is suited better for the illustration of the response matrices compared the nominal proton DPs, which contain a total of 36 DPIs for ABnC and ABC. In the example response matrix, shown in fig. 9.5, for each proton LL DPI, the response depending on the primary energy bin is shown. Almost all DPIs show an equidistant primary energy coverage bin width in log space, except for the first ABC LL DPI. In sec. 7.3.3 the ABnC proton histogram is explained and the observed energy gap between the ABnC and ABC trigger, mainly due to the lower detection limit of the crystal is discussed in detail in sec. 7.3.3. These response matrices are available for all data products, low latency, nominal and burst, so the responses of each DPI can be adjusted to the best fitting and thus observed primary energy spectrum in space.

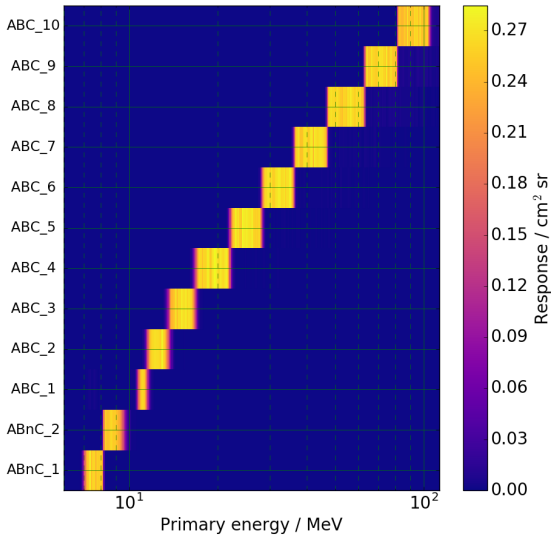

Figure 9.5: Example response matrix for protons with a power law spectrum with an index of -1. The response for all low latency stopping data products (ABnC,ABC) is given.

Data product characterization

Additionally to the response matrices, a unified method to define the energy range and calculate the effective (averaged) responses of a DPI is used. The method, developed by Lara (2019), is able to define the energy range as well as the effective response of a DPI. From the response matrices, these values can be calculated, however, different methods will yield different results for the same DPI of HET, so that a direct comparison of the resulting particle fluxes can be difficult. Thus, the aim is to provide a unified method and characterizing each DPI by four values: the lower energy limit E_{low} and the upper energy limit E_{high}, the effective response factor $\bar{r}$ and an effective energy, E_{eff}. E_{eff} represents a reference energy of the channel, that is used for comparisons to model functions or to fit the resulting flux to obtain an SEP event spectrum. The energy range and the effective response factors are independent of the spectral index. The method is developed by Lara (2019) but is given here for completeness and with additional information.

Each DP provides a count rate C of a given particle type p as a function of its energy E, by providing N energy channels (DPIs). The count rate of a given DPI (i) in a time interval Δt is depending on the response factor r_i(E) and on also the energy dependent particle intensity I_p(E) that, for simplicity, is supposed to be constant over time. This relation is given in eq. 9.5:

$$C_i = \Delta t \int_0^{\inf} I_p(E) r_i(E) dE + \sigma \text{ for } i \in \{0, ..., N-1\} \tag{9.5}$$

σ represents the noise of the channel and counts from other particle species that the channel is not designed for (Lara, 2019). Equation 9.5 can be reduced by introducing upper and lower energy limits, E^i_{high} and E^i_{low}, of a given DPI and an effective response factor $\bar{r_i}$. With this, eq. 9.5 changes to eq. 9.6:

$$C_i = \Delta t \Delta E_i \bar{r_i} I_p(E^{(i)}_{eff}) \tag{9.6}$$

with $\Delta E_i = \mathrm{E}^i_{high}$- E^i_{low} and the particle intensity $I_p(E^{(i)}_{eff})$ at an energy $\mathrm{E}^{(i)}_{eff}$ which is preferably contained in the interval [E^i_{low},E^i_{high}] (Lara, 2019). Thus, $\mathrm{E}^{(i)}_{eff}$ represents the weighted mean energy of a DPI. However, $\mathrm{E}^{(i)}_{eff}$ depends on the spectral response of the DPI, its defined energy limits but also on the spectral shape (spectral index) of the particle intensity, as will be shown later.

Energy limits

The energy limits of a given DPI for HET are defined in such a way, that two adjacent DPIs (i and i+1) do not overlap in primary energy coverage, so that $\mathrm{E}^i_{high} = \mathrm{E}^{i+1}_{low}$. The definition of this value is chosen to be where the two adjacent channels have the same response value. For the first and the last channel the energy limit is defined to be at 50% of the maximum spectral response of the channel.

Effective response factor
The effective response factor $\bar{r_i}$ is defined as an average of the spectral response in logarithmic energy integrated over the full energy range, 0 to infinity, where infinity is the maximum and 0 the minimum of the simulated primary energy range, as given in eq. 9.7:

$$\bar{r_i} = \frac{1}{\Delta \log E_i} \int_0^{\inf} r_i(E) E^{-1} dE = \frac{1}{\Delta \log E_i} \int_1^{\inf} r_i(E) d \log E \tag{9.7}$$

By integration of r_i(E) over the full primary energy range, the complete response of a given DPI is taken into account for the calculation of the effective response $\bar{r_i}$. $\Delta \log E_i$ is the energy range of the DPI in logarithmic energy, $\log(\mathrm{E}^i_{high})$ - $\log(\mathrm{E}^i_{low})$ (Lara, 2019).
Effective energy
Most SEP events can be described over a wide energy range using a power law dependency of the intensity I (Mewaldt et al., 2005, 2007). In this case, the intensity I shows a power law dependency on the energy E with a spectral index γ. The intensity at the reference energy E_0 is given as I_0, as given in eq. 9.8. With this definition of the intensity I given in eq. 9.8, the intensity in eq. 9.5 can be substituted. This results resulting in eq. 9.9, neglecting the contamination σ for simplicity.

$$I = I_0 \left(\frac{E}{E_0} \right)^{\gamma} \tag{9.8}$$

$$C_i = \Delta t I_0 E_0^{-\gamma} \int_0^{\inf} I_p(E) r_i(E) E^{\gamma} dE \tag{9.9}$$

Combining eq. 9.9 with eq. 9.6, eq. 9.10 is obtained.

$$\bar{r_i} \Delta E_i = E_0^{-\gamma} \int_0^{\inf} r_i(E) E^{\gamma} dE \tag{9.10}$$

Solving eq. 9.10, for the reference energy E_0, yields eq. 9.11:

$$E_0 = \left(\frac{1}{\bar{r_i} \Delta E} \int_0^{\infty} r_i(E) E^{\gamma} dE \right)^{(1/\gamma)} \tag{9.11}$$

Combining eq. 9.9 and eq. 9.10 and the fact that $I_0 = I_p(E_0)$, results in the fact that the reference energy E_0 of the power law spectrum is identical to the effective energy E_{eff} of the DPI. Thus, in order to calculate the flux obtained from a given DPI at a reference energy E_0, E_eff, as given in eq. 9.12 needs to be used (Lara, 2019).

$$E^i_{eff,\gamma} = \left(\frac{1}{\bar{r_i} \Delta E} \int_0^{\infty} r_i(E) E^{\gamma} dE \right)^{(1/\gamma)} \tag{9.12}$$

According to eq. 9.12 $E^i_{eff,\gamma}$, depends on the spectral index γ of the given power law and also on the defined energy range of the channel ΔE_i and the effective response $\bar{r_i}$. The integral can be solved numerically using the response $r_i(E)$ of the respective data product item.
With this method by Lara (2019), each DPI can be fully described using the obtained energy range, E^i_{low} - E^i_{high}, the effective response factor, $\bar{r_i}$ and the effective energy $E^{(i,\gamma)}_{eff}$, which is depending on the spectral shape of the measured spectrum. For a spectral index of γ=-1, $E^i_{eff,-1} = \Delta E_i / \Delta \log E_i$ which is the logarithmic mean of the primary energy range of the DPI from E^i_{low} to E^i_{high}.
To give one example, for the two ABnC low latency data product items the energy range and the response factors, as well as the effective energy for power law spectral shape with a spectral index of -1 are given in tab. 9.2. The counts of these two DPIs, received from HET, could thus be directly converted into a particle flux and mapped to an energy range and an effective energy e.g. for comparison with other instruments.
A complete list of all HET DPI energy ranges, responses and effective energies for low latency, nominal and burst are given in the appendices in sec. A.1. In tables 9.3,9.4 and 9.5, a summary of the data products, defined in the scope of this thesis is given. The tables includes the energy ranges for the data products, as calculated with the effective response method given in this section. The cadences are given for the far mode and the conversion to close mode is given by: 5s:1s, 30s:5s, 60s:30s, 300s:60s, 600s:300s. These tables summarize the full capabilities of the HET instrument, as developed in the scope of this work.
The numerically calculated response factors, as given in sec. A.1, can be compared to the analytically determined geometrical factors, given in table 9.1. For the ABnC and ABC trigger, an analytical value of 0.271 cm^2 sr is calculated. The numerical value is ≈0.26 cm^2 sr for the ABnC and ≈0.27 cm^2 sr for the ABC trigger, for the LL proton data products. Both values agree well, within 5%, with the analytically calculated value. For the penetrating trigger, the analytical value of 0.044 cm^2 sr a higher deviation with the numerically calculated value between 0.3 - 0.4 cm^2 sr is observed. In this case, the response functions are highly primary energy dependent. This effect is not taken into account for the analytically calculated value, so that it yields higher results. For the GCR trigger, a analytical value of 0.77 cm^2 sr is calculated. The numerically calculated value is lower by ≈10%. Again, the response functions are depending on the primary energy of the particle, which is not taken into account for the analytically calculated value. Overall all analytically calculated values compare well to the numerically calculated values. However, in all cases the numerically calculated value is lower due to the consideration of the onboard data processing of HET, which may sort out particles with "correct" trajectories due to restrictions of the onboard data processing related to processes like ion fragmentation, secondary particle production. Additionally, the scattering of particles is also taken into account in the

Bin nr.	E_{low} / MeV	E_{high} / MeV	$\bar{r_i}$ / cm^2 sr	E_{eff} / MeV
1	6.95	8.19	0.261	7.66
2	8.19	9.61	0.257	8.88

Table 9.2: Effective response $\bar{r_i}$, the energy range and the effective energy,E_{eff}, of the low latency ABnC DPIs for protons. E_{eff} is determined for a power law spectra with a spectral index of -1. The given numbers are calculated according to the described procedure.

numerically calculated values. Thus, at this point it can be concluded that the method to calculate the effective response factors, using the method described in Lara (2019) provides valid results that are comparable to those of the analytic calculation.
In the following chapter 10, the capabilities of HET for the detection of SEP events are illustrated using the defined data products and the according calculated values for the effective energy, the response and the energy range of a given DPI.

Species	ABnC		ABC		Penetrating
	1D	2D	1D	2D	2D
e^-					
Energy range / MeV/nuc	0.45–9.0	–	1.0–18	–	–
Cadence / s	5	–	5	–	–
# of DPIs	1	–	3	–	–
H					
Energy range / MeV/nuc	7.0–9.6	–	11–105	–	105–∞
Cadence / s	30	–	30	–	60
# of DPIs	5	–	31	–	7
He^3					
Energy range / MeV/nuc	8.3–11	8.1–10	–	13–40	–
Cadence / s	300	60	–	60	–
# of DPIs	6	4	–	5	–
He^4					
Energy range / MeV/nuc	7.1–9.5	6.9–8.4	–	11–104	104–∞
Cadence / s	300	60	–	60	300
# of DPIs	6	4	–	11	7
C, N, O					
Energy range / MeV/nuc	–	13–19	–	22–235	200–∞
Cadence / s	–	600	–	300	600
# of DPIs	–	3 x 5	–	3 x 12	10
Ne, Mg, Si, S					
Energy range / MeV/nuc	–	16–26	–	29–359	358–∞
Cadence / s	–	600	–	600	3600
# of DPIs	–	4 x 5	–	4 x 11	7
Ar, Ca, Fe, Ni					
Energy range / MeV/nuc	–	20–34	–	36–496	466–∞
Cadence / s	–	600	–	600	600
# of DPIs	–	4 x 5	–	4 x 11	Fe: 7

Table 9.3: Summary of the energy ranges of the most recent HET configuration version V0008 for the HET nominal data products. The list of the individual energy ranges of data product items is given in appendices in sec. A.1. The cadences are given for far mode.

Species	ABnC		ABC		Penetrating
	1D	2D	1D	2D	2D
e^-					
Energy range / MeV/nuc	0.45–9.0	–	1.0–18	–	–
Cadence / s	30	–	30	–	–
# of DPIs	1	–	3	–	–
H					
Energy range / MeV/nuc	7.1–9.6	–	11–105	–	105–∞
Cadence / s	30	–	30	–	30
# of DPIs	2	–	10	–	6
He^3					
Energy range / MeV/nuc	8.3–11	8.4–10	–	13–40	–
Cadence / s	300	300	–	300	–
# of DPIs	4	2	–	4	–
He^4					
Energy range / MeV/nuc	7.1–9.5	7.1–8.6	–	11–104	104–∞
Cadence / s	300	300	–	300	300
# of DPIs	4	2	–	8	6
C, N, O					
Energy range / MeV/nuc	–	13–18	–	31–234	200–∞
Cadence / s	–	600	–	600	3600
# of DPIs	–	3 x 2	–	3 x 3	6
Fe					
Energy range / MeV/nuc	–	24–32	–	40–465	511–∞
Cadence / s	–	600	–	3600	3600
# of DPIs	–	2	–	3	2

Table 9.4: Summary of the energy ranges of the most recent HET configuration version V0008 for the HET low latency data products. The list of the individual energy ranges of data product items is given in appendices in sec. A.1.

Species	ABnC		ABC		Penetrating
	1D	2D	1D	2D	2D
e^-					
Energy range / MeV/nuc	0.45–9.0	–	1.0–18	–	–
Cadence / s	1	–	1	–	–
# of DPIs	1	–	3	–	–
H					
Energy range / MeV/nuc	7.0–9.8	–	11–105	–	105–∞
Cadence / s	1	–	1	–	1
# of DPIs	6	–	62	–	7
He^3					
Energy range / MeV/nuc	8.3–11	8.1–10	–	13–40	–
Cadence / s	1	5	–	5	–
# of DPIs	4	4	–	5	–
He^4					
Energy range / MeV/nuc	7.1–9.5	6.9–8.4	–	11–104	104–∞
Cadence / s	1	5	–	5	5
# of DPIs	4	4	–	11	7

Table 9.5: Summary of the energy ranges of the most recent HET configuration version V0008 for the HET burst data products. The list of the individual energy ranges of data product items is given in appendices in sec. A.1.

10. SEP event analysis using HET

HET is designed to measure energetic particles, i.e. electrons, protons and multiple heavy ion species, over a wide energy range. With this, HET supports the investigation of SEP events and their origin and can also support the investigation of other phenomena, like transport effects as described in chapter 4. Because of the telemetry limitations of the Solar Orbiter mission, the onboard data processing, as described in chapter 7 is developed. The particle is analyzed by one of the different HET level 3 triggers and added to a species specific histogram. From these histograms, the number of detected particles in a defined histogram bins are summarized in form of the pre-defined DPIs and provided for further investigation. For HET, two different methods are provided to calculate the particle flux determined by each Data Product Item (DPI) from the measured counts. These methods are explained in sec. 9.2.1. The first method, is the use of response matrices. These matrices contain the response of a DPI to a certain particle species depending on its primary energy. The response matrices can be weighted for different spectral indices to achieve the best-fitting result to the observed SEP event or background spectrum. However, in practice mostly averaged responses and pre-calculated energy ranges for the calculation of the particle flux for a certain DPI is used. Thus, additionally to the response matrices, a method is introduced in sec. 9.2.1, to derive the energy range and effective responses of the DPIs. With this method, the particle flux can be calculated directly, as effective response and the energy range of a channel are already derived. Only the effective energy E_{eff} needs to be adapted depending on the spectral shape of a measured particle event or the background spectrum. In this chapter, the method itself is validated and its uncertainties are derived.
Additionally various SEP event spectra, either similar to typical SEP spectra or based on measurements of individual SEPs are used to examine the capabilities of HET. In the first section of this chapter, the method for this purpose is introduced and illustrated using an artificial proton SEP event. The term "artificial" refers to the fact that this event has never been measured in reality and the intensity of the SEP event, is arbitrarily chosen in this case. However, the spectral shape of the SEP event is comparable to observed SEP events.

After the introduction of the method, an actual SEP event from the time period spanning from late October to early November 2003, as reported in Mewaldt et al. (2005) is used to test the capabilities of HET for real events. Finally, another artificial SEP event, covering all ion species which HET is designed for, is used to present the full capabilities of HET.

10.1 HET fluxes based on simulated proton power law spectra

This section gives a description of the method how a particle flux during an SEP event is calculated into the expected counts of the different DPI of HET. From these counts the flux of the particles is reconstructed using the method by Lara (2019) described in sec. 9.2.1.
To illustrate the method that shall be used to present the capabilities of HET, protons, the most common SEP particles are used. SEP spectra can often be approximated by a power law in the MeV energy range (e.g. Mewaldt et al., 2007). Thus, for the illustration of the method the particle flux I(E), depending in the primary energy E is given by eq. 10.1:

$$I(E) = CE^{-\gamma} \tag{10.1}$$

For this, C defined as 1e5 particles / (cm^2 sr (MeV/nuc)^2) and γ, the spectral index of the SEP event to $\gamma = -1$. Using these values the particle flux for a given energy is calculated using eq. 10.1, as shown in fig. 10.1, where the particle flux for this SEP event is shown in blue. This proton flux represents the integrated particle flux over the whole SEP event duration, often named fluence spectrum, and is thus given in units of particles / (cm^2 sr MeV/nuc) and has no time dependency.
By using the derived response matrices, the counts in each DPI can be calculated. Each response matrix contains the response for a single DPI for 1720 logarithmic spaced bins. Thus, the flux given by eq. 10.1 is integrated for each of the 1720 primary energy bins. By folding the response matrix with the obtained particle flux in each primary energy bin, the number of counts depending on the primary energy bin is obtained. The sum of these counts represent the total number of counts measured by the DPI for the observed SEP event. The integrated particle flux for each primary energy bin is shown in fig. 10.1 in green. As expected, the integrated flux in a logarithmic bin for a power law with an index of -1 is constant. The 1720 primary energy bins offer a resolution of 64 bins per octave. This means, that between a certain logarithmic primary energy value and twice of this logarithmic value, there are 64 logarithmic spaced bins. Thus the spanned primary energy of each primary energy bin is small compared to the absolute

primary energy of the bin and therefore the effect of the spectral shape within each primary energy bin is considered negligible.
The number of counts in each DPI for this artificial particle event are shown in fig. 10.2 in blue for all available nominal proton DPIs (ABnC, ABC and penetrating), except for the last DPI of the penetrating trigger containing the minimal ionizing particles. Due to the fact, that there is no maximum energy of this channel (integral channel), no energy range can be defined and thus this channel is not suited for this illustration. The displayed energy range for each DPI is obtained from the method described in sec. 9.2.1 by Lara (2019) and the 'x' is the calculated geometric mean of the energy range of respective DPI. Some of the DPIs in fig. 10.2 show only a low amount of counts. For these DPIs the covered primary energy range is small and the response is lower, compared to other DPIs. This combination leads to a lower amount of counts compared to other DPIs from the same trigger class. The dashed lines in fig. 10.2 represent the energy regimes of the different triggers: The ABnC and ABC regimes are separated by the black dashed line while the ABC and penetrating trigger energy regimes are separated by the red dashed line.

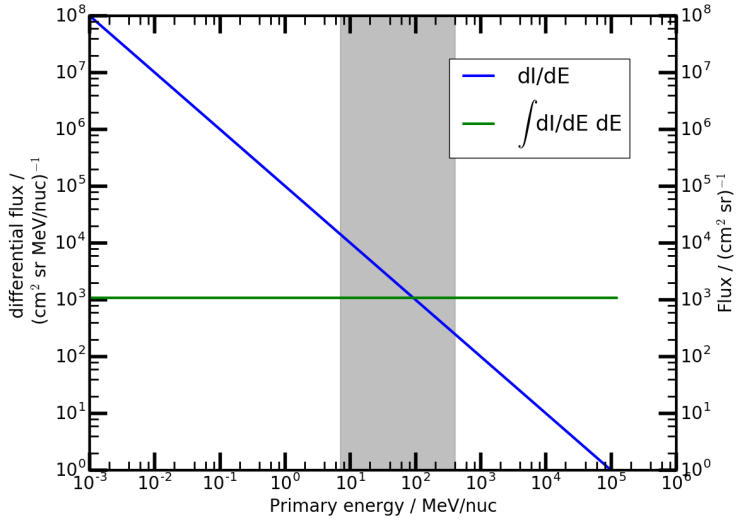

Figure 10.1: The blue line is the particle flux of the artificial proton event with a spectral index of -1. Integrating the flux for the 1720 logarithmic spaced energy bins, the green line is derived, containing the particle flux in a given primary energy range. The gray area represent the nominal energy range of HET for protons excluding the integral channel for relativistic protons.

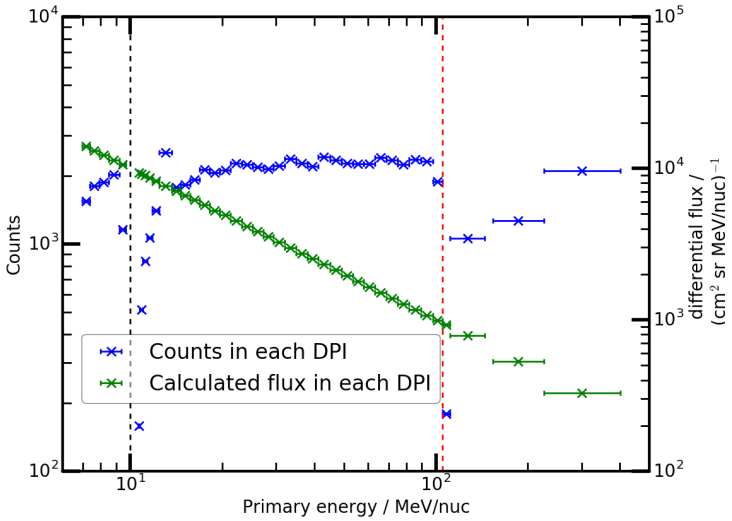

Figure 10.2: From the integrated particle flux in a given primary energy range, the number of counts in a each nominal proton DPI for the ABnC, ABC and penetrating trigger is calculated. These are shown in blue. Applying the calculated effective response factors and energy ranges obtained by the method described in sec. 9.2.1, the particle flux is obtained and is shown in green. The black dashed line separates the ABnC and the ABC energy regimes and the red dashed line separates the ABC and the penetrating trigger energy regimes.

To calculate the particle flux in each DPI, based on the observed counts, the effective response factors calculated with the method described in sec. 9.2.1 by Lara (2019) are used. The calculated flux is shown in fig. 10.2 in green. To estimate the uncertainty that is introduced by using the effective response factors and the geometrical mean of the energy bin range of a DPI, the calculated particle flux is compared to the input spectrum, given in eq. 10.1. The result is shown in fig. 10.3 (a), which shows the model flux in green and the calculated flux in each HET DPI in blue. The relative deviation, shown in the second panel of fig. 10.3 (a), is calculated by subtracting the model flux from the calculated flux and dividing the results by the model flux: $(I_{calc}\text{-}I_{model})/I_{model}$. The value for the model flux, as given in eq. 10.1, is calculated for the energy of the geometrical mean of the primary energy range of the DPI, marked by the 'x' in fig. 10.3 (a). The result shows, that using the provided effective response factors in combination with the calculated energy ranges and the according geometrical mean of this energy range is well suited to reconstruct the model function. The induced maximum systematic uncertainty of ≈1% for the penetrating particles results from the large primary energy ranges of these DPI and the spectral dependence of the response. The result is further improved by using the effective energy of the DPI obtained from the method described in Lara (2019), as shown in fig. 10.3 (b) so that the maximum deviation is reduced to <1%.

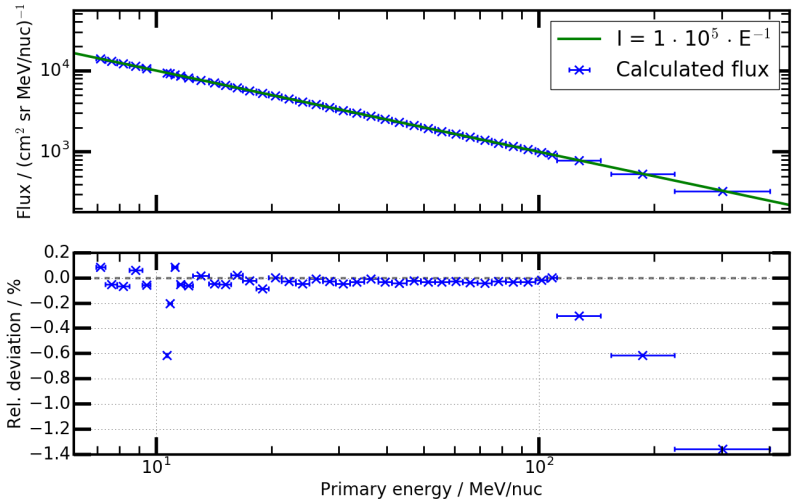

(a) Comparing the calculated particle flux,for each of the DPIs with the model function of the artificial proton event, a good agreement is found. The energy of each DPI, marked by the "x" is calculated using the geometrical mean of the energy range of a given DPI.

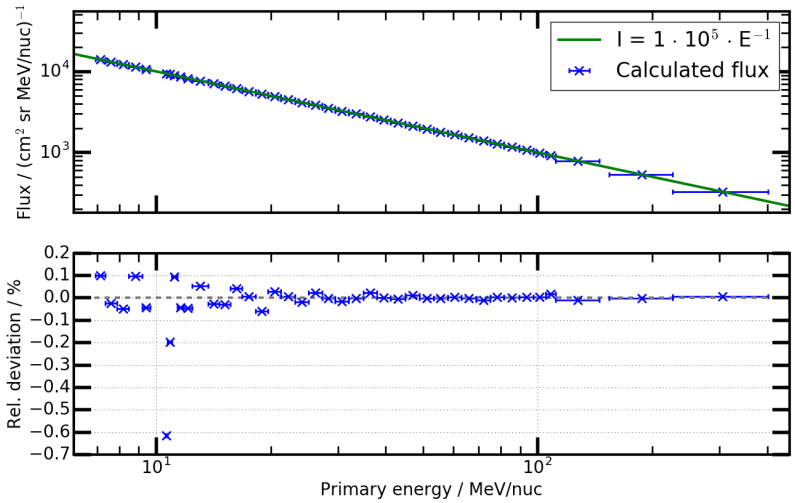

(b) Using the effective energy of each channel, instead of the geometrical mean of the energy width of the channel, the result is further improved.

Figure 10.3: Comparison of the input flux, of the artificial proton event with a spectral index of -1, with the calculated "measured" flux in each HET proton DPI.

The geometrical mean of the DPI primary energy range can only be used for DPIs which show a box-like response or for spectra which resemble a power law with an index of -1. The term "box-like" refers the shape of the response of a DPI. If this is almost constant over the primary energy range covered by the DPI, the response can be considered as "box-like" as the response plotted versus the primary energy range resembles a rectangular box.
The advantage of the method described in sec. 9.2.1 is, that only the effective energy E_{eff} of a DPI needs to be altered in order to match the measured particle energy distribution. The energy range of a DPI and the effective response factor do not need to be altered for different spectral indices. However, to illustrate the necessity to use the correct effective energy for the measured spectrum an SEP event with a different spectral index is used. For this second test case, the spectral shape of the simulated SEP event is given by eq. 10.1. A spectral index γ = -3 is used and the intensity C is identical to the first test case with C = 1e5 particles / (cm^2 sr $(MeV/nuc)^2$). The effective energies, that are used for the illustration are calculated as given in eq. 9.12 in sec. 9.2.1 with the method by Lara (2019). By repeating the same steps as in the first test case, calculating the counts in each DPI and from this calculating the measured flux in each DPI, the flux as given by the model and the measured flux of each DPI can be compared.This is shown in fig. 10.4 (a), in which the flux obtained from the model function and the reconstructed flux is shown. In fig. 10.4 (a), the effective energies for a spectral index of -1 are used, indicated by the 'x' for each DPI, although the spectral index of the model function is defined as γ = -3. While the deviation for some DPI, which show a box-like response function, is still low, some DPIs, especially the DPIs for penetrating particles at high energies, show a large deviation from the model flux when using the wrong effective energies. For these DPIs the response is highly depending in the primary energy of the particle, so that the calculated value of $E^i_{eff,\gamma}$ is depending on the spectral shape. This is further illustrated in tab. 10.1, where the effective energies, E_{eff} for three spectral indices and additionally the geometrical average of the energy range of two selected DPIs is given. As an example for a DPI with a box-like response, the ninth bin of the NOM_ABC_p is used. In this case, the effective energy is not affected by the spectral index. However, E_{eff} of the second DPI of the NOM_HETP_p DP is affected. The response of this DPI declines towards higher energies, which causes the dependence on the spectral index to calculate E_{eff}. In both cases, the geometrical mean of the energy range of the given DPI is in good agreement with the effective energy for a spectral index of -1. For DPIs, which show response dependence on the spectral shape, it is important to use the correct effective energy E_{eff}. The spectral shape of an SEP, can be obtained using DPIs which do not show a high dependence on the spectral shape, e.g. the ABC DPIs.

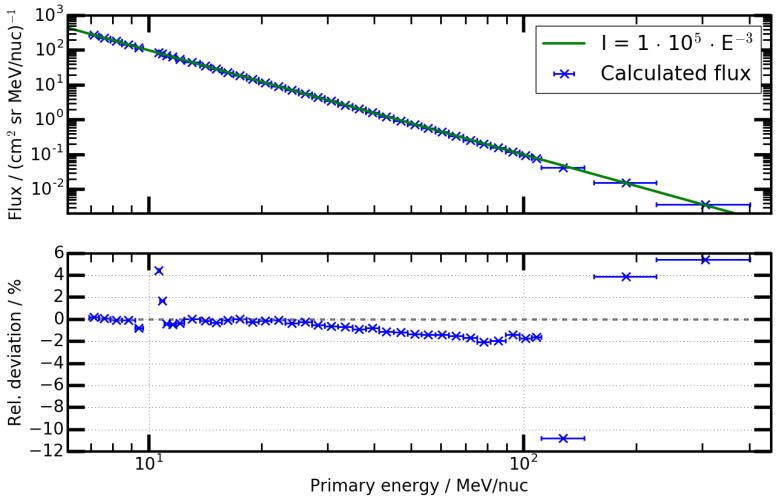

(a) Using the wrong effective energies of a DPI can lead to high deviations from the model function when calculating the particle flux. In this case, the effective energies for a spectral index of -1 have been used for an event with a spectral index of -3.

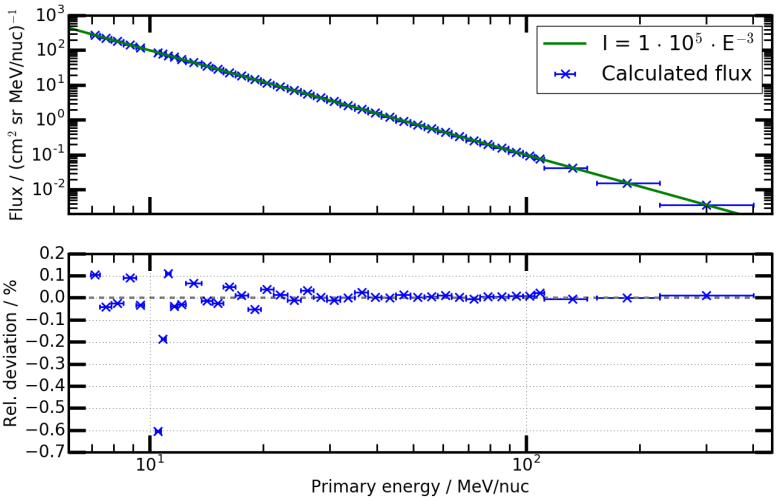

(b) Using the correct effective energy, in this case for a spectral index of -3, the deviation can be reduced to <1%. In reality the spectral index is unknown but can be iteratively identified using the DPIs for which the responses are almost unaffected by the spectral index.

Figure 10.4: An artificial proton event with a spectral index of -3 is used to illustrate the necessity to use the correct effective energy according to the spectral index of the observed spectrum.

DPI	geom. mean / MeV	E_{eff} (γ = -1) / MeV	E_{eff} (γ = -2) / MeV	E_{eff} (γ = -3) / MeV
NOM_HETP_p_2	127.0	127.3	131.8	132.3
NOM_ABC_p_9	16.2	16.2	16.2	16.2

Table 10.1: For two selected DPIs the effective energies E_{eff} for different spectral indices are given. For a spectral index of -1, E_{eff} is comparable to the geometrical mean of the DPIs energy range. The penetrating proton DPI shows a higher dependence in the spectral index compared to the ABC proton DPI.

Therefore in fig. 10.4 (b) the effective energies for a spectral index of -3 are used, which are the correct effective energies for the measured SEP event spectrum with a power law index of -3. This illustrates, that the high deviations observed for some of the DPIs in fig. 10.4 (a) are reduced to <1%. Thus, when the effective energies which are appropriate for the observed spectral index are used a good agreement between the model and the calculated flux is found for all DPIs. Of course, the given sample event is a best case study, as it assumed that contamination by e.g. secondary protons created by heavier ions due to interaction with the housing is already corrected for and statistical uncertainties, e.g. poisson noise is neglected. However, by neglecting these effects, the accuracy of the effective response model for HET itself is studied and its uncertainties can be determined.

10.2 HET flux calculation for a real SEP event spectrum

During a very active period of the Sun during end of October until beginning of November 2003, more than 40 coronal mass ejections, several solar flares and 5 very large SEP events have been observed (Mewaldt et al., 2005). Mewaldt et al. (2005) used different instruments, ULEIS, EPAM and SIS onboard ACE, PET on SAMPEX and EPS on GOES-11 to determine the particle flux of 5 selected events at 1 AU. All five SEP events show a spectral shape in form of two power laws with different spectral indices. The transition between the two power laws is located in the energy range of HET, which makes them interesting for a further investigation with HET. One of the five events, the event with the lowest overall particle flux for the three ion species, is selected for a further evaluation using HET.
In fig. 10.5 the integrated particle flux spectra for proton, helium and oxygen ions are shown. The fluence is calculated by integrating the particle flux over the whole time period of the event, from 21:00 on the 2003-11-04 to 12:00 2003-

11-07 (Mewaldt et al., 2005). For all three ion species, the spectral index at low energies is around ≈-1.5 while at high energies the spectral index is around ≈-4.7 (Mewaldt et al., 2005). Mewaldt et al. (2005) use a so called "Band-function" (Band et al., 1993) given in eq. 10.4 to describe the double power law shape of the spectrum.

$$dJ/dE = CE^{\gamma_a} \exp(-E/E_0) \text{ for } E \leq (\gamma_b - \gamma_a)E_0 \quad (10.2)$$

$$dJ/dE = CE^{\gamma_b} \left\{ [(\gamma_b - \gamma_a)E_0]^{\gamma_b - \gamma_a} \exp(\gamma_a - \gamma_b) \right\} \quad (10.3)$$

$$\text{for } E > (\gamma_b - \gamma_a)E_0 \quad (10.4)$$

The parameters derived by Mewaldt et al. (2005) for this event are given in tab. 10.2.
Using the method described in sec. 10.1, it can be investigated if and with which uncertainties HET would have measured the SEP event spectrum shown in fig 10.5 as obtained by Mewaldt et al. (2005). In fig. 10.6, the model particle flux, as determined by Mewaldt et al. (2005) are compared to the calculated particle flux of the HET proton DPIs. Analog to the procedure presented in sec. 10.1, first the counts for each DPI are calculated and then the effective response factors as well as the effective energy from method described in sec. 9.2.1 are used to calculate the fluxes in the individual DPIs.
Since in reality the determination of the spectral indices in the transition region between the two power laws is difficult, here the spectral indices as given

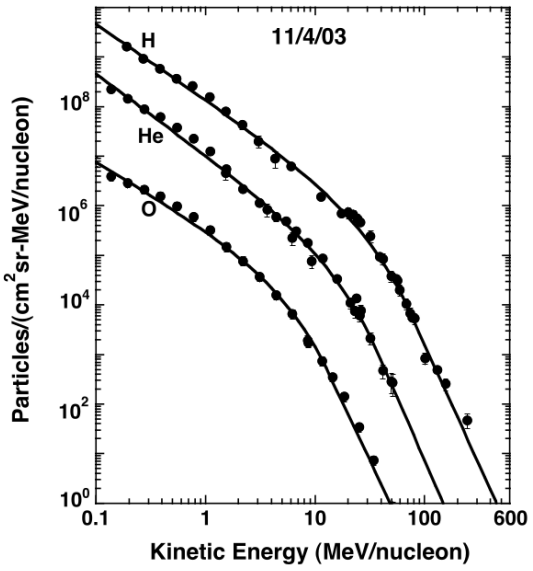

Figure 10.5: Fluence spectra for H, He and O. Using the Band-function, as given in eq. 10.4, the SEP spectrum can be fully described. Figure from Mewaldt et al. (2005).

Ion	C / (cm^2 sr $(MeV/nuc)^2$)	γ_a	γ_b	E_0 / MeV/nuc
H	1.40x10^8	-1.52	-4.86	21.7
He	1.09x10^7	-1.62	-5.06	11.2
O	3.77x10^5	-1.32	-4.65	3.90

Table 10.2: Parameters for the 2003-11-04 SEP event for the different ion species as given by Mewaldt et al. (2005). The parameters can be used in combination with eq. 10.4 to calculate the energy dependent flux of the particle event.

in tab. 10.2 are used, even for the transition region. In reality, the model flux is not known and adjusting the effective energies for each DPI in the transition region would thus not be representative. Therefore, for the last twelve DPIs, the effective energy for a spectral index of γ_b = -4.86 is used and for the other DPIs, the effective energy for a spectral index of γ_a = -1.52 is used. The transition region for this SEP event is between $\approx$ 6 to 60 MeV/nuc. Since the responses of the DPIs in this energy range are all almost box-like, the deviation from the model flux, shown in the lower panel of fig. 10.6 is low. However, an exact determination of the two spectral indices using only HET in case of this event is not possible. Especially in the lower energy range, additional particle instruments like EPD-STEP and EPD-EPT need to be used for an accurate determination of the spectral index, γ_a in the lower energy range. In the higher energy range, HET features several DPIs with box-like responses which can be used to determine the spectral index, γ_b for this SEP event.
In the lower panel of fig. 10.6 the relative deviation between the model function and the flux calculated for the HET DPIs is shown. The deviation for all DPIs is below 1% despite the fact, that the effective energies for the DPIs in the transition region between $\approx$ 6 to 60 MeV/nuc are chosen based on the spectral indices, γ_a = -1.52 and γ_b = -4.86, according to the model. All DPIs offer good counting statistics, so that the uncertainties in particle flux, $\sqrt{n_{DPI}}$, which are given in the upper panel of fig. 10.6 as y-error bars are not visible. Despite the double-power law shape of the spectrum, HET is able to cover and reproduce the spectrum including the transition between the two power laws remarkably well, using the effective response method. This shows, that the method is well suited even for more complex spectra and yields accurate and reliable particle flux values when using the correct effective energies and the according spectral index of the event. Of course, in reality, γ_a and γ_b need to be determined iteratively, as they are not known and HET needs to be supported by additional particle instruments in the lower energy range. Still, HET covers more than one order of magnitude in energy for protons and for this energy range it is well suited for the determination of particle fluxes, using the effective response method.

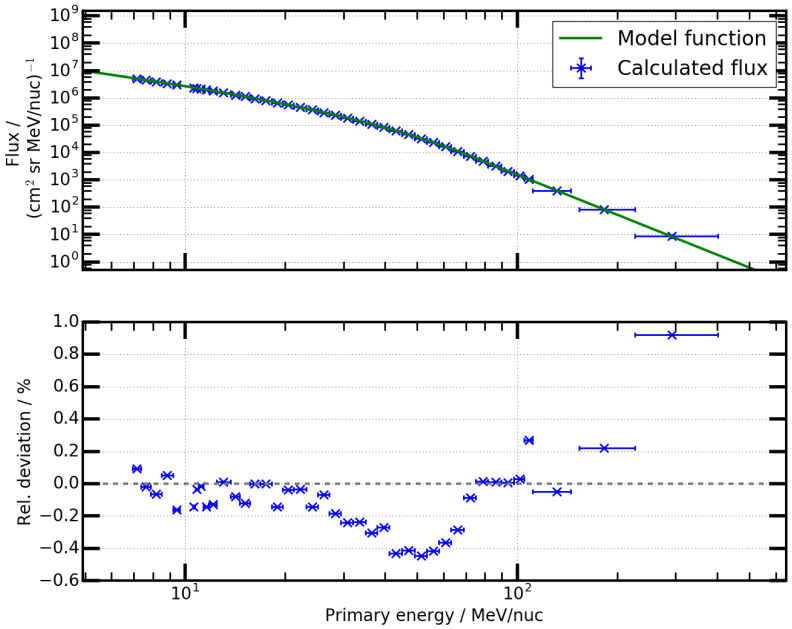

Figure 10.6: Comparing the fluence spectrum for protons obtained by Mewaldt et al. (2005) for the 11/04/03 event and the expected measured fluence spectrum by HET. The uncertainties are <1% as all DPI contain enough counting statistics for the fluence reconstruction despite the steep power law index of γ_b = -4.86. The model function is calculated using eq. 10.4 and the values given in tab. 10.2 for protons.

Performing the same method for the oxygen fluence spectrum, displayed in fig, 10.5, the result shown in fig. 10.7 is obtained. In this case, only a few DPIs of HET contain enough counts for the fluence spectrum reconstruction. The reason for this is the rather low maximum geometrical factor of ≈0.27 cm^2 sr of HET compared to other instruments in combination with the very steep power law index of γ_b = -4.65 for the high energy part of the spectrum. For comparison, the SIS instrument of ACE, used by Mewaldt et al. (2005) to determine the oxygen flux has a geometrical factor of 40 cm^2 sr, a factor of 150 higher compared to HET (Stone et al., 1998). However, in contrast to HET, SIS is specifically designed to measure ions heavier than protons and therefore the geometrical factor can be considerably larger without saturating the instruments electronics due to the detection of highly abundant protons and electrons. In HET, the geometrical factor is identical for the highly abundant electrons and protons and also for the rare heavy ions, so that the counting statistics for the latter are reduced. The bad oxygen counting statistics for the 2003-11-04 SEP event as measured by HET are visualized in the upper panel of fig, 10.5, by the y-error bars, given as $\sqrt{n}$, with n as the counts in the respective DPI. For the two last bins in the upper

panel, the uncertainty is 100%. However, these uncertainties do not illustrate the uncertainty of the used method to calculate the particle fluxes measured for each DPI, but the statistical uncertainties due to the bad counting statistics in case of this SEP event for oxygen ions measured at 1 AU distance to the Sun. In the second panel of fig. 10.7 the relative deviation from the model flux are displayed. Only up to ≈65 MeV/nuc the measured counts in the DPIs are sufficient to achieve a low deviation from the model flux.

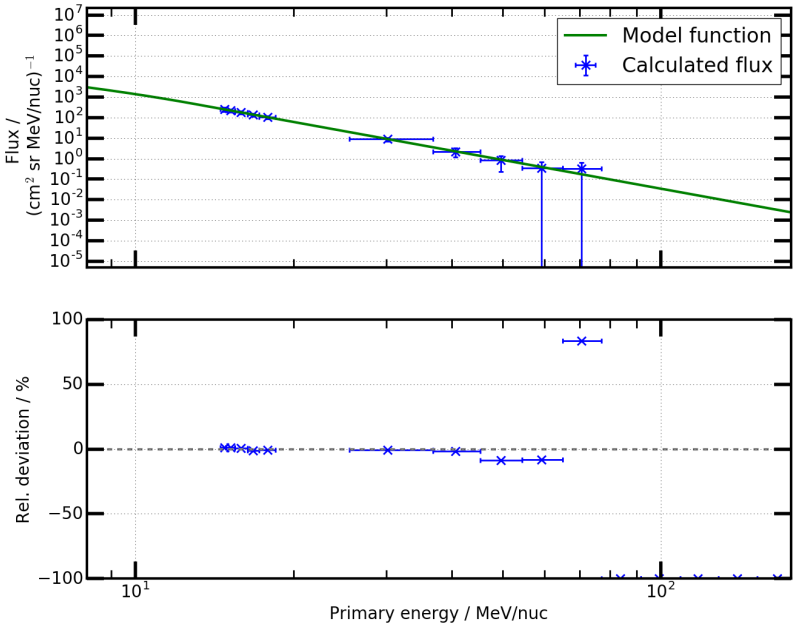

Figure 10.7: For oxygen, only the few displayed DPIs show enough counts for the event of the 11/04/03. Due to the low geometrical factor of HET in combination with the steep power law index of γ_b = -4.65, only a few counts are measured at high energies.

However, the obtained spectra, presented by Mewaldt et al. (2005) and thus their intensities are obtained at ≈1 AU from the Sun where the intensity of the event is decreased compared to distances closer to the Sun. When the SEP event is released from the Sun, its magnetic structure confines the event. During the outward movement of the particles, particles may escape the magnetic field lines by e.g. perpendicular diffusion or scattering. Thus the initially confined particles of the SEP event spread with radial distance. The measured flux thus decreases with radial distance to the Sun. According to Ruzmaikin et al. (2005) the radial intensity of a particle event depending in the distance from the Sun can be approximated by I≈1/r^3 i.e. at a distance of 0.5 AU the flux would be 8 times higher compared to 1 AU and at 0.27 AU, Solar Orbiters closest approach, the

flux would be approximately 13x higher.
As Solar Orbiter will approach the Sun more closely, the intensity of the SEP event can be scaled for other distances, to investigate the impact. In fig. 10.8 the oxygen spectrum of the SEP event is shown as measured at 0.5 AU by HET. With the increased particle intensity, more channels contain a statistically significant number of counts and the deviation of the higher energy channels (around 50 to 60 MeV/nuc) from the model is highly reduced. Thus, also for oxygen HET can be used to investigate this SEP event, although not all channels have statistically significant counts to support this study.

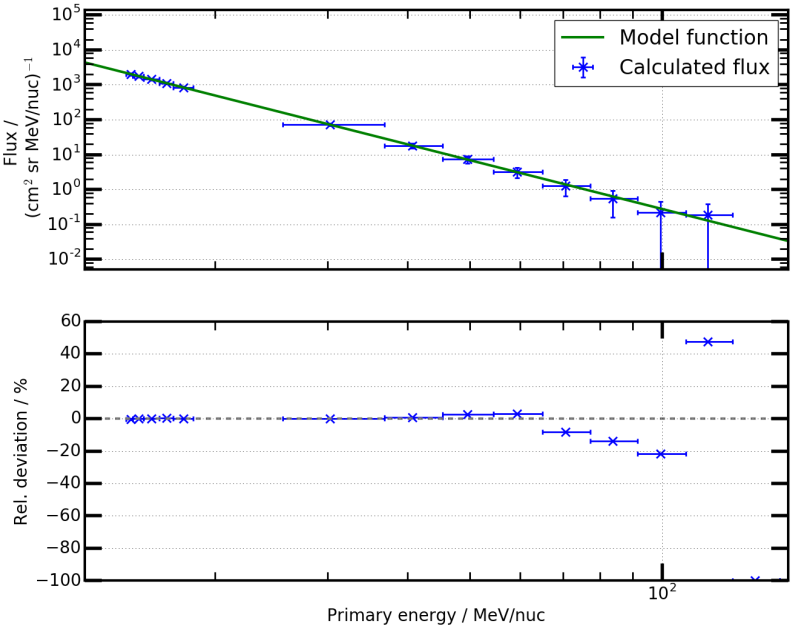

Figure 10.8: Scaling the event closer to the Sun, the particle fluence increases as $\approx 1/r^3$. Due to this, the number of counts increase and more DPIs can be used identify the spectral shape of the SEP event.

Another approach is to investigate the dependence of the spectral index for this SEP event. The spectral index of this SEP event at high energies of γ_b = -4.65 is rather steep. This is the second reason for the poor counting statistics in case of oxygen ions at high energies. In fig. 10.9, the 11/04/03 SEP event is shown with γ_b = -2 for comparison. In this case, all channels show a significant amount of counts and the overall deviation from the model is low.
To summarize the findings for oxygen ions as measured by HET during the 11/04/03 SEP event, it can be concluded that HET is not capable to determine the particle flux over its full energy range. However, during a closer approach to the Sun by Solar Orbiter, for the same event the covered energy range can

be extended and the capability to provide spectral information is also highly depending on the spectral index of the event, as has been illustrated.
Overall it can be concluded, that also for real SEP events, HET is capable of deriving the SEP spectrum for different ion species. However, due to the fact that HET offers only a single geometrical factors for all particle species, for some SEP events HET will not be able to provide spectral information over its full energy range for all ion species.

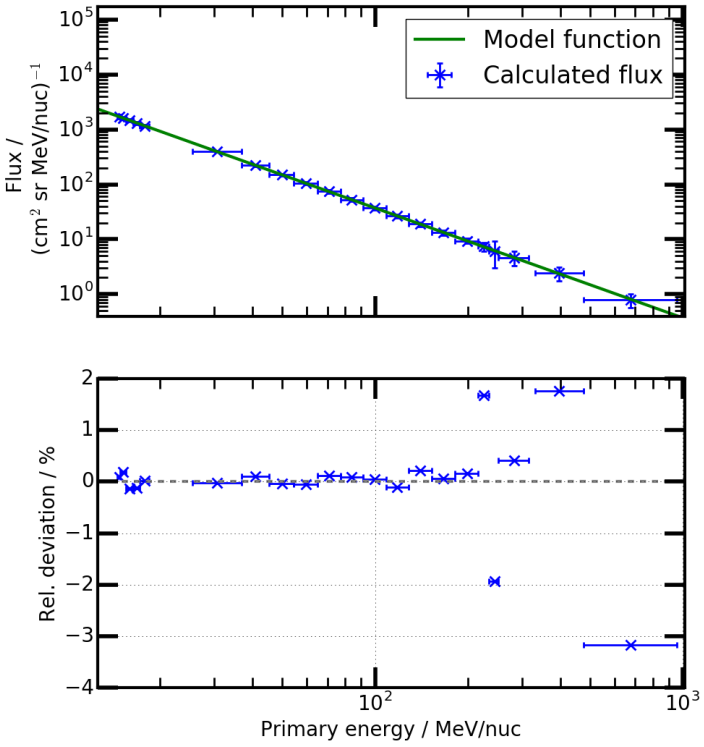

Figure 10.9: To illustrate the dependency of the oxygen ion counts measured by HET depending on the spectral index of the SEP event, the spectrum of the SEP event shown in fig. 10.8 is modified to a spectral index of γ_b = -2 at high energies, instead of -4.65. In this case, all oxygen DPIs show a statistically significant number of counts, so that a good agreement with the input model is found.

10.3 Simulated SEP event for all ion species

In this final part of this chapter, a simulated SEP event in which all ion species, which can be identified by HET is investigated. The artificial SEP event spectrum is described by a simple power law, with an arbitrary intensity C. For protons, the highest intensity is chosen. Based on this maximum intensity, the intensity for each subsequent heavier ion species, is decreased by a factor of 10, for the sake of visibility. The power law index for the event is defined as γ = -3. Figure 10.10 shows the combined result for all ion species. The figure does not only show that the method using the effective response, as derived in sec. 9.2.1, works for all ion species but fig. 10.10 is also well suited to summarizes the ion detection capabilities of HET in one single plot. At low energies, several DPIs for each ion species are obtained from the ABnC trigger. Due to the good ion species separation capabilities of the ABnC trigger, as shown in sec. 7.3.1, these DPIs can be provided for all the ion species, which are mainly abundant in SEP, H, He, C, N, O, Ne, Mg, Si, S, Ar, Ca, Fe and Ni, as given in Reames (2017). For all these ion species, at least 5 DPIs are provided by the ABnC trigger.
At higher energies, the ion species can still be separated due to the design of HET, as described in sec. 7.3.1. By using the BGO scintillation detector, with a thickness of 2 cm, protons up to 100 MeV and heavier ions up to several hundreds of MeV can be stopped in the sensor head of HET. Thus, the total energy of the ions can be determined and the "E / dE/dx vs. E $\cdot$ dE/dx" - technique, as described in sec. 7.3.2 can be applied. Due to this technique, the ion species can be well resolved and the flux for the individual ion species can be determined, even at high energies. Over the full energy range of the ABC trigger at least 11 DPI are supplied for each ion species. For protons even 31 DPIs are available.
At even higher energies, when the ion species penetrate the BGO scintillator, the penetrating trigger is used to supply further DPI, as described in sec. 7.3.5. As the particles no longer stop in the sensor head, the total energy of the ion species can no longer be determined and thus the species resolution is highly reduced. However, for certain ion species, H and He, a species resolution can still be provided. For C, N, O and also for Fe several combined DPIs are supplied. Although, the penetrating trigger provides a number of DPIs, which also include the other ion species, due to the reduced resolution of the penetrating trigger compared to the stopping (ABnC or ABC) triggers, the ion species in these DPIs can not be resolved. Thus, the DPIs of the penetrating trigger for Ne, Mg, Si, S, Ar, Ca and Ni are not shown.
With the capabilities to measure and identify all these different ion species, from H up to Ni, over this large energy range HET will provide the necessary information to investigate the acceleration mechanisms of SEP particles and their transport throughout the heliosphere.

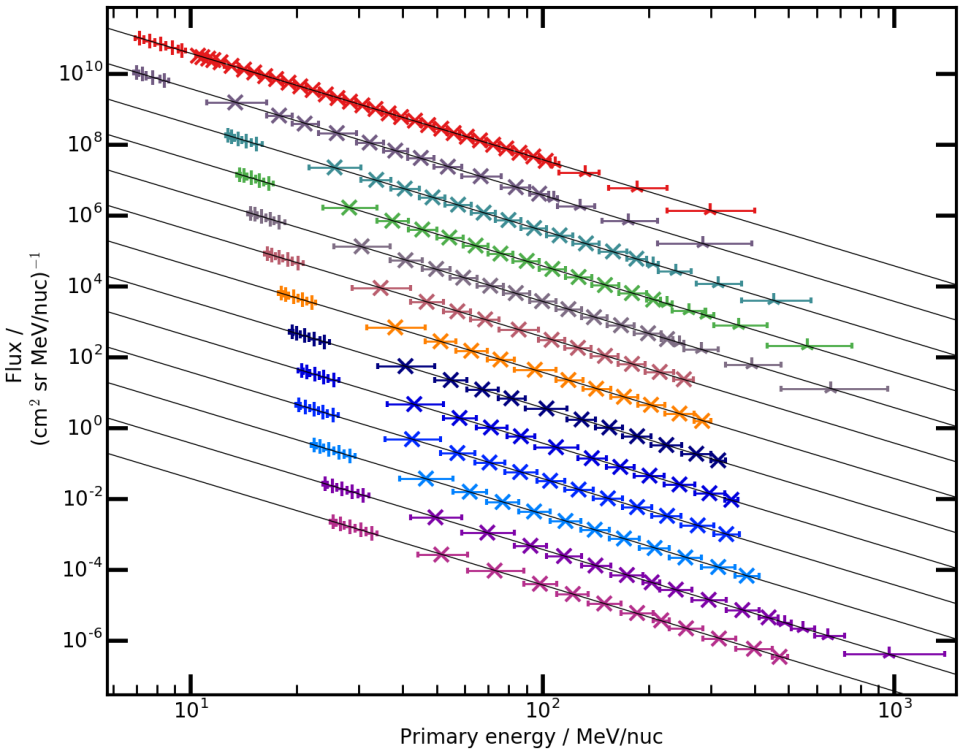

Figure 10.10: For an artificial SEP event with a spectral index of -3, the calculated responses for all ion species, which can be separated and measured by HET are given. The event is scaled in such a way, that the intensity for each ion species is reduced by a factor of 10. The displayed ion species are from top to bottom: H, He, C, N, O, Ne, Mg, Si, S, Ar, Ca, Fe and Ni.

11. Analysis of first mission data

In this chapter, the first data measured by HET onboard Solar Orbiter is presented and analyzed. The main focus is a qualitative analysis of the PHA data provided by HET during the first mission phase. Using the PHA data, the functionality of HET during the mission can be investigated and possible optimizations of the onboard data processing can be developed. Thus, in the first part of this chapter, the PHA data for the different HET level 3 triggers is analyzed and discussed in detail.
In the second part, a preliminary GCR spectrum measured by HET is shown and discussed. As the Sun is currently in the minimum of its eleven year cycle, almost no activity in terms of SEP events is observed. Since the GCR intensity is modulated by the solar activity, they are most prominent during the solar minimum. During these quiet solar times, almost exclusively GCR can be measured in the energy range of HET (Hathaway, 2015). In fig. 11.1 GCR spectra for different ion species for solar minimum and solar maximum are shown. Below 100 MeV/nuc, the spectrum can be well described by a power law shape with a spectral index of $\gamma = +1$ (Kühl and Heber, 2019).

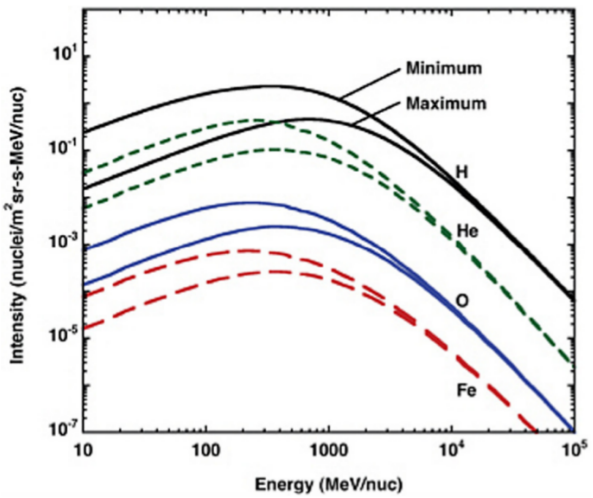

Figure 11.1: Modelled GCR spectra for solar minimum and solar maximum for different ion species (Durante et al., 2019).

11.1 Analysis of first PHA data

The PHA format is introduced in sec. 7.5.2 and the data contains energy depositions and timing information for all HET detectors for single particles detected by HET. Compared to the data product items, which only delivers a number of summarized counts over a defined histogram bin range, the additional information provided by the PHA data makes it well suited to investigate the overall performance of the HET instrument during the mission.
In total HET uses 13 different PHA buffers, each with a size of 1 kB, as described in sec. 7.5.2. The size of the buffers translates for HET to a maximum of 10-15 particles in each PHA buffer. During the near-earth commissioning phase, the PHA cadence is set to 600 s in order to increase the total number of available PHA data for post-launch instrument diagnostics. The buffers contain only particles which are successfully evaluated by the individual level 3 triggers. The assignment of a certain particle to a PHA buffer is performed in the same trigger step when a particle is added to a histogram. Thus, as described in sec. 7.5.2, PHA buffers for different trigger classes and individual particle species are available.
In the following, the PHA data measured between the 28th of Feb. 2020 and the 21st of April 2020 during near-Earth commissioning phase of Solar Orbiter is used to investigate the performance of each individual level 3 trigger of HET. Between the 21st of March and the 1st of April, most scientific instruments, including the whole EPD suite, were switched off, due to operational constraints, so that a total of 44 days of PHA data is used for analysis. To increase the available statistics for the stopping triggers, both directions, e.g. sun and anti-sun, are summarized, i.e. combined in one histogram. In case of the penetrating trigger, both directions are always combined in the same histogram. The PHA data is calibrated on ground using the respective FM1 / FM2 calibration based on the measured temperature at the time of acquisition.

11.1.1 PHA data: ABnC

For the ABnC trigger, five dedicated PHA buffers are available. These buffers are divided into individual buffers for electrons, protons, helium ions and two for heavy ion species, as given in tab. 7.9 in sec. 7.5.2. In fig. 11.2 the combined PHA data from all five ABnC PHA buffers is displayed. As defined in sec. 7.3, AB is the summed energy deposition in the A and B detectors (AB=A+B) and A is the energy deposition in the A detector. Except for the applied calibration factors, the data is not altered and shown as received from the HET FM1 unit.

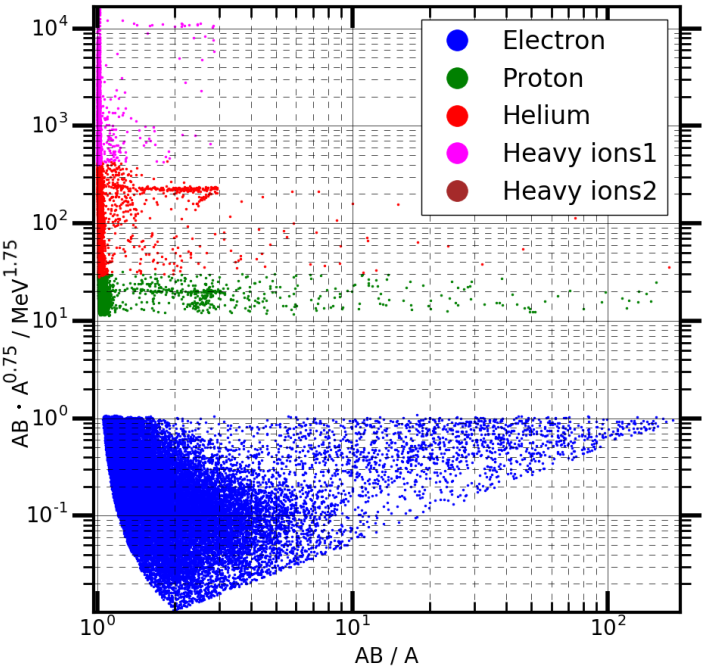

Figure 11.2: Calibrated PHA data from the five ABnC buffers of HET FM1, in sun and anti-sun direction. The PHA data shown here is accumulated over 44 days, resulting of a total number of 37346 single data points or particles contained in the PHA buffers.

ABnC electron
Below 1 $MeV^{1.75}$, the data stored in the electron PHA buffer is shown in blue. In this buffer, primary electrons as well as secondary electrons, created by the interaction of ions with the housing of HET are stored. It is not possible to distinguish primary and secondary electrons as the location in the 2D plot is identical for both populations. The production of secondary electrons by primary ions is explained in sec. 3.2

ABnC proton
Above 10 $MeV^{1.75}$ in fig. 11.2, the particles stored in the proton, the helium and the two buffers for heavy ion species are located. The contents of each buffer are given in a different color. Each buffer is adjacent to the next one in terms of y-axis values. For H and He the hook-shaped particle populations can be identified. However, the majority of the counts is found at low AB/A ratios. This particle population fills all four PHA buffers, so that the primary particle population, which is to be measured, is suppressed in the PHA data.
The level 3 ABnC trigger stores the detected protons in a 1D histogram, which is the basis to generate the ABnC proton data products. The histogram, as generated by the level 3 trigger, is shown in fig. 11.3 for the proton PHA buffer.

The gray boxes illustrate the location of the nominal data product items. At lower energies, the number of detected counts is significantly higher compared to high deposited energies. From the spectral slope of GCR protons, shown in fig. 11.1, this is not expected. Instead, an increase towards higher energies would be expected. Using only the counts supplied by the data products, the origin for this can not be identified. However, using the PHA data, more information is available, so that the origin of the contamination can be further investigated. The origin of these significantly increased number of counts at low deposited energies in the 1D ABnC proton histogram is identified using the He data, which shows an identical behavior.

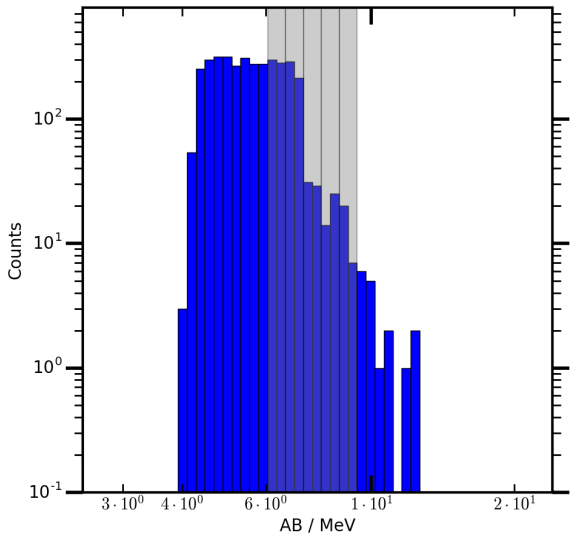

Figure 11.3: 1D ABnC proton histogram as generated by the HET ABnC level 3 trigger, showing the nominal data product items as gray boxes. The histogram contains the data of the proton ABnC PHA buffer.

ABnC helium

Using the ABnC He PHA buffer, the origin of the increased number of counts at low energies in the 1D histograms of H and He is identified. In fig. 11.4 (a) the 1D histogram for He for outer-outer segment coincidences is given. At lower energies, the number of counts in each bin is almost constant and decreases at high energies. Two of the six nominal data product items, the first and the fifth, are used to present the origin of the counts in these data product items using fig. 11.4 (b). In this figure, the axis of identical energy deposition is illustrated using a dashed line. Along this axis, all particles deposit the same total energy in AB and are thus added to the same bin in fig. 11.4 (a). The contents of the two colored data product items in panel (a) are shown with the same colors in panel

(b). Although the fifth DPI (red) contains some He ions, they are dominated by the contaminating particle species. Thus, particles from the contaminating population as well as primary He ions are then no longer distinguishable. A correct flux for primary He ions could thus not be calculated from the ABnC 1D He histogram for outer-outer coincidences without a proper contamination correction. The same is true for protons, where the counts in the lower energy bins result mainly from the contaminating population. The origin of the contamination is discussed in detail in this section under "ABnC contamination - origin and solution". Additionally, a solution for the removal of the contaminating particle population by the onboard data processing of HET is developed, which is also explained in that part.

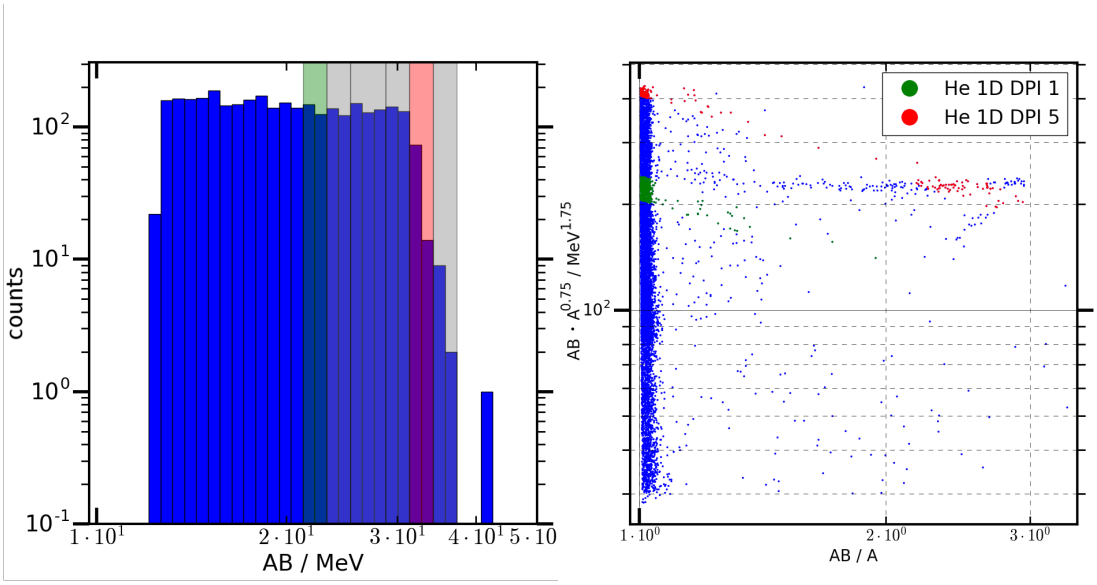

(a) The 1D ABnC He histogram for outer-outer segment coincidences. The semi-transparent boxes resemble the nominal data product items for this histogram. The first and the fifth boxes are colored for identification in panel (b).

(b) In blue, all particles from the ABnC He PHA buffer are shown. The contribution of these particle to respective DPIs is illustrated. The dashed line represents the axis of identical energy deposition of the particles.

Figure 11.4: Using the ABnC He PHA buffer, the origin for the high number of counts at lower energies in the 1D ABnC H and He histograms is presented. In both plots the first and fifth He nominal data product item are highlighted in green and red respectively.

In the 2D ABnC He histogram for non-outer-outer segment coincidences, the contamination is confined in the first data product item. The histogram is shown

in fig. 11.5 with all particles from the ABnC He PHA buffer. The ABnC level 3 trigger creates two histograms for He, based on the SSD segment coincidences. For outer-outer SSD segment coincidences, detected He ions are added to the 1D histogram, for non-outer-outer SSD segment coincidences, the detected He ions are added to the 2D histogram. However, to increase the available statistics, this SSD segment coincidence restriction is not applied to produce fig. 11.5. The impact of the contaminating population for the 2D histograms, is that the first data product item at low energies contains counts from this population and the PHA buffer mostly filled with particles from the contaminating population. However, from the sparse counts located in the other nominal data product items, it can be concluded that the location of the nominal data product items for ^{4}He is correct and the 2D histogram is well capable of delivering the correct ^{4}He flux in the ABnC energy range. ^{3}He is much rarer compared to ^{4}He in the GCR and thus can not be seen in this data set.

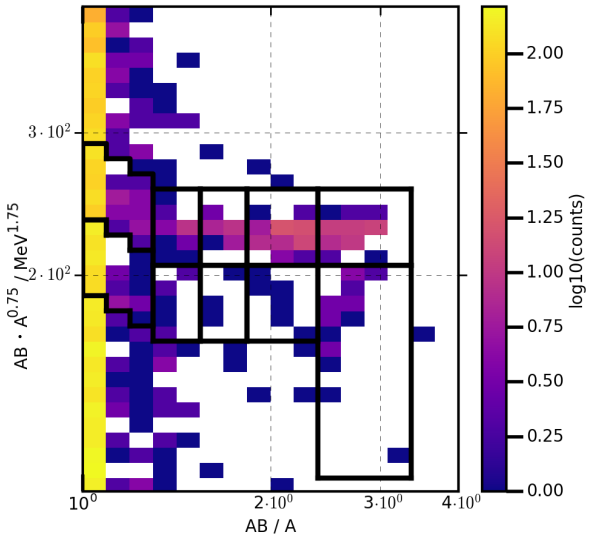

Figure 11.5: Shown is the 2D ABnC He histogram using all entries from the ABnC He PHA buffer without detector segment coincidence restrictions. A few ^{4}He counts in the nominal data product items at higher energies can be seen. At low AB/A values, the contaminating particle population is found but is confined to the first nominal data product item.

ABnC heavy ions

For heavier ion species, there are no statistics in the ABnC heavy ion PHA buffers, except for the contaminating population, as shown in fig. 11.2. Thus the histogram is not displayed in this case.

ABnC contamination - origin and solution

In table 11.1 the number of primary ions compared to the number of particles in the contaminating population are compared. All particles below an AB/A ratio of 1.2 are considered as contamination. The number of primary particles is calculated more restrictively. For H only particles between an AB/A ratio of 1.2 and 3.5 and between 13 and 21 $\text{MeV}^{1.75}$ are considered as primary particles. For He only particles between an AB/A ratio of 1.2 and 3.5 and between 150 and 260 $\text{MeV}^{1.75}$ are considered as primary particles. Within these limits, the primary particle population of the respective ion species is located according to simulation data presented in sec. 7.3.2. The numbers, given in table 11.1 show the high amount of contaminating particles compared to the number of primary particles. Due to the very low primary to contaminating particle ratio, a correction of the transmitted data product items is prone to large uncertainties. Thus, a suppression of the contaminating particle population directly during the measurement by the onboard data processing of HET is derived. To investigate

Ion species	Primary particles	Contaminating particles	Primary part. / contaminating part.
H	217	3380	0.06
He	255	6416	0.04

Table 11.1: Estimation of the primary particle to contaminating particle ratio in the ABnC H and He PHA buffers.

the origin of the contaminating particle species, a GEANT4 simulation of carbon ions with a simulation setup described in sec. 5 is used. The carbon ions are used as an example for all heavy ion species. In fig. 11.6 (a) the result of the simulation is shown after it is processed by the ABnC trigger. By introducing a y-axis value cut of 2700 $\text{MeV}^{1.75}$, the main particle population and the contaminating population can be separated. The primary energy distributions of these two populations are displayed in fig. 11.6 (b). The contaminating population originates from a far higher energy range, that matches that of the ABC trigger and extends up to the maximum simulated energy of $\approx$ 350 MeV/nuc. However, since the highly energetic particles from the contaminating population do not trigger the C detector, they are not treated as ABC and instead as ABnC. Although the simulation only contains contaminating particles that enter the instrument either through the nominal field of view or by penetrating the collimator, the origin of the contaminating particle population is identified. Heavy ion species penetrate the housing of HET and deposit a high amount of energy in the A detector. In the B detector only a low amount of energy is deposited, so that it is suspected, that this energy deposition originates from secondary particles, created in the interaction of the heavy ion with the housing of HET. Therefore, the contami-

nating population is found at low AB/A ratios. In fig. 11.7, this scenario for the origin of the contaminating particle population is sketched.

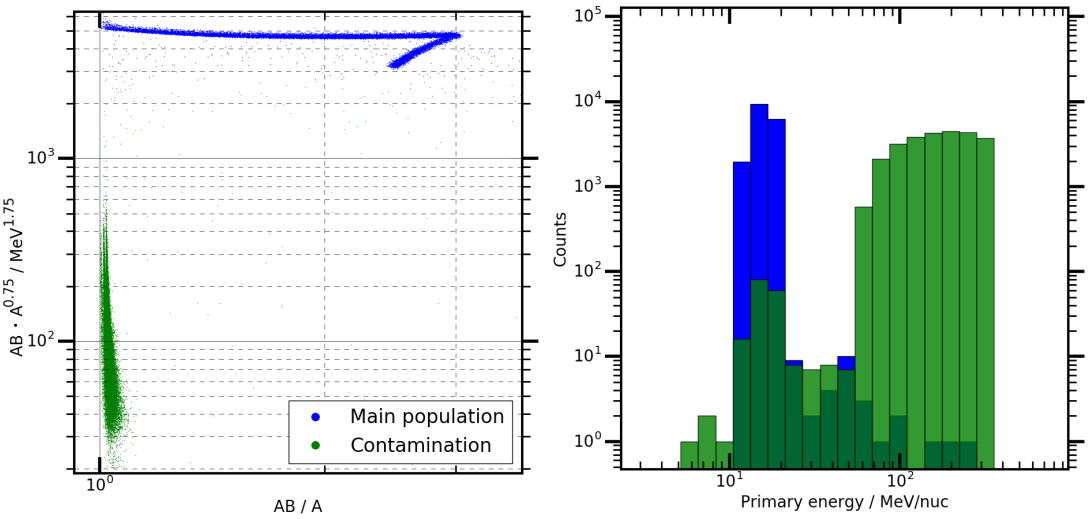

(a) The main particle population and the contaminating particle population can be divided by a y-axis value cut of 2700 $MeV^{1.75}$.

(b) Displayed are the primary energy distributions of the main and the contaminating particle distributions shown in panel (a).

Figure 11.6: Using a GEANT4 simulation of carbon ions with an energy range of 5 MeV/nuc up to ≈350 MeV/nuc, the origin of the contaminating particle population is investigated.

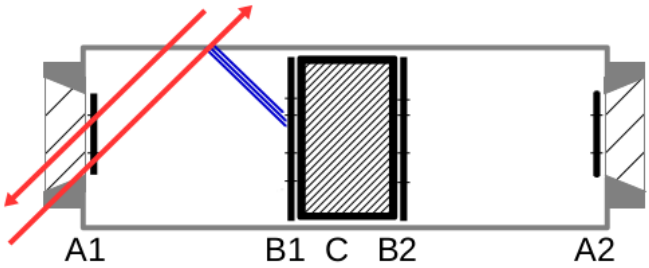

Figure 11.7: The red arrows indicate highly energetic ions which can penetrate the instruments housing and even the collimator. These ions deposit large quantities of energy in the A detector. Due to the interaction of the ions with the instrument housing, secondary particles are created, indicated by the blue arrows, which deposit more than 50 keV in the B detector and resulting in a valid ABnC particle detection.

In case of an isotropic radiation, particles can also enter the sensor head compartment from the top or the sides of the instrument and create the same effect. Therefore, the geometrical factor for the contaminating population is significantly higher compared to the particles which enter the sensor head through the nominal field of view. In case of the GCR the spectrum shows an increase towards higher energies, which leads to an additional increase in the amount of contaminating particles, which leads to the high number of observed contaminating particles compared to the particles of the main particle population. The contaminating particles can not be directly identified and rejected with HET, as HET has no anti-coincidence around the sensor head compartment. However, using the AB/A ratio, the contamination can be highly reduced. From the results obtained from the carbon simulation, it can be concluded that ion species in the 1D histogram can be contaminated by all heavier ion species.
To remove the contamination for the ABnC 1D histograms of H and He and also from all ABnC ion PHA buffers, a minimal AB/A ratio of 1.2 is introduced in the ABnC level 3 trigger with EPT-HET configuration V0008 uploaded to both HET flight units on the 12.05.2020. This means, that the energy deposition in B needs to be at least 20% of the energy deposition in A. The 2D ABnC histograms for He and heavy ion species are not affected by the configuration update. In fig. 11.8 the 1D ABnC He histogram is shown using a minimal AB/A ratio of 1.2 to remove the contamination. The same data is displayed as in fig. 11.4 but the data is re-processed using the minimal AB/A ratio of 1.2. With this, the contamination can be fully removed.

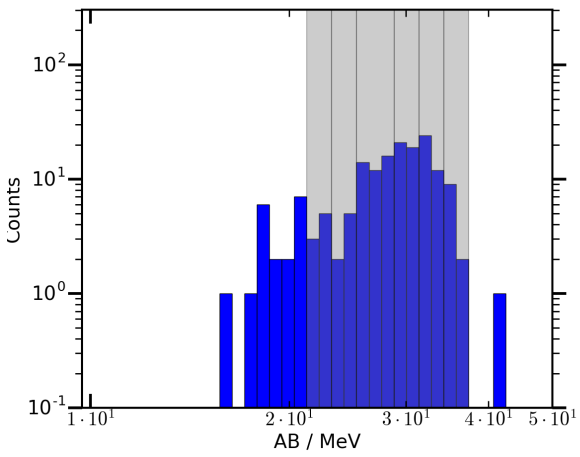

Figure 11.8: By using a minimal AB/A ratio before an event is added to the ABnC 1D H or He histogram, the contamination is removed. Here the ABnC 1D He histogram is shown with the same data as in fig. 11.4, but with a minimal AB/A ratio of 1.2.

Because of the introduced AB/A threshold, the lower energy limits of the 1D H and He data product items are slightly shifted towards higher energies. The change for the two He isotopes and for H is given in table 11.2. In the table, the bin numbers of the referenced nominal data products are given. As ^{4}He has nominally no response in the first bin of the 1D histogram, for this species bins number two and three are given.
A possible contamination by heavier particles of the 1D histograms was expected, as shown in fig. 7.8 of sec. 7.3.2. However, the onboard data processing was designed for the detection of SEP events. In case of these events the contamination is expected to be highly reduced, as the particle flux is drastically reduced towards higher energies, as described in sec. 10.2. Still, due to the applied restriction in the AB/A ratio, also the contamination of the 1D ABnC histograms during SEP events is reduced and the effect on the energy ranges of the affected DPIs is very low, as given in table 11.2.

Ion	Bin #	Old prim. energy range / MeV/nuc	Resp. factor / cm^2 sr	New prim. energy range / MeV/nuc	Resp. factor / cm^2 sr
H	1	6.94 - 7.36	0.267	7.05 - 7.35	0.254
^{3}He	1	8.16 - 8.62	0.157	8.29 - 8.62	0.149
^{4}He	2	6.90 - 7.09	0.141	6.96 - 7.06	0.079
^{4}He	3	7.09 - 7.88	0.160	7.10 - 7.88	0.161

Table 11.2: Changes in primary energy range and response factor due to the introduction of a minimal AB/A ratio of 1.2 to remove the contaminating particle population from the 1D ABnC H and He histograms. The displayed energy ranges and responses are given for the NO_HETB_p and NO_HETB_he data products. The primary energy ranges and the response factor is calculated according to the effective response factor method presented in sec. 9.2.1.

11.1.2 PHA data: ABC

Analog to evaluation of the ABnC PHA buffers, the available data of the ABC PHA buffers are inspected in order to assure a correct onboard data processing functionality. For this, the same time period as the one for the ABnC PHA data evaluation is used. The ABC trigger features five dedicated PHA buffers for electrons, protons, helium and two for heavy ion species. In fig. 11.9 the combined data of all five ABC PHA buffers is displayed. All five PHA buffers combined contain 147009 particles. As defined in sec. 7.3, ABC is the summed energy deposition in the A,B and C detectors (ABC=A+B+C).

ABC electron

At low y-axis values, electrons detected by the ABC trigger are shown in blue. The primary electron population, as expected from the simulations is shown in fig.11.10 for comparison. Due to the observed electron population in fig. 11.9 it can be concluded that mostly secondary electrons are detected during the observed time period.

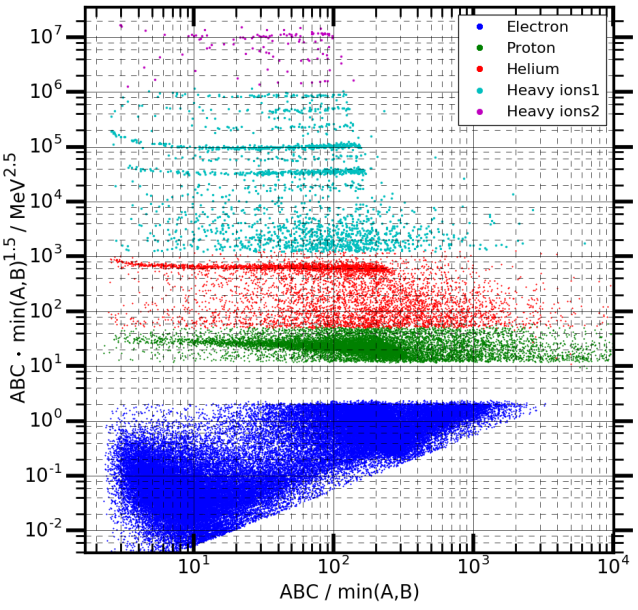

Figure 11.9: The data of all five ABC PHA buffers for sun and anti-sun direction of the HET FM1 unit is shown. The PHA data shown here is accumulated over 44 days. For this figure, the H and He PHA statistics are reduced by a factor of four for the sake of visualization.

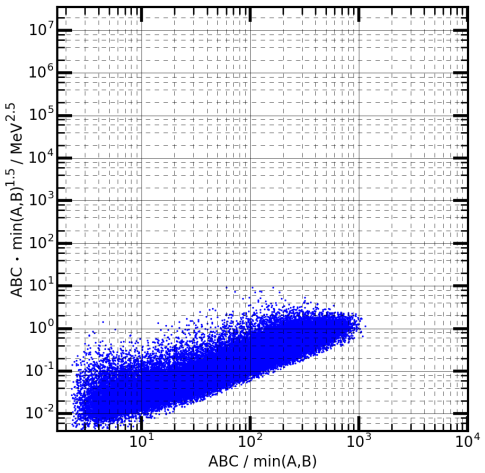

Figure 11.10: Geant4 simulation of electrons in a primary energy range of 0.1 to 100 MeV processed by the ABC trigger. This shows the expected primary electron location in fig. 11.9 with the exact same axis scaling for easier visual comparison to fig. 11.9.

ABC proton

In fig. 11.9, the content of the proton PHA buffer is shown in green. The location of the primary proton population is well visible and agrees with the simulations, as shown in sec. 7.3.2 in fig. 7.8. In fig. 11.11 the 1D proton histogram is shown. The number of counts increases towards higher energies due to the positive spectral index of the GCR in this energy range (Simpson, 1983). At an energy deposition of 105 MeV a drop in the number of counts is expected from the simulations. At this energy, the protons penetrate the C detector and trigger the B detector behind the C detector and are thus not added to the 1D ABC proton histogram. The observed number of counts in the histogram, shown in fig. 11.11 drops at slightly lower energies ($\approx 5-10\%$) than expected from the simulation, presented in sec. 7.3.3 in fig. 7.14. The reason for this could be either because of an incorrect energy calibration value of the C detector itself and at least partially due to the possibility of ionization quenching of protons stopping in the scintillator.

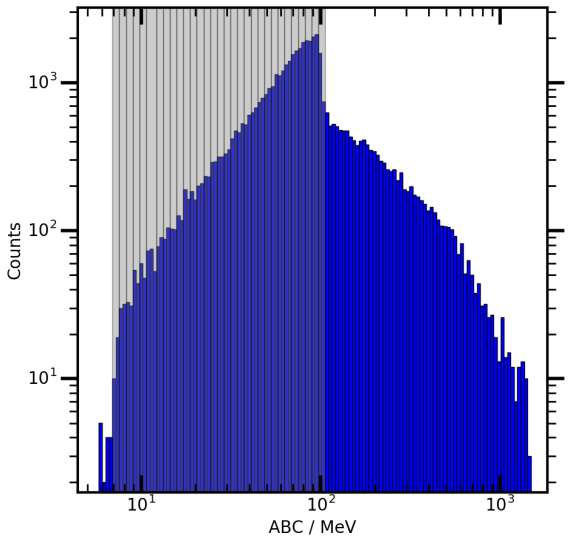

Figure 11.11: 1D ABC histogram of the proton ABC PHA buffer. The gray boxes represent the nominal data product items. A significant amount of counts above ≈105 is not expected from primary protons in the energy range between 5 to 200 MeV.

The next steps to identify the origin of the mismatch between the simulation and the measured data, would be to perform an in-flight validation of the calibration of the C detector. This can be done using for example the PHA buffer of the penetrating particle trigger, which contains measurements of relativistic protons, which are well suited for this purpose. Furthermore, the offset of the histogram compared to the simulations due the possibility of ionization quenching induced by protons can be investigated. In contrast to particles penetrating the scintillator, the energy deposition per path length is higher for particles stopping in the scintillator and thus the light loss due to ionization quenching is increased. Protons are not included in the ionization quenching prediction model by Tammen (2016b), as the amount of lost scintillation light when measuring protons is considered to be in the order of a few percent, even for protons stopping in the scintillator (Tammen, 2016b). However, using proton measurements from HIMAC, the exact amount of light loss for stopping protons in this energy range can be determined and if, in combination with a possible calibration offset, this can explain the observed mismatch between simulation and measurement.
Furthermore, from the simulations, as presented in fig. 7.14 of sec. 7.3.3, an energy deposition by primary protons, significantly above ≈ 200 MeV is not expected. Still, in the PHA data total energy depositions of up to ≈1 GeV are observed. Using GEANT4 simulation data from the setup given in chapter 5 of He, C, N, O and Fe ions, a possible source of these high energy depositions is identified. In this case, particles are simulated from a source surface in front of the instrument

and the energy range of the different ion species ranges from 5 MeV/nuc up to $200 \cdot Z \cdot \sqrt{A}$ MeV/nuc. With the charge, Z, and the mass, A, of the respective ion species. The ion abundances of SEP events are not taken into account in this case, because the aim is to clarify whether heavy ion species in general are able to produce events which mimic a valid primary proton detection. The resulting 1D ABC proton histogram, containing secondary particles from these heavy ion species is shown in fig. 11.12. Heavy ions are able to produce ion fragments which deposit large amounts of energy up to 1 GeV in the scintillation detector. However, the exact mechanism, how these large energies are deposited while the resulting event is still identified as a valid ABC proton remains to be identified. The heavy ion species do not only create counts at high energies in the 1D ABC proton histogram, but also in the nominal proton range and thus contribute to the data product items for primary protons, as shown in fig. 11.12. The next open steps to investigate the contamination of primary protons by heavier ion species is to perform a fully isotropic simulation for all heavy ion species and furthermore, to identify the exact mechanism how the observed high energy deposition in the C detector is created by the heavy ions. Using fully isotropic simulations, the response factors for heavy ions, which contaminate the proton data product items can be derived and from the measured heavy ion fluxes, correction factors for these data products can be derived.

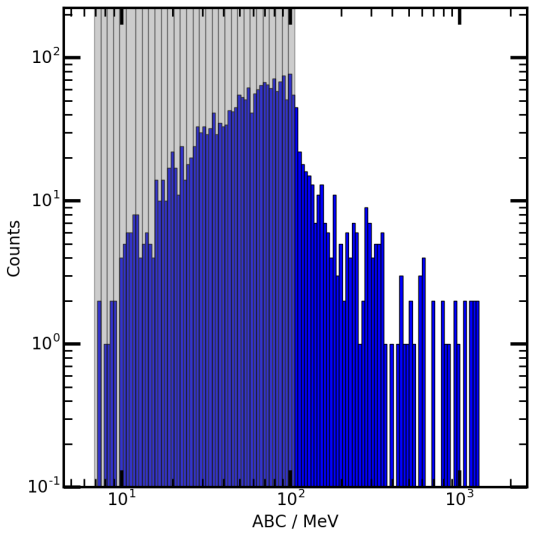

Figure 11.12: The 1D ABC proton histogram, showing the contamination by He, C, N, O and Fe ions of a GEANT4 simulation. The gray boxes represent the nominal ABC proton data products.

ABC helium

In fig. 11.13 the 2D ABC He histogram is shown for the data obtained from the ABC He PHA buffer. Since ^{3}He is rare in the GCR, only ^{4}He is observed. Comparing the measured histogram with the simulations, given in fig. 7.17 of sec. 7.3.3, it can be concluded that the position of ^{4}He in the 2D histogram as well as the position of the data product items is as expected.

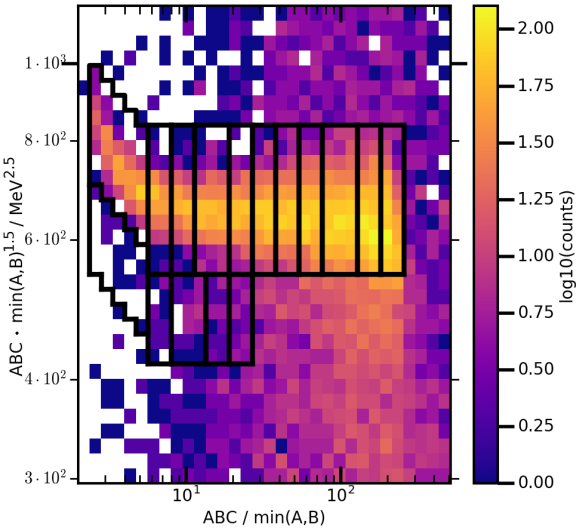

Figure 11.13: 2D ABC He histogram showing the data of the ABC He PHA buffer.

ABC heavy ion species

In fig. 11.14 the data of the two ABC heavy ion species PHA buffers is shown in the 2D ABC heavy ion species histogram. In the nominal data product items, the most common GCR species are visible. Among these are C, N, O, Ne, Mg, Si and Fe, according to table 11.3, from Simpson (1983). Even Li and B are visible, right below the C nominal data product items. All of these ion species are located where they were predicted by the performed GEANT4 simulation. Even the upward bending tail at lower x-axis values is measured as predicted. It can be concluded, that the HET ABC trigger works as predicted for heavy ions as the most abundant ion species are present in the data and can be well resolved and separated using the applied E · dE/dx vs E/ dE/dx-technique. A direct comparison of the measured abundances, with the abundances given in table 11.3, is not possible. Although the heavy ion data product items of the different ion species are vertically aligned, the primary energy range of each data product item for the different ion species is different. However, using the derived primary energy ranges and effective responses, the C to O ratio, as measured by HET can be calculated. These two ion species show the best available statistics. For the calculation, C data product items 7 to 12, covering an energy range of 73.5 to 197.3 MeV/nuc are used and for O the data product items 6 to 11, covering an

energy range of 77.1 to 216 MeV/nuc are used. By using these DPIs, roughly the same energy range is covered. The DPIs are counted from low ABC/min(A,B) values towards higher values, as displayed in fig. 11.14. The energy range of the individual data product items are given in the appendices sec. A.1. The integrated particle fluxes in this energy range, in particles/ (MeV/nuc cm^2 sr) are calculated and the statistical uncertainty is derived. The results and the comparison to the literature values by Simpson (1983) are given in table 11.4. The total counts in the used DPIs for C are 287 and for O are 267, which explains the rather large statistical uncertainty for the C to O ratio calculated with HET. Still, the C to O ratio determined with the data measured by HET is comparable to the reference value and well withing the uncertainty ranges.
The C to N ratio can also be determined with HET, although N shows sparse counts. For C the same data product items are used as before. For N, the data product items 6 to 11 are used, covering an energy range of 69.7 to 197.5 MeV/nuc. For N a total of 50 counts are measured. Due to the bad counting statistics of N in case of the HET measurement, the uncertainty of the measurement is even larger than for the C to O ratio. The determined ratio is comparable to reference values by (Simpson, 1983), however due to the large uncertainty, no statement about the performance of HET can be made using the C to N ratio. With more statistics available, a more accurate determination of the GCR ion flux ratios, also for other heavy ion species, can be performed in the future.
Still, the C/N ratio shows a good agreement with the reference values, as shown in table 11.4, and thus it can be concluded, that the ion separation works and that the individual heavy ion fluxes can be determined using HET, as long as enough statistics are available. Furthermore, the location of the individual ion species in the histogram agrees with the simulations, so that all ion species are contained in the defined data product items.

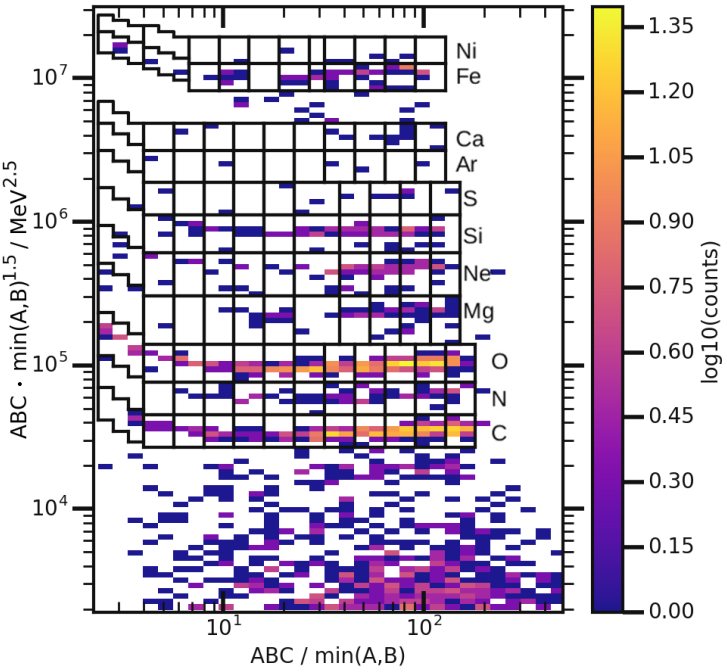

Figure 11.14: Displayed is the 2D ABC heavy ion species histogram using the two ABC heavy ion species PHA buffers.

11.1.3 PHA data: penetrating trigger

The HET penetrating trigger uses two PHA buffers. One PHA buffer for light ion species up to carbon and the other for all ions from carbon up to iron. This separation is necessary, as otherwise the rare heavy ion species are suppressed in the PHA buffer by the more abundant lighter ion species. The selection of the PHA buffer is based on the energy deposition in the C detector. If the energy deposition is below 600 MeV the buffer for lighter ions is selected, and in case the energy is above this value, the event is stored in the buffer for heavy ions species. The PHA buffers for light ion species contains a total of 58570 particles and the PHA buffer for heavier ion species contains 335 particles. The particles stored in both buffers are shown in fig, 11.15 without any modifications to the data. The protons as well as the He ions are located exactly where they are expected from the simulation. The 2D HET penetrating trigger histogram, showing the simulation data, is given in sec. 7.3.5 in fig. 7.25 for comparison. Comparing the output of the simulation and the PHA data, a good agreement regarding the locations of the individual ion species is in the histogram is found. For H and He the statistics are good enough so that even the tails towards higher and lower min(A1,B1)/min(A2,B2)-values can be seen. As described in sec. 7.3.5, these

Ion species	Abundance	Ion species	Abundance
He	41700 ± 3000	S	16.4±1.2
Li	100 ± 6	Cl	3.6±0.5
Be	45 ± 5	Ar	6.3±0.6
B	210± 9	K	5.1±0.6
C	851 ± 29	Ca	13.5±1.0
N	194 ± 8	Sc	2.9±0.5
O	777 ± 28	Ti	10.7±0.9
F	18.3± 1.3	V	5.7±0.6
Ne	112±6	Cr	10.9±1.0
Na	27.3±3.4	Mn	7.2±1.2
Mg	143±6	Fe	60.2±3.2
Al	25.2±3.0	Co	0.2±0.1
Si	100	Ni	2.9±0.4
P	4±0.7		

Table 11.3: GCR ion abundances in the energy range between 70 to 280 MeV/nuc, measured at 1 AU, normalized to Si=100 (Simpson, 1983).

	HET value	Reference value
C/O	1.24±0.48	1.10 ±0.08
C/N	5.37 ±2.5	4.32±0.16

Table 11.4: GCR C/O and C/N flux ratio for the time interval from 28.02.20 until 21.04.20 as determined with HET are given. For comparison reference values given in table 11.3 by Simpson (1983) are used. The reference values are given in an energy range of 70 – 280 MeV/nuc. For HET the energy range is ≈ 70 – 200 MeV/nuc.

tails originate from ions, which loose sufficient energy in the C detector, so that the energy deposition in the SSDs on both sides of the C detector is different. For highly relativistic particles, this is no longer the case, as the energy loss in the C detector is small compared to their total energy. Particles in the tails at positive min(A1,B1)/min(A2,B2)-values are thus coming from the A2B2-side. As shown in fig. 11.1, compared to the light ion species H and He, the flux of heavy ion species in the GCR is highly reduced. However, still the location of the relativistic C, N and O is visible, which also matches with the expected location from the simulations. Thus it can be concluded that the HET level 3 penetrating trigger works as expected and location of the different ion species in the histogram of the measured data in respect to the defined data product items is correct.

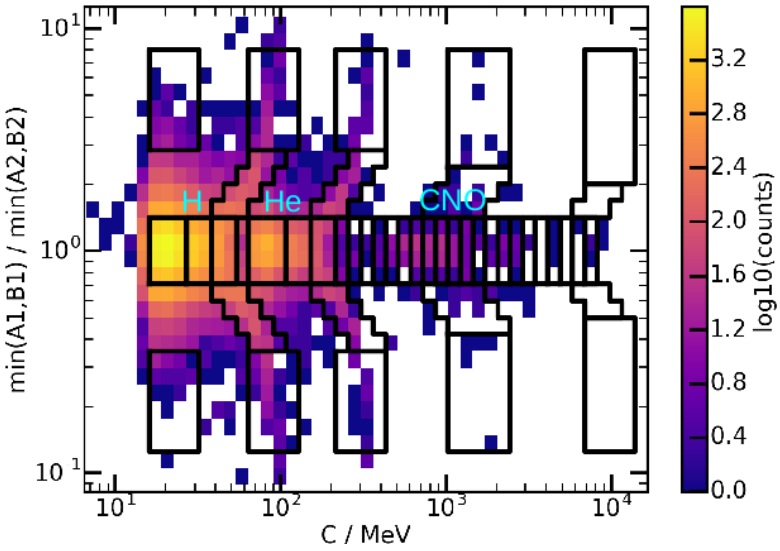

Figure 11.15: The HET penetrating trigger histogram with the nominal data product items shown as black boxes. The data is obtained from the two penetrating trigger PHA buffers.

11.1.4 PHA data: GCR trigger

The GCR trigger has an extended field of view compared to the other trigger classes, as only a coincidence of the two B detectors is required. Thus, even particles entering the sensor head through the housing are accepted. Due to the limited number of PHA buffers, the GCR trigger does not have an individual PHA buffer to store the detected particles. Instead, it stores the valid GCR trigger events in the invalid PHA buffer. HET features one PHA buffer, where all invalid or rejected particles of the other trigger classes are stored. Out of the 80332 particles stored in the invalid PHA buffer, 4942 particles fulfill the GCR trigger requirements, as described in sec. 7.3.6. By applying these requirements

to the data of the invalid PHA buffer, the 1D histogram of the GCR trigger can be created using this PHA data. The 1D GCR histogram is shown in fig. 11.16. Between an energy deposition of 10 to 50 MeV, protons are located in the histogram. The MIPs peak of the protons around 20 MeV is clearly visible and the according data product items for the protons are shown in gray. Around an energy deposition of 70 MeV, the He MIP peak is located, followed by the MIPs peaks of the heavier ion species. Even without an individual PHA buffer, the statistics are sufficient to show, that the design of this histogram and its according data product items is correct.

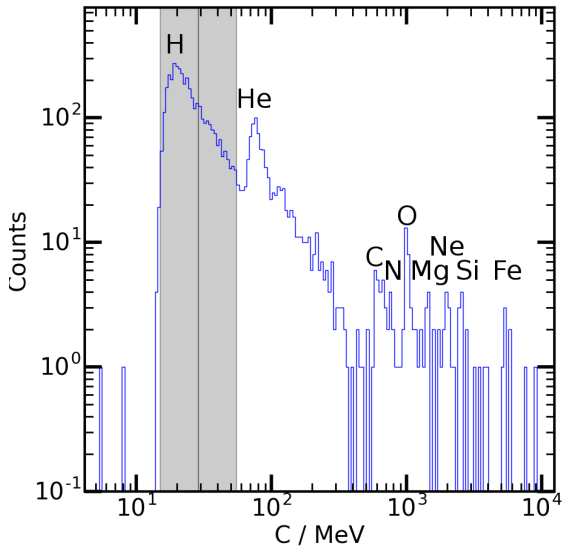

Figure 11.16: The GCR 1D histogram with data from invalid PHA buffer. The gray boxes show the nominal data product items for H. The MIPS peaks are label with the corresponding ion species.

11.1.5 Conclusion for PHA data

From the qualitative analysis of the first PHA data of HET during the Solar Orbiter mission, it can be concluded that the data looks promising and that many aspects of the onboard data processing work as expected. For different trigger classes and ion species, the main particle populations are contained in the designed data product items, for example ^{4}He in the 2D ABnC and the 2D ABC He histograms, the different heavy ion species in the 2D ABC heavy ion species histogram, as well as all ion species in the penetrating 2D histogram. The same is true for the GCR trigger. Using the 2D heavy ion histogram, the C/O ratio of the GCRs is determined and shows a good agreement with the literature. However, based on the PHA data also some deficiencies are identified. The contamination of the 1D ABnC H and He histograms by heavy ion species is identified, analyzed

and corrected for. A possible origin is identified, based on simulation data. The developed correction was uploaded to both flight model units on 12.05.20 as configuration version V0008. By introducing a requirement in the ABnC level 3 trigger, AB/B≥1.2, the contamination caused by high-energy heavy ions can be rejected from the histograms as well as all ABnC PHA buffers except for the electron PHA buffer, which is unaffected by this change. Furthermore the 1D ABC histogram contains counts at very high energy deposition values. These are significantly above the nominal or expected primary proton energy range. It is shown, that heavy ion species are able to create these large energy depositions in the C detector and the detected particle is then added to the 1D ABC H histogram. Although the exact mechanism remains to be clarified, first steps to further investigate this issue are suggested. As HET is fully configurable, even during the mission, changes to the onboard data processing can still be applied if necessary.

11.2 Proton GCR flux calculation

Using the calculated response factors, as described in sec. 9.2.1, the counts provided by the HET data products can be converted into particle fluxes and quantitatively analyzed and compared to other instruments. In fig. 11.17 the GCR proton particle flux, as measured by HET for the sun direction is shown. However, the relativistic penetrating data products, shown in red are bi-directional. To calculate the GCR proton flux, the nominal data product items for protons are used for the time interval between the first of April 2020 to the 30th of April 2020. Each trigger class is assigned a different color in the plot. The primary energy value for each data product item is the effective energy E_{eff} for a spectral index of $\gamma = +1$. The statistical uncertainty of the individual data product items are shown.
Some of the features, shown in fig. 11.17, can be explained from the information gained from the PHA buffer analysis performed in the different sections of chapter 11. The first two data product items of the ABnC trigger show a large proton flux compared to the other ABnC bins. This is related to the contamination of the 1D ABnC proton histogram by heavy ion species, discussed in sec. 11.1.1.
The first data product items of the ABC trigger in fig. 11.17 show a highly increased flux compared to the subsequent DPIs. As discussed in sec. 11.1.2, the calibration value of the C detector could be too low, which would lead to a shift of the 1D ABC proton histogram, as shown in fig. 11.11 towards lower deposited energies compared to the simulation. This leads to an increased number of counts in the DPIs at lower deposited energies and to a decreased number of counts in DPIs at the highest deposited energy, in case of the GCR spectral shape. A possible contribution to the observed shift towards lower energies could be due to the effect of ionization quenching for protons stopping in the scintillator. This would

lead to a similar effect as a too low energy calibration factor for the C detector. Thus, both observed features, too high flux in the lowest DPIs and a too low flux in the highest DPIs of the proton ABC data product, can be related to a calibration offset in combination with ionization quenching of protons stopping in the scintillator.
At higher energies, the non relativistic and relativistic data products are shown. The last bin shows a reduced flux compared to the other relativistic and non-relativistic penetrating products. A possible explanation for this is that the response factor of the channel is only calculated up to 2 GeV and thus, the primary energy range of this DPI is not correctly calculated. As the Flux is given per MeV, the energy range of the data product item has a major impact on the calculated response factors and thus on the calculated particle flux. Furthermore the exact position of the marker, "x", is incorrect, due to the limited maximum energy range used to determine the response of this data product item.
For comparison, the SOHO-EPHIN proton fluxes are also given in fig. 11.17 for the same time interval including systematic and statistic uncertainties (Kühl and Heber, 2019). Currently, the determined flux of the ABC HET data products is a factor of two above the fluxes determined by EPHIN. As described in sec. 11.1.2 a possible contamination of the 1D ABC proton histogram by heavy ions, which could contribute to the higher proton flux observed by HET, needs to be investigated. Ignoring the lower ABC data product items, for the reasons stated above, at least the same spectral shape is observed. In case of the higher energy ABnC data products, a better agreement with the proton fluxes determined by EPHIN is observed.
At this point, HET provides GCR proton fluxes comparable, but a factor of two higher, to the measured fluxes of other established instruments. Therefore it will be necessary to investigate a number of effects and cases in order to decrease the mismatch in the measured fluxes.
In fig. 11.18, the GCR proton flux for the same time interval as given in fig. 11.17 is shown for both HET flight units and all directions. Both units show the same behavior regarding to too high observed flux rates for the first data product items of the ABnC and ABC trigger. The last three ABnC data product items, between 7 to 10 MeV primary energy show a spread in the observed particle flux, that is independent of the telescopes viewing direction. As shown in fig. 11.17 the statistical uncertainties for these data product items are very large, as the number of counts, even for an acquisition time of 1 month are in the order of a few single counts. The non-relativistic penetrating data product items show a deviation in the order of 20%, which can not be attributed to the statistical uncertainties. The ABC data product items above a primary energy of $\approx$15 MeV as well as the relativistic penetrating data product items agree well for the different viewing directions.
From the comparison of the two HET units onboard Solar Orbiter and the different viewing directions, it can be concluded, that both units and all viewing

directions behave similarly. As expected from the isotropic GCR particle flux, all viewing directions measure a comparable proton flux. However, both units and all directions show the same deficiencies regarding the high flux values in the first ABnC and ABC trigger DPIs. At least for the ABnC trigger, a first optimizations is developed and applied to both units, so that the ABnC proton data products are expected to deliver the correct particle flux. First steps for the investigation of the mismatch between the pre-flight simulations and the first measurements are suggested, in order to identify the origin and if necessary to develop optimizations for the onboard data processing.

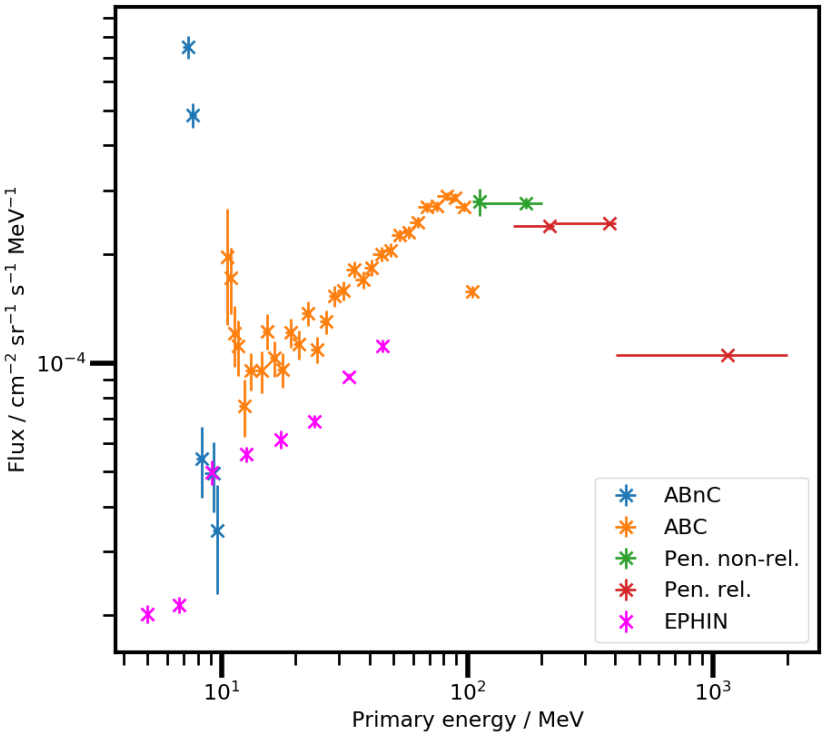

Figure 11.17: The GCR proton flux determined for the time period between the 1st of April until the 30th of April 2020. The nominal data product items of the different level 3 trigger classes are shown in different colors for a better distinction. The unexpected high and low proton fluxes observed for the ABnC and ABC trigger are encircled. For comparison, the EPHIN data for the same time interval is shown (Kühl and Heber, 2019). Comparing the EPHIN GCR proton flux and the GCR proton flux determined with the ABC HET data products, an increase by a factor of two for HET is observed.

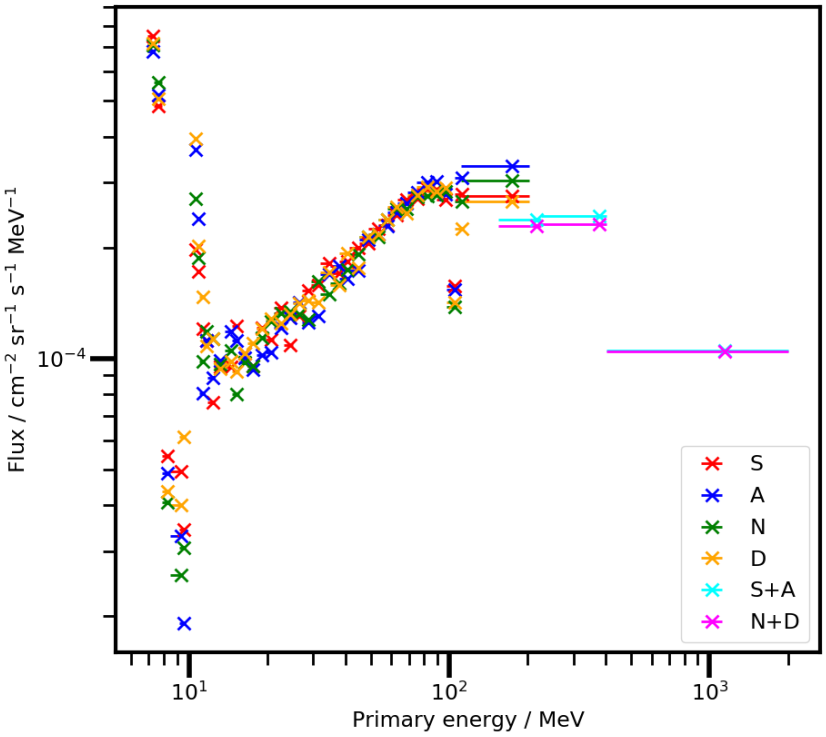

Figure 11.18: GCR proton flux as measured by the two HET flight models FM1 and FM2. The data product items for the relativistic penetrating particles are bi-directional and thus given per unit, all other data product items are given per direction. Due to the large amount of overlapping data product items, y-error bars are not shown for the sake of visibility.

12. Summary and outlook

As part of Solar Orbiter's EPD suite, HET is designed to measure Solar Energetic Particles (SEPs) emitted from the Sun. Using the combination of remote sensing instruments and the in-situ measured energy and composition dependent SEP particle fluxes, the open questions of the scientific heliospheric community regarding the origin and the acceleration mechanisms of SEPs can be addressed. HET covers the highest energy range of EPD and is capable to identify different particles species in an energy range from several MeV/nuc up to ≈100 MeV for protons and several hundreds of MeV/nuc for heavier ion species. Above this energy range, the particle identification capabilities of HET are reduced for heavier ion species, but still protons and helium ions can be clearly identified.
For the development of the onboard data processing of HET the use of simulations, describing the interaction of energetic charged particles with HET, is inevitable. Furthermore, scintillation detectors show a non-linear behavior in their light-output when detecting heavy highly energetic charged particles, known as ionization quenching, which is not considered in the simulations. The resulting discrepancy between deposited energy, as obtained from the simulations, and the measured energy in the scintillation detector needs to be taken into account for the development of HET's onboard data processing. To apply existing ionization quenching prediction models to HET, it was necessary to investigate a possible temperature dependence of the effect of ionization quenching, which is not included in current quenching prediction models. This pre-development activity is necessary, as HET will operate in a temperature unstable environment during the Solar Orbiter mission, in which the instrument temperature is depending on the distance of the spacecraft to the Sun and its orientation. Thus, in the scope of this thesis, an additional particle detection instrument, the BGO-Thermal instrument, was designed and built to perform detailed thermal studies for HET. Using the BGO-Thermal instrument, it was shown, that the scintillation light loss induced by ionization quenching is independent of temperature and that existing quenching prediction models can be used for the development of the onboard data processing of HET. The results have been published in "Nuclear Instruments and Methods in Physics Research Section B" (Elftmann et al., 2019). To the current day, no other studies regarding the temperature dependence of ionization quenching are known to the author.

Based on the results of the BGO-Thermal experiment studies, an existing ionization quenching prediction model in combination with GEANT4 simulations, performed as part of this thesis, was used for the development of the onboard data processing of HET. For the simulations a digital model of HET, including all necessary components of the sensor head compartment was created. The simulations predict the interaction of highly energetic charged particles with HET and are thus the baseline for the design of the developed onboard data processing. As no other complete documentation of this onboard data processing exists, a complete and detailed description of the developed onboard data processing of HET is provided. The level of detail is necessary to utilize and correctly interpret the data provided by HET. A partial documentation on HET and the data products provided by the onboard data processing are published as part of the EPD instrument paper in "Astronomy & Astrophysics" (Rodriguez-Pacheco et al., 2019). The publication contains a basic documentation of all four telescopes of the instrument suite. The development of a complex onboard data processing for HET is necessary, as for the complete EPD suite, a maximum data rate of 3000 bps is allocated. Therefore, particles measured by HET are directly evaluated by the instrument. The developed onboard data processing is able to identify particle species, based on pre-defined criteria. Different ion and particle species can be resolved and even the two He isotopes ^{3}He and ^{4}He can be distinguished, which is important for SEP event studies. The detected particles are categorized and evaluated. During the evaluation process the energy deposition in different detectors of HET is analyzed and compared to pre-defined thresholds. In doing so, the mis-identification and resulting contamination of other ion species is highly reduced. Based on the energy and species of the measured particle, counters in pre-defined histograms are incremented. The design of the histograms is optimized to provide the necessary resolution for the particle separation within the histograms. Thus, the developed particle evaluation process performs a sophisticated analysis of measured particles directly onboard HET in order to preselect the data based on scientific aspects and to identify and reject possible contamination. The onboard data processing as well as the definitions and optimizations of the pre-defined histograms are well documented in this work in order to provide this necessary information to scientists working with HET.
A transmission of the complete histograms exceeds the telemetry budget of HET, so that only pre-defined parts of the histograms, called data products, with defined cadences are routinely sent to Earth. The data products are used to determine the in-situ particle environment. The definition of the data products is also an essential part of this work as they define the available energy and time resolution provided by the instrument. Therefore the definition of these data products and their cadences was performed according to the needs of the scientific community and in accordance to the instrument design requirements. To convert the measured count rates provided by the individual data products into particle fluxes response factors have to be well determined. In the scope of this

thesis, these response factors for all data products of HET are calculated, taking into account the instruments geometry as well as the full data evaluation of the onboard data processing. With these response factors, the in-situ energetic particle environment as measured by HET can be determined.
Using the developed data products and response factors, the capabilities of HET for the detection of SEP events are investigated. For this, simulated particle events with expected spectral properties and also measurements of previous SEP events by other instruments are used. The analysis shows, that HET is able to provide spectral and composition information for SEP events over a wide energy range using the defined energy ranges and effective response factors derived for the data product items. With sufficient counting statistics available, the uncertainties induced by the use of effective responses and defined energy ranges for the data product items are below 1%. However, the exact energy range and temporal resolution in which the spectral and composition information can be provided is limited by the counting statistics and thus depending on the particle species, since the abundance of heavy ion species in SEP events is low.
To verify and test the data processing and the location of the data products in the histograms before launch, experimental data from a heavy ion accelerator is used. The data is calibrated and compared to the simulation data. By this, the simulation data as well as the quenching prediction model is verified and the discrepancies between experiment and simulation are within the uncertainties of the quenching prediction model. Thus, the calculated measured energies of the different particle species from the simulations are well able to reflect the reality. A quantitative evaluation of the onboard data processing based on sample measurements shows a good agreement with the simulation. Due to these results, it was concluded, that the onboard data processing, developed on the basis of particle simulations, is working as expected for real particles and is ready for the start of the mission.
After the launch of Solar Orbiter, the onboard data processing and the performance of HET is further tested and validated using the first months of available data. The study yields promising results, as both HET units, FM1 and FM2 onboard Solar Orbiter, operate nominally. In most aspects, the developed onboard data processing works as expected. The particle species separation scheme works and for most data products, it can already be concluded that they contain the ion species as predicted by the simulations. However, not for all ion species enough statistics are available to confirm a correct definition of all data products. Based on this first data, optimizations regarding the suppression of particle species contamination are already developed and installed on the FM units in the scope of this work. It can be concluded that the onboard data processing of HET, developed in the scope of this thesis, delivers plausible results and works as expected in many aspects. Still, certain aspects of the onboard data processing, identified with the first data, require further in-depth studies to develop improvements for example the observed shift in energy of the ABC 1D proton histogram. Possible

causes for this effect are presented, namely a calibration factor offset of the C detector or ionization quenching of stopping protons. Both effects could lead to the histogram shift towards lower energies.

Outlook

HET is a complex instrument, using different detector types for the measurement and identification of highly energetic charged particles. Using these measurements, HET will help to investigate the origin and acceleration mechanisms of SEPs. However, during the current unusually quiet solar minimum period, the Sun rarely produces SEP events. Still, few SEP events are observed close to the Sun, as measured by Parker Solar Probe, a mission with a comparable orbit to that of Solar Orbiter (McComas et al., 2019). With Solar Orbiter moving deeper into the heliosphere, these SEP events will also be observable with HET and the other instruments onboard Solar Orbiter. In combination with the measurements by Parker Solar Probe, new insights into the origin and acceleration processes of SEPs will be obtained by multi-point observations close to the Sun. Even during this quiet time period, HET can be used to investigate other energetic particle phenomena. Due to the unique orbit of Solar Orbiter, covering distances between 0.27 to 1.2 AU to the Sun, for example the radial dependence of the Anomalous Cosmic Ray (ACR) particle flux and composition can be investigated. The same studies can be performed at higher energies, for the Galactic Cosmic Rays (GCRs). Using this thesis as a documentation in addition with the developed tools, the data measured during these quiet solar period, can be used to further optimize the onboard data processing based on the measured fully isotropic energetic particle environment observed in space.

With the data acquired during the first month and the experiences gained in the development of the onboard data processing of HET, already some improvements for a possible successor of HET can be derived:

- HET, especially the ABnC trigger, is susceptible to contamination by particles entering the instrument not through the nominal field of view. By using an anti-coincidence detector system around the sensor head compartment, particles entering the instrument outside the nominal field of view can be identified and rejected.

- Although the BGO scintillator offers a high stopping power for energetic charged particles, it introduces several difficulties. As the scintillation light yield in BGO is highly depending on temperature, $\approx 1\%/°\mathrm{C}$, the use of this scintillation material during a mission with varying temperatures is difficult. The calibration value for the scintillation detector needs to be adapted frequently. Additionally, the effect of ionization quenching, present in scintillators, introduces uncertainties to the deposited energy in the scintillation detector. Both effects are not found in SSDs, so that a stack of SSDs, covering a lower energy range compared to HET should be considered as an alternative for future missions.

Bibliography

Agostinelli, S. et al. Geant4: a simulation toolkit. *Nuclear Instruments and Methods in Physics Research Section A: Accelerators, Spectrometers, Detectors and Associated Equipment*, 506(3):250–303, jul 2003. ISSN 01689002. doi: 10.1016/S0168-9002(03)01368-8. URL `http://linkinghub.elsevier.com/retrieve/pii/S0168900203013688`.

Agueda, N. et al. Release timescales of solar energetic particles in the low corona. *Astronomy and Astrophysics*, 570:1–12, 2014. ISSN 14320746. doi: 10.1051/0004-6361/201423549.

Allison, J. and Amako, K. Geant4 developments and applications. *IEEE Transactions on Nuclear Science*, 53(1):270–278, 2006. URL `http://ieeexplore.ieee.org/xpls/abs_all.jsp?arnumber=1610988`.

Antonucci, E. et al. Metis: the Solar Orbiter visible light and ultraviolet coronal imager. *Astronomy & Astrophysics*, jun 2019. ISSN 0004-6361. doi: 10.1051/0004-6361/201935338. URL `https://www.aanda.org/10.1051/0004-6361/201935338`.

Aschwanden, M.J. The localization of particle acceleration sites in solar flares and CMES. *Space Science Reviews*, 124(1-4):361–372, 2006. ISSN 00386308. doi: 10.1007/s11214-006-9095-9.

Avdeichikov, V. and Bergholt, L. Light output and energy resolution of CsI, YAG, GSO, BGO and LSO scintillators for light ions. *Nuclear Instruments and Methods in Physics Research*, 349:216–224, 1994. URL `http://www.sciencedirect.com/science/article/pii/0168900294906238`.

Band, D. et al. BATSE observations of gamma-ray burst spectral diversity. In *AIP Conference Proceedings 280*, pages 872–876, 1993. doi: 10.1063/1.44238. URL `http://aip.scitation.org/doi/abs/10.1063/1.44238`.

Belsky, A.N. et al. Crossluminescence in ionic crystals. *Journal of Electron Spectroscopy and Related Phenomena*, 79:111–116, 1996. ISSN 03682048. doi: 10.1016/0368-2048(96)02815-0.

Birks, J.B. Scintillations from Organic Crystals: Specific Fluorescence and Relative Response to Different Radiations. *Proceedings of the Physical Society. Section A*, 64(10):874, 1951. ISSN 0370-1298. doi: 10.1088/0370-1298/64/10/303. URL http://stacks.iop.org/0370-1298/64/i=10/a=303.

Bloch, F. Zur Bremsung rasch bewegter Teilchen beim Durchgang durch Materie. *Annalen der Physik*, 408(3):285–320, 1933. ISSN 00033804. doi: 10.1002/andp.19334080303. URL http://doi.wiley.com/10.1002/andp.19334080303.

Böttcher, S.I. Analysis of a 207 Bi spectrum measured with a Hamamatsu photo diode , a tsh310 based preamp , and the heti irena. Technical report, 2011. URL http://www.ieap.uni-kiel.de/et/people/stephan/solo/spectra/irena/2011-06-01-Bi207.pdf. Date Accessed: 17-05-2020.

Böttcher, S.I. Calibration of HET/EPT Flight Models using data obtained in thermal Vacuum. Technical report, 2018. URL http://www.ieap.uni-kiel.de/et/people/stephan/solo/eda/gse/hetept/tvcal/hetept-tvcal.pdf. Date Accessed: 17-05-2020.

Bučík, R. et al. 3 He-rich Solar Energetic Particles in Helical Jets on the Sun . *The Astrophysical Journal*, 852(2):76, 2018. ISSN 1538-4357. doi: 10.3847/1538-4357/aa9d8f.

Buranurak, S. et al. Temperature variations as a source of uncertainty in medical fiber-coupled organic plastic scintillator dosimetry. *Radiation Measurements*, 56:307–311, 2013. ISSN 13504487. doi: 10.1016/j.radmeas.2013.01.049. URL http://dx.doi.org/10.1016/j.radmeas.2013.01.049.

Buttighoffer, A. Solar electron beams associated with radio type III bursts: Propagation channels observed by Ulysses between 1 and 4 AU. *Astronomy and Astrophysics*, 335(1):295–302, 1998. ISSN 00046361.

Cane, H.V. and Reames, D.V. The relationship between energetic particles and flare properties for impulsive solar flares. *The Astrophysical Journal Supplement Series*, 73(Reames 1988):253, jun 1990. ISSN 0067-0049. doi: 10.1086/191457. URL http://adsabs.harvard.edu/doi/10.1086/191457.

Cane, H.V., McGuire, R.E. and von Rosenvinge, T.T. Two classes of solar energetic particle events associated with impulsive and long-duration soft X-ray flares. *The Astrophysical Journal*, 301:448, feb 1986. ISSN 0004-637X. doi: 10.1086/163913. URL http://adsabs.harvard.edu/doi/10.1086/163913.

Carr, C. et al. A Magnetometer For The Solar Orbiter Mission. *The Second Solar Orbiter Workshop, 16-20 October 2006, Athens, Greece, ESA Publ Div (2007)*, (June 2014), 2006. URL https://www.researchgate.net/publication/41625175_A_Magnetometer_For_The_Solar_Orbiter_Mission.

Chaiphaksa, W. et al. Moh's hardness Scale and micro vicker's hardness study of bgo and lyso inorganic scintillators. *Journal of Physics: Conference Series*, 970(1), 2018. ISSN 17426596. doi: 10.1088/1742-6596/970/1/012005.

Christian, E.R. *Evidence for Anomalous Cosmic Ray Hydrogen.* PhD thesis, California Institute of Technology, 1987. URL `https://thesis.library.caltech.edu/2309/`.

Cummings, A.C. et al. Anomalous cosmic rays in the heliosheath. *AIP Conference Proceedings*, 1039(2008):343–348, 2008. ISSN 0094243X. doi: 10.1063/1.2982469.

D. Wright, S.I. A SHORT GUIDE TO CHOOSING PHYSICS LISTS, 2013. URL `http://geant4.in2p3.fr/IMG/pdf_PhysicsLists.pdf`.

Dalla, S. et al. Time dependence of Fe/O ratio within a 3D solar energetic particle propagation model including drift. *Astronomy & Astrophysics*, 598: A73, feb 2017. ISSN 0004-6361. doi: 10.1051/0004-6361/201628618. URL `http://www.aanda.org/10.1051/0004-6361/201628618`.

Desai, M.I. et al. The seed population for energetic particles accelerated by CME-driven shocks. *Space Science Reviews*, 124(1-4):261–275, 2006. ISSN 00386308. doi: 10.1007/s11214-006-9109-7.

Desai, M. and Giacalone, J. Large gradual solar energetic particle events. *Living Reviews in Solar Physics*, 13(1):1–132, 2016. ISSN 16144961. doi: 10.1007/s41116-016-0002-5.

Dikpati, M. and Charbonneau, P. A Babcock-Leighton Flux Transport Dynamo with Solar-like Differential Rotation. *The Astrophysical Journal*, 518(1):508–520, 2002. ISSN 0004-637X. doi: 10.1086/307269.

Dikpati, M. and Gilman, P.A. Global solar dynamo models: Simulations and predictions. *Journal of Astrophysics and Astronomy*, 29(1-2):29–39, 2008. ISSN 02506335. doi: 10.1007/s12036-008-0004-3.

Dow Corning. Space-Grade Encapsulant, 2013. URL `http://www.syscoindia.com/catalogs/DC-93-500.pdf`. Date Accessed: 17-05-2020.

Drake, J.F. et al. A magnetic reconnection mechanism for ion acceleration and abundance enhancements in impulsive flares. *Astrophysical Journal*, 700(1 PART 2), 2009. ISSN 15384357. doi: 10.1088/0004-637X/700/1/L16.

Dresing, N. et al. Statistical survey of widely spread out solar electron events observed with STEREO and ACE with special attention to anisotropies. *Astronomy & Astrophysics*, 567:A27, 2014. ISSN 0004-6361. doi: 10.1051/0004-6361/201423789.

Duatis, J.S.C.d.V. EPD TM/TC Interface Control Document. Technical Report 2, Revision:8, SENER - Cerdanyola del Vallès, 2015.

Durante, M. et al. Applied nuclear physics at the new high-energy particle accelerator facilities. *Physics Reports*, 800:1–37, 2019. ISSN 03701573. doi: 10.1016/j.physrep.2019.01.004. URL `https://doi.org/10.1016/j.physrep.2019.01.004`.

Elftmann, R. et al. Temperature dependence of ionization quenching in BGO scintillators. *Nuclear Instruments and Methods in Physics Research, Section B: Beam Interactions with Materials and Atoms*, 451:93–98, 2019. ISSN 0168583X. doi: 10.1016/j.nimb.2019.05.038.

Eljen-Technology. General purpose plastic scintillator EJ-200, EJ-204, EJ-208, EJ-212. Technical Report 888, 2016. URL `https://eljentechnology.com/images/products/data_sheets/EJ-200_EJ-204_EJ-208_EJ-212.pdf`.

ESA. Solar Orbiter Definition Study. (July), 2011. URL `https://sci.esa.int/documents/34903/36699/1567255601145-Solar-Orbiter_RB_Issue_1_2011-07-22.pdf`. Date Accessed: 18.05.20.

ESA. ESA's Solar Orbiter Mission: Summary, 2020a. URL `http://sci.esa.int/solar-orbiter/51168-summary/`. Date Accessed: 08.05.20.

ESA. Solar Orbiter - Orbit, 2020b. URL `https://www.cosmos.esa.int/web/solar-orbiter-new/orbit`. Date Accessed: 08.05.20.

Fisk, L.A. and Gloeckler, G. Acceleration of Suprathermal Tails in the Solar Wind. *The Astrophysical Journal*, 686(2):1466–1473, 2008. ISSN 0004-637X. doi: 10.1086/591543.

Fisk, L.A., Kozlovsky, B. and Ramaty, R. An Interpretation of the Observed Oxygen and Nitrogen Enhancements in Low-Energy Cosmic Rays. *The Astrophysical Journal*, 190:L35, may 1974. ISSN 0004-637X. doi: 10.1086/181498. URL `http://adsabs.harvard.edu/doi/10.1086/181498`.

Gloeckler, G. et al. Unusual composition of the solar wind in the 2-3 May 1998 CME observed with SWICS on ACE. *Geophysical Research Letters*, 26(2): 157–160, 1999. ISSN 00948276. doi: 10.1029/1998GL900166.

Gomez, A.M. EPT-HET Thermal Analysis Report. Technical report, IDR/UPM, 2017. SO-EPD-KIE-RP-0030-iss3_rev1.

Gómez-Herrero, R. et al. Circumsolar energetic particle distribution on 2011 November 3. *Astrophysical Journal*, 799(1), 2015. ISSN 15384357. doi: 10.1088/0004-637X/799/1/55.

Guo, Y. et al. Solar probe plus mission design overview and mission profile. In *24th International Symposium on Space Flight Dynamics (ISSFD), Laurel, Maryland*, 2014.

Hamamatsu Photonics. Si PIN photodiode. Technical report, 2012. URL `https://www.hamamatsu.com/resources/pdf/ssd/s3590-08_etc_kpin1052e.pdf`. Date Accessed: 17-05-2020.

Hassler, D.M. et al. The Radiation Assessment Detector (RAD) investigation. *Space Science Reviews*, 170(1-4):503–558, 2012. ISSN 00386308. doi: 10.1007/s11214-012-9913-1.

Hathaway, D.H. The solar cycle. *Living Reviews in Solar Physics*, 12(1), 2015. ISSN 16144961. doi: 10.1007/lrsp-2015-4.

Horn, D., Ball, G. and Galindo-Uribarri, A. The mass dependence of CsI (Tl) scintillation response to heavy ions. *Nuclear Instruments and Methods in Physics Research Section A: Accelerators, Spectrometers, Detectors and Associated Equipment*, 320:273–276, 1992. URL `http://www.sciencedirect.com/science/article/pii/0168900292907853`.

Howard, R. et al. The Solar Orbiter Heliospheric Imager (SoloHI). *Astronomy & Astrophysics*, pages 1–23, 2019. ISSN 0004-6361. doi: 10.1051/0004-6361/201935202.

Kahler, S.W. The correlation between solar energetic particle peak intensities and speeds of coronal mass ejections: Effects of ambient particle intensities and energy spectra. *Journal of Geophysical Research: Space Physics*, 106(A10):20947–20955, 2001. ISSN 2169-9402. doi: 10.1029/2000ja002231.

Kallenrode, M.B. *Space Physics*. Advanced Texts in Physics. Springer Berlin Heidelberg, Berlin, Heidelberg, 2004. ISBN 978-3-642-05829-5. doi: 10.1007/978-3-662-09959-9. URL `http://link.springer.com/10.1007/978-3-662-09959-9`.

Kemmer, J. Improvement of detector fabrication by the planar process. *Nuclear Inst. and Methods in Physics Research, A*, 226(1):89–93, 1984. ISSN 01689002. doi: 10.1016/0168-9002(84)90173-6.

Klecker, B. et al. Anomalous Composition and Energy Spectra of Cosmic Rays below 20 MeV/Nucleon. In *International Cosmic Ray Conference*, volume 2 of *International Cosmic Ray Conference*, page 786, aug 1975.

Klecker, B. et al. Composition and energy spectra of cosmic rays between 0.6 and 24 MeV per nucleon during quiet times - Transition from a solar to the anomalous component. *The Astrophysical Journal*, 212(June 2015):290, 1977. ISSN 0004-637X. doi: 10.1086/155047.

Knoll, G.F. *Radiation detection and measurement*. John Wiley & Sons, 4 edition, 2010. ISBN 978-0-470-13148-0. URL https://www.wiley.com/en-us/Radiation+Detection+and+Measurement%2C+4th+Edition-p-9780470131480.

Krucker, S. et al. The Spectrometer/Telescope for Imaging X-rays (STIX). *Astronomy & Astrophysics*, jan 2020. ISSN 0004-6361. doi: 10.1051/0004-6361/201937362. URL https://www.aanda.org/10.1051/0004-6361/201937362.

Kühl, P. and Heber, B. Revising More Than 20 Years of EPHIN Ion Flux Data-A New Data Product for Space Weather Applications. *Space Weather*, 17(1): 84–98, 2019. ISSN 15427390. doi: 10.1029/2018SW002114.

Kulkarni, S. HET FM/FS Crystal Wrapping Procedure. Technical Report 1, IEAP Kiel, 2014a. SO-EPD-KIE-PR-0015-iss1_rev0_HET_FM-FS_Crystal_Wrapping_procedure.

Kulkarni, S. Glueing procedure for HET PQM-FM-FS photodiodes. Technical Report 1, IEAP Kiel, 2014b. SO-EPD-KIE-PR-0006-iss1_rev0_Gluing_procedure_for_HET_PQM-FM-FS_photodiodes.

Kumar, S., Reshi, B.A. and Varma, R. Comparison of Silicon, Germanium, Gallium Nitride, and Diamond for using as a detector material in experimental high energy physics. *Results in Physics*, 11(September):461–474, 2018. ISSN 22113797. doi: 10.1016/j.rinp.2018.08.045. URL https://doi.org/10.1016/j.rinp.2018.08.045.

Landau, L.D. ON THE ENERGY LOSS OF FAST PARTICLES BY IONISATION. In *Collected Papers of L.D. Landau*, volume 201, pages 417–424. Elsevier, 1965. doi: 10.1016/B978-0-08-010586-4.50061-4. URL https://www.sciencedirect.com/science/article/pii/B9780080105864500614.

Lara, F.E. Characterisation of energy channels for EPD data products. Technical report, University of Alcalá, Department of Physics and Mathematics, 2019.

Lindhard, J. and Sörensen, A.H. Relativistic theory of stopping for heavy ions. *Physical Review A*, 53(4):2443–2456, apr 1996. ISSN 1050-2947. doi: 10.1103/PhysRevA.53.2443. URL https://link.aps.org/doi/10.1103/PhysRevA.53.2443.

Lindström, G. Radiation damage in silicon detectors. *Nuclear Instruments and Methods in Physics Research, Section A: Accelerators, Spectrometers, Detectors and Associated Equipment*, 512(1-2):30–43, 2003. ISSN 01689002. doi: 10.1016/S0168-9002(03)01874-6.

Lockwood, J.A. Forbush decreases in the cosmic radiation. *Space Science Reviews*, 12(5):658–715, 1971. ISSN 00386308. doi: 10.1007/BF00173346.

MakeItFrom.com. Material Properties Database, 2019a. URL `https://www.makeitfrom.com/material-properties/ESD-Safe-Alumina`. Date Accessed: 2019-06-20.

MakeItFrom.com. Material Properties Database, 2019b. URL `https://www.makeitfrom.com/material-properties/Unfilled-PTFE`. Date Accessed: 2019-06-20.

Maksimovic, M. et al. The Solar Orbiter Radio and Plasma Waves (RPW) instrument. *Astronomy & Astrophysics*, apr 2020. ISSN 0004-6361. doi: 10.1051/0004-6361/201936214. URL `https://www.aanda.org/10.1051/0004-6361/201936214`.

Malandraki, O.E. et al. High energy solar particle events forecasting and analysis: The HESPERIA project. *Proceedings of Science*, 30-July-20, 2015. ISSN 18248039. doi: 10.22323/1.236.0215.

Marquardt, J. et al. Energy spectra of carbon and oxygen with HELIOS E6: Radial gradients of anomalous cosmic ray oxygen within 1 AU. *Astronomy and Astrophysics*, 610:1–5, 2018. ISSN 14320746. doi: 10.1051/0004-6361/201731490.

Marsch, E. et al. INTERHELIOS - Sun and Heliosphere Observer. *Crossroads for European Solar and Heliospheric Physics. Recent Achievements and Future Mission Possibilities*, 417:91, 1998. URL `https://ui.adsabs.harvard.edu/abs/1998ESASP.417...91M/abstract`.

Marsch, E. et al. Solar orbiter, a high-resolution mission to the sun and inner heliosphere. *Advances in Space Research*, 29(12):2027–2040, 2002. ISSN 02731177. doi: 10.1016/S0273-1177(02)00148-5.

Martin, C. EPT-HET FM Configuration Item Data List / As Built Configuration List. Technical report, IEAP Kiel, 2016. SO-EPD-KIE-LI-0011_iss1_rev3_EPT-HET_FM_CIDL-ABCL.

Mason, G.M., Mazur, J.E. and Dwyer, J.R. [TSUP]3[/TSUP]H[CLC]e[/CLC] Enhancements in Large Solar Energetic Particle Events. *The Astrophysical Journal*, 525(2):L133–L136, nov 1999. ISSN 0004637X. doi: 10.1086/312349. URL `http://stacks.iop.org/1538-4357/525/i=2/a=L133`.

McComas, D.J. et al. Weaker solar wind from the polar coronal holes and the whole Sun. *Geophysical Research Letters*, 35(18):1–5, 2008. ISSN 00948276. doi: 10.1029/2008GL034896.

McComas, D.J. et al. Probing the energetic particle environment near the Sun. *Nature*, 576(7786):223–227, 2019. ISSN 14764687. doi: 10.1038/s41586-019-1811-1.

Melcher, C.L. and Schweitzer, J.S. Temperature Dependence. *IEEE Transactions on Nuclear Science*, 32(1):2006–2007, 1985. doi: 10.1007/978-94-007-5509-3.

Meroli, S., Passeri, D. and Servoli, L. Energy loss measurement for charged particles in very thin silicon layers. *Journal of Instrumentation*, 6(06): P06013–P06013, jun 2011. ISSN 1748-0221. doi: 10.1088/1748-0221/6/06/P06013. URL `http://stacks.iop.org/1748-0221/6/i=06/a=P06013?key=crossref.12b099eb48bd6948fb1635ef9928b7f2`.

Mewaldt, R.A. Solar energetic particle composition, energy spectra, and space weather. *Space Science Reviews*, 124(1-4):303–316, 2006. ISSN 00386308. doi: 10.1007/s11214-006-9091-0.

Mewaldt, R.A. et al. Proton, helium, and electron spectra during the large solar particle events of October-November 2003. *Journal of Geophysical Research: Space Physics*, 110(A9):1–23, 2005. ISSN 21699402. doi: 10.1029/2005JA011038.

Mewaldt, R.A. et al. Long-term fluences of solar energetic particles from H to Fe. *Space Science Reviews*, 130(1-4):323–328, 2007. ISSN 00386308. doi: 10.1007/s11214-007-9200-8.

Mewaldt, R. et al. The Elemental Composition of 4-30 MeV/nuc Cosmic Ray Nuclei with 1 <= Z <= 8. In *International Cosmic Ray Conference*, volume 2 of *International Cosmic Ray Conference*, page 798, aug 1975. URL `https://ui.adsabs.harvard.edu/abs/1975ICRC....2..798M/abstract`.

Minasyants, G.S., Minasyants, T.M. and Tomozov, V.M. Variations in the Fe/O value resulting from changes in the ion energy in flows of accelerated solar particles. *Geomagnetism and Aeronomy*, 56(6):652–660, 2016. ISSN 0016-7932. doi: 10.1134/s0016793216060128.

Moraal, H. Cosmic ray modulation studies in the outer heliosphere. *Nuclear Physics B (Proceedings Supplements)*, 33(1-2):161–178, 1993. ISSN 09205632. doi: 10.1016/0920-5632(93)90088-N.

MORI, K., NISHIMURA, H. and NAKAYAMA, M. SCINTILLATION MECHANISM OF Bi 4 Ge 3 O 12. *Nonlinear Optics*, 29(10-12):609–613, dec 2002. ISSN 1058-7268. doi: 10.1080/1058726021000045081. URL `https://www.tandfonline.com/doi/abs/10.1080/1058726021000045081`.

Moyal, J. Theory of ionization fluctuations. *The London, Edinburgh, and Dublin Philosophical Magazine and Journal of Science*, 46(374):263–280, mar 1955. ISSN 1941-5982. doi: 10.1080/14786440308521076. URL `http://www.tandfonline.com/doi/abs/10.1080/14786440308521076`.

Müller-Mellin, R. et al. COSTEP - Comprehensive Suprathermal and Energetic Particle Analyser. *Solar Physics*, 162(1-2):483–504, dec 1995. ISSN 0038-0938. doi: 10.1007/BF00733437. URL `http://link.springer.com/10.1007/BF00733437`.

Nitta, N.V. et al. Solar Sources of Impulsive Solar Energetic Particle Events and Their Magnetic Field Connection to the Earth. *The Astrophysical Journal*, 650 (1):438–450, 2006. ISSN 0004-637X. doi: 10.1086/507442.

Parker, E.N. Dynamics of the Interplanetary Gas and Magnetic Fields. *The Astrophysical Journal*, 128(9):664, nov 1958. ISSN 0004-637X. doi: 10.1086/146579. URL `http://adsabs.harvard.edu/doi/10.1086/146579`.

Pedrini, C. Scintillation mechanisms and limiting factors on each step of relaxation of electronic excitations. *Physics of the Solid State*, 47(8):1406–1411, 2005. URL `http://link.springer.com/article/10.1134/1.2014478`.

Pedrini, C. et al. Fluorescence Properties of CeF 3 and of Some Other Cerium Doped Crystals and Glasses Under VUV and X-RAY Synchrotron Excitation . *MRS Proceedings*, 348:225–234, 1994. ISSN 0272-9172. doi: 10.1557/proc-348-225.

Peralta, L. Temperature dependence of plastic scintillators. *Nuclear Instruments and Methods in Physics Research, Section A: Accelerators, Spectrometers, Detectors and Associated Equipment*, 883(October 2017):20–23, 2018. ISSN 01689002. doi: 10.1016/j.nima.2017.11.041. URL `https://doi.org/10.1016/j.nima.2017.11.041`.

Pidol, L. et al. Optical properties and energy levels of Ce3+ in lutetium pyrosilicate scintillator crystal. *Journal of Applied Physics*, 95(12):7731–7737, 2004. ISSN 00218979. doi: 10.1063/1.1738524.

Reames, D.V. The two sources of solar energetic particles. *Space Science Reviews*, 175(1-4):53–92, 2013. ISSN 00386308. doi: 10.1007/s11214-013-9958-9.

Reames, D.V. *Solar Energetic Particles*, volume 932 of *Lecture Notes in Physics*. Springer International Publishing, Cham, 2017. ISBN 978-3-319-50870-2. doi: 10.1007/978-3-319-50871-9. URL `http://link.springer.com/10.1007/978-3-319-50871-9`.

Reid, H.A.S. and Ratcliffe, H. A review of solar type III radio bursts. *Research in Astronomy and Astrophysics*, 14(7):773–804, 2014. ISSN 16744527. doi: 10.1088/1674-4527/14/7/003.

Rochus, P. et al. The Solar Orbiter EUI instrument: The Extreme Ultraviolet Imager. *Astronomy & Astrophysics*, pages 1–23, jan 2020. ISSN 0004-6361. doi: 10.1051/0004-6361/201936663. URL https://www.aanda.org/10.1051/0004-6361/201936663.

Rodriguez-Pacheco, J. et al. The Energetic Particle Detector. Energetic particle instrument suite for the Solar Orbiter mission. *Astronomy & Astrophysics*, (2013):1–35, may 2019. ISSN 0004-6361. doi: 10.1051/0004-6361/201935287. URL https://www.aanda.org/10.1051/0004-6361/201935287.

Ruzmaikin, A. et al. The radial dependence of solar energetic particle fluxes. In *Solar Wind 11/SOHO 16, Connecting Sun and Heliosphere*, number 592, pages 441–444, 2005. URL https://ui.adsabs.harvard.edu/abs/2005ESASP.592..441R/.

Saint-Gobain Crystals. CsI (Tl), CsI (Na) Cesium Iodide Scintillation Material. Technical report, 2017. URL https://www.crystals.saint-gobain.com/sites/imdf.crystals.com/files/documents/csitl-and-na-material-data-sheet.pdf. Date Accessed: 17-05-2020.

Santin, Giovanni (ESA / ESTEC and RheaTech Ltd, O.b.o.t.G.C. General Particle Source - GPS. Technical report, 2008. URL https://indico.in2p3.fr/event/443/contributions/30784/attachments/24861/30635/GSantin_Geant4_Annecy2008_Optics_v13.ppt. Date Accessed: 18-05-2020.

Saro, S. et al. Large size foil-microchannel plate timing detectors. *Nuclear Instruments and Methods in Physics Research Section A: Accelerators, Spectrometers, Detectors and Associated Equipment*, 381(2-3):520–526, nov 1996. ISSN 01689002. doi: 10.1016/S0168-9002(96)00651-1. URL https://linkinghub.elsevier.com/retrieve/pii/S0168900296006511.

Schwenn, R. Space Weather: The Solar Perspective. *Living Reviews in Solar Physics*, 3(2), 2006. URL http://www.livingreviews.org/lrsp-2006-2. Date Accessed: 17-05-2020.

Shah, N. et al. Microhardness and radiation damage studies of proton irradiated Kapton films. *Radiation Measurements*, 36(1-6 SPEC.):699–702, 2003. ISSN 13504487. doi: 10.1016/S1350-4487(03)00229-4.

Simpson, J.A. Elemental and Isotopic Composition of the Galactic Cosmic Rays. *Annual Review of Nuclear and Particle Science*, 33(1):323–382, dec

1983. ISSN 0163-8998. doi: 10.1146/annurev.ns.33.120183.001543. URL http://www.annualreviews.org/doi/10.1146/annurev.ns.33.120183.001543.

Solanki, S., del Toro Iniesta, J. and Woch, J. The Polarimetric and Helioseismic Imager on Solar Orbiter. *Astronomy & Astrophysics*, jul 2019. ISSN 0004-6361. doi: 10.1051/0004-6361/201935325. URL https://www.aanda.org/10.1051/0004-6361/201935325.

Southwood, D. *Cosmic Vision: Space science for Europe 2015-2025*. Number 247. 2005. ISBN 9290924896.

SPICE Consortium. The Solar Orbiter SPICE instrument: An extreme UV imaging spectrometer. *Astronomy & Astrophysics*, (35338), sep 2019. ISSN 0004-6361. doi: 10.1051/0004-6361/201935574. URL https://www.aanda.org/10.1051/0004-6361/201935574.

Stone, E. et al. The Solar Isotope Spectrometer for the Advanced Composition Explorer. *Space Science Reviews*, 86(1/4):357–408, 1998. ISSN 00386308. doi: 10.1023/A:1005027929871. URL http://link.springer.com/10.1023/A:1005027929871.

Sullivan, J. Geometric factor and directional response of single and multi-element particle telescopes. *Nuclear Instruments and Methods*, 95(1):5–11, aug 1971. ISSN 0029554X. doi: 10.1016/0029-554X(71)90033-4. URL https://linkinghub.elsevier.com/retrieve/pii/0029554X71900334.

Tammen, J. *Disputation: Simulations and Tests for the High-Energy-Telescope on Solar Orbiter*. Disputation, Christian-Albrechts-Universität Kiel, 2016a.

Tammen, J. et al. Quenching comparison of BGO and BSO for heavy ions. *Nuclear Instruments and Methods in Physics Research, Section B: Beam Interactions with Materials and Atoms*, 360:129–138, 2015. ISSN 0168583X. doi: 10.1016/j.nimb.2015.07.127. URL http://dx.doi.org/10.1016/j.nimb.2015.07.127.

Tammen, J. *Simulations and Tests for the High-Energy-Telescope on Solar Orbiter*. Phd thesis, Christian-Albrechts-Universität Kiel, 2016b. URL https://macau.uni-kiel.de/receive/diss_mods_00018708.

TE-Connectivity. Surface Sensor for High Rel {&} Aerospace, 2014. URL https://datasheet.ciiva.com/16388/escc-surface-sensor-g15k4d489-16388830.pdf.

Tonetto, F. et al. Optimizing performances of CsI(Tl) crystals with a photodiode readout. *Nuclear Instruments and Methods in Physics Research Section A: Accelerators, Spectrometers, Detectors and Associated Equipment*, 420(1-2):

181–188, jan 1999. ISSN 01689002. doi: 10.1016/S0168-9002(98)01136-X. URL http://linkinghub.elsevier.com/retrieve/pii/S016890029801136X.

Tsuchida, N. et al. Temperature dependence of gamma-ray excited scintillation time profile and light yield of GSO, YSO, YAP and BGO. *Nuclear Instruments and Methods in Physics Research, Section A: Accelerators, Spectrometers, Detectors and Associated Equipment*, 385(2):290–298, 1997. ISSN 01689002. doi: 10.1016/S0168-9002(97)84721-3.

van Eijk, C.W.E. Development of inorganic scintillators. *Nuclear Instruments and Methods in Physics Research Section A: Accelerators, Spectrometers, Detectors and Associated Equipment*, 392(1-3):285–290, jun 1997. ISSN 01689002. doi: 10.1016/S0168-9002(97)00239-8. URL http://linkinghub.elsevier.com/retrieve/pii/S0168900297002398.

Van Eijk, C.W. Inorganic-scintillator development. *Nuclear Instruments and Methods in Physics Research, Section A: Accelerators, Spectrometers, Detectors and Associated Equipment*, 460(1):1–14, 2001. ISSN 01689002. doi: 10.1016/S0168-9002(00)01088-3.

Verscharen, D., Klein, K.G. and Maruca, B.A. The multi-scale nature of the solar wind. 2019. URL https://link.springer.com/article/10.1007/s41116-019-0021-0. Date Accessed: 17-05-2020.

von Rosenvinge, T. and McDonald, F. IMP-6, 7 and 8 Observations of the Composition and Time Variations of Low Energy Cosmic Rays. In *International Cosmic Ray Conference*, volume 2 of *International Cosmic Ray Conference*, page 792, aug 1975. URL adsabs.harvard.edu/abs/1975ICRC....2..792V.

Walsh, A. and De Groof, A. Orbit Plots: February 2020 Trajectory, 2020. URL https://issues.cosmos.esa.int/solarorbiterwiki/display/SOSP/Orbit+Plots. Date Accessed: 17-05-2020.

Webb, D.F. and Howard, T.A. Coronal mass ejections: Observations. *Living Reviews in Solar Physics*, 9(3), 2012. ISSN 16144961. URL http://www.livingreviews.org/lrsp-2012-3.

Webber, W. et al. Further Studies of the New Component of Cosmic Rays at Low Energies. In *International Cosmic Ray Conference*, volume 12 of *International Cosmic Ray Conference*, page 4233, jan 1975. URL https://ui.adsabs.harvard.edu/abs/1975ICRC...12.4233W/abstract. Date Accessed: 17-05-2020.

Weber, S. et al. Comparison of LuYAP, LSO, and BGO as scintillators for high resolution PET detectors. *IEEE Transactions on Nuclear Science*, 50(5):1370–1372, oct 2003. ISSN 0018-9499. doi: 10.1109/TNS.2003.817952. URL http://ieeexplore.ieee.org/lpdocs/epic03/wrapper.htm?arnumber=1236934.

Wiedenbeck, M.E. *Elemental and isotopic composition measurements of galactic cosmic rays*, volume 1516. 2013. ISBN 9780735411371. doi: 10.1063/1.4792559.

Williams, R.T. and Song, K.S. The self-trapped exciton. *Journal of Physics and Chemistry of Solids*, 51(7):679–716, 1990. ISSN 00223697. doi: 10.1016/0022-3697(90)90144-5.

Wimmer-Schweingruber, R.F. et al. The Lunar Lander Neutron and Dosimetry (LND) Experiment on Chang'E 4. 2020. URL `http://arxiv.org/abs/2001.11028`.

Zeitlin, C. and La Tessa, C. The role of nuclear fragmentation in particle therapy and space radiation protection. *Frontiers in Oncology*, 6(MAR):1–13, 2016. ISSN 2234943X. doi: 10.3389/fonc.2016.00065.

Zhao, L.L. et al. ACR Proton Acceleration Associated with Reconnection Processes beyond the Heliospheric Termination Shock. *The Astrophysical Journal*, 886(2):144, 2019. ISSN 1538-4357. doi: 10.3847/1538-4357/ab4db4.

A. Appendices

A.1 HET V0008 data product specifications

In the following, the data product specifications for all HET data products of the HET configuration version V0008 are given. This is the most recent configuration on both HET flight models, updated on 12.05.20, when this thesis was submitted. The energy ranges, responses and the effective energy E_{eff} is calculated according to the method presented in sec. 9.2.1. E_{eff} is given for a spectral index of $\gamma = -2$.

DP name	Spec.	Bin	Cad.	E_{min} / MeV/nuc	E_{max} / MeV/nuc	Response / cm^2 sr	$E_{eff}(\gamma = -2)$ / MeV/nuc
LL_HETB_p_S	H	1	30	7.06	8.19	0.258	7.60
LL_HETB_p_S	H	2	30	8.19	9.61	0.257	8.88
LL_HETC_p_S	H	1	30	10.75	11.57	0.271	11.13
LL_HETC_p_S	H	2	30	11.57	13.68	0.269	12.59
LL_HETC_p_S	H	3	30	13.68	16.82	0.268	15.18
LL_HETC_p_S	H	4	30	16.82	22.10	0.270	19.30
LL_HETC_p_S	H	5	30	22.10	28.33	0.269	25.07
LL_HETC_p_S	H	6	30	28.33	36.39	0.271	32.19
LL_HETC_p_S	H	7	30	36.39	47.05	0.270	41.53
LL_HETC_p_S	H	8	30	47.05	63.11	0.269	54.74
LL_HETC_p_S	H	9	30	63.11	81.66	0.271	72.19
LL_HETC_p_S	H	10	30	81.66	104.80	0.262	93.05
LL_HETP_p_S	H	1	30	104.94	111.29	0.030	108.60
LL_HETP_p_S	H	2	30	111.29	144.84	0.040	131.80
LL_HETP_p_E	H	1	30	154.55	401.24	0.035	251.51
LL_HETP_p_E	H	2	30	401.24	2002.25	0.033	882.10
LL_HETB_e_S	e	1	30	0.45	0.90	0.119	0.72
LL_HETC_e_S	e	1	30	1.02	2.40	0.219	1.57
LL_HETC_e_S	e	2	30	2.40	5.99	0.217	3.96
LL_HETC_e_S	e	3	30	5.99	17.96	0.235	11.19
LL_HETB_he3_S	^{3}He	1	300	8.43	9.28	0.102	8.84
LL_HETB_he3_S	^{3}He	2	300	9.28	10.21	0.102	9.73
LL_HETB_he4_S	^{4}He	1	300	7.12	7.88	0.099	7.49
LL_HETB_he4_S	^{4}He	2	300	7.88	8.64	0.101	8.26
LL_HETC_he3_S	^{3}He	1	300	13.00	18.73	0.263	15.61
LL_HETC_he3_S	^{3}He	2	300	18.73	24.14	0.244	21.27
LL_HETC_he3_S	^{3}He	3	300	24.14	30.96	0.247	27.39
LL_HETC_he3_S	^{3}He	4	300	30.96	39.66	0.252	35.14
LL_HETC_he4_S	^{4}He	1	300	11.09	16.38	0.263	13.47
LL_HETC_he4_S	^{4}He	2	300	16.38	21.07	0.267	18.58
LL_HETC_he4_S	^{4}He	3	300	21.07	27.22	0.260	23.95
LL_HETC_he4_S	^{4}He	4	300	27.22	35.24	0.258	30.92
LL_HETC_he4_S	^{4}He	5	300	35.24	49.02	0.255	41.52
LL_HETC_he4_S	^{4}He	6	300	49.02	63.67	0.239	55.96
LL_HETC_he4_S	^{4}He	7	300	63.67	84.10	0.212	73.20
LL_HETC_he4_S	^{4}He	8	300	84.10	103.94	0.195	93.40
LL_HETB_he_S	^{3}He	1	300	8.31	8.94	0.155	8.62
LL_HETB_he_S	^{3}He	2	300	8.94	10.23	0.155	9.56
LL_HETB_he_S	^{3}He	3	300	10.23	10.55	0.027	10.43

Table A.1: LL data product specifications. Energy range, response and E_{eff} are calculated as described in sec. 9.2.1. Responses for _E data products are given for particles from one direction. Values for _S stand exemplarily for all directions, i.e. _S, _N and _D.

DP name	Spec.	Bin	Cad.	E_{min} / MeV/nuc	E_{max} / MeV/nuc	Response / cm^2 sr	$E_{eff}(\gamma = -2)$ / MeV/nuc
LL_HETB_he_S	^{3}He	4	-	-	-	-	-
LL_HETB_he_S	^{4}He	1	-	-	-	-	-
LL_HETB_he_S	^{4}He	2	300	7.06	7.88	0.162	7.46
LL_HETB_he_S	^{4}He	3	300	7.88	8.82	0.155	8.34
LL_HETB_he_S	^{4}He	4	300	8.82	9.52	0.169	9.19
LL_HETP_he_S	^{4}He	1	300	104.18	109.93	0.034	107.23
LL_HETP_he_S	^{4}He	2	300	109.93	140.59	0.044	127.24
LL_HETP_he_E	^{4}He	1	300	148.26	392.84	0.035	241.04
LL_HETP_he_E	^{4}He	2	300	392.84	2006.32	0.034	886.51
LL_HETB_cno_S	C	1	600	12.82	13.94	0.261	13.38
LL_HETB_cno_S	C	2	600	13.94	15.92	0.251	14.90
LL_HETB_cno_S	C	3	-	-	-	-	-
LL_HETB_cno_S	C	4	-	-	-	-	-
LL_HETB_cno_S	C	5	-	-	-	-	-
LL_HETB_cno_S	C	6	-	-	-	-	-
LL_HETB_cno_S	N	1	-	-	-	-	-
LL_HETB_cno_S	N	2	-	-	-	-	-
LL_HETB_cno_S	N	3	600	13.87	15.25	0.257	14.54
LL_HETB_cno_S	N	4	600	15.25	17.13	0.258	16.17
LL_HETB_cno_S	N	5	-	-	-	-	-
LL_HETB_cno_S	N	6	-	-	-	-	-
LL_HETB_cno_S	O	1	-	-	-	-	-
LL_HETB_cno_S	O	2	-	-	-	-	-
LL_HETB_cno_S	O	3	-	-	-	-	-
LL_HETB_cno_S	O	4	-	-	-	-	-
LL_HETB_cno_S	O	5	600	14.87	16.33	0.258	15.59
LL_HETB_cno_S	O	6	600	16.33	18.47	0.262	17.38
LL_HETC_cno_S	C	1	600	30.52	57.41	0.266	41.80
LL_HETC_cno_S	C	2	600	57.41	112.76	0.261	80.32
LL_HETC_cno_S	C	3	600	112.76	196.92	0.251	148.53
LL_HETC_cno_S	C	4	-	-	-	-	-
LL_HETC_cno_S	C	5	-	-	-	-	-
LL_HETC_cno_S	C	6	-	-	-	-	-
LL_HETC_cno_S	C	7	-	-	-	-	-
LL_HETC_cno_S	C	8	-	-	-	-	-
LL_HETC_cno_S	C	9	-	-	-	-	-
LL_HETC_cno_S	N	1	-	-	-	-	-
LL_HETC_cno_S	N	2	-	-	-	-	-
LL_HETC_cno_S	N	3	-	-	-	-	-

Table A.2: LL data product specifications. Energy range, response and E_{eff} are calculated as described in sec. 9.2.1. Responses for _E data products are given for particles from one direction. Values for _S stand exemplarily for all directions, i.e. _S, _N and _D.

DP name	Spec.	Bin	Cad.	E_{min} / MeV/nuc	E_{max} / MeV/nuc	Response / cm^2 sr	$E_{eff}(\gamma = -2)$ / MeV/nuc
LL_HETC_cno_S	N	4	600	33.88	64.62	0.266	46.77
LL_HETC_cno_S	N	5	600	64.62	127.12	0.261	90.55
LL_HETC_cno_S	N	6	600	127.12	216.06	0.252	165.42
LL_HETC_cno_S	N	7	-	-	-	-	-
LL_HETC_cno_S	N	8	-	-	-	-	-
LL_HETC_cno_S	N	9	-	-	-	-	-
LL_HETC_cno_S	O	1	-	-	-	-	-
LL_HETC_cno_S	O	2	-	-	-	-	-
LL_HETC_cno_S	O	3	-	-	-	-	-
LL_HETC_cno_S	O	4	-	-	-	-	-
LL_HETC_cno_S	O	5	-	-	-	-	-
LL_HETC_cno_S	O	6	-	-	-	-	-
LL_HETC_cno_S	O	7	600	36.84	70.83	0.264	51.09
LL_HETC_cno_S	O	8	600	70.83	139.71	0.261	99.59
LL_HETC_cno_S	O	9	600	139.71	234.37	0.244	180.73
LL_HETP_cno_S	C	1	3600	198.43	213.18	0.037	205.60
LL_HETP_cno_S	C	2	3600	213.18	263.91	0.039	239.03
LL_HETP_cno_S	N	1	3600	216.52	232.96	0.036	225.27
LL_HETP_cno_S	N	2	3600	232.96	289.73	0.038	261.30
LL_HETP_cno_S	O	1	3600	234.97	252.20	0.038	244.25
LL_HETP_cno_S	O	2	3600	252.20	315.06	0.038	283.12
LL_HETP_cno_E	C	1	3600	267.94	366.56	0.038	312.05
LL_HETP_cno_E	C	2	3600	366.56	2020.57	0.035	850.63
LL_HETP_cno_E	N	1	3600	292.59	756.89	0.037	467.72
LL_HETP_cno_E	N	2	3600	756.89	2008.46	0.034	1224.25
LL_HETP_cno_E	O	1	3600	330.95	2002.36	0.036	804.84
LL_HETP_cno_E	O	2	-	-	-	-	-
LL_HETB_fe_S	Fe	1	600	24.40	27.78	0.247	26.06
LL_HETB_fe_S	Fe	2	600	27.78	32.01	0.259	29.83
LL_HETC_fe_S	Fe	1	3600	82.99	155.84	0.264	113.89
LL_HETC_fe_S	Fe	2	3600	155.84	265.23	0.259	203.46
LL_HETC_fe_S	Fe	3	3600	265.23	464.03	0.246	350.65
LL_HETP_fe_S	Fe	1	3600	511.49	592.36	0.036	549.70
LL_HETC_T_p_S	H	1	5	13.71	26.08	0.271	18.93
LL_HETC_T_p_S	H	2	5	26.08	51.12	0.270	36.63
LL_HETC_T_p_S	H	3	5	51.12	104.83	0.267	73.52
LL_HETC_T_e_S	e	1	5	1.02	2.46	0.214	1.58

Table A.3: LL data product specifications. Energy range, response and E_{eff} are calculated as described in sec. 9.2.1. Responses for _E data products are given for particles from one direction. Values for _S stand exemplarily for all directions, i.e. _S, _N and _D.

DP name	Spec.	Bin	Cad.	E_{min} / MeV/nuc	E_{max} / MeV/nuc	Response / cm^2 sr	$E_{eff}(\gamma = -2)$ / MeV/nuc
NO_HETB_p_S	H	1	30	7.04	7.35	0.254	7.20
NO_HETB_p_S	H	2	30	7.35	7.89	0.255	7.62
NO_HETB_p_S	H	3	30	7.89	8.48	0.259	8.19
NO_HETB_p_S	H	4	30	8.48	9.18	0.254	8.84
NO_HETB_p_S	H	5	30	9.18	9.64	0.239	9.43
NO_HETB_tail_high_p_S	H	1	30	9.51	10.08	0.195	9.79
NU_HETB_tail_low_p_S	H	1	600	10.00	10.73	0.239	10.36
NO_HETC_p_S	H	1	30	10.60	10.69	0.181	10.55
NO_HETC_p_S	H	2	30	10.73	10.98	0.218	10.82
NO_HETC_p_S	H	3	30	10.98	11.35	0.257	11.18
NO_HETC_p_S	H	4	30	11.35	11.80	0.272	11.59
NO_HETC_p_S	H	5	30	11.80	12.43	0.271	12.13
NO_HETC_p_S	H	6	30	12.43	13.68	0.264	13.05
NO_HETC_p_S	H	7	30	13.68	14.61	0.269	14.15
NO_HETC_p_S	H	8	30	14.61	15.65	0.267	15.14
NO_HETC_p_S	H	9	30	15.65	16.82	0.268	16.24
NO_HETC_p_S	H	10	30	16.82	18.20	0.268	17.50
NO_HETC_p_S	H	11	30	18.20	19.65	0.269	18.93
NO_HETC_p_S	H	12	30	19.65	21.24	0.272	20.45
NO_HETC_p_S	H	13	30	21.24	23.12	0.267	22.18
NO_HETC_p_S	H	14	30	23.12	25.09	0.274	24.12
NO_HETC_p_S	H	15	30	25.09	27.20	0.270	26.16
NO_HETC_p_S	H	16	30	27.20	29.44	0.270	28.35
NO_HETC_p_S	H	17	30	29.44	31.97	0.268	30.75
NO_HETC_p_S	H	18	30	31.97	34.88	0.273	33.49
NO_HETC_p_S	H	19	30	34.88	37.90	0.274	36.48
NO_HETC_p_S	H	20	30	37.90	41.18	0.264	39.62
NO_HETC_p_S	H	21	30	41.18	44.99	0.273	43.22
NO_HETC_p_S	H	22	30	44.99	49.07	0.270	47.19
NO_HETC_p_S	H	23	30	49.07	53.38	0.269	51.41
NO_HETC_p_S	H	24	30	53.38	58.03	0.269	55.92
NO_HETC_p_S	H	25	30	58.03	63.10	0.269	60.80
NO_HETC_p_S	H	26	30	63.10	68.97	0.270	66.30
NO_HETC_p_S	H	27	30	68.97	75.11	0.274	72.38
NO_HETC_p_S	H	28	30	75.11	81.64	0.268	78.83
NO_HETC_p_S	H	29	30	81.64	89.46	0.258	85.99
NO_HETC_p_S	H	30	30	89.46	97.63	0.264	93.89
NO_HETC_p_S	H	31	30	97.63	104.88	0.263	101.73
NO_HETP_p_S	H	1	30	104.94	111.29	0.030	108.60
NO_HETP_p_S	H	2	30	111.29	144.84	0.040	131.80
NO_HETP_p_E	H	1	60	153.89	225.70	0.033	186.57
NO_HETP_p_E	H	2	60	225.70	401.13	0.037	303.94
NO_HETP_p_E	H	3	60	401.13	2002.25	0.033	882.05
NO_HETB_H_p_S	H	1	5	7.06	9.60	0.258	8.24
NO_HETC_H_p_S	H	1	5	10.76	18.20	0.269	13.99
NO_HETC_H_p_S	H	2	5	18.20	42.98	0.270	28.02
NO_HETC_H_p_S	H	3	5	42.98	104.82	0.268	67.36
NO_HETB_e_S	e	1	5	0.45	0.90	0.119	0.72
NO_HETC_e_S	e	1	5	1.02	2.40	0.219	1.57
NO_HETC_e_S	e	2	5	2.40	5.99	0.217	3.96
NO_HETC_e_S	e	3	5	5.99	17.96	0.235	11.19
NO_HETC_H_e_S	e	1	60	38.13	95.89	0.064	59.49
NO_HETB_he3_S	^{3}He	1	60	8.14	8.42	0.102	8.29
NO_HETB_he3_S	^{3}He	2	60	8.42	8.84	0.101	8.63
NO_HETB_he3_S	^{3}He	3	60	8.84	9.60	0.100	9.21
NO_HETB_he3_S	^{3}He	4	60	9.60	10.21	0.101	9.90
NO_HETB_he4_S	^{4}He	1	60	6.88	7.11	0.098	7.00
NO_HETB_he4_S	^{4}He	2	60	7.11	7.45	0.097	7.29
NO_HETB_he4_S	^{4}He	3	60	7.45	8.15	0.097	7.79
NO_HETB_he4_S	^{4}He	4	60	8.15	8.64	0.105	8.39
NU_HETB_he34_S	^{3}He	1	-	-	-	-	-
NU_HETB_he34_S	^{3}He	2	300	10.27	12.59	0.101	11.36
NU_HETB_he34_S	^{4}He	1	300	8.66	9.82	0.097	9.21
NU_HETB_he34_S	^{4}He	2	300	9.82	10.69	0.098	10.24
NO_HETC_he3_S	^{3}He	1	60	13.00	18.73	0.263	15.61
NO_HETC_he3_S	^{3}He	2	60	18.73	22.23	0.236	20.38
NO_HETC_he3_S	^{3}He	3	60	22.23	28.57	0.244	25.16
NO_HETC_he3_S	^{3}He	4	60	28.57	33.94	0.247	31.09
NO_HETC_he3_S	^{3}He	5	60	33.94	39.68	0.266	36.71
NO_HETC_he4_S	^{4}He	1	60	11.09	16.38	0.263	13.47
NO_HETC_he4_S	^{4}He	2	60	16.38	19.40	0.264	17.82

Table A.4: NO data product specifications. Energy range, response and E_{eff} are calculated as described in sec. 9.2.1. Responses for _E data products are given for particles from one direction. Values for _S stand exemplarily for all directions, i.e. _S, _N and _D. Cadences are given for far mode, conversion to close mode cadences is 5s:1s, 30s:5s, 60s:30s, 300s:60s, 600s:300s.

DP name	Spec.	Bin	Cad.	E_{min} / MeV/nuc	E_{max} / MeV/nuc	Response / cm^2 sr	$E_{eff}(\gamma = -2)$ / MeV/nuc
NO_HETC_he4_S	^{4}He	3	60	19.40	23.02	0.263	21.12
NO_HETC_he4_S	^{4}He	4	60	23.02	29.51	0.265	26.05
NO_HETC_he4_S	^{4}He	5	60	29.51	35.24	0.253	32.21
NO_HETC_he4_S	^{4}He	6	60	35.24	41.24	0.264	38.10
NO_HETC_he4_S	^{4}He	7	60	41.24	49.02	0.247	45.03
NO_HETC_he4_S	^{4}He	8	60	49.02	58.79	0.235	53.71
NO_HETC_he4_S	^{4}He	9	60	58.79	76.35	0.227	66.99
NO_HETC_he4_S	^{4}He	10	60	76.35	91.86	0.202	83.78
NO_HETC_he4_S	^{4}He	11	60	91.86	104.01	0.189	97.66
NO_HETB_he_S	^{3}He	1	30	8.29	8.62	0.149	8.45
NO_HETB_he_S	^{3}He	2	30	8.62	9.26	0.154	8.94
NO_HETB_he_S	^{3}He	3	30	9.26	10.23	0.155	9.74
NO_HETB_he_S	^{3}He	4	30	10.23	10.55	0.027	10.43
NO_HETB_he_S	^{3}He	5	-	-	-	-	-
NO_HETB_he_S	^{3}He	6	-	-	-	-	-
NO_HETB_he_S	^{4}He	1	-	-	-	-	-
NO_HETB_he_S	^{4}He	2	30	6.96	7.06	0.078	7.04
NO_HETB_he_S	^{4}He	3	30	7.10	7.88	0.161	7.48
NO_HETB_he_S	^{4}He	4	30	7.88	8.48	0.159	8.18
NO_HETB_he_S	^{4}He	5	30	8.48	9.17	0.155	8.82
NO_HETB_he_S	^{4}He	6	30	9.17	9.52	0.179	9.38
NO_HETP_he_S	^{4}He	1	300	104.18	109.93	0.034	107.23
NO_HETP_he_S	^{4}He	2	300	109.93	140.59	0.044	127.24
NO_HETP_he_E	^{4}He	1	300	147.42	212.18	0.035	176.43
NO_HETP_he_E	^{4}He	2	300	212.18	392.84	0.035	289.58
NO_HETP_he_E	^{4}He	3	300	392.84	2006.32	0.034	886.51
NO_HETP_he_E	^{4}He	4	-	-	-	-	-
NU_HETP_lbb_E	Li	1	-	-	-	-	-
NU_HETP_lbb_E	Li	2	600	162.71	182.60	0.032	171.00
NU_HETP_lbb_E	Li	3	600	182.60	236.26	0.035	207.25
NU_HETP_lbb_E	Li	4	600	236.26	325.33	0.034	276.89
NU_HETP_lbb_E	Li	5	600	325.33	464.05	0.037	391.58
NU_HETP_lbb_E	Be	1	600	248.11	336.74	0.034	287.67
NU_HETP_lbb_E	Be	2	600	336.74	510.45	0.034	414.76
NU_HETP_lbb_E	Be	3	600	510.45	1073.85	0.036	769.37
NU_HETP_lbb_E	Be	4	600	1073.85	2008.66	0.024	1460.05
NU_HETP_lbb_E	Be	5	-	-	-	-	-
NU_HETP_lbb_E	B	1	600	633.46	1831.61	0.032	1067.39
NU_HETP_lbb_E	B	2	-	-	-	-	-
NU_HETP_lbb_E	B	3	-	-	-	-	-
NU_HETP_lbb_E	B	4	-	-	-	-	-
NU_HETP_lbb_E	B	5	-	-	-	-	-
NO_HETC_c_S	C	1	300	21.66	30.48	0.263	25.68
NO_HETC_c_S	C	2	300	30.48	37.00	0.276	33.60
NO_HETC_c_S	C	3	300	37.00	44.64	0.255	40.66
NO_HETC_c_S	C	4	300	44.64	52.83	0.264	48.55
NO_HETC_c_S	C	5	300	52.83	62.50	0.266	57.46
NO_HETC_c_S	C	6	300	62.50	73.47	0.268	67.82
NO_HETC_c_S	C	7	300	73.47	86.76	0.266	80.01
NO_HETC_c_S	C	8	300	86.76	102.24	0.263	94.44
NO_HETC_c_S	C	9	300	102.24	121.55	0.257	111.77
NO_HETC_c_S	C	10	300	121.55	144.25	0.254	132.76
NO_HETC_c_S	C	11	300	144.25	173.18	0.239	158.20
NO_HETC_c_S	C	12	300	173.18	197.31	0.237	184.82
NO_HETC_n_S	N	1	300	23.67	33.86	0.266	28.31
NO_HETC_n_S	N	2	300	33.86	41.53	0.265	37.48
NO_HETC_n_S	N	3	300	41.53	49.91	0.266	45.51
NO_HETC_n_S	N	4	300	49.91	59.50	0.259	54.44
NO_HETC_n_S	N	5	300	59.50	69.72	0.278	64.42
NO_HETC_n_S	N	6	300	69.72	82.41	0.261	75.95
NO_HETC_n_S	N	7	300	82.41	97.63	0.263	89.91
NO_HETC_n_S	N	8	300	97.63	115.86	0.264	106.59
NO_HETC_n_S	N	9	300	115.86	137.70	0.252	126.58
NO_HETC_n_S	N	10	300	137.70	164.20	0.253	150.43
NO_HETC_n_S	N	11	300	164.20	197.55	0.239	179.84
NO_HETC_n_S	N	12	300	197.55	216.52	0.255	206.54
NO_HETC_o_S	O	1	300	25.52	36.80	0.267	30.66
NO_HETC_o_S	O	2	300	36.80	45.36	0.262	40.87
NO_HETC_o_S	O	3	300	45.36	54.49	0.266	49.76
NO_HETC_o_S	O	4	300	54.49	64.97	0.267	59.54
NO_HETC_o_S	O	5	300	64.97	77.17	0.257	70.86

Table A.5: NO data product specifications. Energy range, response and E_{eff} are calculated as described in sec. 9.2.1. Responses for _E data products are given for particles from one direction. Values for _S stand exemplarily for all directions, i.e. _S, _N and _D. Cadences are given for far mode, conversion to close mode cadences is 5s:1s, 30s:5s, 60s:30s, 300s:60s, 600s:300s.

DP name	Spec.	Bin	Cad.	E_{min} / MeV/nuc	E_{max} / MeV/nuc	Response / cm^2 sr	$E_{eff}(\gamma = -2)$ / MeV/nuc
NO_HETC_o_S	O	6	300	77.17	91.58	0.255	84.03
NO_HETC_o_S	O	7	300	91.58	108.82	0.260	99.75
NO_HETC_o_S	O	8	300	108.82	128.78	0.263	118.23
NO_HETC_o_S	O	9	300	128.78	152.75	0.263	140.29
NO_HETC_o_S	O	10	300	152.75	182.17	0.250	167.01
NO_HETC_o_S	O	11	300	182.17	216.62	0.248	199.09
NO_HETC_o_S	O	12	300	216.62	234.75	0.209	225.86
NO_HETB_c_S	C	1	300	12.54	12.81	0.217	12.74
NO_HETB_c_S	C	2	300	12.81	13.30	0.261	13.07
NO_HETB_c_S	C	3	300	13.30	13.94	0.258	13.63
NO_HETB_c_S	C	4	300	13.94	14.81	0.258	14.38
NO_HETB_c_S	C	5	300	14.81	15.93	0.241	15.36
NO_HETB_n_S	N	1	300	13.52	13.81	0.206	13.76
NO_HETB_n_S	N	2	300	13.81	14.42	0.244	14.14
NO_HETB_n_S	N	3	300	14.42	15.25	0.250	14.83
NO_HETB_n_S	N	4	300	15.25	16.08	0.258	15.67
NO_HETB_n_S	N	5	300	16.08	17.14	0.255	16.61
NO_HETB_o_S	O	1	300	14.51	14.85	0.221	14.75
NO_HETB_o_S	O	2	300	14.85	15.45	0.265	15.17
NO_HETB_o_S	O	3	300	15.45	16.33	0.246	15.90
NO_HETB_o_S	O	4	300	16.33	17.18	0.272	16.77
NO_HETB_o_S	O	5	300	17.18	18.47	0.255	17.83
NU_HETB_cno_S	C	1	600	15.93	19.66	0.258	17.70
NU_HETB_cno_S	N	1	600	17.14	21.37	0.257	19.14
NU_HETB_cno_S	O	1	600	18.51	22.93	0.255	20.61
NO_HETP_cno_S	C	1	600	198.43	213.18	0.037	205.60
NO_HETP_cno_S	C	2	600	213.18	263.91	0.039	239.03
NO_HETP_cno_S	N	1	600	216.52	232.96	0.036	225.27
NO_HETP_cno_S	N	2	600	232.96	289.73	0.038	261.30
NO_HETP_cno_S	O	1	600	234.97	252.20	0.038	244.25
NO_HETP_cno_S	O	2	600	252.20	315.06	0.038	283.12
NO_HETP_cno_E	C	1	-	-	-	-	-
NO_HETP_cno_E	C	2	-	-	-	-	-
NO_HETP_cno_E	C	3	600	273.39	366.62	0.037	316.64
NO_HETP_cno_E	C	4	600	366.62	578.37	0.037	459.54
NO_HETP_cno_E	C	5	600	578.37	2020.57	0.034	1070.33
NO_HETP_cno_E	C	6	-	-	-	-	-
NO_HETP_cno_E	N	1	600	284.29	305.66	0.028	291.70
NO_HETP_cno_E	N	2	600	305.66	434.89	0.037	363.47
NO_HETP_cno_E	N	3	600	434.89	756.94	0.037	574.08
NO_HETP_cno_E	N	4	600	756.94	2008.57	0.034	1225.31
NO_HETP_cno_E	N	5	-	-	-	-	-
NO_HETP_cno_E	N	6	-	-	-	-	-
NO_HETP_cno_E	O	1	600	330.71	476.28	0.037	395.62
NO_HETP_cno_E	O	2	600	476.28	957.11	0.037	676.60
NO_HETP_cno_E	O	3	600	957.11	2003.50	0.034	1374.94
NO_HETP_cno_E	O	4	-	-	-	-	-
NO_HETP_cno_E	O	5	-	-	-	-	-
NO_HETP_cno_E	O	6	-	-	-	-	-
NU_HETC_ne_S	Ne	1	600	28.77	42.16	0.260	34.82
NU_HETC_ne_S	Ne	2	600	42.16	52.26	0.260	46.90
NU_HETC_ne_S	Ne	3	600	52.26	62.46	0.277	57.17
NU_HETC_ne_S	Ne	4	600	62.46	75.26	0.257	68.57
NU_HETC_ne_S	Ne	5	600	75.26	97.35	0.272	85.66
NU_HETC_ne_S	Ne	6	600	97.35	115.58	0.262	106.23
NU_HETC_ne_S	Ne	7	600	115.58	137.49	0.264	126.26
NU_HETC_ne_S	Ne	8	600	137.49	163.93	0.262	150.57
NU_HETC_ne_S	Ne	9	600	163.93	195.19	0.258	179.58
NU_HETC_ne_S	Ne	10	600	195.19	235.95	0.242	215.09
NU_HETC_ne_S	Ne	11	600	235.95	268.42	0.241	251.70
NU_HETC_mg_S	Mg	1	600	31.62	46.38	0.266	38.27
NU_HETC_mg_S	Mg	2	600	46.38	56.72	0.272	51.31
NU_HETC_mg_S	Mg	3	600	56.72	69.43	0.265	62.75
NU_HETC_mg_S	Mg	4	600	69.43	82.95	0.274	75.93
NU_HETC_mg_S	Mg	5	600	82.95	108.82	0.262	95.04
NU_HETC_mg_S	Mg	6	600	108.82	129.92	0.265	118.69
NU_HETC_mg_S	Mg	7	600	129.92	155.83	0.269	142.08
NU_HETC_mg_S	Mg	8	600	155.83	186.05	0.263	170.17
NU_HETC_mg_S	Mg	9	600	186.05	222.35	0.260	203.52
NU_HETC_mg_S	Mg	10	600	222.35	268.74	0.251	244.84
NU_HETC_mg_S	Mg	11	600	268.74	299.99	0.226	284.29

Table A.6: NO data product specifications. Energy range, response and E_{eff} are calculated as described in sec. 9.2.1. Responses for _E data products are given for particles from one direction. Values for _S stand exemplarily for all directions, i.e. _S, _N and _D. Cadences are given for far mode, conversion to close mode cadences is 5s:1s, 30s:5s, 60s:30s, 300s:60s, 600s:300s.

DP name	Spec.	Bin	Cad.	E_{min} / MeV/nuc	E_{max} / MeV/nuc	Response / cm^2 sr	$E_{eff}(\gamma = -2)$ / MeV/nuc
NU_HETC_si_S	Si	1	600	34.01	49.33	0.264	40.95
NU_HETC_si_S	Si	2	600	49.33	60.84	0.270	54.83
NU_HETC_si_S	Si	3	600	60.84	74.75	0.259	67.48
NU_HETC_si_S	Si	4	600	74.75	89.16	0.274	81.66
NU_HETC_si_S	Si	5	600	89.16	117.41	0.262	102.49
NU_HETC_si_S	Si	6	600	117.41	141.14	0.266	128.91
NU_HETC_si_S	Si	7	600	141.14	168.21	0.269	154.50
NU_HETC_si_S	Si	8	600	168.21	203.02	0.258	185.33
NU_HETC_si_S	Si	9	600	203.02	248.62	0.247	224.76
NU_HETC_si_S	Si	10	600	248.62	300.01	0.247	272.97
NU_HETC_si_S	Si	11	600	300.01	330.35	0.230	314.77
NU_HETC_s_S	S	1	600	36.09	52.24	0.263	43.41
NU_HETC_s_S	S	2	600	52.24	64.75	0.270	58.14
NU_HETC_s_S	S	3	600	64.75	79.00	0.263	71.46
NU_HETC_s_S	S	4	600	79.00	94.83	0.266	86.60
NU_HETC_s_S	S	5	600	94.83	125.90	0.260	109.39
NU_HETC_s_S	S	6	600	125.90	151.74	0.260	138.27
NU_HETC_s_S	S	7	600	151.74	182.12	0.267	166.52
NU_HETC_s_S	S	8	600	182.12	221.25	0.265	201.19
NU_HETC_s_S	S	9	600	221.25	270.24	0.244	244.70
NU_HETC_s_S	S	10	600	270.24	329.11	0.243	297.90
NU_HETC_s_S	S	11	600	329.11	358.88	0.223	343.53
NU_HETB_ne_S	Ne	1	600	16.20	16.63	0.229	16.50
NU_HETB_ne_S	Ne	2	600	16.63	17.36	0.258	16.99
NU_HETB_ne_S	Ne	3	600	17.36	18.23	0.267	17.80
NU_HETB_ne_S	Ne	4	600	18.23	19.44	0.257	18.83
NU_HETB_ne_S	Ne	5	600	19.44	20.89	0.255	20.16
NU_HETB_mg_S	Mg	1	600	17.69	18.19	0.240	18.01
NU_HETB_mg_S	Mg	2	600	18.19	18.96	0.269	18.59
NU_HETB_mg_S	Mg	3	600	18.96	20.16	0.247	19.55
NU_HETB_mg_S	Mg	4	600	20.16	21.34	0.271	20.75
NU_HETB_mg_S	Mg	5	600	21.34	22.66	0.275	22.02
NU_HETB_si_S	Si	1	600	19.03	19.45	0.273	19.34
NU_HETB_si_S	Si	2	600	19.45	20.43	0.246	19.96
NU_HETB_si_S	Si	3	600	20.43	21.65	0.253	21.04
NU_HETB_si_S	Si	4	600	21.65	23.22	0.241	22.43
NU_HETB_si_S	Si	5	600	23.22	24.78	0.257	23.99
NU_HETB_s_S	S	1	600	20.19	20.85	0.225	20.59
NU_HETB_s_S	S	2	600	20.85	21.77	0.270	21.32
NU_HETB_s_S	S	3	600	21.77	23.18	0.244	22.48
NU_HETB_s_S	S	4	600	23.18	24.55	0.269	23.88
NU_HETB_s_S	S	5	600	24.55	26.37	0.248	25.47
NU_HETB_wpen_nemgsis_S	Ne	1	600	20.93	25.76	0.257	23.22
NU_HETB_wpen_nemgsis_S	Mg	1	600	22.69	28.28	0.251	25.35
NU_HETB_wpen_nemgsis_S	Si	1	600	24.80	30.54	0.256	27.52
NU_HETB_wpen_nemgsis_S	S	1	600	26.39	32.57	0.253	29.33
NU_HETP_nemgsis_E	Ne	1	-	-	-	-	-
NU_HETP_nemgsis_E	Ne	2	-	-	-	-	-
NU_HETP_nemgsis_E	Ne	3	-	-	-	-	-
NU_HETP_nemgsis_E	Ne	4	-	-	-	-	-
NU_HETP_nemgsis_E	Ne	5	-	-	-	-	-
NU_HETP_nemgsis_E	Ne	6	3600	358.25	487.41	0.037	416.27
NU_HETP_nemgsis_E	Ne	7	3600	487.41	915.03	0.038	668.39
NU_HETP_nemgsis_E	Mg	1	-	-	-	-	-
NU_HETP_nemgsis_E	Mg	2	-	-	-	-	-
NU_HETP_nemgsis_E	Mg	3	-	-	-	-	-
NU_HETP_nemgsis_E	Mg	4	3600	398.22	445.29	0.037	418.30
NU_HETP_nemgsis_E	Mg	5	3600	445.29	707.36	0.036	557.25
NU_HETP_nemgsis_E	Mg	6	3600	707.36	1999.36	0.035	1180.00
NU_HETP_nemgsis_E	Mg	7	-	-	-	-	-
NU_HETP_nemgsis_E	Si	1	-	-	-	-	-
NU_HETP_nemgsis_E	Si	2	-	-	-	-	-
NU_HETP_nemgsis_E	Si	3	3600	430.48	529.67	0.037	474.04
NU_HETP_nemgsis_E	Si	4	3600	529.67	938.01	0.036	699.64
NU_HETP_nemgsis_E	Si	5	3600	938.01	2010.18	0.036	1354.15
NU_HETP_nemgsis_E	Si	6	-	-	-	-	-
NU_HETP_nemgsis_E	Si	7	-	-	-	-	-
NU_HETP_nemgsis_E	S	1	-	-	-	-	-
NU_HETP_nemgsis_E	S	2	3600	467.94	589.39	0.036	520.65
NU_HETP_nemgsis_E	S	3	3600	589.39	1117.22	0.035	804.42
NU_HETP_nemgsis_E	S	4	3600	1117.22	2004.20	0.035	1455.52

Table A.7: NO data product specifications. Energy range, response and E_{eff} are calculated as described in sec. 9.2.1. Responses for _E data products are given for particles from one direction. Values for _S stand exemplarily for all directions, i.e. _S, _N and _D. Cadences are given for far mode, conversion to close mode cadences is 5s:1s, 30s:5s, 60s:30s, 300s:60s, 600s:300s.

DP name	Spec.	Bin	Cad.	E_{min} / MeV/nuc	E_{max} / MeV/nuc	Response / cm^2 sr	$E_{eff}(\gamma = -2)$ / MeV/nuc
NU_HETP_nemgsis_E	S	5	-	-	-	-	-
NU_HETP_nemgsis_E	S	6	-	-	-	-	-
NU_HETP_nemgsis_E	S	7	-	-	-	-	-
NU_HETC_ar_S	Ar	1	600	35.67	51.21	0.267	42.80
NU_HETC_ar_S	Ar	2	600	51.21	64.03	0.267	57.32
NU_HETC_ar_S	Ar	3	600	64.03	77.93	0.273	70.76
NU_HETC_ar_S	Ar	4	600	77.93	96.10	0.256	86.60
NU_HETC_ar_S	Ar	5	600	96.10	115.43	0.267	105.34
NU_HETC_ar_S	Ar	6	600	115.43	138.83	0.265	126.67
NU_HETC_ar_S	Ar	7	600	138.83	168.10	0.263	153.04
NU_HETC_ar_S	Ar	8	600	168.10	204.00	0.261	185.73
NU_HETC_ar_S	Ar	9	600	204.00	247.60	0.256	225.68
NU_HETC_ar_S	Ar	10	600	247.60	305.92	0.239	276.07
NU_HETC_ar_S	Ar	11	600	305.92	361.40	0.233	332.39
NU_HETC_ca_S	Ca	1	600	39.18	55.53	0.264	46.67
NU_HETC_ca_S	Ca	2	600	55.53	69.26	0.268	62.05
NU_HETC_ca_S	Ca	3	600	69.26	85.32	0.264	76.99
NU_HETC_ca_S	Ca	4	600	85.32	105.11	0.258	94.78
NU_HETC_ca_S	Ca	5	600	105.11	128.25	0.245	116.10
NU_HETC_ca_S	Ca	6	600	128.25	154.43	0.248	140.72
NU_HETC_ca_S	Ca	7	600	154.43	188.08	0.240	170.70
NU_HETC_ca_S	Ca	8	600	188.08	228.78	0.241	207.89
NU_HETC_ca_S	Ca	9	600	228.78	282.22	0.242	254.78
NU_HETC_ca_S	Ca	10	600	282.22	352.36	0.232	315.43
NU_HETC_ca_S	Ca	11	600	352.36	412.67	0.228	380.85
NO_HETC_fe_S	Fe	1	600	42.12	58.86	0.267	49.82
NO_HETC_fe_S	Fe	2	600	58.86	82.94	0.270	69.98
NO_HETC_fe_S	Fe	3	600	82.94	102.71	0.266	92.52
NO_HETC_fe_S	Fe	4	600	102.71	128.63	0.258	115.02
NO_HETC_fe_S	Fe	5	600	128.63	155.84	0.270	141.67
NO_HETC_fe_S	Fe	6	600	155.84	192.43	0.263	173.53
NO_HETC_fe_S	Fe	7	600	192.43	215.24	0.251	203.73
NO_HETC_fe_S	Fe	8	600	215.24	265.23	0.260	238.94
NO_HETC_fe_S	Fe	9	600	265.23	332.62	0.246	297.29
NO_HETC_fe_S	Fe	10	600	332.62	412.65	0.252	370.11
NO_HETC_fe_S	Fe	11	600	412.65	465.66	0.228	438.22
NU_HETC_ni_S	Ni	1	600	44.10	61.08	0.260	51.83
NU_HETC_ni_S	Ni	2	600	61.08	88.19	0.256	73.47
NU_HETC_ni_S	Ni	3	600	88.19	109.73	0.267	98.25
NU_HETC_ni_S	Ni	4	600	109.73	134.50	0.266	121.64
NU_HETC_ni_S	Ni	5	600	134.50	167.21	0.253	150.04
NU_HETC_ni_S	Ni	6	600	167.21	206.35	0.234	185.53
NU_HETC_ni_S	Ni	7	600	206.35	229.07	0.240	217.02
NU_HETC_ni_S	Ni	8	600	229.07	284.75	0.241	255.66
NU_HETC_ni_S	Ni	9	600	284.75	353.45	0.245	317.81
NU_HETC_ni_S	Ni	10	600	353.45	450.16	0.230	399.18
NU_HETC_ni_S	Ni	11	600	450.16	496.00	0.242	471.61
NU_HETB_ar_S	Ar	1	600	19.86	20.49	0.244	20.26
NU_HETB_ar_S	Ar	2	600	20.49	21.72	0.244	21.10
NU_HETB_ar_S	Ar	3	600	21.72	23.04	0.262	22.37
NU_HETB_ar_S	Ar	4	600	23.04	24.44	0.266	23.75
NU_HETB_ar_S	Ar	5	600	24.44	26.17	0.258	25.33
NU_HETB_ca_S	Ca	1	600	22.00	22.72	0.247	22.41
NU_HETB_ca_S	Ca	2	600	22.72	23.85	0.273	23.29
NU_HETB_ca_S	Ca	3	600	23.85	25.45	0.250	24.65
NU_HETB_ca_S	Ca	4	600	25.45	27.29	0.244	26.36
NU_HETB_ca_S	Ca	5	600	27.29	29.25	0.265	28.26
NO_HETB_fe_S	Fe	1	600	23.66	24.41	0.291	24.09
NO_HETB_fe_S	Fe	2	600	24.41	26.03	0.241	25.23
NO_HETB_fe_S	Fe	3	600	26.03	27.78	0.253	26.90
NO_HETB_fe_S	Fe	4	600	27.78	29.80	0.257	28.77
NO_HETB_fe_S	Fe	5	600	29.80	32.01	0.261	30.90
NU_HETB_ni_S	Ni	1	600	24.83	25.88	0.234	25.39
NU_HETB_ni_S	Ni	2	600	25.88	27.23	0.273	26.56
NU_HETB_ni_S	Ni	3	600	27.23	29.27	0.246	28.26
NU_HETB_ni_S	Ni	4	600	29.27	31.47	0.247	30.36
NU_HETB_ni_S	Ni	5	600	31.47	33.79	0.259	32.62
NU_HETB_wpen_arcafeni_S	Ar	1	600	26.22	31.09	0.252	28.58
NU_HETB_wpen_arcafeni_S	Ca	1	600	29.35	35.96	0.259	32.47
NU_HETB_wpen_arcafeni_S	Fe	1	600	32.02	39.19	0.255	35.44
NU_HETB_wpen_arcafeni_S	Ni	1	600	33.83	41.16	0.257	37.35

Table A.8: NO data product specifications. Energy range, response and E_{eff} are calculated as described in sec. 9.2.1. Responses for _E data products are given for particles from one direction. Values for _S stand exemplarily for all directions, i.e. _S, _N and _D. Cadences are given for far mode, conversion to close mode cadences is 5s:1s, 30s:5s, 60s:30s, 300s:60s, 600s:300s.

DP name	Spec.	Bin	Cad.	E_{min} / MeV/nuc	E_{max} / MeV/nuc	Response / cm^2 sr	$E_{eff}(\gamma = -2)$ / MeV/nuc
NO_HETP_fe_S	Fe	1	600	465.76	509.51	0.039	486.89
NO_HETP_fe_S	Fe	2	600	509.51	592.36	0.035	549.18
NO_HETP_fe_E	Fe	1	600	593.70	719.33	0.037	649.09
NO_HETP_fe_E	Fe	2	600	719.33	1388.40	0.035	989.75
NO_HETP_fe_E	Fe	3	600	1388.40	2014.59	0.036	1623.36
NU_HETG_p_E	H	1	300	158.46	375.13	0.726	246.28
NU_HETG_p_E	H	2	300	375.13	2006.50	0.641	862.54

Table A.9: NO data product specifications. Energy range, response and E_{eff} are calculated as described in sec. 9.2.1. Responses for _E data products are given for particles from one direction. Values for _S stand exemplarily for all directions, i.e. _S, _N and _D. Cadences are given for far mode, conversion to close mode cadences is 5s:1s, 30s:5s, 60s:30s, 300s:60s, 600s:300s.

DP name	Spec.	Bin	Cad.	E_{min} / MeV/nuc	E_{max} / MeV/nuc	Response / cm^2 sr	$E_{eff}(\gamma = -2)$ / MeV/nuc
B2_HETB_p_S	H	1	1	7.04	7.35	0.254	7.20
B2_HETB_p_S	H	2	1	7.35	7.62	0.260	7.49
B2_HETB_p_S	H	3	1	7.62	8.19	0.253	7.91
B2_HETB_p_S	H	4	1	8.19	8.82	0.255	8.50
B2_HETB_p_S	H	5	1	8.82	9.52	0.251	9.17
B2_HETB_p_S	H	6	1	9.52	9.78	0.108	9.66
B2_HETC_p_S	H	1	-	-	-	-	-
B2_HETC_p_S	H	2	1	10.61	10.72	0.138	10.58
B2_HETC_p_S	H	3	1	10.72	10.84	0.185	10.72
B2_HETC_p_S	H	4	1	10.84	10.97	0.253	10.90
B2_HETC_p_S	H	5	1	10.97	11.15	0.228	11.08
B2_HETC_p_S	H	6	1	11.15	11.34	0.278	11.27
B2_HETC_p_S	H	7	1	11.34	11.57	0.251	11.47
B2_HETC_p_S	H	8	1	11.57	11.78	0.310	11.70
B2_HETC_p_S	H	9	1	11.78	12.12	0.244	11.97
B2_HETC_p_S	H	10	1	12.12	12.42	0.291	12.28
B2_HETC_p_S	H	11	1	12.42	12.81	0.270	12.63
B2_HETC_p_S	H	12	1	12.81	13.70	0.253	13.26
B2_HETC_p_S	H	13	1	13.70	14.10	0.289	13.90
B2_HETC_p_S	H	14	1	14.10	14.61	0.263	14.38
B2_HETC_p_S	H	15	1	14.61	15.14	0.254	14.88
B2_HETC_p_S	H	16	1	15.14	15.64	0.287	15.40
B2_HETC_p_S	H	17	1	15.64	16.24	0.258	15.95
B2_HETC_p_S	H	18	1	16.24	16.81	0.275	16.54
B2_HETC_p_S	H	19	1	16.81	17.46	0.274	17.14
B2_HETC_p_S	H	20	1	17.46	18.20	0.262	17.85
B2_HETC_p_S	H	21	1	18.20	18.94	0.263	18.59
B2_HETC_p_S	H	22	1	18.94	19.65	0.276	19.31
B2_HETC_p_S	H	23	1	19.65	20.37	0.277	20.03
B2_HETC_p_S	H	24	1	20.37	21.23	0.267	20.83
B2_HETC_p_S	H	25	1	21.23	22.10	0.275	21.69
B2_HETC_p_S	H	26	1	22.10	23.12	0.259	22.64
B2_HETC_p_S	H	27	1	23.12	24.08	0.274	23.63
B2_HETC_p_S	H	28	1	24.08	25.09	0.274	24.63
B2_HETC_p_S	H	29	1	25.09	26.08	0.277	25.63
B2_HETC_p_S	H	30	1	26.08	27.20	0.264	26.68
B2_HETC_p_S	H	31	1	27.20	28.33	0.266	27.81
B2_HETC_p_S	H	32	1	28.33	29.44	0.275	28.93
B2_HETC_p_S	H	33	1	29.44	30.74	0.264	30.14
B2_HETC_p_S	H	34	1	30.74	31.97	0.271	31.44
B2_HETC_p_S	H	35	1	31.97	33.39	0.274	32.76
B2_HETC_p_S	H	36	1	33.39	34.87	0.272	34.22
B2_HETC_p_S	H	37	1	34.87	36.39	0.271	35.72
B2_HETC_p_S	H	38	1	36.39	37.89	0.276	37.29
B2_HETC_p_S	H	39	1	37.89	39.42	0.259	38.78
B2_HETC_p_S	H	40	1	39.42	41.18	0.268	40.38
B2_HETC_p_S	H	41	1	41.18	42.97	0.268	42.22
B2_HETC_p_S	H	42	1	42.97	44.99	0.278	44.14
B2_HETC_p_S	H	43	1	44.99	47.05	0.270	46.19
B2_HETC_p_S	H	44	1	47.05	49.07	0.270	48.27
B2_HETC_p_S	H	45	1	49.07	51.12	0.271	50.31
B2_HETC_p_S	H	46	1	51.12	53.38	0.268	52.49
B2_HETC_p_S	H	47	1	53.38	55.69	0.266	54.79
B2_HETC_p_S	H	48	1	55.69	58.03	0.272	57.09
B2_HETC_p_S	H	49	1	58.03	60.57	0.267	59.53
B2_HETC_p_S	H	50	1	60.57	63.10	0.271	62.15
B2_HETC_p_S	H	51	1	63.10	65.87	0.273	64.81
B2_HETC_p_S	H	52	1	65.87	68.97	0.267	67.74
B2_HETC_p_S	H	53	1	68.97	72.04	0.275	70.90
B2_HETC_p_S	H	54	1	72.04	75.11	0.274	73.96
B2_HETC_p_S	H	55	1	75.11	78.10	0.278	77.09
B2_HETC_p_S	H	56	1	78.10	81.64	0.260	80.45
B2_HETC_p_S	H	57	1	81.64	85.22	0.259	83.98
B2_HETC_p_S	H	58	1	85.22	89.46	0.257	87.81
B2_HETC_p_S	H	59	1	89.46	93.55	0.264	91.96
B2_HETC_p_S	H	60	1	93.55	97.63	0.264	95.95
B2_HETC_p_S	H	61	1	97.63	101.69	0.263	100.06
B2_HETC_p_S	H	62	1	101.69	104.86	0.264	103.98
B2_HETP_p_S	H	1	1	104.94	111.29	0.030	108.60
B2_HETP_p_S	H	2	1	111.29	144.84	0.040	131.80
B2_HETP_p_E	H	1	1	153.89	225.70	0.033	186.57

Table A.10: BU data product specifications. Energy range, response and E_{eff} are calculated as described in sec. 9.2.1. Responses for _E data products are given for particles from one direction. Values for _S stand exemplarily for all directions, i.e. _S, _N and _D.

DP name	Spec.	Bin	Cad.	E_{min} / MeV/nuc	E_{max} / MeV/nuc	Response / cm^2 sr	$E_{eff}(\gamma = -2)$ / MeV/nuc
B2_HETP_p_E	H	2	1	225.70	401.13	0.037	303.94
B2_HETP_p_E	H	3	1	401.13	2002.25	0.033	882.05
B2_HETB_he3_S	^{3}He	1	5	8.14	8.42	0.102	8.29
B2_HETB_he3_S	^{3}He	2	5	8.42	8.84	0.101	8.63
B2_HETB_he3_S	^{3}He	3	5	8.84	9.60	0.100	9.21
B2_HETB_he3_S	^{3}He	4	5	9.60	10.21	0.101	9.90
B2_HETB_he4_S	^{4}He	1	5	6.88	7.11	0.098	7.00
B2_HETB_he4_S	^{4}He	2	5	7.11	7.45	0.097	7.29
B2_HETB_he4_S	^{4}He	3	5	7.45	8.15	0.097	7.79
B2_HETB_he4_S	^{4}He	4	5	8.15	8.65	0.104	8.39
B2_HETB_he4_S	^{4}He	5	5	8.65	9.82	0.096	9.21
B2_HETB_he4_S	^{4}He	6	5	9.82	10.69	0.098	10.24
B2_HETC_he3_S	^{3}He	1	5	13.00	18.73	0.263	15.61
B2_HETC_he3_S	^{3}He	2	5	18.73	22.23	0.236	20.38
B2_HETC_he3_S	^{3}He	3	5	22.23	28.57	0.244	25.16
B2_HETC_he3_S	^{3}He	4	5	28.57	33.94	0.247	31.09
B2_HETC_he3_S	^{3}He	5	5	33.94	39.68	0.266	36.71
B2_HETC_he4_S	^{4}He	1	5	11.09	16.38	0.263	13.47
B2_HETC_he4_S	^{4}He	2	5	16.38	19.40	0.264	17.82
B2_HETC_he4_S	^{4}He	3	5	19.40	23.02	0.263	21.12
B2_HETC_he4_S	^{4}He	4	5	23.02	29.51	0.265	26.05
B2_HETC_he4_S	^{4}He	5	5	29.51	35.24	0.253	32.21
B2_HETC_he4_S	^{4}He	6	5	35.24	41.24	0.264	38.10
B2_HETC_he4_S	^{4}He	7	5	41.24	49.02	0.247	45.03
B2_HETC_he4_S	^{4}He	8	5	49.02	58.79	0.235	53.71
B2_HETC_he4_S	^{4}He	9	5	58.79	76.35	0.227	66.99
B2_HETC_he4_S	^{4}He	10	5	76.35	91.86	0.202	83.78
B2_HETC_he4_S	^{4}He	11	5	91.86	104.01	0.189	97.66
B2_HETB_he_S	^{3}He	1	1	8.31	8.94	0.155	8.62
B2_HETB_he_S	^{3}He	2	1	8.94	10.23	0.155	9.56
B2_HETB_he_S	^{3}He	3	1	10.23	10.55	0.027	10.43
B2_HETB_he_S	^{3}He	4	-	-	-	-	-
B2_HETB_he_S	^{4}He	1	-	-	-	-	-
B2_HETB_he_S	^{4}He	2	1	7.06	7.88	0.162	7.46
B2_HETB_he_S	^{4}He	3	1	7.88	8.82	0.155	8.34
B2_HETB_he_S	^{4}He	4	1	8.82	9.52	0.169	9.19
B2_HETP_he_S	^{4}He	1	5	104.18	109.93	0.034	107.23
B2_HETP_he_S	^{4}He	2	5	109.93	140.59	0.044	127.24
B2_HETP_he_E	^{4}He	1	5	147.42	212.18	0.035	176.43
B2_HETP_he_E	^{4}He	2	5	212.18	392.84	0.035	289.58
B2_HETP_he_E	^{4}He	3	5	392.84	2006.32	0.034	886.51
B2_HETB_e_S	e	1	1	0.42	0.87	0.088	0.69
B2_HETC_e_S	e	1	1	1.02	2.40	0.219	1.57
B2_HETC_e_S	e	2	1	2.40	5.99	0.217	3.96
B2_HETC_e_S	e	3	1	5.99	17.96	0.235	11.19
B2_HETG_p_E	H	1	5	157.07	186.60	0.733	173.77
B2_HETG_p_E	H	2	5	186.60	244.74	0.734	216.58
B2_HETG_p_E	H	3	5	244.74	319.51	0.722	284.33
B2_HETG_p_E	H	4	5	319.51	442.69	0.708	386.00
B2_HETG_p_E	H	5	5	442.69	681.12	0.810	585.21
B2_HETG_p_E	H	6	5	681.12	2002.47	0.472	1125.50

Table A.11: Burst data product specifications. Energy range, response and E_{eff} are calculated as described in sec. 9.2.1. Responses for _E data products are given for particles from one direction. Values for _S stand exemplarily for all directions, i.e. _S, _N and _D. The B2_HETB_e and B2_HETC_e data products are only generated in far mode, as the are routinely supplied with the burst cadence as a nominal data product in close mode.

A.2 BGO-Thermal experiment publication

In the following, the publication "Temperature dependence of ionization quenching in BGO scintillators" as part of this work, published in Nuclear Inst. and Methods in Physics Research B, is appended.

Nuclear Inst. and Methods in Physics Research B 451 (2019) 93–98

Contents lists available at ScienceDirect

Nuclear Inst. and Methods in Physics Research B

journal homepage: www.elsevier.com/locate/nimb

Temperature dependence of ionization quenching in BGO scintillators

R. Elftmann*, S. Boden, J.C. Terasa, R.F. Wimmer-Schweingruber

Institut für Experimentelle und Angewandte Physik, Universität Kiel, 24105 Kiel, Germany

ARTICLE INFO

Keywords:
BGO
Scintillator
Temperature dependence
Ions
Quenching

ABSTRACT

Scintillation detectors are commonly used as radiation detectors. For the detection of heavy ions a non-linearity in scintillation light output is observed which is known as ionization quenching. In this paper we investigate whether the ionization quenching for BGO scintillators depends on temperature. This would impact the validity of ionization quenching correction models in temperature unstable environments. We measured temperature dependent light output curves for several ion species at different energies at the Heavy Ion Medical Accelerator in Chiba (HIMAC), Japan. We find that the normalized temperature dependent light output curves show the same temperature dependence for all ion species and energies. Therefore, we conclude that the effect of ionization quenching in BGO is independent of temperature. Thus the temperature dependence of scintillation light output and the effect of ionization quenching are independent and can be separately correct by the already developed models for the scintillation light output of BGO.

1. Introduction

Scintillation detectors are used in many different applications such as radiation and particle detection or medical screening devices as well as in challenging temperature environments like oil-well logging or even space missions [12]. For particle detection the very high stopping power of inorganic scintillation detectors is important especially for space-missions since detector mass and size are restricted. Because of this, scintillation detectors with high density and high atomic numbers are often chosen for these purposes, e.g. thallium-doped caesium iodide for the Mars Science Laboratory's Radiation Assessment Detector on NASA's Curiosity rover [5] or $Bi_4Ge_3O_{12}$ (BGO) for the High Energy Telescope (HET) [15] on ESA's Solar Orbiter [11,14]. However, the light output of many commonly used inorganic scintillation detectors is strongly temperature dependent [21,13,20]. Therefore, a temperature dependent calibration for scintillation detectors in temperature unstable environments is necessary.

For BGO various studies to investigate the temperature dependent light output using γ-rays have been performed [12,21,20]. [12] suggested that electron excitations to radiationless transitions compete with the normal scintillation process. With increasing temperature the probability for the excitation to a radiationless transition increases and less scintillation light is produced. This effect is known as thermal quenching. It is unclear whether the results from the γ-ray studies may be applied to the detection of hadrons as well, as to our knowledge no temperature studies have been performed with ions so far. The detection of ions with scintillation detectors is more challenging compared to the detection of light particles like γ-rays or cosmic muons. For ions heavier than hydrogen the loss of scintillation light due to so called ionization quenching has to be considered since it was found that high ionization densities lead to an increase in non-radiative transitions [9]. To calculate the light loss, models are developed which are dependent on ion species, ion energy and the scintillator material [9,17]. Due to the unavailability of temperature studies with heavy ions, the temperature dependence of these particles is unknown. Therefore it is unclear if the ionization quenching correction models also need to be temperature dependent.

In this paper we investigate whether thermal- and ionization quenching are coupled in BGO scintillators. If this is the case, we would expect two trends in the temperature dependent light output curves. The first trend that we would expect is an increase in light output at lower temperatures similar to the findings in the previous studies [12,21,20]. Additionally, we would expect a second trend regarding ion species and also regarding their energy. While high energy protons do not show the effect of ionization quenching, it is very distinct for heavier particles that create high ionization densities along their particle tracks according to Eq. (1). Eq. (1) is an approximation of the Bethe-Bloch-Equation [10] where Z is the charge and E the energy of the incident particle. Therefore we expect different slopes for example for protons and each of the heavier ion species in the temperature dependent light output curves in case the two effects are coupled.

* Corresponding author.
E-mail address: elftmann@physik.uni-kiel.de (R. Elftmann).

https://doi.org/10.1016/j.nimb.2019.05.038
Received 18 March 2019; Received in revised form 8 May 2019; Accepted 13 May 2019
Available online 18 May 2019
0168-583X/ © 2019 Elsevier B.V. All rights reserved.

$$\frac{dE}{dx} \propto \frac{Z^2}{E} \quad (1)$$

To increase the available number of temperature dependent light output curves we do not only use different ion species, but also different energies for each ion species. By using polyethylene (PE) absorbers we reduce the particle's energy, and this leads to higher ionization densities along the particle track in the scintillator according Eq. (1). The higher ionization densities lead to an increase in ionization quenching.

For Solar Orbiter's HET the outcome of this study is vital, since its main purpose is to measure high energy ions in a challenging temperature environment. The orbit of the mission reaches as close to the sun as 0.3 astronomical units and out to earth orbit at 1 astronomical unit. For HET the expected temperature range is between −30 °C and +17 °C. If both light loss mechanisms were coupled, ionization quenching models would need to be temperature dependent as well. If thermal- and ionization quenching are independent, the correct energy deposition in scintillation detectors may be determined by a combination of a thermal calibration and the classical ion species and energy dependent quenching model.

2. Ionization quenching

Organic, as well as inorganic scintillators suffer from an effect known as ionization quenching. The effect manifests itself as a non-linearity in the light output of the scintillator, and was first described in detail by Birks [9]. For particles that produce only low ionization densities in scintillation materials, the light output per path length, dL/dx is proportional to the energy loss of the particle per path length dE/dx. The proportionality factor S is called the material specific scintillation efficiency:

$$\frac{dL}{dx} = S\frac{dE}{dx} \quad (2)$$

For high energy heavy ions this relation is no longer valid, since these produce very high ionization densities which lead to non-radiative de-excitations and thus a loss in scintillation light. For these particles Eq. (2) transforms into Eq. (3), the so called Birks law, with an additional parameter k_B which is the material specific Birks constant [9]:

$$\frac{dL}{dx} = S\frac{\frac{dE}{dx}}{1 + k_B\frac{dE}{dx}} \quad (3)$$

To illustrate the effect of ionization quenching we use measurements performed with an engineering model of Solar Orbiter's HET at the Heavy Ion Medical Accelerator in Chiba (HIMAC), Japan [7]. In Fig. 1 we compare measurements (in black) of different ion species with the corresponding GEANT4 (Geometry And Tracking) simulations in red [1] for some exemplary energies. The HET consists of four silicon detectors. Two are located in front of a hexagonal, 2 cm thick BGO crystal and two are located behind the crystal. Silicon detectors are unaffected by ionization quenching. To create Fig. 1 we used the data of one of the front silicon detectors and the data of the BGO crystal itself. The GEANT4 simulation calculates the energy deposition in both detector materials but does not include electron–hole pair or scintillation light creation in the detectors. Hence, the effect of ionization quenching is not taken into account in the simulation. For protons, experimental and simulation data agree very well for the scintillator and the silicon detector. For heavier ions a mismatch between simulation and experiment for the scintillator is observed due to ionization quenching. In order to calculate the deposited energy for heavy ions from the measured light output, a scintillator specific quenching model has to be used e.g. [17,8]. For instance, using a data set from HIMAC with multiple energies, the Birks constant k_B as utilized in Eq. (3) is determined for BGO in Tammen et al. [17]. However, here the displayed data is merely used for illustration purposes, since a determination of the Birks constant is not necessary for the investigation of the temperature dependency of ionization quenching.

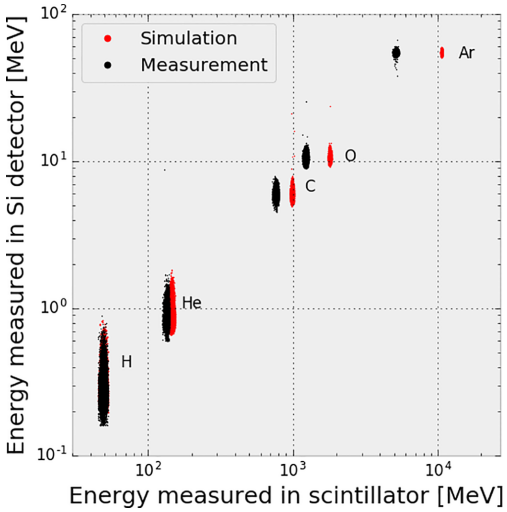

Fig. 1. Illustration of ionization quenching in BGO scintillators using data taken with an engineering model of Solar Orbiter's HET. A comparison of experimental and simulation data for different ion species is displayed. For ions heavier than Protons ionization quenching induced mismatch between simulation and experiment is observed for the scintillator.

3. Instrument description

For our study we used and constructed an instrument that was designed to perform thermal experiments at high energy ion beam facilities. The instrument consists of a detector compartment (i) and an electronics compartment (ii) which are both shown on the right hand side of Fig. 2. The contents of both compartments are described in detail in the following sections.

3.1. Detectors

The detector compartment contains two detectors, a hexagonal, 2 cm thick BGO scintillator manufactured by Scionix Holland and a Hamamatsu photo diode used as a tracking detector. The scintillator is

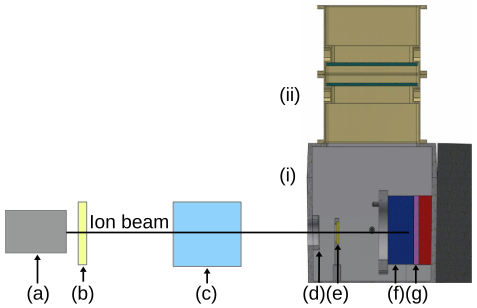

Fig. 2. Schematic of the experimental setup including CAD image of the instrument. The distance between the beam exit and the instrument is ≈60 cm. See text for further explanation.

Table 1
For each ion species three absorber thicknesses are investigated and sampled with different temperatures. The order of temperatures represents the order in which the data was taken.

Ion species – Prim. energy [MeV/nuc]	Absorber thickness [mm]	Temperatures [°C]
H - 180		
	0	24.5, 28.8, 20.7, 11.9, −2.2, −7.8
	120	−7.8, −2.1, 11.8, 20.4, 31.9, 24.8
	180	24.8, 32.6, 20.7, 11.9, −2.2, −7.9
C - 400		
	0	24.5, 21.4, 16.2, 9.0, −0.8, −4.0
	150	−3.6, −0.4, 8.8, 15.8, 20.8, 24.8
	210	24.8, 21.1, 16.0, 9.0, −0.3, −3.5
Ne - 600		
	0	24.2, 32.6, 19.4, 11.5, −2.6, −8.4
	160	−8.1, −2.5, 11.1, 19.1, 31.9, 24.6
	270	−8.3, −2.5, 11.6, 19.4, 24.7, 32.9
Fe - 500		
	0	24.7, 34.4, 21.6, 16.3, 8.7, −0.6, −5.8
	20	−5.7, −0.3, 8.7, 15.9, 20.9, 35.3, 24.9
	60	24.8, 16.1, 9.1

glued directly onto a Hebei TEC1-120706 Peltier device [6] to control its temperature. The Peltier device itself is mounted on a copper block that acts as a heat sink and conducts the heat to a radiator. The light produced by the scintillator is detected by two Hamamatsu S3590-19 PIN photodiodes [4]. These are glued to two opposing outer surfaces of the crystal using Dow Corning 93–500 Space Grade Encapsulant [2], a transparent rubber-like space-grade glue. This detection technique is inherited from HET. The scintillation crystal surfaces are roughened prior to gluing to optimize the optical coupling. A combination of 3 layers of Millipore cellulose filtration paper and several layers of PTFE tape is used to avoid the loss of scintillation light [19]. Since the surface of the Peltier device is made of white ceramics no additional reflective material is inserted in-between the crystal and the Peltier device. The temperature of the crystal is measured directly on one of the outer crystal surfaces with a TE Connectivity G15K4D489 space qualified thermistor [18] with negative temperature coefficient (NTC). The thermistor is glued to the scintillation crystal surface using Dow Corning 93–500. The tracking photodiode, a Hamamatsu S3590-19 PIN photodiode, is used to confine the measured ion beam to an entrance window. To ensure light-tightness of the detector compartment, the window is covered with a 50 µm thick Al foil. The housing features a purge-inlet for N_2 purging to avoid condensation on the crystal during low temperature tests.

3.2. Read-out electronics

The read-out electronics are located directly above the detector box and thus well decoupled from temperature influence. The signals of all three photodiodes are preamplified using charge sensitive preamplifiers followed by shapers with 2.2 µs shaping time and 1× and 14× gain. The preamplifiers are directly mounted on the pins of the photodiodes. The preamplified signal is digitized with two analog-to-digital converters (ADC) for each preamplifier using an field-programmable gate array (FPGA) readout at 3 MHz from which the pulse-height of each signal is reconstructed. The pulse height of the voltage signal, in mV, correlates linearly with the energy measured in the detector. Apart from the preamplifiers, the readout electronics are located in the electronics compartment of the instrument. The electronics readout system is the direct predecessor of the electronics of the HET instrument.

4. Experimental setup & description

The experiment was conducted at a beam line at the HIMAC facility in Japan. HIMAC provides a mono-energetic high energy ion beam. We measure the energy deposition in our scintillation detector for different temperatures, ion energies and species. The experimental setup is displayed in Fig. 2. Directly behind the beam exit (a), a thin plastic scintillator (b) is located which is part of the HIMAC setup and measures the ion flux. The beam diameter is adjusted to ≈1 cm for each ion species. To reduce the primary energy of the ions, PE blocks (c) of different thicknesses are used. The ions enter the instrument through the instrument entrance window (d) and are detected by the tracking photodiode (e). Depending on their energy and mass, the ions either penetrate or stop in the BGO scintillator (f). During the experiment, the scintillator temperature is controlled remotely by adjusting the power of the Peltier device (g). The instrument is horizontally and vertically adjusted with the beam line by using laser levels. Prior to the start of the experiment, the instrument housing is purged with N_2 for 15 min and then continuously throughout the experiment to avoid condensation on the crystal. After the setup and pre-purging is complete, the experiment is performed in the following way for each ion species:

1. Select the absorber thickness.
2. Adjust Peltier power to achieve the desired crystal temperature.
3. Wait for temperature equilibrium of the crystal.
4. Continuously take data until sufficient statistics are acquired.

The temperatures for each ion species and absorber thickness are given in Table 1 in the order in which they were measured. The ions are emitted from the accelerator in bunches, so called spills. For our measurements we chose an intensity of ≈1000 ions/ spill, with a spill duration of 2.2 s. The spill amplitude follows a Gaussian distribution. For each ion we selected three different absorber thicknesses each representing a distinct point of the Bragg curve. Fig. 3 shows the Bragg curve for carbon ions to illustrate the selection of absorber thicknesses. The displayed data were simulated with GEANT4 using a simplified experimental setup. The absorber thicknesses for each ion species were chosen such that one measurement is performed without an absorber, a second one with an absorber thickness so that the particle still penetrates the BGO scintillator and the third one with a high absorber thickness so that the particle stops in the scintillator. The idea of this method is to observe the temperature behavior for each ion species at different energies. By altering the ion's energy also the energy deposition per path length, dE/dx, of the ion in the scintillator is altered according to Eq. (1). Since ionization quenching is dependent on the dE/dx of the particle we thus receive additional data points for our investigation.

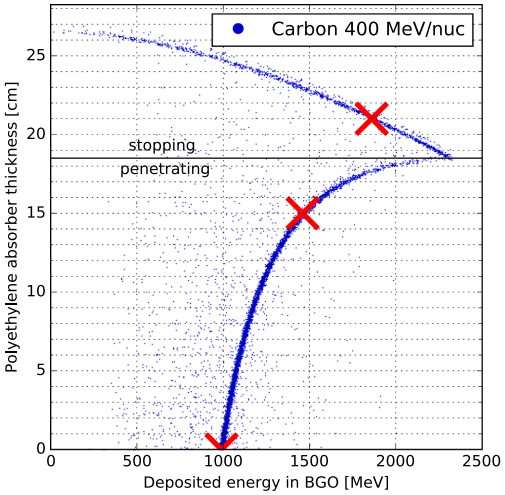

Fig. 3. Selection of absorber thicknesses, shown using the example of carbon ions. Above the black line, ions are stopping in the BGO crystal, below the black line ions penetrate the crystal. The red crosses mark the absorber thicknesses we choose for our study. (For interpretation of the references to colour in this figure legend, the reader is referred to the web version of this article.)

5. Data evaluation

For the evaluation of the acquired experimental data a pre-selection is performed. First a temperature stable time interval is chosen for each data set. From this interval the mean temperature for the data set is calculated. This is illustrated in Fig. 4. The data measured during the selected time period is further analyzed regarding the track of each detected ion. Due to beam dispersion and scattering in the absorber, not all ions will enter the instrument through the entrance window.

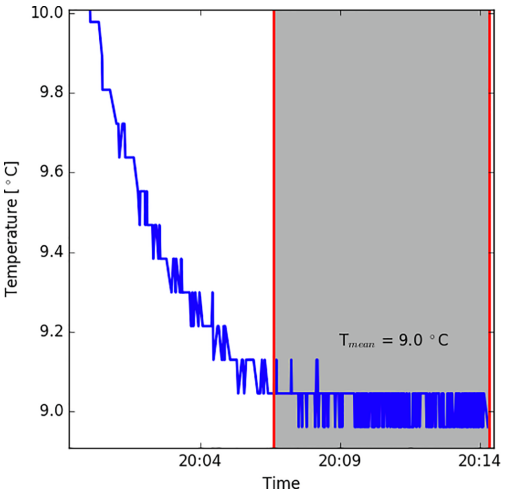

Fig. 4. Temperature selection for the carbon data displayed in Fig. 5. The grey area illustrates the selected time interval for this measurement for which the mean temperature, T_{mean} is calculated.

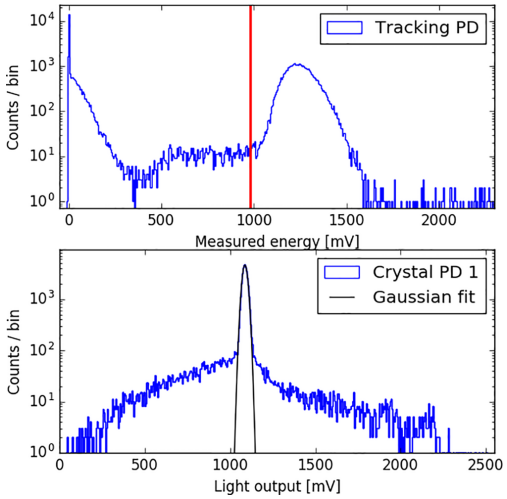

Fig. 5. Example plot showing the data filtering and analysis for carbon ions measured without an absorber at 9.0 °C. The displayed data is taken from the time interval displayed in Fig. 4. The upper panel shows the temperature restricted tracking photodiode data. The red line illustrates the minimal energy threshold at 980 mV. The lower panel shows the temperature restricted data of one of the scintillator readout photodiodes that contains only events that are above the minimum energy threshold in the tracking photodiode. The background is created due to scattering and fragmentation in the scintillation crystal but a signal-to-noise ratio of more than 100 is still achieved.

Therefore the ions detected in the BGO crystal will not form a distinct peak but will be smeared out or lead to additional peaks. To correct for this, a minimum energy threshold in the tracking photodiode is defined for each ion species and absorber-thickness combination. The threshold is chosen such that it is located just below the main ion peak. Finally we determine the light output of the crystal from the pre-selected data by fitting a Gaussian function to the main ion peak. For the light output evaluation we only use the data of readout photodiode 1 due to technical problems with readout photodiode 2. In Fig. 5 the data filtering and fitting is illustrated using carbon ions at 9.0 °C. This procedure is performed for all ion species and each absorber-thickness to investigate the individual temperature dependence of the light output. As an example we show the temperature dependence of the light output for carbon ions with an energy of 400 MeV/nuc with two different absorber thicknesses in Fig. 6. These curves are created for all ion species and each absorber-thickness combinations and are normalized to the light output value at 20.0 °C. The light output at 20 °C is determined using linear interpolation between the two data points closest to 20.0 °C. Using the normalized light output of all ions species and energies we can compare their temperature dependency. The normalized light outputs of all ion species and absorber-thickness combinations are displayed in Fig. 7.

6. Estimation of uncertainties

In this section we discuss possible error sources and their handling. We divided the discussion for every measurement parameter and error source.

6.1. Temperature error estimation

The temperature of the scintillation crystal is measured by a thermistor which is glued directly to the scintillator surface and included in

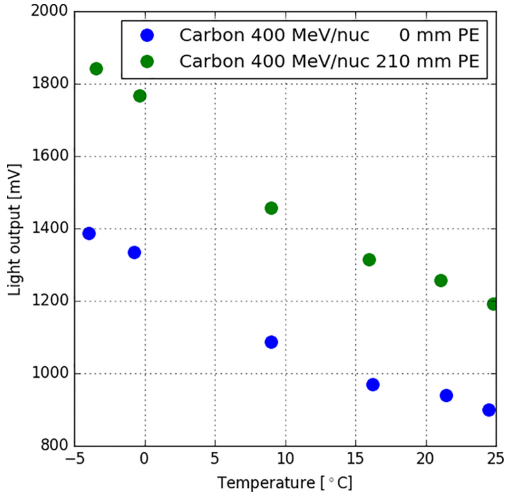

Fig. 6. Illustration of two light output curves for carbon with an initial energy of 400 MeV/nuc measured with two different PE absorber thicknesses. For further analysis the light output is normalized to the light output at 20.0 °C for each ion species and absorber thickness combination.

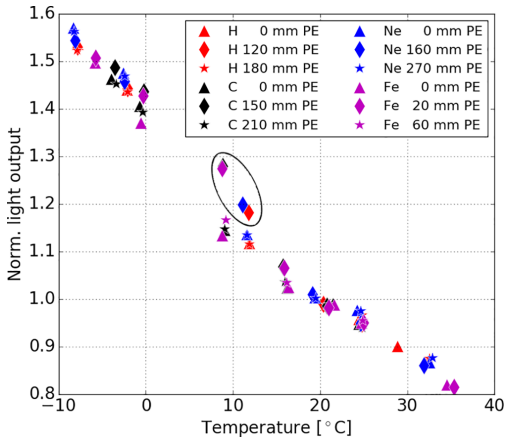

Fig. 7. Normalized light output of all ion species and PE absorber thickness combinations given in Table 1 as a function of temperature. The circled data points are separately discussed in the text.

the scintillator wrapping. The thermistor is read out by an ADC circuit of the instrument. To calculate the temperature from the thermistor resistance, we use Eq. (4), combined with Eq. (5) for the ADC voltage divider circuit. The values for the ADC reference voltage U_{ref} and the voltage divider resistor R_1 are given by design and for T_{25} and β_{25} the values are taken from the datasheet [18]. Eq. (4) is derived from the Steinhart-Hart equation [16] using $A=(1/T_0) - (1/\beta)\ln(R_0)$, $B = 1/\beta$ and $C = 0$ and solving for T. A calibrated Electronic Temperature Instruments (ETI) reference thermometer [3] is used to determine the error of our temperature measurement. It was found that the error over the complete temperature range of the experiment is below 0.5 °C. We also determined the standard deviation of the temperature in each chosen time interval for all measurements. The maximum determined standard deviation for all data points is below 0.1 °C.

$$T(R) = \frac{\beta}{\ln\left(\frac{R}{R_{25}}\right) + \frac{\beta}{T_{25}}} \tag{4}$$

$$R(T) = R_1 \frac{U(T)}{U_{ref} - U(T)} \tag{5}$$

6.2. Light output error estimation

The light output for each measurement is determined with a Gaussian fit to the main ion peak. Due to the high ion count statistics that are available for each measurement and the very good signal to noise ratio, the standard error of the mean is below 1% for all measurements.

6.3. Influence of electronics temperature

To investigate the effect of temperature changes of the electronics compartment during the experiment we use the signal of the tracking photodiode. We found that the position of the main ion peak in the data of the tracking photodiode changes less than 1% over the complete temperature range. A direct quantification of the temperature variation of the preamplifiers in our setup is not possible. However, we suspect that the temperature of the preamplifiers is almost stable, since the preamplifiers of the readout photodiodes are well insulated from the crystal by the wrapping and are only connected to the photodiodes by the two thin pins. The preamplifier of the tracking photodiode is well separated from the crystal. For the preamplifiers we use C0G temperature compensating capacitors, so we do not expect a significant temperature dependent gain influence. Even if this would be present, it would affect all measurements performed at the same temperature in the same way and thus the displayed result of the normalized temperature dependent light output curves in Fig. 7 would not change.

6.4. Light detection technique

There are four encircled data points in Fig. 7 that do not fit the trend of the others ion species. These data points are located between 8.5 and 12.0 °C and their normalized light output is slightly higher than that of the other data points in that temperature range. The affected data points are from H 120 mm PE, C 150 mm PE, Ne 160 mm PE and Fe 20 mm PE. The reason for the slightly higher light output has been investigated and we conclude that it is related to our light detection method. The light coupling of our readout photodiodes is influenced by temperature. This is related to our technique of glueing the photodiodes to the crystal. At lower temperatures the glue between the readout photodiode and the crystal surface detaches from the silicon of the photodiode. This creates a small bubble that reduces the light detection efficiency. The effect is completely reproducible and affects all performed measurements in the same way at least below 0 °C and above 20 °C. In the temperature range between 0 °C and 20 °C we find four data points that show a systematic offset. The glue detachment and re-attachment happen at different temperatures, leading to a hysteresis in the data displayed in Fig. 7. This hypothesis is backed up by the fact that all four data points that do not fit the general trend have been measured from low to high temperatures as shown in Table 1. Readout photodiode 2 is affected by this effect to a much higher degree, which is why we selected readout photodiode 1 for the detailed evaluation of the data.

Since all measurements are affected in the same way, given that they are measured either from low to high or high to low temperatures, we conclude the our results are still valid. However, a thermal calibration of our detector system is not applicable for other detector systems.

7. Discussion & conclusions

For the detection of heavy ions with scintillation detectors ionization quenching models have to be used to correct for the non-linearity in scintillation light output. If the measurement is performed in a temperature unstable environment we need to assure that thermal quenching and ionization quenching do not affect each other and that the ionization quenching models are valid for all temperatures. With our results, displayed in Fig. 7, we show that the predicted trend of the light output with temperature is present. However, no trend regarding the ion species or ion energy (absorber thickness) can be observed, as the slope for all measured ion species is identical within measurement uncertainties. Thus we conclude that thermal quenching is independent of ionization quenching in BGO. Hence we can conclude that the increase in non-radiative transitions due to high ionization densities is independent of temperature. With this result we provide evidence that a thermal calibration with γ-rays or cosmic muons may be used for all ion species and energies, and the effect of ionization quenching can be separately accounted for with the already developed ionization quenching models e.g. [17]. Furthermore, our results could contribute data for the development of future theories on the origin of ionization quenching in BGO.

Since the induced non-linearities in light output due to thermal- and ionization quenching are dependent on the scintillation material a validation of our results for other scintillation materials than BGO needs to be performed in future studies.

Acknowledgements

We would thank the NIRS-HIMAC team, especially Yukio Uchihori and Satoshi Kodaira, for the opportunity to perform research with their accelerator, and their Accelerator Engineering Corporation (AEC) for smooth beam times. This work was supported by Grant 50 OT 1202 and 50 OT 1702 from the German Space Agency (DLR).

References

[1] AgostAgostinelli, S., Allison, J., Amako, K., Apostolakis, J., Araujo, H., Arce, P., Asai, M., Axen, D., Banerjee, S., Barrand, G., Behner, F., Bellagamba, L., Boudreau, J., Broglia, L., Brunengo, A., Burkhardt, H., Chauvie, S., Chuma, J., Chytracek, R., Cooperman, G., Cosmo, G., Degtyarenko, P., Dell'Acqua, A., Depaola, G., Dietrich, D., Enami, R., Feliciello, A., Ferguson, C., Fesefeldt, H., Folger, G., Foppiano, F., Forti, A., Garelli, S., Giani, S., Giannitrapani, R., Gibin, D., Gómez Cadenas, J., González, I., Gracia Abril, G., Greeniaus, G., Greiner, W., Grichine, V., Grossheim, A., Guatelli, S., Gumplinger, P., Hamatsu, R., Hashimoto, K., Hasui, H., Heikkinen, A., Howard, A., Ivanchenko, V., Johnson, A., Jones, F., Kallenbach, J., Kanaya, N., Kawabata, M., Kawabata, Y., Kawaguti, M., Kelner, S., Kent, P., Kimura, A., Kodama, T., Kokoulin, R., Kossov, M., Kurashige, H., Lamanna, E., Lampén, T., Lara, V., Lefebure, V., Lei, F., Liendl, M., Lockman, W., Longo, F., Magni, S., Maire, M., Medernach, E., Minamimoto, K., Mora de Freitas, P., Morita, Y., Murakami, K., Nagamatu, M., Nartallo, R., Nieminen, P., Nishimura, T., Ohtsubo, K., Okamura, M., O'Neale, S., Oohata, Y., Paech, K., Perl, J., Pfeiffer, A., Pia, M., Ranjard, F., Rybin, A., Sadilov, S., Di Salvo, E., Santin, G., Sasaki, T., Savvas, N., Sawada, Y., Scherer, S., Sei, S., Sirotenko, V., Smith, D., Starkov, N., Stoecker, H., Sulkimo, J., Takahata, M., Tanaka, S., Tcherniaev, E., Safai Tehrani, E., Tropeano, M., Truscott, P., Uno, H., Urban, L., Urban, P., Verderi, M., Walkden, A., Wander, W., Weber, H., Wellisch, J., Wenaus, T., Williams, D., Wright, D., Yamada, T., Yoshida, H., Zschiesche, D., 2003. Geant4-a simulation toolkit. Nucl. Instrum. Methods Phys. Res. Section A 506 (3), 250–303. URL http://linkinghub.elsevier.com/retrieve/pii/S0168900203013688.

[2] Dow Corning, Space-Grade Encapsulant. Accessed March 14, 2019. http://www.syscoindia.com/catalogs/DC-93-500.pdf.

[3] ETI LTD, Precision Reference Thermometer datasheet. Accessed March 14, 2019. https://thermometer.co.uk/temperature-and-thermometer-calibration-equipment/919-reference-thermometer.html.

[4] Hamamatsu Photonics, Si PIN photodiode datasheet. Accessed March 14, 2019. https://www.hamamatsu.com/resources/pdf/ssd/s3204-08_etc_kpin1051e.pdf.

[5] D.M. Hassler, C. Zeitlin, R.F. Wimmer-Schweingruber, S. Böttcher, C. Martin, J. Andrews, E. Böhm, D.E. Brinza, M.A. Bullock, S. Burmeister, B. Ehresmann, M. Epperly, D. Grinspoon, J. Köhler, O. Kortmann, K. Neal, J. Peterson, A. Posner, S. Rafkin, L. Seimetz, K.D. Smith, Y. Tyler, G. Weigle, G. Reitz, F.A. Cucinotta, The Radiation Assessment Detector (RAD) investigation, Space Sci. Rev. 170 (1–4) (2012) 503–558.

[6] Hebei I.T. (Shanghai) Co., L., Performance Specifications of TEC1-12706. Accessed March 14, 2019. http://peltiermodules.com/peltier.datasheet/TEC1-12706.pdf.

[7] Y. Hirao, H. Ogawa, S. Yamada, Y. Sato, T. Yamada, K. Sato, A. Itano, M. Kanazawa, K. Noda, K. Kawachi, M. Endo, T. Kanai, T. Kohno, M. Sudou, S. Minohara, A. Kitagawa, F. Soga, E. Takada, S. Watanabe, K. Endo, M. Kumada, S. Matsumoto, Heavy ion synchrotron for medical use -HIMAC project at NIRS-Japan-, Nucl. Phys., Section A 538 (C) (1992) 541–550.

[8] D. Horn, G. Ball, A. Galindo-Uribarri, The mass dependence of CsI (Tl) scintillation response to heavy ions, Nucl. Instrum. Methods Phys. Res. Section A 320 (1992) 273–276 URL: http://www.sciencedirect.com/science/article/pii/0168900292907853.

[9] J.B. Birks, Scintillations from organic crystals: specific fluorescence and relative response to different radiations, Proc. Phys. Soc. Section A 64 (10) (1951) 874 URL: http://stacks.iop.org/0370-1298/64/i=10/a=303.

[10] J. Lindhard, A.H. Sørensen, Relativistic theory of stopping for heavy ions, Phys. Rev. A 53 (4) (1996) 2443–2456 URL: https://journals.aps.org/pra/pdf/10.1103/PhysRevA.53.2443 , https://link.aps.org/doi/10.1103/PhysRevA.53.2443.

[11] E. Marsch, R. Marsden, R. Harrison, R. Wimmer-Schweingruber, B. Fleck, Solar orbiter-mission profile, main goals and present status, Adv. Space Res. 36 (8) (2005) 1360–1366.

[12] C.L. Melcher, J.S. Schweitzer, Temperature dependence, IEEE Trans. Nucl. Sci. 32 (1) (1985) 2006–2007.

[13] M. Moszyński, A. Nassalski, A. Syntfeld-Kazuch, T. Szcześniak, W. Czarnacki, D. Wolski, G. Pausch, J. Stein, Temperature dependences of LaBr 3(Ce), LaCl3(Ce) and NaI(Tl) scintillators, Nucl. Instrum. Methods Phys. Res., Section A 568 (2) (2006) 739–751.

[14] D. Müller, R.G. Marsden, O.C. St. Cyr, H.R. Gilbert, Solar orbiter, Solar Phys. 285 (1–2) (2013) 25–70 URL: http://link.springer.com/10.1007/s11207-012-0085-7.

[15] J. Rodriguez Pacheco, R.F. Wimmer-Schweingruber, G.M. Mason, G.C. Ho, M. Prieto, H. Seifert, G.B. Andrews, S.R. Kulkarni, L. Panitzsch, S. Boden, I. Cernuda, F.E. Lara, C. Terasa, J. Almena, S. Begley, J.J. Blanco, A. Carrasco, R. Castillo, C. Drews, A.R. Dupont, C. Gordillo, D.K. Haggerty, J.R. Hayes, B. Heber, M.E. Hill, S. Kerem, V. Knierim, S. Kolbe, A. Kulemzin, D. Lario, W.J. Lees, S. Liang, D. Meziat, A. Montalvo, K.S. Nelson, P. Parra, R. Paspirgilis, A. Ravanbakhsh, M. Richards, C.E. Schlemm, B. Schuster, L. Seimetz, J. Steinhagen, J. Tammen, K. Tyagi, T. Varela, J. Yu, N. Agueda, A. Aran, T. Horbury, B. Klecker, E. Kontar, S. Krucker, O. Malandraki, C.J. Owen, D. Pacheco, B. Sanahuja, R. Vainio, J.J. Connell, S. Dalla, O. Gevin, N. Gopalswamy, Y.Y. Kartavykh, K. Kudela, O. Limousin, P. Makela, G. Mann, A. Posner, J.M. Ryan, J. Soucek, S. Hofmeister, N. Vilmer, A. Walsh, L. Wang, K. Wirth, Q. Zong, The Energetic Particle Detector (EPD), submitted, Astronomy Astrophys. (2019).

[16] J.S. Steinhart, S.R. Hart, Calibration curves for thermistors, Deep-Sea Res. Oceanogr. Abstracts 15 (4) (1968) 497–503.

[17] J. Tammen, R. Elftmann, S.R. Kulkarni, S.I. Böttcher, R.F. Wimmer-Schweingruber, Quenching comparison of BGO and BSO for heavy ions, Nuclear Instrum. Methods Phys. Res., Section B 360 (2015) 129–138, https://doi.org/10.1016/j.nimb.2015.07.127.

[18] TE-Connectivity, Surface Sensor for High Rel & Aerospace datasheet. Accessed March 14, 2019. https://datasheet.ciiva.com/16388/escc-surface-sensor-g15k4d489-16388830.pdf.

[19] F. Tonetto, U. Abbondanno, M. Chiari, P. Milazzo, L. Travaglini, Optimizing performances of CsI(Tl) crystals with a photodiode readout, Nucl. Instrum. Methods Phys. Res. Section A 420 (1–2) (Jan 1999) 181–188 URL: http://linkinghub.elsevier.com/retrieve/pii/S016890029801136X.

[20] N. Tsuchida, M. Ikeda, T. Kamae, M. Kokubun, Temperature dependence of gamma-ray excited scintillation time profile and light yield of GSO, YSO, YAP and BGO, Nucl. Instrum. Methods Phys. Res., Section A 385 (2) (1997) 290–298.

[21] S. Weber, D. Christ, M. Kurzeja, R. Engels, G. Kemmerling, H. Halling, Comparison of LuYAP, LSO, and BGO as scintillators for high resolution PET detectors, IEEE Trans. Nucl. Sci. 50 (5) (Oct 2003) 1370–1372 http://ieeexplore.ieee.org/lpdocs/epic03/wrapper.htm?arnumber=1236934.

Acknowledgments

An dieser Stelle bedanke ich mich bei Allen, die mich während meiner Dissertation und der Arbeit an HET unterstützt haben.

Insbesondere bedanke ich mich bei meinem Doktorvater Prof. Wimmer-Schweingruber für die Möglichkeit zur Promotion sowie der Gelegenheit an einer Mission wie Solar Orbiter teilzuhaben. Durch das mir entgegen gebrachte Vertrauen, wurde ich mit vielen verschiedenen Aufgaben und Projekten betraut, wodurch ich mich fachlich sowie persönlich weiterentwickeln und wichtige Erfahrungen für meine zukünftige Laufbahn sammeln konnte.

Ein weiterer Dank gilt dem gesamten Kieler Solar Orbiter Team. Speziell bei Christoph und Sebastian möchte ich mich für die Hilfe und Unterstützung in allen Aspekten bedanken.

Weiterhin danke ich Patrick Lars und Henning für das langwierige Korrekturlesen und das produktive Feedback.

Dank gilt auch meiner, Familie, aber vor Allem meiner Freundin Jasmin, die mich mit viel Geduld und Rücksicht durch alle Phasen meiner Promotion begleitet hat.

Erklärung

Ich versichere an Eides Statt, dass ich die vorliegende Dissertation in Form und Inhalt eigentständig angefertigt habe. Abgesehen von der Beratung durch meine Betreuer und der angegebenen Literatur wurde die Arbeit ohne fremde Hilfe erstellt. Ich versichere, dass ich keine andere als die angegebene Literatur verwendet habe. Diese Versicherung bezieht sich auch auf alle in dieser Arbeit enthaltenen Grafiken und bildlichen Darstellungen.
Die Arbeit als Ganzes wurde bisher keiner anderen Prüfungsbehörde vorgelegt.
Teile der Arbeit wurden bereits in Fachzeitschriften veröffentlicht und sind als solche gekennzeichnet. Die Quellennachweise der in den einzelnen Veröffentlichungen referenzierten Inhalte finden sich in der jeweiligen Veröffentlichung selbst und werden nicht zusätzlich im Quellennachweis dieser Arbeit aufgeführt. Für das Einbinden der Veröffentlichungen in diese Arbeit wurde die ausdrückliche Genehmigung der publizierenden Fachzeitschrift eingeholt.
Weiterhin erkläre ich, dass mir kein akademischer Grad entzogen wurde.
Ich erkläre abschließend, dass die Arbeit unter Einhaltung der Regeln guter wissenschaftlicher Praxis der Deutschen Forschungsgemeinschaft entstanden ist.

Kiel, Mai 2020

Robert Elftmann